Changing process of global tropospheric ozone distribution and related chemistry: a study with a coupled chemistry GCM

Kengo Sudo

Doctoral Dissertation

Department of Earth and Planetary Science
Graduate School of Science
The University of Tokyo

February 14, 2003

Abstract

Tropospheric chemistry and its changing process are simulated with a global chemical model which has been newly developed in this study. The model, developed in the framework of the Center for Climate System Research/National Institute for Environment Studies (CCSR/NIES) atmospheric general circulation model, is aimed to study tropospheric photochemistry and its influences on climate. The chemical component of the model simulates the O_3-HO_x-NO_x-CH_4-CO photochemical system and oxidation of nonmethane hydrocarbons and sulphur species. The model generally reproduces observed distributions and seasonal variations of ozone and its precursors well. The model calculates a net chemical ozone production of 367 TgO_3/yr in the global troposphere (4746 TgO_3/yr production and 4379 TgO_3/yr destruction). The estimated net O_3 flux from the stratosphere is 531 TgO_3/yr, well within the range suggested by recent studies. The calculated global OH concentration leads to a global mean CH_4 lifetime of 9.4 years in this simulation (the IPCC estimate is 9.6 years). This study estimates about 60% increase in tropospheric ozone since preindustrial times, and the resulting global mean radiative forcing from tropospheric ozone is 0.49 W m^{-2} (0.40 longwave, 0.09 shortwave), well comparable with the estimated methane forcing. The model has been used also in a simulation of the tropical tropospheric ozone changes observed during the 1997-1998 El Niño. The simulation, focused on the role of meteorological conditions in tropical ozone distribution, suggests that the observed large-scale ozone changes in the tropics are principally attributed to the horizontal shifts in the Walker Circulation, convection pattern, and water vapor associated with the El Niño event. In this study, tropospheric ozone and sulfate distributions for the next hundred years to 2100 are also simulated. For the simulation, two kinds of experiments were set up to evaluate impacts of emission change and climate change independently. In the experiment considering emission change only, global tropospheric ozone burden increased from 325 Tg in 1990 to 467 Tg (+44%) in 2100, showing significant increase in the low to midlatitudes in the Northern Hemisphere including eastern Asia (+53% in 2100). With climate change, the ozone increase was reduced in the remote lower troposphere due to more efficient ozone destruction by the reaction with water vapor, while it was enhanced in the upper troposphere in the midlatitudes according to the increase in stratospheric ozone influx predicted in the model. The simulation also indicated that the sulfate formation in liquid phase was enhanced by the increases in O_3 and H_2O_2 after around 2050 particularly in the low latitudes as in India. Global mean methane concentration increased to $\sim$4 ppmv in 2100 with emission change only, but to 3.3 ppmv with climate change as well, reflecting the impact of temperature and water vapor increases on the methane lifetime. This future simulation predicted significant increases in O_3 and sulfate aerosol particularly in eastern Asia including India to Japan for the next fifty or hundred years with considerable increases in both nitrates (NO_3^-) and sulfate (SO_4^{2-}) deposition, implying a serious environmental problem of ozone pollution and acid deposition (acid rain) for eastern Asia in future.

Acknowledgements

The studies in this thesis have been supported by many people. I am really grateful to **Prof. Masaaki Takahashi** at the Center for Climate System Research (CCSR), the University of Tokyo for a number of discussions and encouragements in the present works and for providing nice and comfortable studying environments. I wish to thank **Dr. Hajime Akimoto** at Institute for Global Change Research Frontier Research System for Global Change (FRSGC) for many comments and encouragements. I would like to give special thanks to the late **Dr. Atusi Numaguti** at the Hokkaido University (main developer of the CCSR/NIES AGCM) for many discussions and effective suggestions for the modeling works in this study. I wish to dedicate this thesis to the memory of Dr. Atusi Numaguti. **Dr. Seita Emori** at the FRSGC is appreciated for his interest in my study and comments on the climate modeling. I would thank **Dr. Masayuki Takigawa** at the FRSGC for his providing output data from his three-dimensional stratospheric chemical model and his great efforts in developing a fine transport scheme which is used also in this study, and also for many discussions and comments since he used to be at CCSR. I wish to thank **Mr. Jun-ichi Kurokawa** at the Fijitsu FIP Ltd. for his study to initiate the tropospheric chemistry modeling in the CCSR/NIES GCM. His work was my first motivation for this study. I would thank **Dr. Toshihiko Takemura** at the Kyushu University for many comments on the aerosol simulation in the CCSR/NIES GCM and encouragements in my work. I wish to thank **Mr. Kenjiro Toyota** at the FRSGC for providing useful information of atmospheric chemistry. **Mr. Manuel Capouet** at the Belgian Institute for Space Aeronomy is greatly appreciated for a lot of discussions and useful comments. **Dr. Hiroshi Kanzawa** at the National Institute for Environmental Studies (NIES) is greatly appreciated for his understanding of my study and invaluable comments. I wish to thank **Dr. Toru Nozawa** at the NIES for many comments and discussions on the climate simulation in the CCSR/NIES AGCM and for providing the data of future emission scenarios. **Dr. Tatsuya Nagashima** at the NIES is appreciated for many discussions and his encouragements with his funny words. I would express my gratitude to **Dr. Sushil Chandra** and **Dr. Jerry Ziemke** at the NASA/Goddard Space Flight Center for providing data on the tropospheric column ozone derived by the CCD technique and for invaluable comments. I also thank **Dr. Masatomo Fujiwara** and **Dr. Masato Shiotani** at the Kyoto University for their stimulating me. **Dr. Yutaka Kondo** at the University of Tokyo and **Dr. Kazuyuki Kita** at the Ibaraki University are greatly appreciated for their interests in my work and many discussions, especially on the TRACE-P observation. I would thank **Dr. Hideharu Akiyoshi** at the NIES for various comments and providing data for the modeling in this study. I am grateful to **all stuffs and students of the CCSR**, for supporting my work. **Dr. Ryo Furue** has helped me much with the maintenance work for the computers of the *Takahashi-lab*. **The all members of the Takahashi-lab.** are appreciated. I would give special thanks to **Ms. Yoko Takahashi** for her help in various aspects.

For this study, I use the ECMWF data provided from the Center for Global Environmental Research (CGER) at the NIES. The SX-6 computing system at the NIES has been used through much of the calculations in this study. For this thesis, I use **gtool**, **GrADS**, **gnuplot**, **Vis5D**, **Tgif**, and **LaTeX 2**$_{\varepsilon}$ on the Sun/Enterprise-250 machine (**gaia**), Sun/Blade-1000 machine (**boreas**), and VT-alpha machines (**helios** and **ishtar**) of the *Takahashi-lab.*, and on my Linux (Statabo/Kondara/Vine packages) PCs (**statabo**, **jaico** and **nobita**).

Finally, I would express my gratitude to my parents for their hearty support for many years.

Contents

Chapter 1

Introductory Remarks

1.1 Tropospheric ozone: background

The direct and indirect impact of human activities on the atmospheric environment and climate is one of the biggest concerns in recent atmospheric science. The chemical composition of the atmosphere has been changed largely by increase in anthropogenic emissions associated with industry, car traffic, and land use. In addition to well-mixed gases like carbon dioxide (CO_2) and methane (CH_4), reactive species such as ozone (O_3) and its precursors (carbon monoxide CO, nitrogen oxides NO_x, nonmethane hydrocarbons NMHCs, etc.), and aerosols have been increased globally over the past century [e.g., *WMO*, 1990; *Crutzen and Zimmermann*, 1991; *Levy et al.*, 1997; *Wang and Jacob*, 1998d], as anthropogenic emissions have risen dramatically. In particular, ozone increase by several-fold has been observed in the northern midlatitudes since preindustrial times [*Staehelin et al.*, 1994; *Marenco et al.*, 1994]. While ozone in the stratosphere (ozone layer) has a beneficial role to shield us from sun (ultraviolet) light, tropospheric ozone displays a destructive side. Since ozone reacts strongly with other molecules, it can severely damage the human health and plants including some important agricultural crops [e.g., *World Health Organization (WHO)*, 1996a, b] , and is a key pollutant in smog hanging over many cities around the world. In addition, tropospheric ozone is a significant greenhouse gas that absorbs both longwave (terrestrial) and shortwave (solar) radiation [*Wang et al.*, 1980; *Lacis et al.*, 1990]. The effect of tropospheric ozone increase on climate since preindustrial times has typically been estimated to be a radiative forcing between 0.3 and 0.5 W m^{-2} [*Forster et al.*, 1996; *Berntsen et al.*, 1997b; *Mickley et al.*, 1999; *Roelofs and Lelieveld*, 2000, etc.], comparable with the estimated methane forcing as shown in Figure 1.1 (from the Intergovernmental Panel on Climate Change, IPCC). Since tropospheric ozone is chemically destroyed on a timescale of a week to a month, distribution of tropospheric ozone quickly responds to emission change and leads to a quick impact on climate unlike well-mixed greenhouse gases (i.e., CO_2, CH_4, halofluorocarbons HFCs, and nitrous oxide N_2O). It should also be noted that the radiative forcing from tropospheric ozone is distributed inhomogeneously, being generally larger in polluted areas particularly in the Northern Hemisphere, because of short lifetime of tropospheric ozone. Ozone has also a critical importance for tropospheric photochemistry to activate chemical

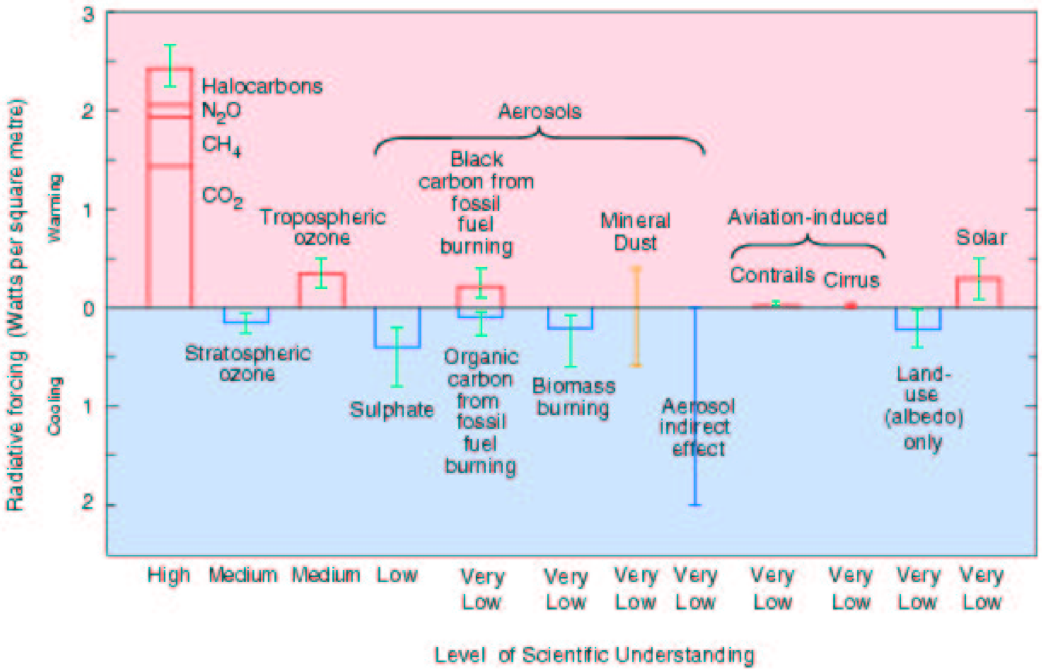

Figure 1.1. The global mean radiative forcing (W m^{-2}) of the climate system for the year 2000, relative to 1750, taken from *Intergovernmental Panel on Climate Change (IPCC)* [2001].

reactions and control the lifetime of other chemical species (oxidizing capacity) through formation of hydroxy radical (OH). As illustrated in Figure 1.2, tropospheric ozone chemistry much controls the lifetimes and hence the levels of CH_4 and HFCs. This ‘indirect’ effect of tropospheric chemistry has been shown to make a significant contribution to the total radiative forcing [*Hauglustaine et al.*, 1994; *Johnson and Derwent*, 1996; *Fuglestvedt et al.*, 1996; *Daniel and Solomon*, 1998; *Wild et al.*, 2001b]. Also, ozone chemistry plays an important role in the formation process of sulfate aerosol which has direct (sunlight scattering) and indirect (cloud condensation nuclei, CCN) climate effects as shown in Figure 1.1. Concurrently, sulfate is a major cause of acid rain as well as nitrates NO_3^- formed from NO_x. Tropospheric ozone chemistry, therefore, acts as an important interface for both the climate system and the atmospheric environment.

There are two kinds of sources for tropospheric ozone; stratospheric influx associated with the stratosphere-troposphere exchange (STE) and in-situ photochemical production in the troposphere. According to recent studies, photochemical ozone production in the troposphere is the primary source for global tropospheric ozone, typically estimated at 3000-5000 TgO_3/yr, with influx from the stratosphere of 300-700 TgO_3/yr [e.g., *Müller and Brasseur*, 1995; *Roelofs et al.*, 1997; *Wang et al.*, 1998b; *Hauglustaine et al.*, 1998; *Roelofs and Lelieveld*, 2000; *McLinden et al.*, 2000]. This indicates a significant net production of ozone in the troposphere and implies a large importance of the impact of anthropogenic emission change on the future atmosphere.

Because of spatially inhomogeneous formation and short chemical lifetime of ozone in the tro-

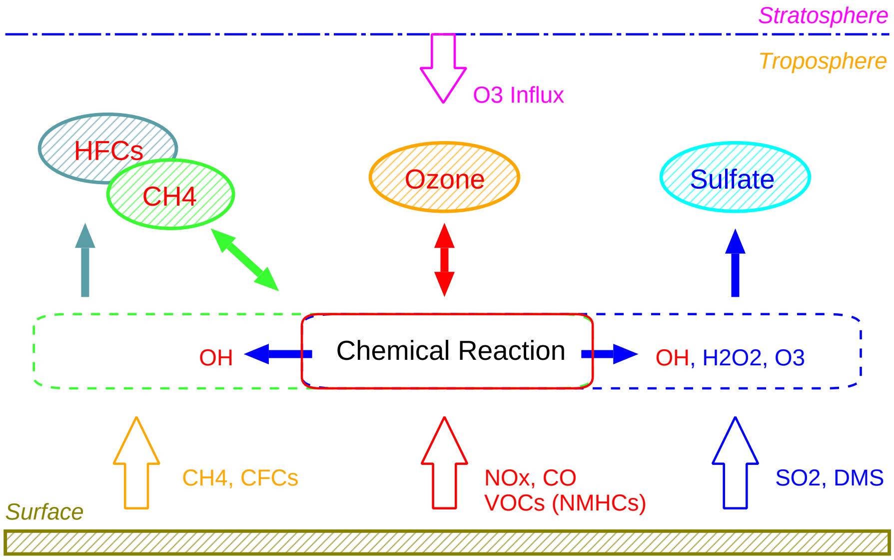

Figure 1.2. Schematic illustration of the relationship among tropospheric ozone, other greenhouse gases (CH_4, HFCs), and sulfate aerosol.

posphere, spatial and temporal distributions of tropospheric ozone are highly variable. Vertical distribution of tropospheric ozone is observed with ozonesondes in some locations as by the WOUDC (World Ozone and Ultraviolet Radiation Data Centre) [e.g., *Logan*, 1999] and the SHADOZ (Southern Hemisphere Additional Ozonesonde) program [*Thompson et al.*, 2002] and aircraft campaigns (e.g., NASA Global Tropospheric Experiments). These observations, however, do not cover the global region concurrently. Although many techniques have been developed to derive tropospheric ozone distribution from satellite measurements [*Jiang and Yung*, 1996; *Kim and Newchurch*, 1996; *Hudson and Thompson*, 1998; *Ziemke et al.*, 1998; *Thompson and Hudson*, 1999; *Kim et al.*, 2001; *Ziemke et al.*, 2001; *Newchurch et al.*, 2002; *Chandra et al.*, 2002b], they are generally limited to only tropical latitudes at the present.

1.2 Objectives of this study

As discussed above, tropospheric ozone and involving chemistry play important roles in the climate system (Figure 1.1 and Figure 1.2), and thereby the problem of how tropospheric chemistry changes toward the future is a large concern. Since the impact of changes in tropospheric chemistry on the atmospheric environment and climate as mentioned above is at the global scale, global investigation of the behavior of individual chemical species and each process in three dimensions is needed. For this purpose, global chemical models, which include both dynamical and chemical processes, are very useful and informative to understand tropospheric chemistry involving global tropospheric ozone distribution. Such models are also helpful to supplement and analyze observations as mentioned above.

In this dissertation, a new global three-dimensional chemical model for the troposphere is developed and evaluated in detail. The model, based on a general circulation model, calculates dynamical, physical, and chemical processes interactively. A detailed on-line simulation of tropospheric O_3-HO_x-NO_x-CH_4-CO chemistry and NMHCs chemistry has been implemented in the model. Then, changing processes of tropospheric ozone chemistry including the radiative forcing from tropospheric ozone are investigated with the developed model.

The following chapters begin with the description of the developed model followed by model evaluation (chapter 2). This chapter gives descriptions of chemistry, emissions, and deposition in the model as presented in *Sudo et al.* [2002a], with detailed evaluation of the model results based on *Sudo et al.* [2002b]. Global budgets of several important species are also presented in the chapter. Chapter 3 describes the modeled tropospheric ozone increase since preindustrial times and the resultant radiative forcing of tropospheric ozone estimated by the model. In chapter 4, the role of natural meteorological conditions (grid/subgrid scale transport, water vapor distribution, etc.) in tropospheric ozone chemistry is investigated, focusing on the large-scale changes in tropical tropospheric ozone observed in an El Niño year as presented in *Sudo and Takahashi* [2001]. This chapter also evaluates the tropical tropospheric ozone distributions simulated by the model with satellite derived data. Chapter 5 presents the simulations of tropospheric chemistry involving tropospheric ozone and sulfate distributions for the next hundred years to 2100 according to the IPCC Special Report on Emission Scenarios (SRES). The simulations assess the effect of anthropogenic emission changes on tropospheric ozone, and related chemical processes including acid deposition. The simulations also demonstrate the impact of climate change on tropospheric ozone and methane distributions, considering emission change and climate change independently. Finally, chapter 6 summarizes the overall results in this dissertation and suggests remaining problems in atmospheric chemistry modeling and further subjects for future prediction.

Chapter 2

Global Chemical Model of the Troposphere

2.1 Introduction

As discussed in the previous chapter, tropospheric ozone and related chemistry have significant roles in the climate system and atmospheric environment. With limited observations available for tropospheric chemistry involving ozone distribution, numerical models are needed to investigate tropospheric ozone chemistry and to assess its impact on global climate (e.g., global radiative forcing from tropospheric ozone). There have been various global modeling studies of tropospheric ozone, chemistry, and transport up to the present [*Levy et al.*, 1985; *Crutzen and Zimmermann*, 1991; *Roelofs and Lelieveld*, 1995; *Müller and Brasseur*, 1995; *Roelofs et al.*, 1997; *Berntsen and Isaksen*, 1997a; *Wang et al.*, 1998a, b; *Brasseur et al.*, 1998; *Hauglustaine et al.*, 1998; *Lawrence et al.*, 1999; *Horowitz et al.*, 2002]. Models in those studies generally include photochemical reactions in the troposphere to consider ozone formation and destruction. The photochemical chain reaction which produces ozone is initiated and maintained by reactive radicals as illustrated in Figure 2.1. While volatile organic compounds (VOCs) act as "fuel" in the ozone formation process, NO_x (= $NO + NO_2$), most important species, partially function as a catalysis "engine" in the formation process (NO also plays a key role in the regeneration of the reactive radicals and the further progress of the reactions). In the process, other important products such as peroxy acetyl nitrate, nitric acid, aldehydes, organic acids, particulates and many short-lived radical species are formed from the VOCs degradation. The significance of VOCs in the ozone formation process increases in the polluted (NO_x rich) atmospheres as in urban sites [*Chameides et al.*, 1992; *Konovalov*, 2002]. Also, VOCs, reacting with OH rapidly, have great impacts on the global OH radical field, oxidizing capacity of the atmosphere. However, several of the above global models ignore higher VOCs (non-methane hydrocarbons, NMHCs) and employ a simple NO_x-CH_4-CO chemistry [e.g., *Roelofs and Lelieveld*, 1995; *Lawrence et al.*, 1999], because of heavy demands on computer time by NMHCs chemistry. The previous studies of *Müller and Brasseur* [1995], *Wang et al.* [1998a, b], *Brasseur et al.* [1998], *Hauglustaine et al.* [1998], and *Horowitz et al.* [2002] have simulated global tropospheric chemistry including NMHCs. The simulations of *Wang et al.* [1998c], *Horowitz et al.* [1998], and *Roelofs and Lelieveld* [2000] reported the influence of NMHCs (particularly of iso-

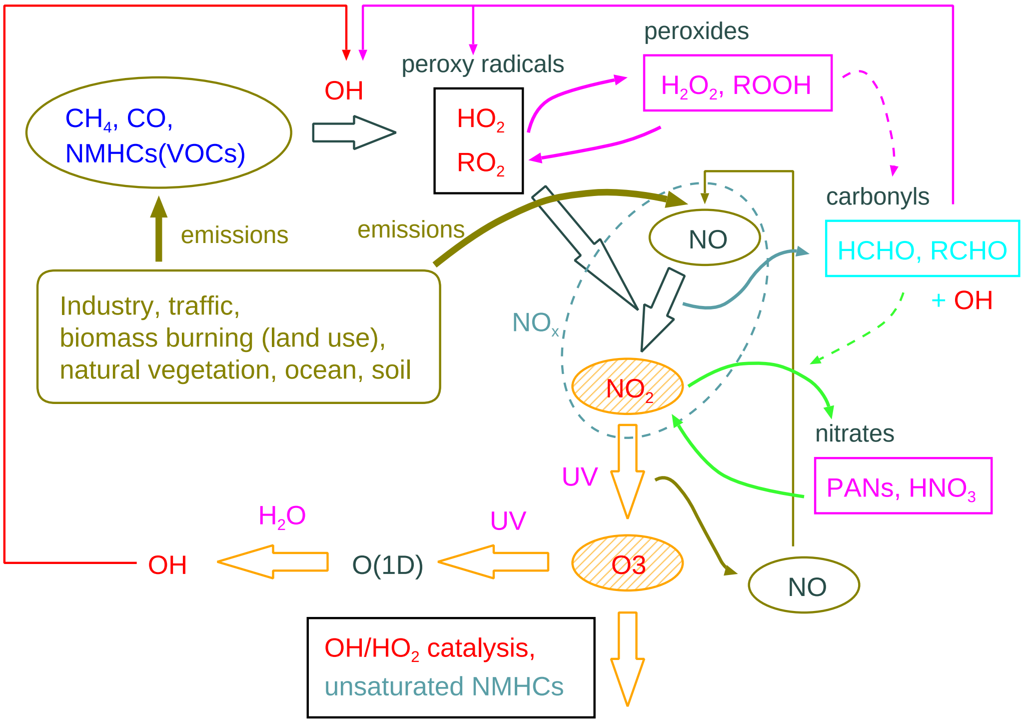

Figure 2.1. The fundamental flow of tropospheric chemistry producing ozone from NO_x and hydrocarbons. Also shown is formation of reservoir species like peroxides and nitrates.

prene) on ozone formation and the global OH field.

Many of the global chemical models developed so far use meteorological variables such as wind and temperature prescribed “off-line” without considering the feedback from tropospheric ozone forcing [*Müller and Brasseur*, 1995; *Berntsen and Isaksen*, 1997a; *Horowitz et al.*, 1998; *Haywood et al.*, 1998; *Wang et al.*, 1998a; *Brasseur et al.*, 1998]. This kinds of models ignore the short-term and synoptic-scale correlations between tropospheric ozone and meteorological variables such as clouds and temperature [*Pickering et al.*, 1992; *Sillman and Samson*, 1995], and may not be suitable for accurate simulation of the future climate system. On the contrary, several model studies consider “on-line” simulation of tropospheric ozone and meteorology, incorporating chemistry into general circulation models (GCMs) [e.g., *Roelofs and Lelieveld*, 1995, 2000; *Mickley et al.*, 1999]. While such models are useful to investigate interactions between tropospheric chemistry and climate, they are computationally heavy in general and may have limitations in spatial resolution compared to “off-line” models.

In this study, a global chemical model for the troposphere has been developed. The model, named CHemical AGCM for Study of atmospheric Environment and Radiative forcing (CHASER), has been developed in the framework of the Center for Climate System Research (CCSR), University of Tokyo/National Institute for Environmental Studies (NIES) atmospheric GCM (AGCM). This model, CHASER, is aimed to study tropospheric ozone and related chemistry, and their impacts on climate. The model includes a detailed simulation of tropospheric chemistry including

NMHCs. The chemistry component is coupled with the CCSR/NIES AGCM to allow the interactions between climate and tropospheric chemistry (i.e., ozone and CH_4 distributions) in the model. As mentioned in the previous chapter, tropospheric ozone chemistry is much responsible for formation of sulfate which has significant direct/indirect climate effects (Figure 1.1). As the sulfate formation process is important in the climate system as well as ozone, and in turn has some impacts on tropospheric chemistry especially on hydrogen peroxide (H_2O_2), it was opted to be simulated on-line in the present version of CHASER. Although sulfate simulation is implemented and is reflected on the calculation of heterogeneous reactions in the model, note that it is not linked to the radiative transfer code in the AGCM at this stage.

The following sections present description and evaluation of the CHASER model which is based on the CCSR/NIES AGCM. The CCSR/NIES AGCM has been also used for an on-line global simulation of stratospheric chemistry and dynamics [*Takigawa et al.*, 1999], and for a global simulation of the aerosol distribution and optical thickness of various origins [*Takemura et al.*, 2000, 2001]. The principal objective of CHASER is to investigate the global distributions and budgets of ozone and related tracers, and the radiative forcing from tropospheric ozone. Additionally, CHASER can be used to assess the global impact of changes in the atmospheric composition on climate. Principal description and evaluation of the CHASER model (the previous version) are presented in *Sudo et al.* [2002a, b]. CHASER has been employed in a simulation study of tropospheric ozone changes during the 1997-1998 El Niño event [*Sudo and Takahashi*, 2001] (see chapter 4).

A detailed description of the present version of CHASER is given in section 2.2 which includes descriptions of chemistry, emissions, deposition processes. In section 2.3, model results are evaluated in detail with a number of observations. Conclusions from this model development are in section 2.4. In the end of this chapter, evaluation of transport and deposition processes and description of aqueous-phase reactions implemented in the model are given (Appendix 2A, B, respectively).

2.2 Model description

As mentioned above, the CHASER model is based on the CCSR/NIES atmospheric general circulation model (AGCM). The present version of CHASER uses the CCSR/NIES AGCM, version 5.6. Basic features of the CCSR/NIES AGCM have been described by *Numaguti* [1993]. The newly implemented physical processes were presented by *Numaguti et al.* [1995]. This AGCM adopts a radiation scheme based on the k-distribution and the two-stream discrete ordinate method [*Nakajima and Tanaka*, 1986]. A detailed description of the radiation scheme adopted in the AGCM is given by *Nakajima et al.* [1995]. The prognostic Arakawa-Schubert scheme is employed to simulate cumulus (moist) convection [cf. *Numaguti et al.*, 1995]. *Emori et al.* [2001] evaluates the cumulus convection scheme in a simulation of precipitation over East Asia. (see also the description by *Numaguti* [1999] for further details of the hydrological processes in the model). The level 2 scheme of turbulence closure by *Mellor and Yamada* [1974] is used for the estimation of the vertical diffusion

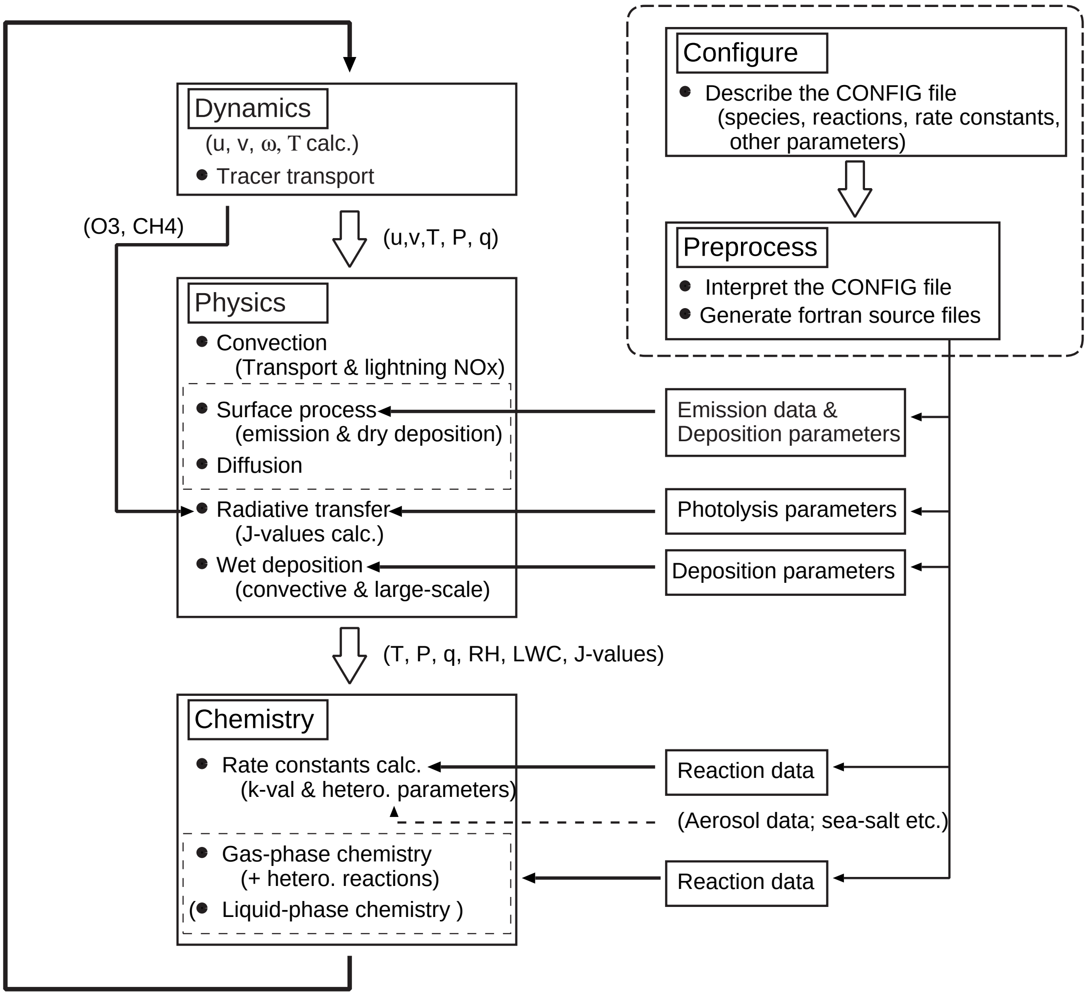

Figure 2.2. The flow of calculation in the CHASER model. Dynamics, physics, chemistry processes are evaluated at each time step in the CCSR/NIES AGCM. Configurations of the chemical scheme such as a choice of species, reactions and reaction rates are automatically processed by the preprocessor to set up the model through input files

coefficient. The orographic gravity wave momentum deposition in the AGCM is parameterized following *McFarlane* [1987]. The AGCM generally reproduces the climatology of meteorological fields. In climatological simulations, CHASER uses climatological data of sea surface temperature (SST) as an input to the AGCM. In simulations of a specific time period, analyzed data of wind velocities, temperature, and specific humidity from the European Center for Medium-Range Weather Forecasts (ECMWF) are used as a constraint in addition to SST data of a corresponding year, because it may be difficult to validate just climatological output from the model with observations in a certain period.

In CHASER, dynamical and physical processes such as tracer transport, vertical diffusion, surface emissions, and deposition are simulated in the flow of the AGCM calculation (Figure 2.2). The chemistry component of CHASER calculates chemical transformations (gas and liquid phase chemistry and heterogeneous reactions) using variables of the AGCM (temperature, pressure, humidity, etc.). In the radiation component, radiative transfer and photolysis rates are calculated by using the concentrations of chemical species calculated in the chemistry component. The dynamical and physical components of CHASER are evaluated with a time step of 20 or 30 min. Time step for chemical reactions in this study is opted to be 10 min. In this study, the model adopts a horizontal spectral resolution of T42 (approximately, 2.8° longitude × 2.8° latitude) with 32 layers in the vertical from the surface up to about 3 hPa (about 40 km) altitude. CHASER uses the σ coordinate system in the vertical. The 32 layers are centered approximately at 995, 980, 950, 900, 830, 745, 657, 576, 501, 436, 380, 331, 288, 250, 218, 190, 165, 144, 125, 109, 95, 82, 72, 62, 54, 47, 40, 34, 27, 19, 11, and 3 hPa, resulting in a vertical resolution of 1 km in the free troposphere and much of the lower stratosphere for an accurate representation of vertical transport such as the stratosphere-troposphere exchange (STE).

The present version of CHASER calculates the concentrations of 53 chemical species from the surface up to about 20 km altitude. The concentrations of O_3, NO_x, N_2O_5, and HNO_3 in the stratosphere (above 20 km altitude) are prescribed using monthly averaged output data from a three-dimensional stratospheric chemical model [*Takigawa et al.*, 1999]. For the O_3 distribution (> 20 km), the data of *Takigawa et al.* [1999] were scaled by using zonal mean satellite data from the Halogen Occultation Experiment project (HALOE) [*Russel et al.*, 1993; *Randel*, 1998], since the latest version of the stratospheric chemical model [*Takigawa et al.*, 1999] tends to slightly overestimate the O_3 concentrations in the tropical lower stratosphere. The concentrations in the stratosphere ($>$ 20km) in the model are nudged to those data with a relaxation time of one day at each time step.

In CHASER, advective transport is simulated by a 4th order flux-form advection scheme of the monotonic van Leer [*van Leer*, 1977], except for the vicinity of the poles. For a simulation of advection around the poles, the flux-form semi-Lagrangian scheme of *Lin and Rood* [1996] is used. Vertical transport associated with moist convection (updrafts and downdrafts) is simulated in the framework of the cumulus convection scheme (the prognostic Arakawa-Schubert scheme) in the AGCM. In the boundary layer, equations of vertical diffusion and surface emission and deposition fluxes are solved implicitly. The adopted transport scheme is evaluated in Appendix 2A (page 102) together with evaluation of the deposition scheme.

Information about the CHASER model can also be obtained via the CHASER web site (http://atmos.ccsr.u-tokyo.ac.jp/~kengo/chaser).

2.2.1 Chemistry

The chemistry component of CHASER includes 37 tracers (transported) and 17 non-tracers (radical species and members of family tracers). Table 2.1 shows chemical species considered in CHASER. Ozone and nitrogen oxides ($NO + NO_2 + NO_3$) are transported as families (O_x and NO_x respectively). The concentrations of nitrogen (N_2), oxygen (O_2), water vapor (H_2O), and

Table 2.1. Chemical Species Considered in CHASER

No.	Name	Family [a]	Description
Tracers			
01	O_x	$O_3 + O + O(^1D)$	O_x family (ozone and atmoic oxygen)
02	NO_x	$NO + NO_2 + NO_3$	NO_x family
03	N_2O_5	single	nitrogen pentoxide
04	HNO_3	single	nitric acid
05	HNO_4	single	peroxynitric acid
06	H_2O_2	single	hydrogen peroxide
07	CO	single	carbon monoxide
08	C_2H_6	single	ethane
09	C_3H_8	single	propane
10	C_2H_4	single	ethene
11	C_3H_6	single	propene
12	ONMV	single	other NMVOCs [b]
13	C_5H_8	single	isoprene
14	$C_{10}H_{16}$	single	terpenes
15	CH_3COCH_3	single	acetone
16	CH_2O	single	formaldehyde
17	CH_3CHO	single	acetaldehyde
18	NALD	single	nitrooxy acetaldehyde
19	MGLY	single	methylglyoxal and other C_3 aldehydes
20	HACET	single	hydroxyacetone and C_3 ketones
21	MACR	single	methacrolein, methylvinylketone and C_4 carbonyls
22	PAN	single	peroxyacetyl nitrate
23	MPAN	single	higher peroxyacetyl nitrates
24	ISON	single	isoprene nitrates
25	CH_3OOH	single	methyl hydro-peroxide
26	C_2H_5OOH	single	ethyl hydro-peroxide
27	C_3H_7OOH	single	propyl hydro-peroxide
28	HOROOH	single	peroxides from C_2H_4 and C_3H_6
29	ISOOH	single	hydro-peroxides from $ISO_2 + HO_2$
30	CH_3COOOH	single	paracetic acid
31	MACROOH	single	hydro-peroxides from $MACRO_2 + HO_2$
32	$O_x(S)$	$O_3(S) + O(^1D)(S)$	O_x family from the stratosphere
33	SO_2	single	sulfur dioxide
34	DMS	single	dimethyl sulfide
35	SO_4	single	sulfate (non sea-salt)
36	^{222}Rn	single	radon(222)
37	^{210}Pb	single	lead(210)
Non-Tracers [c]			
01	OH		hydroxyl radical
02	HO2		hydroperoxyl radical
03	CH_3O2		methyl peroxy radical
04	C_2H_5O2		ethyl peroxy radical
05	C_3H_7O2		propyl peroxy radical
06	CH_3COO_2		peroxy acetyl radical
07	$CH_3COCH_2O_2$		acetylmethyl peroxy radical
08	$HOC_2H_4O_2$		hydroxy ethyl peroxy radical
09	$HOC_3H_6O_2$		hydroxy propyl peroxy radical
10	ISO_2		peroxy radicals from $C_5H_8 + OH$

Table 2.1. (continued)

No.	Name	Family [a]	Description
11	$MACRO_2$		peroxy radicals from MACR + OH
12	$CH_3SCH_2O_2$		dimethyl sulfide peroxy radical

[a] For transport
[b] Non Methane Volatile Organic Compounds
[c] Not including member species of family tracers

hydrogen (H_2) are determined from the AGCM calculation. In this study, CH_4 is not considered as a tracer because of uncertainty in the natural emission amount of CH_4 and its long chemical lifetime (8-11 years). In the model, CH_4 concentration is assumed to be 1.77 ppmv and 1.68 ppmv in the northern and the southern hemisphere, respectively. N_2O concentration in the model is also fixed to 0.3 ppmv uniformally in the global.

The present version of CHASER includes 26 photolytic reactions and 111 chemical reactions including heterogenous and aqueous-phase reactions (Table 2.2 and Table 2.3). It considers NMHCs oxidation as well as the O_x-HO_x-NO_x-CH_4-CO chemical system. Oxidations of ethane (C_2H_6), propane (C_3H_8), ethene (C_2H_4), propene (C_3H_6), isoprene (C_5H_8), and terpenes ($C_{10}H_{16}$, etc.) are included explicitly. Degradation of other NMHCs is represented by the oxidation of a lumped species named other non-methane volatile organic compounds (ONMV) as in the IMAGES model [*Müller and Brasseur*, 1995] and the MOZART model [*Brasseur et al.*, 1998]. The model adopted a condensed isoprene oxidation scheme of *Pöschl et al.* [2000] which is based on the Master Chemical Mechanism (MCM, Version 2.0) [*Jenkin et al.*, 1997]. Terpenes oxidation is largely based on *Brasseur et al.* [1998] (the MOZART model). Acetone is believed to be an important source of HO_x in the upper troposphere and affect the background PAN formation in spite of its low photochemical activity. Acetone chemistry and propane oxidation are, therefore, included in this study, based on the MCM, Version 2.0.

Dentener and Crutzen [1993] suggested that heterogeneous hydrosis of N_2O_5 on aqueous-phase aerosols can reduce NO_x levels and hence ozone production in polluted areas. In addition, several studies have shown the possibility that heterogeneous reactions of HO_2 and some peroxy radicals (RO_2) from unsaturated hydrocarbons like isoprene may occur on aqueous-phase aerosols [*Jaeglé et al.*, 1999; *Jacob*, 2000]. *Meilinger et al.* [2001] have also suggested an importance of heterogeneous reactions on liquid and ice (cirrus) clouds for the ozone and HO_x budgets in the tropopause region. In this study, the heterogeneous reaction of "$N_2O_5 \rightarrow 2\ HNO_3$" is included with an uptake coefficient γ of 0.1 on aqueous-phase aerosols and 0.01 on ice particles [*Sander et al.*, 2000]. Reactions of HO_2 and RO_2 on aerosols are tentatively included in this study as listed in Table 2.3, with γ values based on *Jacob* [2000]. The heterogeneous loss rate β for the species i

Table 2.2. Photolytic Reactions Included in CHASER

No.	Reaction	Ref.
J1)	$O_3 + h\nu \rightarrow O(^1D) + O_2$	1,2
J2)	$O_3 + h\nu \rightarrow O + O_2$	1,2
J3)	$H_2O_2 + h\nu \rightarrow 2\ OH$	1
J4)	$NO_2 + h\nu \rightarrow NO + O$	1
J5)	$NO_3 + h\nu \rightarrow 0.1\ NO + 0.9\ NO_2 + 0.9\ O_3$	1
J6)	$N_2O_5 + h\nu \rightarrow NO_2 + NO_3$	1
J7)	$HNO_3 + h\nu \rightarrow NO_2 + OH$	1
J8)	$HNO_4 + h\nu \rightarrow NO_2 + HO_2$	1
J9)	$PAN + h\nu \rightarrow CH_3COO_2 + NO_2$	1
J10)	$CH_3OOH + h\nu \rightarrow CH_2O + OH + HO_2$	1
J11)	$C_2H_5OOH + h\nu \rightarrow CH_3CHO + OH + HO_2$	1
J12)	$C_3H_7OOH + h\nu \rightarrow 0.24\ C_2H_5O_2 + 0.09\ CH_3CHO + 0.18\ CO + 0.7\ CH_3COCH_3$ $+ OH + HO_2$	1
J13)	$CH_3COCH_3 + h\nu \rightarrow CH_3COO_2 + CH_3O_2$	3
J14)	$HOROOH + h\nu \rightarrow 0.25\ CH_3CHO + 1.75\ CH_2O + HO_2 + OH + H_2O$	1
J15)	$CH_3COOOH + h\nu \rightarrow CH_3O_2 + CO_2 + OH$	4
J16)	$CH_2O + h\nu \rightarrow CO + 2\ HO_2$	1
J17)	$CH_2O + h\nu \rightarrow CO + 2\ H_2$	1
J18)	$CH_3CHO + h\nu \rightarrow CH_3O_2 + CO + HO_2$	5
J19)	$ISOOH + h\nu \rightarrow MACR + CH_2O + OH + HO_2$	1
J20)	$ISON + h\nu \rightarrow NO_2 + MACR + CH_2O + HO_2$	1,6,7
J21)	$MACR + h\nu \rightarrow CH_3COO_2 + CH_2O + CO + HO_2$	6,7,8
J22)	$MPAN + h\nu \rightarrow MACRO_2 + NO_2$	1
J23)	$MACROOH + h\nu \rightarrow OH + 0.5\ HACET + 0.5\ CO + 0.5\ MGLY + 0.5\ CH_2O + HO_2$	1
J24)	$HACET + h\nu \rightarrow CH_3COO_2 + CH_2O + HO_2$	1,6
J25)	$MGLY + h\nu \rightarrow CH_3COO_2 + CO + HO_2$	5,6,7
J26)	$NALD + h\nu \rightarrow CH_2O + CO + NO_2 + HO_2$	5

References: 1, *DeMore et al.* [1997]; 2, *Talukdar et al.* [1998]; 3, *Gierczak et al.* [1998]; 4, *Müller and Brasseur* [1995]; 5, *Atkinson et al.* [1999]. 6, *Jenkin et al.* [1997]; 7, *Pöschl et al.* [2000]; 8, *Carter* [1990].

Table 2.3. Chemical Reactions Included in CHASER (Gas/liquid-phase and Heterogeneous Reactions)

No.	Reaction	Rate	Ref.
K1)	$O(^1D) + O_2 \rightarrow O + O_2$	$k_1 = 3.20E\text{-}11\ exp(70/T)$	1
K2)	$O(^1D) + N_2 \rightarrow O + N_2$	$k_2 = 1.80E\text{-}11\ exp(110/T)$	1
K3)	$O(^1D) + H_2O \rightarrow 2\ OH$	$k_3 = 2.20E\text{-}10$	1
K4)	$O(^1D) + N_2O \rightarrow 2\ NO$	$k_4 = 6.70E\text{-}11$	1
K5)	$O + O_2 + M \rightarrow O_3 + M$	$k_5 = 6.40E\text{-}34\ exp(300/T)^{2.3}$	1
K6)	$H_2 + O(^1D) \rightarrow OH + HO_2$	$k_6 = 1.10E\text{-}10$	1
K7)	$H_2 + OH \rightarrow HO_2 + H_2O$	$k_7 = 5.50E\text{-}12\ exp(-2000/T)$	1
K8)	$O + HO_2 \rightarrow OH + O_2$	$k_8 = 3.00E\text{-}11\ exp(200/T)$	1
K9)	$O + OH \rightarrow HO_2 + O_2$	$k_9 = 2.20E\text{-}11\ exp(120/T)$	1
K10)	$O_3 + OH \rightarrow HO_2 + O_2$	$k_{10} = 1.50E\text{-}12\ exp(-880/T)$	1
K11)	$O_3 + HO_2 \rightarrow OH + 2\ O_2$	$k_{11} = 2.00E\text{-}14\ exp(-680/T)$	1
K12)	$O + NO_2 \rightarrow NO + O_2$	$k_{12} = 5.60E\text{-}12\ exp(180/T)$	1

Table 2.3. (continued)

No.	Reaction	Rate	Ref.
K13)	$O_3 + NO \rightarrow NO_2 + O_2$	k_{13} = 3.00E-12 exp(-1500/T)	1
K14)	$O_3 + NO_2 \rightarrow NO_3 + O_2$	k_{14} = 1.20E-13 exp(-2450/T)	1
K15)	$OH + HO_2 \rightarrow H_2O + O_2$	k_{15} = 4.80E-11 exp(250/T)	1
K16)	$OH + H_2O_2 \rightarrow H_2O + HO_2$	k_{16} = 2.90E-12 exp(-160/T)	1
K17)	$HO_2 + NO \rightarrow NO_2 + OH$	k_{17} = 3.50E-12 exp(250/T)	1
K18)	$HO_2 + HO_2 \rightarrow H_2O_2 + O_2$	$k_{18} = (k_a + k_b [M])\, k_c$ k_a = 2.30E-13 exp(600/T) k_b = 1.70E-33 exp(1000/T) k_c = 1 + 1.40E-21 [H_2O] exp(2200/T)	1
K19)	$OH + NO_2 + M \rightarrow HNO_3 + M$	k_0 = 2.40E-30 $(300/T)^{3.1}$ k_∞ = 1.70E-11 $(300/T)^{2.1}$ $F_c = 0.6$	1
K20)	$OH + HNO_3 \rightarrow NO_3 + H_2O$	$k_{20} = k_a + k_b [M] /(1 + k_b [M]/k_c)$ k_a = 2.40E-14 exp(460/T) k_b = 6.50E-34 exp(1335/T) k_c = 2.70E-17 exp(2199/T)	1
K21)	$NO_2 + NO_3 + M \rightarrow N_2O_5 + M$	k_0 = 2.00E-30 $(300/T)^{4.4}$ k_∞ = 1.40E-12 $(300/T)^{0.7}$ $F_c = 0.6$	1
K22)	$N_2O_5 + M \rightarrow NO_2 + NO_3 + M$	$k_{22} = k_{21}$ /(2.70E-27 exp(11000/T))	1
K23)	$N_2O_5 + H_2O \rightarrow 2\ HNO_3$	k_{23} = 2.10E-21	1
K24)	$NO_3 + NO \rightarrow 2\ NO_2$	k_{24} = 1.50E-11 exp(170/T)	1
K25)	$NO_2 + HO_2 + M \rightarrow HNO_4 + M$	k_0 = 1.80E-31 $(300/T)^{3.2}$ k_∞ = 4.70E-12 $(300/T)^{1.4}$ $F_c = 0.6$	1
K26)	$HNO_4 + M \rightarrow NO_2 + HO_2 + M$	$k_{26} = k_{18}$ /(2.10E-27 exp(10900/T))	1
K27)	$HNO_4 + OH \rightarrow NO_2 + H_2O + O_2$	k_{27} = 1.30E-12 exp(380/T)	1
	— *CH_4 oxidation* —		
K28)	$CH_4 + OH \rightarrow CH_3O_2 + H_2O$	k_{28} = 2.45E-12 exp(-1775/T)	1
K29)	$CH_4 + O(^1D) \rightarrow CH_3O_2 + OH$	k_{29} = 1.50E-10	2
K30)	$CH_3O_2 + NO \rightarrow CH_2O + NO_2 + HO_2$	k_{30} = 3.00E-12 exp(280/T)	1
K31)	$CH_3O_2 + CH_3O_2 \rightarrow 1.8\ CH_2O + 0.6\ HO_2$	k_{31} = 2.50E-13 exp(190/T)	1
K32)	$CH_3O_2 + HO_2 \rightarrow CH_3OOH + O_2$	k_{32} = 3.80E-13 exp(800/T)	1
K33)	$CH_3OOH + OH \rightarrow 0.7\ CH_3O_2 + 0.3\ CH_2O + 0.3\ OH + H_2O$	k_{33} = 3.80E-12 exp(200/T)	1
K34)	$CH_2O + OH \rightarrow CO + HO_2 + H_2O$	k_{34} = 1.00E-11	1
K35)	$CH_2O + NO_3 \rightarrow HNO_3 + CO + HO_2$	k_{35} = 6.00E-13 exp(-2058/T)	3
K36)	$CO + OH \rightarrow CO_2 + HO_2$	k_{36} = 1.50E-13 (1 + 0.6 P_{atm})	1
	— *C_2H_6 and C_3H_8 oxidation* —		
K37)	$C_2H_6 + OH \rightarrow C_2H_5O_2 + H_2O$	k_{37} = 8.70E-12 exp(-1070/T)	1
K38)	$C_2H_5O_2 + NO \rightarrow CH_3CHO + NO_2 + HO_2$	k_{38} = 2.60E-12 exp(365/T)	1
K39)	$C_2H_5O_2 + HO_2 \rightarrow C_2H_5OOH + O_2$	k_{39} = 7.50E-13 exp(700/T)	1
K40)	$C_2H_5O_2 + CH_3O_2 \rightarrow 0.8\ CH_3CHO + 0.6\ HO_2$	k_{40} = 3.10E-13	4
K41)	$C_2H_5OOH + OH \rightarrow 0.286\ C_2H_5O_2 + 0.714\ CH_3CHO + 0.714\ OH + H_2O$	k_{41} = 1.13E-11 exp(55/T)	4

Table 2.3. (continued)

No.	Reaction	Rate	Ref.
K42)	$C_3H_8 + OH \rightarrow C_3H_7O_2 + H_2O$	k_{42} = 1.50E-17 T^2 exp(-44/T)	4
K43)	$C_3H_7O_2 + NO \rightarrow NO_2 + 0.24\ C_2H_5O_2 + 0.09\ CH_3CHO + 0.18\ CO + 0.7\ CH_3COCH_3 + HO_2$	k_{43} = 2.60E-17 exp(360/T)	4
K44)	$C_3H_7O_2 + HO_2 \rightarrow C_3H_7OOH + O_2$	k_{44} = 1.51E-13 exp(1300/T)	4
K45)	$C_3H_7O_2 + CH_3O_2 \rightarrow 0.8\ C_2H_5O_2 + 0.3\ CH_3CHO + 0.6\ CO + 0.2\ CH_3COCH_3 + HO_2$	k_{45} = 2.00E-13	4
K46)	$C_3H_7OOH + OH \rightarrow 0.157\ C_3H_7O_2 + 0.142\ C_2H_5O_2 + 0.053\ CH_3CHO + 0.106\ CO + 0.666\ CH_3COCH_3 + 0.843\ OH + 0.157\ H_2O$	k_{46} = 2.55E-11	4
K47)	$CH_3COCH_3 + OH \rightarrow CH_3COCH_2O_2 + H_2O$	k_{47} = 5.34E-18 T^2 exp(-230/T)	4
K48)	$CH_3COCH_2O_2 + NO \rightarrow NO_2 + CH_3COO_2 + CH_2O$	k_{48} = 2.54E-12 exp(360/T)	4
K49)	$CH_3COCH_2O_2 + NO_3 \rightarrow NO_2 + CH_3COO_2 + CH_2O$	k_{49} = 2.50E-12	4
K50)	$CH_3COCH_2O_2 + HO_2 \rightarrow$ HACET $+ O_2$	k_{50} = 1.36E-13 exp(1250/T)	4
K51)	HACET + OH $\rightarrow 0.323\ CH_3COCH_2O_2$ + 0.677 MGLY + 0.677 OH	k_{51} = 9.20E-12	4
	— C_2H_4 and C_3H_6 oxidation —		
K52)	$C_2H_4 + OH + M \rightarrow HOC_2H_4O_2 + M$	k_0 = 1.00E-28 $(300/T)^{0.8}$ k_∞ = 8.80E-12 F_c = 0.6	1
K53)	$C_2H_4 + O_3 \rightarrow 1.37\ CH_2O + 0.63\ CO + 0.12\ OH + 0.12\ HO_2 + 0.1\ H_2 + 0.2\ CO_2 + 0.4\ H_2O + 0.8\ O_2$	k_{53} = 1.20E-14 exp(-2630/T)	1
K54)	$HOC_2H_4O_2 + NO \rightarrow NO_2 + HO_2 + 2\ CH_2O$	k_{54} = 9.00E-12	2
K55)	$HOC_2H_4O_2 + HO_2 \rightarrow$ HOROOH $+ O_2$	k_{48} = 6.50E-13 exp(650/T)	5
K56)	$C_3H_6 + OH + M \rightarrow HOC_3H_6O_2 + M$	k_0 = 8.00E-27 $(300/T)^{3.5}$ k_∞ = 3.00E-11 F_c = 0.5	2
K57)	$C_3H_6 + O_3 \rightarrow 0.5\ CH_2O + 0.5\ CH_3CHO + 0.36\ OH + 0.3\ HO_2 + 0.28\ CH_3O_2 + 0.56\ CO$	k_{57} = 6.50E-15 exp(-1900/T)	1
K58)	$HOC_3H_6O_2 + NO \rightarrow NO_2 + CH_3CHO + CH_2O + HO_2$	k_{58} = 9.00E-12	2
K59)	$HOC_3H_6O_2 + HO_2 \rightarrow$ HOROOH $+ O_2$	k_{59} = 6.50E-13 exp(650/T)	5
K60)	HOROOH + OH $\rightarrow 0.125\ HOC_2H_4O_2 + 0.023\ HOC_3H_6O_2$ + 0.114 MGLY $+ 0.114\ CH_3COO_2 + 0.676\ CH_2O + 0.438\ CO + 0.85\ OH + 0.90\ HO_2 + H_2O$	k_{60} = 3.80E-12 exp(200/T)	5
	— other NMVOCs oxidation —		
K61)	ONMV + OH $\rightarrow 0.3\ C_2H_5O_2 + 0.02\ C_3H_7O_2 + 0.468\ ISO_2 + CH_2O + HO_2 + H_2O$	k_{61} = 1.55E-11 exp(-540/T)	5
	— acetaldehyde degradation etc. —		
K62)	$CH_3CHO + OH \rightarrow CH_3COO_2 + H_2O$	k_{62} = 5.60E-12 exp(270/T)	1
K63)	$CH_3CHO + NO_3 \rightarrow CH_3COO_2 + HNO_3$	k_{63} = 1.40E-12 exp(-1900/T)	1
K64)	$CH_3COO_2 + NO \rightarrow NO_2 + CH_3O_2 + CO_2$	k_{64} = 5.30E-12 exp(360/T)	1
K65)	$CH_3COO_2 + NO_2 + M \rightarrow$ PAN + M	k_0 = 9.70E-29 $(300/T)^{5.6}$ k_∞ = 9.30E-12 $(300/T)^{1.5}$	1

Table 2.3. (continued)

No.	Reaction	Rate	Ref.
		$F_c = 0.6$	
K66)	$PAN + M \rightarrow CH_3COO_2 + NO_2 + M$	$k_{66} = k_{65}$ /(9.00E-29 exp(14000/T))	1
K67)	$CH_3COO_2 + HO_2 \rightarrow CH_3COOOH + O_2$	k_{67} = 4.50E-13 exp(1000/T) /(1 + 1/(3.30E2 exp(-1430/T)))	1
K68)	$CH_3COO_2 + HO_2 \rightarrow CH_3COOH + O_3$	k_{68} = 4.50E-13 exp(1000/T) /(1 + 3.30E2 exp(-1430/T))	1
K69)	$CH_3COOOH + OH \rightarrow CH_3COO_2 + H_2O$	k_{69} = 6.85E-12	6
K70)	$CH_3COO_2 + CH_3O_2 \rightarrow CH_3O_2 + CH_2O + HO_2 + CO_2 + O_2$	k_{70} = 1.30E-12 exp(640/T) /(1 + 1/(2.20E6 exp(-3820/T)))	1
K71)	$CH_3COO_2 + CH_3O_2 \rightarrow CH_3COOH + CH_2O + O_2$	k_{71} = 1.30E-12 exp(640/T) /(1 + 2.20E6 exp(-3820/T))	1
K72)	$CH_3COO_2 + CH_3COO_2 \rightarrow 2\ CH_3O_2 + 2\ CO_2 + O_2$	k_{72} = 2.90E-12 exp(500/T)	1
	— C_5H_8 (Isoprene) and $C_{10}H_{16}$ (Terpene) oxidation —		
K73)	$C_5H_8 + OH \rightarrow ISO_2$	k_{66} = 2.45E-11 exp(410/T)	6
K74)	$C_5H_8 + O_3 \rightarrow 0.65\ MACR + 0.58\ CH_2O + 0.1\ MACRO_2 + 0.1\ CH_3COO_2 + 0.08\ CH_3O_2 + 0.28\ HCOOH + 0.14\ CO + 0.09\ H_2O_2 + 0.25\ HO_2 + 0.25\ OH$	k_{74} = 7.86E-15 exp(-1913/T)	6
K75)	$C_5H_8 + NO_3 \rightarrow ISON$	k_{75} = 3.03E-12 exp(-446/T)	6
K76)	$ISO_2 + NO \rightarrow 0.956\ NO_2 + 0.956\ MACR + 0.956\ CH_2O + 0.956\ HO_2 + 0.044\ ISON$	k_{76} = 2.54E-12 exp(360/T)	6
K77)	$ISO_2 + HO_2 \rightarrow ISOOH$	k_{77} = 2.05E-13 exp(1300/T)	6
K78)	$ISO_2 + ISO_2 \rightarrow 2\ MACR + CH_2O + HO_2$	k_{78} = 2.00E-12	6
K79)	$ISOOH + OH \rightarrow MACR + OH$	k_{79} = 1.00E-10	6
K80)	$ISON + OH \rightarrow NALD + 0.2\ MGLY + 0.1\ CH_3COO_2 + 0.1\ CH_2O + 0.1\ HO_2$	k_{80} = 1.30E-11	6
K81)	$MACR + OH \rightarrow MACRO_2$	k_{81} = 0.5 (4.13E-12 exp(452/T) + 1.86E-11 exp(175/T))	6
K82)	$MACR + O_3 \rightarrow 0.9\ MGLY + 0.45\ HCOOH + 0.32\ HO_2 + 0.22\ CO + 0.19\ OH + 0.1\ CH_3COO_2$	k_{82} = 0.5 (1.36E-15 exp(-2112/T) + 7.51E-16 exp(-1521/T))	6
K83)	$MACRO_2 + NO \rightarrow NO_2 + 0.25\ HACET + 0.25\ CO + 0.25\ CH_3COO_2 + 0.5\ MGLY + 0.75\ CH_2O + 0.75\ HO_2$	k_{83} = 2.54E-12 exp(360/T)	6
K84)	$MACRO_2 + HO_2 \rightarrow MACROOH$	k_{84} = 1.82E-13 exp(1300/T)	6
K85)	$MACRO_2 + MACRO_2 \rightarrow HACET + MGLY + 0.5\ CH_2O + 0.5\ CO$	k_{85} = 2.00E-12	6
K86)	$MACRO_2 + NO_2 + M \rightarrow MPAN + M$	k_0 = 9.70E-29 $(300/T)^{5.6}$ k_∞ = 9.30E-12 $(300/T)^{1.5}$ $F_c = 0.6$	1,6
K87)	$MPAN + M \rightarrow MACRO_2 + NO_2 + M$	$k_{87} = k_{86}$ /(9.00E-29 exp(14000/T))	1,6
K88)	$MPAN + OH \rightarrow NO_2 + 0.2\ MGLY + 0.1\ CH_3COO_2 + 0.1\ CH_2O + 0.1\ HO_2$	k_{88} = 3.60E-12	4
K89)	$MACROOH + OH \rightarrow MACRO_2 + H_2O$	k_{89} = 3.00E-11	6

Table 2.3. (continued)

No.	Reaction	Rate	Ref.
K90)	MGLY + OH → CH_3COO_2 + CO	$k_{90} = 1.50E{-}11$	6
K91)	MGLY + NO_3 → CH_3COO_2 + CO + HNO_3	$k_{91} = 1.44E{-}12 \exp(-1862/T)$	6
K92)	NALD + OH → CH_2O + CO + NO_2	$k_{92} = 5.60E{-}12 \exp(270/T)$	6
K93)	$C_{10}H_{16}$ + OH → 1.3 ISO_2 + 0.6 CH_3COCH_3	$k_{93} = 1.20E{-}11 \exp(444/T)$	7
K94)	$C_{10}H_{16}$ + O_3 → 1.3 MACR + 1.16 CH_2O + 0.2 $MACRO_2$ + 0.2 CH_3COO_2 + 0.16 CH_3O_2 + 0.56 HCOOH + 0.28 CO + 0.18 H_2O_2 + 0.5 HO_2 + 0.5 OH	$k_{94} = 9.90E{-}16 \exp(-730/T)$	5
K95)	$C_{10}H_{16}$ + NO_3 → 1.2 ISO_2 + NO_2	$k_{95} = 5.60E{-}11 \exp(-650/T)$	5
	— SO_2 oxidation (gas-phase) —		
K96)	SO_2 + OH + M → SO_4 + HO_2 + M	$k_0 = 3.00E{-}31\ (300/T)^{3.3}$ $k_\infty = 1.50E{-}12$ $F_c = 0.6$	1
K97)	SO_2 + O_3 → SO_4 + O_2	$k_{97} = 3.00E{-}12 \exp(-7000/T)$	1
	— DMS oxidation —		
K98)	DMS + OH → $CH_3SCH_2O_2$ + H_2O	$k_{98} = 1.20E{-}11 \exp(-260/T)$	1,4
K99)	DMS + OH → SO_2 + 1.2 CH_3O_2	$k_{99} = k_a \tanh(k_b/k_a)$ $k_a = 1.8E{-}11$ $k_b = 5.2E{-}12 + 4.7E{-}15\ (T-315)^2$	1,4
K100)	$CH_3SCH_2O_2$ + NO → NO_2 + 0.9 SO_2 + 0.9 CH_3O_2 + 0.9 CH_2O	$k_{100} = 8.00E{-}12$	4
K101)	$CH_3SCH_2O_2$ + $CH_3SCH_2O_2$ → SO_2 + CH_3O_2 + CH_2O	$k_{101} = 2.00E{-}12$	4
K102)	DMS + NO_3 → SO_2 + HNO_3	$k_{102} = 1.90E{-}13 \exp(500/T)$	1
	— Heterogeneous reactions ^{a}*—*		
H1)	N_2O_5 → 2 HNO_3	$\gamma_1^{liq} = 0.1$, $\gamma_1^{ice} = 0.01$	8,9
H2)	HO_2 → 0.5 H_2O_2 + 0.5 O_2	$\gamma_2^{liq} = 0.1$, $\gamma_2^{ice} = 0.01$	9
H3)	$HOC_2H_4O_2$ → HOROOH	$\gamma_3^{liq} = 0.1$, $\gamma_3^{ice} = 0.01$	9
H4)	$HOC_3H_6O_2$ → HOROOH	$\gamma_4^{liq} = 0.1$, $\gamma_4^{ice} = 0.01$	9
H5)	ISO_2 → ISOOH	$\gamma_5^{liq} = 0.07$, $\gamma_5^{ice} = 0.01$	9
H6)	$MACRO_2$ → MACROOH	$\gamma_6^{liq} = 0.07$, $\gamma_6^{ice} = 0.01$	9
H7)	CH_3COO_2 → products	$\gamma_7^{liq} = 0.004$, $\gamma_7^{ice} = 0.$	9
	— SO_2 oxidation (liquid-phase) —		
A1)	S(IV)^b+ O_3(aq) → SO_4	$l_1(\mathrm{T},[\mathrm{H}^+])$ ^{c}	10
A2)	S(IV) + H_2O_2(aq) → SO_4	$l_2(\mathrm{T},[\mathrm{H}^+])$ ^{c}	10

T, temperature (K); P_{atm}, pressure (atm); [M], air number density (cm^{-3}); [H_2O], water vapor density (cm^{-3}); The three-body reaction rates are computed by $k = (k_0[\mathrm{M}])/(1+k_0[\mathrm{M}]/k_\infty)F_c^{\{1+[\log_{10}(k_0[\mathrm{M}]/k_\infty)]^2\}^{-1}}$. References: 1, *DeMore et al.* [1997]; 2, *Atkinson et al.* [2000]; 3, *Cantrell et al.* [1985]; 4, *Jenkin et al.* [1997]; 5, *Müller and Brasseur* [1995]; 6, *Pöschl et al.* [2000]; 7, *Carter* [1990]; 8, *Dentener and Crutzen* [1993]; 9, *Jacob* [2000]; 10, *Hoffmann and Calvert* [1985].

[a] Considered for liquid-phase aerosols (uptake coefficient γ^{liq}) and ice cloud particles (γ^{ice}).

[b] S(IV) denotes the sum of SO_2(aq), HSO_3^-, and SO_3^{2-} in aqueous phase.

[c] Reaction rate constants as a function of T and [H^+] are given in Appendix 2B (page 106).

is given by the following, according to *Schwartz* [1986], *Dentener and Crutzen* [1993], and *Jacob* [2000].

$$\beta_i = \sum_j \left(\frac{4}{v_i \gamma_{ij}} + \frac{R_j}{D_{ij}} \right)^{-1} \cdot A_j \tag{2.1}$$

where v_i is the mean molecular speed (cm s^{-1}) of the species i (calculated as $\sqrt{8R_gT/(\pi M_i)} \times 10^2$, R_g: the gas constant, T: temperature, M: molecular mass), D_{ij} is the gaseous mass transfer (diffusion) coefficient (cm^2 s^{-1}) of the species i for the particle type j given as a function of the diffusive coefficient for i and the effective radius R_j (cm) for the particle type j [e.g., *Frössling*, 1938; *Perry and Green*, 1984], and A_j are the surface area density (cm^2 cm^{-3}) for the particle type j. In this study, j denotes sulfate aerosol, sea-salt aerosol, and liquid/ice particles in cumulus and large-scale clouds. In a run without sulfate simulation, concentrations of both sulfate and sea-salt are prescribed using the monthly averaged output from the global aerosol model [*Takemura et al.*, 2000] which is also based on the CCSR/NIES AGCM, whereas the model uses sulfate distributions calculated on-line in the model in a run including sulfate simulation (this study). Those concentrations are converted to the surface area densities A_j by assuming the log-normal distributions of particle size with mode radii variable with the relative humidity (RH). In the conversion, an empirical relation of *Tabazadeh et al.* [1997] and *Sander et al.* [2000] is also employed to estimate the weight percentage (%) of H_2SO_4/H_2O (sulfate) aerosol. The effective radius R_j for aerosols is calculated as a function of RH as in the aerosol model of *Takemura et al.* [2000]. In the case of reactions on cloud particles, spatially inhomogeneous distributions of clouds in the model grids should be taken into account in fact, since using the grid averaged surface area densities for clouds would lead to an overestimation of β in Equation 2.1 particularly for radical species with short lifetimes (i.e., due to unrealistic loss outside clouds). In this study, heterogeneous reactions on cloud particles for HO_2 and RO_2 radicals are applied only when the grid cloud fraction in the AGCM is 1 (100% cloud coverage). To estimate the surface area density for cloud particles, the liquid water content (LWC) and ice water content (IWC) in the AGCM are converted using the cloud droplet distribution of *Battan and Reitan* [1957] and the relation between IWC and the surface area density [*McFarquhar and Heymsfield*, 1996; *Lawrence and Crutzen*, 1998] (for ice clouds). In the simulation, Equation 2.1 gives τ ($\equiv 1/\beta$) of 1-5 min for $\gamma = 0.1$ in the polluted boundary layers (e.g., Europe) in accordance with the sulfate distributions, and τ ranging from several hours to a few days in the upper troposphere for $\gamma = 0.1$ (for liquid) and $\gamma = 0.01$ (for ice).

In this study, the model also includes the sulfate formation process with the gas and liquid-phase oxidation of SO_2 and dimethyl sulfide (DMS) as listed in Table 2.3. Details of the SO_2 oxidation in liquid-phase in the model (reaction A1 and A2) are described in Appendix 2B of this chapter (page 106). As described above, simulated sulfate distributions are reflected on-line on the calculation of the heterogeneous loss rates (Equation 2.1).

Reaction rate constants for the reactions listed in Table 2.2 and Table 2.3 are mainly taken from

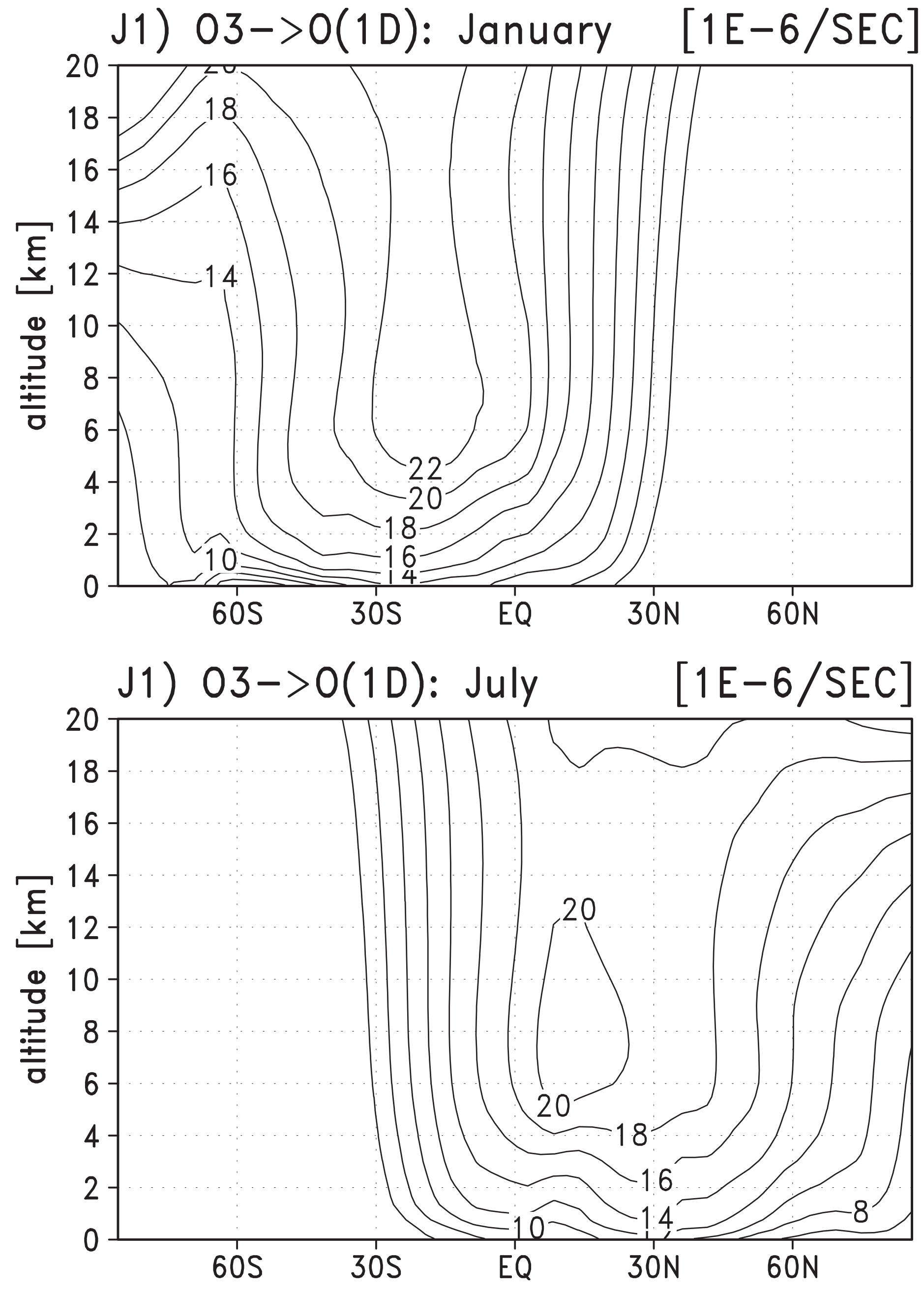

Figure 2.3. Zonally averaged photolysis rate (10^{-6} sec^{-1}) of the O_3 to $O(^1D)$ photolysis calculated for January and July.

DeMore et al. [1997] and *Atkinson et al.* [2000], and *Sander et al.* [2000] for updated reactions. The quantum yield for $O(^1D)$ production in ozone photolysis (J1) is based on *Talukdar et al.* [1998]. The photolysis rates (J-values) are calculated on-line by using temperature and radiation fluxes computed in the radiation component of CHASER. The radiation scheme adopted in CHASER (based on the CCSR/NIES AGCM) considers the absorption and scattering by gases, aerosols and clouds, and the effect of surface albedo. In the CCSR/NIES AGCM, the original wavelength resolution for the radiation calculation is relatively coarse in the ultraviolet and the visible wavelength regions as in general AGCMs. Therefore, the wavelength resolution in these wavelength regions has been improved for the photochemistry in CHASER. In addition, representative absorption cross sections and quantum yields for individual spectral bins are evaluated depending on the optical thickness computed in the radiation component, in a way similar to *Landgraf and Crutzen* [1998]. The photolysis rate for the $O_3 \rightarrow O(^1D)$ reaction calculated for January and July can be seen in Figure 2.3.

CHASER uses an Euler Backward Iterative (EBI) method to solve the gas-phase chemical reaction system. The method is largely based on *Hertel et al.* [1993] which increases the efficiency of the iteration process by using analytical solutions for strongly coupled species (e.g., OH-HO_2). For liquid-phase reactions, a similar EBI scheme is used to consider the time integration of concentrations in bulk phase (gas+liquid phase; see Appendix 2B, page 106). The chemical equations in both gas and liquid-phase are solved with a time step of 10 min in this study. Configurations of the chemical scheme such as a choice of species, reactions and reaction rates are automatically processed by the preprocessor to set up the model through input files (Figure 2.2). Therefore, the chemical reaction system as listed in Table 2.2 and Table 2.3 can be easily changed by an user.

2.2.2 Emissions

Surface emissions are considered for CO, NO_x, NMHCs, and sulfur species of SO_2 and DMS in this study (Table 2.4). Anthropogenic emissions associated with industry (e.g., fossil fuel combustion) and car traffic are based on the Emission Database for Global Atmospheric Research (EDGAR) Version 2.0 [*Olivier et al.*, 1996]. NMHCs emissions from ocean are taken from *Müller* [1992] as in the MOZART model. In the previous version of CHASER [*Sudo et al.*, 2002a], acetone (CH_3COCH_3) emission from ocean was not taken into account, and underestimation of acetone was found over remote Pacific areas by a factor of 2 [*Sudo et al.*, 2002b]. The model, in this study, includes oceanic acetone emissions amounting to 12 TgC/yr in the global in view of the simulation by *Jacob et al.* [2002]. The geographical distribution of biomass burning is taken from *Hao and Liu* [1994]. The emission rates of NMHCs by biomass burning were generally scaled to the values adopted in the MOZART model [*Brasseur et al.*, 1998]. The active fire (Hot Spot) data derived from Advanced Very High Resolution Radiometer (AVHRR) and Along Track Scanning Radiometer (ATSR) [*Arino et al.*, 1999] are used as a scaling factor to simulate the seasonal variation of biomass burning emissions. In this study, we estimated the timing of biomass burning emissions, using the hot spot data for 1999 derived from ATSR. We assumed that individual daily hot spots in a model grid cause emissions which decline in a time scale of 20 days in that grid. The temporal resolution for biomass burning emissions is 10 days in this study. Simulated biomass burning emissions in South America have peaks in late August and September (e.g., CO emission, Figure 2.4). In South Africa, biomass burning emissions begin in May or June near the equator and shift southward with having a peak in October, whereas they begin in July in South America. Consequently,

Table 2.4. Global Emissions of Trace Gases Considered in CHASER

	Indu.[a]	B.B[b]	Vegi.[c]	Ocean	Soil	Ligh.[d]	Airc.[e]	Volc.[f]	Total
NO_x	23.10	10.19	0.00	0.00	5.50	5.00[g]	0.55	0.00	44.34
CO	337.40	929.17	0.00	0.00	0.00	0.00	0.00	0.00	1266.57
C_2H_6	3.16	6.62	1.20	0.10	0.00	0.00	0.00	0.00	11.80
C_3H_8	5.98	2.53	1.60	0.11	0.00	0.00	0.00	0.00	10.22
C_2H_4	2.01	16.50	4.30	2.76	0.00	0.00	0.00	0.00	25.57
C_3H_6	0.86	7.38	1.20	3.36	0.00	0.00	0.00	0.00	12.80
CH_3COCH_3	1.02	4.88	11.20	12.00	0.00	0.00	0.00	0.00	29.10
ONMV	34.30	17.84	20.00	4.00	0.00	0.00	0.00	0.00	76.14
C_5H_8	0.00	0.00	400.00	0.00	0.00	0.00	0.00	0.00	400.00
$C_{10}H_{16}$	0.00	0.00	102.00	0.00	0.00	0.00	0.00	0.00	102.00
SO_2	71.83	2.64	0.00	0.00	0.00	0.00	0.09	4.80	79.41
DMS	0.00	0.00	0.00	14.93[g]	0.00	0.00	0.00	0.00	14.93

Units are TgN/yr for NO_x, TgCO/yr for CO, TgC/yr for NMHCs., and TgS/yr for SO_2 and DMS.
[a] Industry.
[b] Biomass Burning.
[c] Vegetaion.
[d] Lightning NO_x.
[e] Aircraft.
[f] Volcanic.
[g] Calculated in the model (see the text).

biomass burning emissions in South America are concentrated in August and September in comparison to South Africa. In South America, surface CO concentrations calculated by using this biomass burning emission seasonality have their peaks in September (see section 2.3.1), in good agreement with observations in South America. CO has industrial emission sources as well as biomass burning emission. Figure 2.5 shows the distribution of CO surface emission for three distinct seasons. Large CO emission is found in industrial regions (principally America, Europe, China, and India) as well as emissions of other trace gases. Biomass burning emission is most intensive in North Africa (January), in South America, and South Africa (September-October) as also seen in Figure 2.4. In April, large emission is found in southeastern Asia in accordance with biomass burning around the Thailand and northern India. In addition to surface emission, there are indirect CO sources from the oxidation of methane and NMHCs (computed in the model). The global CO source from the methane and NMHCs oxidation is estimated at 1514 Tg/yr in CHASER (the detailed budget of the tropospheric CO in CHASER is shown in section 2.3.1).

For NO_x, emissions from aircraft and lightning are considered as well as surface emission. Data for aircraft NO_x emission (0.55 TgN/yr) are taken from the EDGAR inventory. It is assumed that lightning NO_x production amounts to 5.0 TgN/yr in this study. In CHASER, lightning NO_x production is calculated in each time step using the parameterization of *Price and Rind* [1992] linked to the convection scheme of the AGCM. In the model, lightning flash frequencies in clouds are calculated

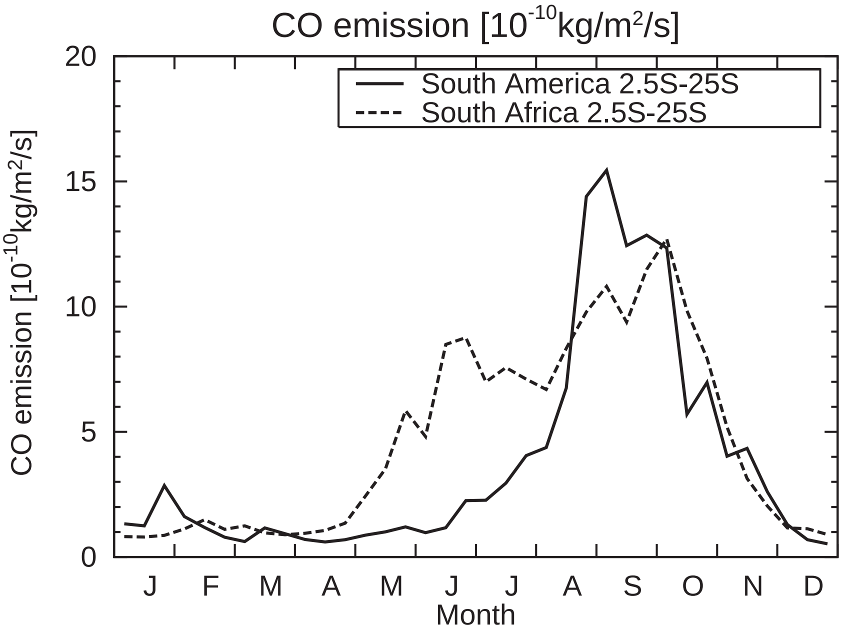

Figure 2.4. Seasonal variations of CO surface emission averaged over South America (2.5°S-25°S) and South Africa (2.5°S-25°S) in the model.

with using the cloud-top height (H) determined from the AGCM convection, and are assumed to be proportional to $H^{4.92}$ and $H^{1.73}$ for continental and marine convective clouds, respectively. The proportions of could-to-ground (CG) flashes and intracloud (IC) flashes (CG/IC) are also calculated with H, following *Price et al.* [1997] (NO_x production by CG flashes is assumed to be 10 times as efficient as by IC flashes). Computed lightning NO_x emission is redistributed vertically by updrafts and downdrafts in the AGCM convection scheme after distributed uniformally in the vertical. As a consequence, computed lightning NO_x emission is transported to the upper tropospheric layers and fractionally to the lower layers in the model (leading to C-shape profiles) as studied by *Pickering et al.* [1998]. The distributions of aircraft and lightning NO_x emissions in the model are shown in Figure 2.6. The aircraft emission seems to have an importance for the NO_x budget in the northern mid-high latitudes especially in wintertime. The lightning emission is generally intense over the continents in the summer-hemisphere. In July, lightning NO_x production is most intensive in the monsoon region like southeastern Asia and North Africa where convective activity is high in this season. NO_x also has an emission source from soils (5.5 TgN/yr) in the model. Soil NO_x emission is prescribed using monthly data for soil NO_x emission from *Yienger and Levy* [1995], obtained via the Global Emissions Inventory Activity (GEIA) [*Graedel et al.*, 1993].

Biogenic emissions from vegetation are considered for NMHCs. The monthly data by *Guenther et al.* [1995], obtained via the GEIA inventory, are used for isoprene, terpenes, ONMV, and other NMHCs emissions. Isoprene emission and terpenes emission are reduced by 20% to 400 TgC/yr and 102 TgC/yr respectively following *Houweling et al.* [1998] and *Roelofs and Lelieveld*

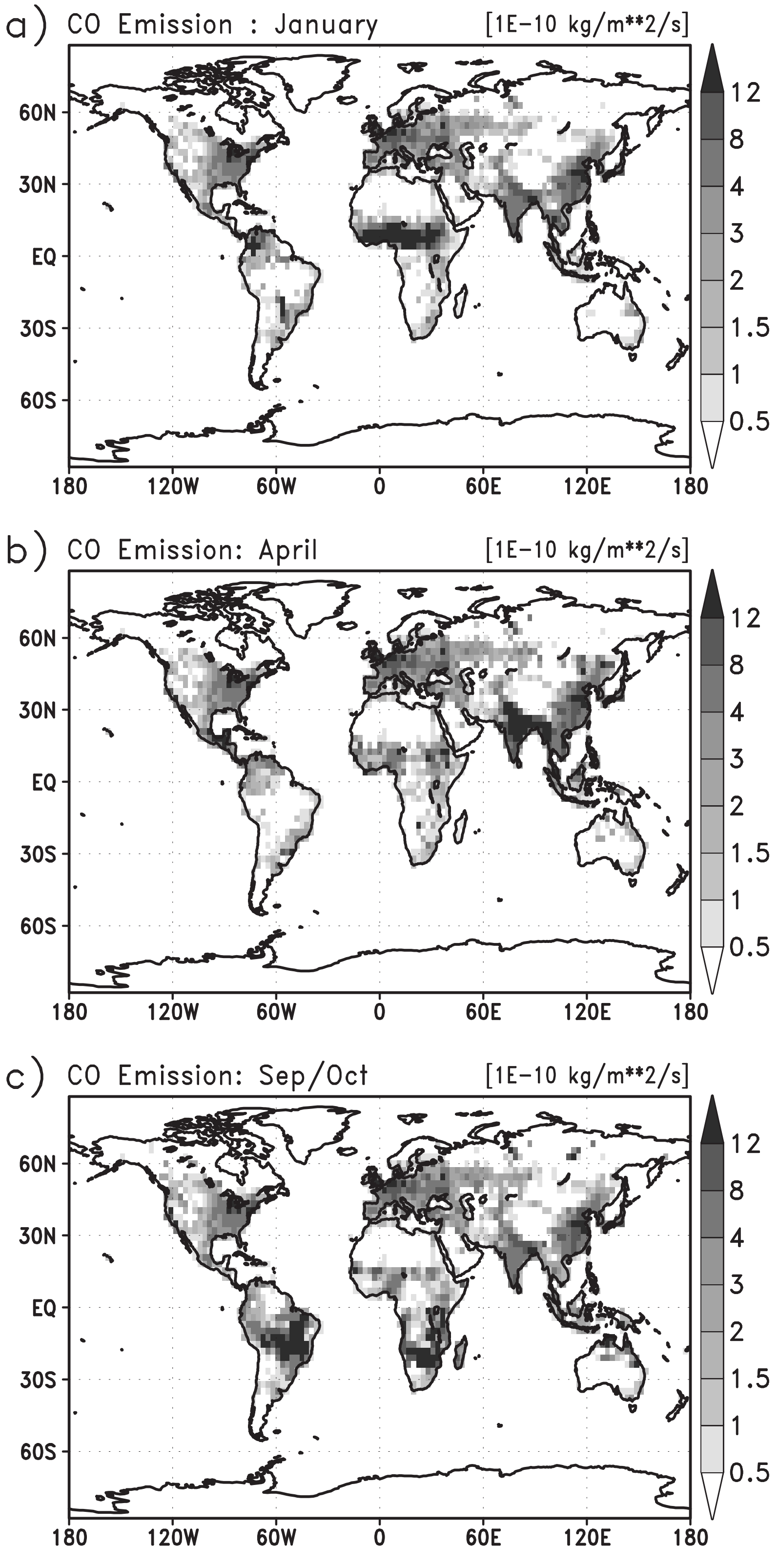

Figure 2.5. Distributions of CO surface emission (10^{-10} kg m^{-2} s^{-1}) considered in the model in January (a), July (b), and September-October (c) average.

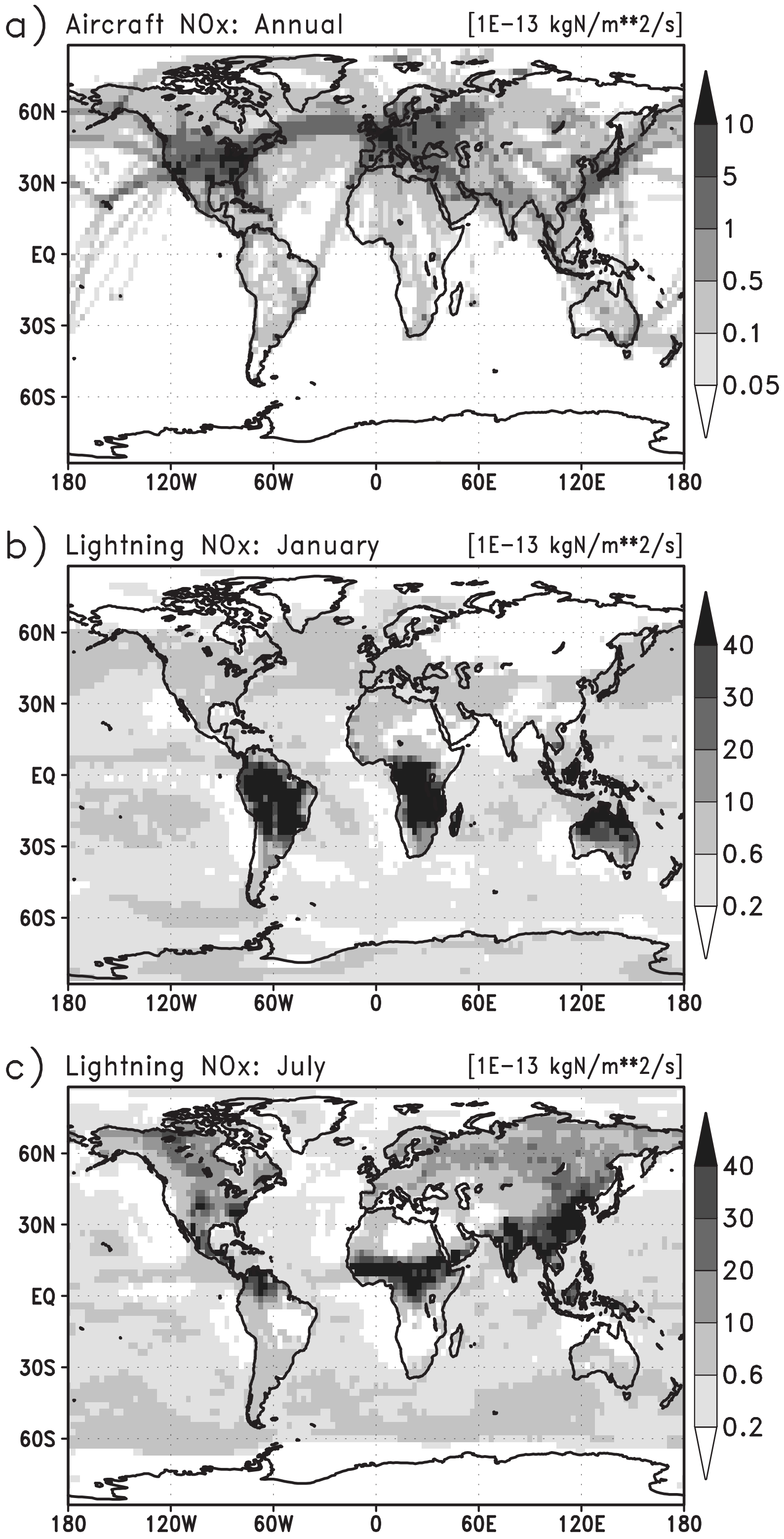

Figure 2.6. Distributions of aircraft and lightning NO_x emission (column total) in CHASER. (a) Aircraft emission (annual mean). (b), (c) lightning emission calculated for January and July respectively.

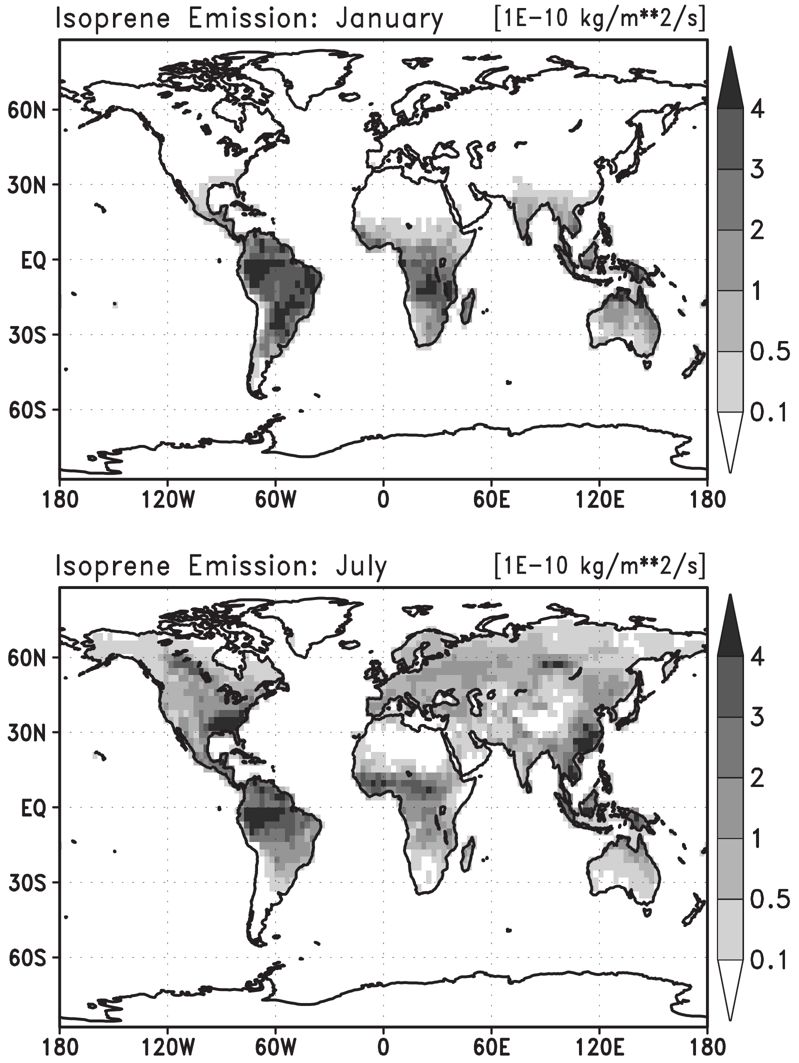

Figure 2.7. Distributions of isoprene (C_5H_8) surface emission for January and July.

[2000]. The diurnal cycle of isoprene emission is simulated using solar incidence at the surface. For terpenes emission, the diurnal cycle is parameterized using surface air temperature in the model [*Guenther et al.,* 1995]. Figure 2.7 shows the distributions of isoprene emission for January and July in the model. Isoprene emission is dominantly large in the tropical region through a year as well as other biogenic NMHCs emissions. In July, isoprene emission is large through much of the continent in the northern hemisphere, with showing significant values in the eastern United States and eastern Asia.

For the sulfate simulation, SO_2 emissions from industry, biomass burning, volcanos, and aircraft are considered using the EDGAR and GEIA database [*Olivier et al.*, 1996; *Andres and Kasgnoc*, 1998], with DMS emission from ocean. As in the aerosol model of *Takemura et al.* [2000], the DMS flux from ocean F_{DMS} (kg m$^{-2}s^{-1}$) is given as a function of the downward solar flux F_S (W m^{-2}) at the surface, using the following simple parameterization [*Bates et al.*, 1987].

$$F_{\mathrm{DMS}} = 3.56 \times 10^{-13} + 1.08 \times 10^{-14} \times F_{\mathrm{S}} \tag{2.2}$$

This applies to the ocean grids with no sea ice cover in the model. Note that this parameterization ignores other factors controlling the DMS flux such as distribution of planktonic bacteria [e.g., *Six and Maier-Reimer*, 1996].

2.2.3 Deposition

Deposition processes significantly affect the distribution and budget of trace gas species (e.g., O_3, NO_x, HO_x). The CHASER model considers dry deposition at the surface and wet scavenging by precipitation.

Dry deposition

In CHASER, dry deposition scheme is largely based on a resistance series parameterization of *Wesely* [1989] and applied for ozone (O_x), NO_x, HNO_3, HNO_4, PAN, MPAN, ISON, H_2O_2, CO, CH_3COCH_3, CH_2O, MGLY, MACR, HACET, SO_2, DMS, SO_4 and peroxides like CH_3OOH (see Table 2.1) in this study. Dry deposition velocities (v_d) for the lowermost level of the model are computed as

$$v_d = \frac{1}{r_a + r_b + r_s} \tag{2.3}$$

where r_a, r_b, r_s are the aerodynamic resistance, the surface canopy (quasi-laminar) layer resistance, and the surface resistance respectively. r_a has no species dependency and is calculated using surface windspeed and bulk coefficient computed for the model's lowest level in the AGCM. r_b is calculated using friction velocity computed in the AGCM and the Shumid number (calculated with the kinematic viscosity of air and the diffusive coefficient for individual species). Finally, the most important resistance r_s is calculated as a function of surface (vegetation) type over land and species using temperature, solar influx, precipitation, snow cover ratio, and the effective Henry's law constant calculated for individual species in the AGCM. r_s over sea and ice surface are taken to be the values used in *Brasseur et al.* [1998] (e.g., $v_d(O_3)$ = 0.075 cm s^{-1} over sea and ice). The above parameterization, for gaseous species, can not apply for sulfate aerosol (SO_4). In this study, deposition of SO_4 is simulated using a constant velocity v_d of 0.1 (cm s^{-1}). The effect of dry deposition on the concentration of each species in the lowest layer is evaluated together with surface emissions and vertical diffusion by solving the diffusion equations implicitly.

Figure 2.8 shows the calculated 24-hour average deposition velocities (cm s^{-1}) of ozone in January and July. The values show the deposition velocities calculated for the surface elevation. Deposition velocities of ozone are generally higher than 0.1 cm s^{-1}, except for the high latitudes in winter where solar influx is less intense and much of the surface is covered with snow. In July, ozone deposition velocity ranges from 0.2 to 0.5 cm s^{-1} over land surface in the northern hemisphere (0.3-0.7 cm s^{-1} in daytime), in good agreement with the observations [*Van Pul*, 1992; *Ritter et al.*, 1994; *Jacob et al.*, 1992; *Massman et al.*, 1994]. In the tropical rain forest region (e.g., the Amazon Forest), deposition velocities are high with a range of 0.7-1.2 cm s^{-1} throughout a year, in agreement with the observations [*Fan et al.*, 1990].

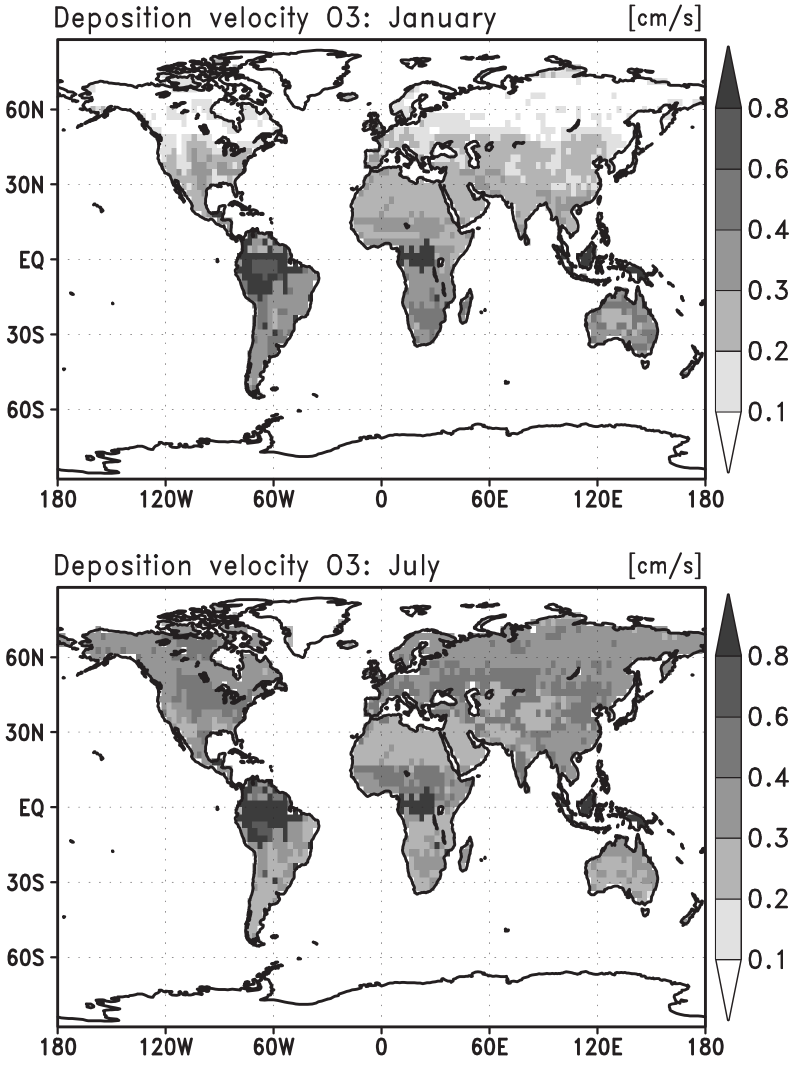

Figure 2.8. Calculated 24-hour average deposition velocities (cm/s) for ozone at the surface in January and July.

Wet deposition

Wet deposition due to large-scale condensation and convective precipitation is considered in two different ways in the model; in-cloud scavenging (rain-out) and below-cloud scavenging (wash-out). A choice of gaseous species which are subject to wet deposition is determined from their effective Henry's law constant in standard conditions (H_s, $T = 298.15$ K). In the present model configuration, wet deposition is applied for species whose H_s are greater than 10^2 M atm^{-1} for both in-cloud and below-cloud scavenging. In this study, the model considers wet deposition for HNO_3, HNO_4, CH_2O, MGLY, HACET, ISON, SO_2, SO_4 and peroxides (H_2O_2, CH_3OOH, etc.), Note that the wet deposition scheme in the previous version of CHASER [*Sudo et al.*, 2002a] does not separate liquid and ice precipitations and ignores the reemission process of dissolved species to the atmosphere, assuming irreversible scavenging. Those processes are newly included in this study as described in the following.

For in-cloud scavenging, the first-order parameterization of *Giorgi and Chameides* [1985] is employed and is extended to incorporate deposition on ice particles. The scheme consists of three processes; deposition associated with liquid precipitation (scavenging loss rate β_l, s^{-1}), with ice precipitation (β_i), and with gravitational settling of ice particles in cirrus clouds (β_s). In this study, deposition on ice particles (i.e., β_i and β_s) is considered only for HNO_3 and H_2O_2. The total loss rate β due to in-cloud scavenging is given by:

$$\beta = \beta_l + \beta_i + \beta_s, \tag{2.4}$$

where

$$\beta_l = \frac{W_l \cdot HRT}{1 + L \cdot HRT + I \cdot K_i} \tag{2.5}$$

$$\beta_i = \frac{W_i \cdot K_i}{1 + L \cdot HRT + I \cdot K_i} \tag{2.6}$$

$$\beta_s = \frac{W_s \cdot K_i}{1 + L \cdot HRT + I \cdot K_i} \tag{2.7}$$

with L and I the liquid and ice water contents (g cm^{-3}), H the effective Henry's law constant, R the gas constant, K_i the ice/gas partitioning coefficient, W_l, W_i and W_s the tendencies (g cm^{-3} s^{-1}) for liquid precipitation, ice precipitation (snow), and gravitational settling of ice particles, respectively. L, I, W_l, W_i, and W_s are computed with respect to convective and large-scale clouds in the AGCM. The tendency due to cloud particle settling W_s are calculated with the terminal velocities of ice cloud particles estimated as a function of I [*Lawrence and Crutzen*, 1998]. The ice/gas uptake partitioning coefficient K_i for H_2O_2 is calculated as a function of temperature according to *Lawrence and Crutzen* [1998]. For HNO_3, K_i is taken to be a large value ($> 10^{10}$), assuming efficient HNO_3 uptake on ice surface. The downward flux of ice-soluble species (HNO_3 and H_2O_2 in this study) associated with cloud gravitational settling (β_s) is treated as a gas-phase flux and is reevaluated in the model grids below clouds.

In the case of below-cloud scavenging, reversible scavenging is considered, which allows reemission of species dissolved in raindrops or precipitating particles to the atmosphere. The tendency of gas-phase concentrations in the ambient atmosphere C_g (g cm^{-3}) due to below-cloud scavenging is given by:

$$\frac{dC_g}{dt} = -K_g(d) \cdot S_p \cdot (C_g - C_e) \tag{2.8}$$

with d the raindrop size (cm) calculated according to *Mason* [1971] and *Roelofs and Lelieveld* [1995], K_g the mass transfer coefficient of a gaseous molecule to a drop calculated by an empirical correlation [e.g., *Frössling*, 1938] as a function of the raindrop size d, the kinematic viscosity of air, the diffusive coefficients, and the terminal velocity of raindrops computed using an empirical relation to d, S_p the surface area density (cm^2/cm^3) of raindrop in the atmosphere, C_e the gas-phase concentration (g cm^{-3}) on the drop surface in equilibrium with the aqueous-phase concentration. The equilibrium concentration C_e is given as:

$$C_e = \frac{C}{HRT} \tag{2.9}$$

with C the aqueous-phase concentration in raindrops (g cm^{-3}) calculated by:

$$C = \frac{F}{P} \tag{2.10}$$

with P the precipitation flux (g cm^{-2} s^{-1}) of rain, and F the flux (g cm^{-2} s^{-1}) of the species dissolved in raindrops (i.e., deposition flux of the species originating from scavenging in the above layers). For the tendency of the ambient mixing ratio Q (g g^{-1}) in the model grids, Eq. 2.8 can be rewritten as:

$$\frac{dQ}{dt} = -\beta_Q(Q - Q_e) \tag{2.11}$$

where $\beta_Q \equiv K_g S_p$ is the scavenging or reemission rate, and Q_e is the equilibrium mixing ratio given by:

$$Q_e = \frac{C}{\rho HRT} = \frac{F}{\rho PHRT} \tag{2.12}$$

with ρ the atmospheric density (g cm^{-3}). Assuming a spherical raindrop, S_p is given as:

$$S_p = L_p \frac{6}{d} \tag{2.13}$$

with L_p the raindrop density (g cm^{-3}) determined from the precipitation flux and the terminal velocity of raindrops, and thereby β_Q is calculated as:

$$\beta_Q = K_g S_p = \frac{6 L_p K_g}{d} \tag{2.14}$$

In the actual scheme, the above calculated β_Q is modified to meet the following mass conservation between C_g (gas-phase) and C (aqueous-phase).

$$\frac{dC_g}{dt} + L_p \frac{dC}{dt} = 0 \tag{2.15}$$

The same type of calculation can apply also for ice precipitation (snow), using K_i and I instead of HRT and L, respectively. The terminal velocity of snowflakes is calculated following *Lawrence and Crutzen* [1998]. In this study, below-cloud scavenging due to ice precipitation is applied only for HNO_3 and H_2O_2 using K_i as used for in-cloud scavenging. For HNO_3, a highly soluble species ($H > 10^{10}$ M atm^{-1}), Q_e is generally calculated to be much small relative to Q ($Q_e \ll Q$), which leads to irreversible scavenging. For moderately soluble species like CH_2O and peroxides, reemission from raindrops ($Q_e > Q$ in Eq. 2.11) is calculated near the surface in the model. In the case of particulate species (SO_4 in this study), below-cloud scavenging is evaluated using the following first-order loss rate:

$$\beta = E\frac{\pi}{4}(d+d_a)^2(v_p - v_a)N_p \tag{2.16}$$

with E the collision efficiency as a function of d, d_a the aerosol particle diameter (cm), v_p and v_a the terminal velocities of raindrops and aerosol particles, and N_p the raindrop number density (cm^{-3}). The aerosol particle diameter d_a is calculated depending on RH in the model. The terminal velocity v_a is estimated by the Stokes's law with a slip correction factor [*Allen and Raabe*, 1982]:

$$v_a = \frac{g\rho_a d^2}{18\eta} \cdot \left[1 + 2\frac{\lambda}{d_a}\left(1.21 + 0.4\exp\left(-0.39\frac{d_a}{\lambda}\right)\right)\right] \tag{2.17}$$

where ρ_a is the aerosol density, η and λ are the viscosity and mean free path of air, and g is the gravitational acceleration. This calculation of v_a is also used for the gravitational settling process of aerosol particles in the model. For both gaseous and particulate species, the model also considers the reemission process of dissolved species due to reevaporation of rain or snow in the falling path.

With the above described schemes for in-cloud and below-cloud scavenging, concentrations of individual species dissolved in precipitation are predicted in the model as by Eq 2.10. Figure 2.9 displays the contributions by HNO_3 and SO_4 deposition to the pH value in precipitation (i.e., effect on acid rain) calculated at the surface for January. The contributions are calculated as:

$$\mathrm{pA_N} = -\log[\mathrm{NO_3^-}] \tag{2.18}$$

$$\mathrm{pA_S} = -\log[\mathrm{SO_4^{2-}}] \tag{2.19}$$

using the concentrations (eq l^{-1}) of HNO_3 and SO_4 ($[\mathrm{NO_3^-}], [\mathrm{SO_4^{2-}}]$) in precipitation as with pH ($\equiv -\log[\mathrm{H^+}]$). The contribution by SO_4 deposition ($\mathrm{pA_S}$) appears to be generally larger than that by HNO_3 deposition ($\mathrm{pA_N}$), with showing 4.3-4.0 in the polluted areas around Europe and eastern Asia. Relatively low values of $\mathrm{pA_N}$ (4.8-5.0) in the northern high latitudes are due partly to HNO_3 deposition associated with precipitation and sedimentation of ice particles from the upper troposphere and the lower stratosphere. If $[\mathrm{SO_4^{2-}}]$ is assumed to be neutralized by cations such as $\mathrm{Ca^{2+}}$, $\mathrm{Mg^{2+}}$, and $\mathrm{NH_3^+}$ in precipitation, pH is estimated as $\mathrm{pA_N}$. On this assumption, the distribution of precipitation pH ($\equiv \mathrm{pA_N}$) derived from this simulation (i.e., Figure 2.9a) is well comparable with the estimation by the WMO [*Whelpdale and Miller*, 1989].

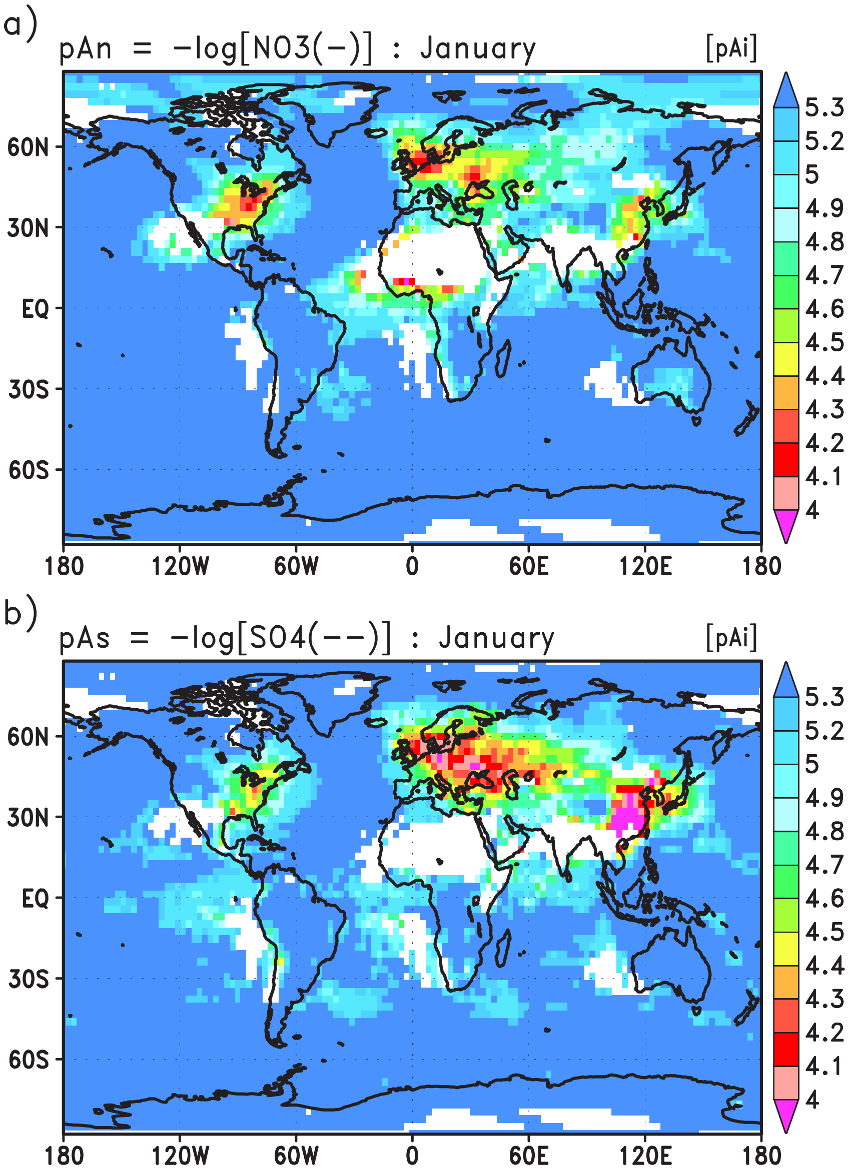

Figure 2.9. Simulated distributions of (a) $\mathrm{pA_N}(= -\log[\mathrm{NO_3^-}])$ and (b) $\mathrm{pA_S}(= -\log[\mathrm{SO_4^{2-}}])$ in precipitation to show the contribution by HNO_3 and SO_4 deposition to precipitation pH in the model (for January). Shown are averages volume-weighed with precipitation amount.

The simulated concentrations of nitrates (NO_3^-) and sulfate (SO_4^{2-}) in precipitation are also evaluated with the observation operated by the EMEP network. Figure 2.10 and 2.11 compare the simulated and observed seasonal variation of NO_3^- (mgN l^{-1}) and SO_4^{2-} (mgS l^{-1}) in precipitation for the EMEP sites (during 1978-1995). Both compare concentrations of NO_3^- and SO_4^{2-} volume-weighed with precipitation amount for every month. For both NO_3^- and SO_4^{2-}, the model well captures the observed concentrations, calculating 0-1 mgN l^{-1} for NO_3^- and 0-2 mgS l^{-1} for SO_4^{2-}. The calculation generally shows higher variabilities (indicated by boxes) in winter for both NO_3^- and SO_4^{2-}. The same kind of comparison is also made for wet deposition flux of NO_3^- and SO_4^{2-} with the EMEP data (Figure 2.12 and 2.13). The modeled deposition flux appears to be well comparable with the observation, showing ranges of 0.1-0.5 kgN ha^{-1} month^{-1} for NO_3^- and 0.1-1 kgS ha^{-1} month^{-1} for SO_4^{2-}. The model generally captures the observed seasonal variation associated with chemical production of nitric acid (HNO_3) and sulfate (SO_4^{2-}) and with precipitation. The simulated wet deposition flux in the day-to-day calculations is highly variable (indicated by boxes in the figures) as well as the large annual variation of the observation (error bars). The agreement between the simulation and observation appears to imply successful simulation of the deposition scheme adopted in this study. It should be, however, noted that the above comparisons depend much on precipitation itself simulated by the GCM. Further evaluation of precipitation is needed to validate the nitrates and sulfate simulation in this study (see section 2.3.2 and section 2.3.5 for the simulation of HNO_3 and sulfate).

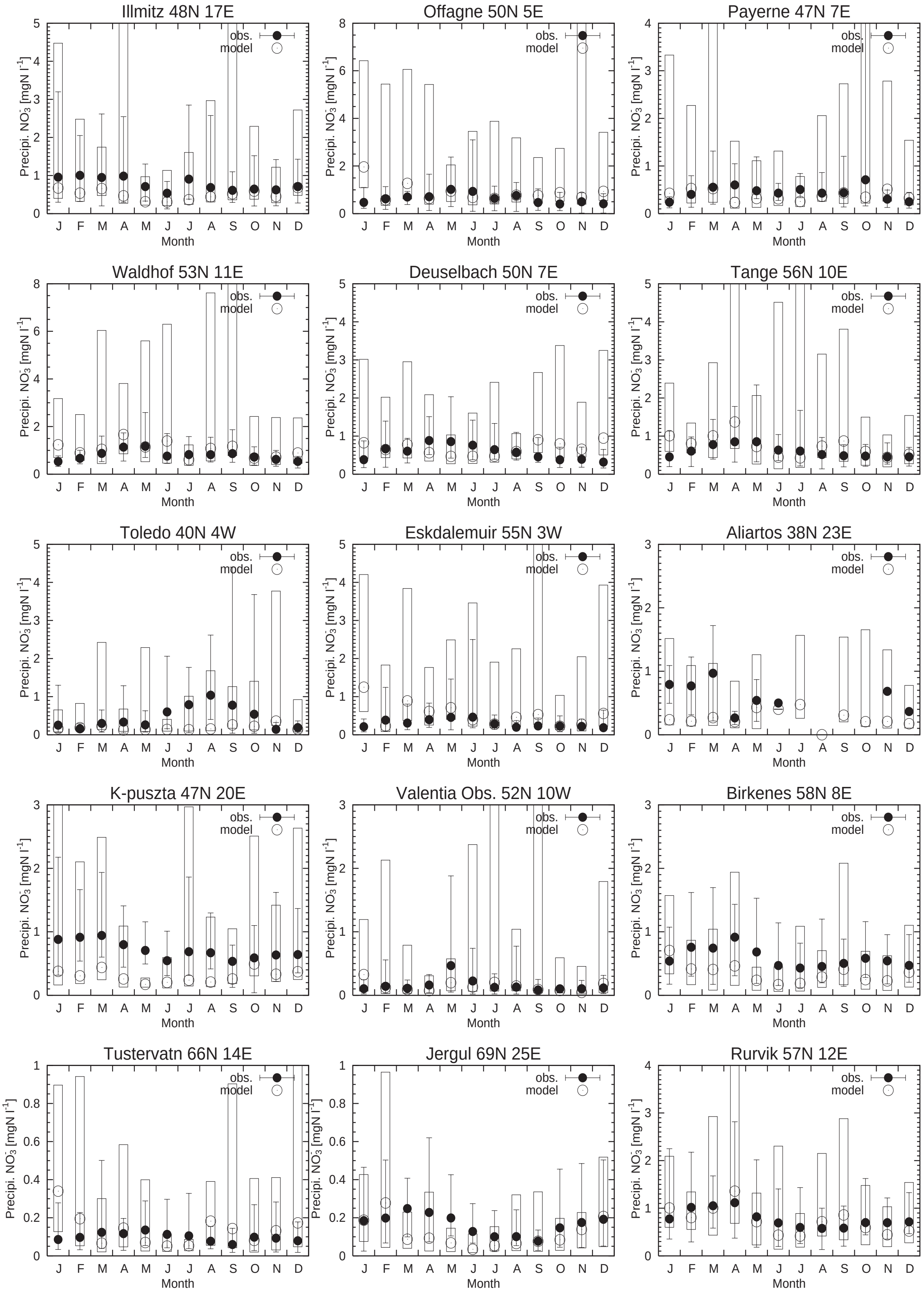

Figure 2.10. Seasonal variations of NO_3^- in precipitation (mgN l^{-1}) observed (solid circles) and calculated (open circles with boxes showing the range) at the surface sites. Both the observations and calculations are volume-weighed with precipitation amount. The ranges of annual variation of the observation (during 1978-1995) are also shown with error bars. The observations are taken from the EMEP network.

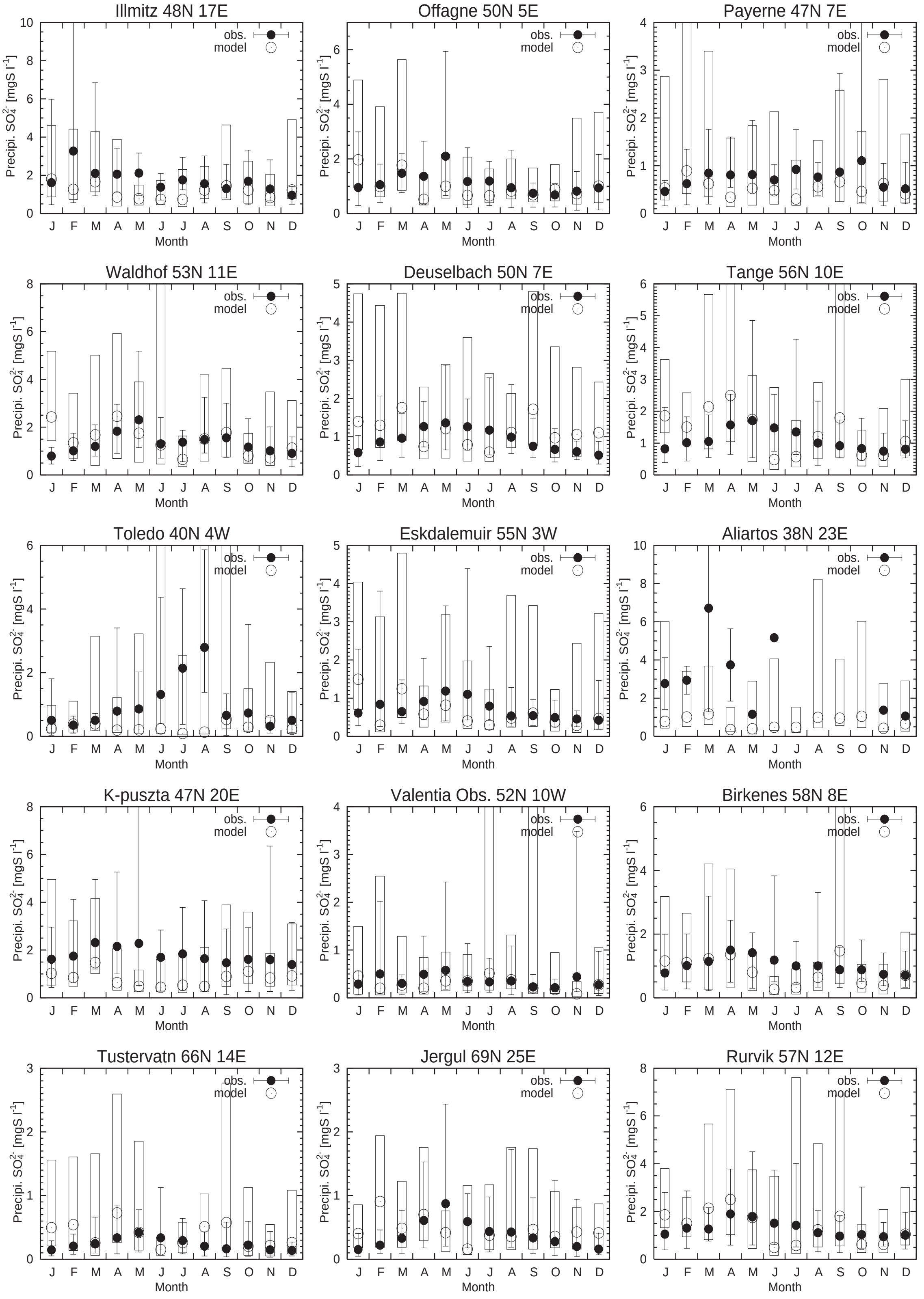

Figure 2.11. Same as Figure 2.10 but for SO_4^{2-} in precipitation (mgS l^{-1}).

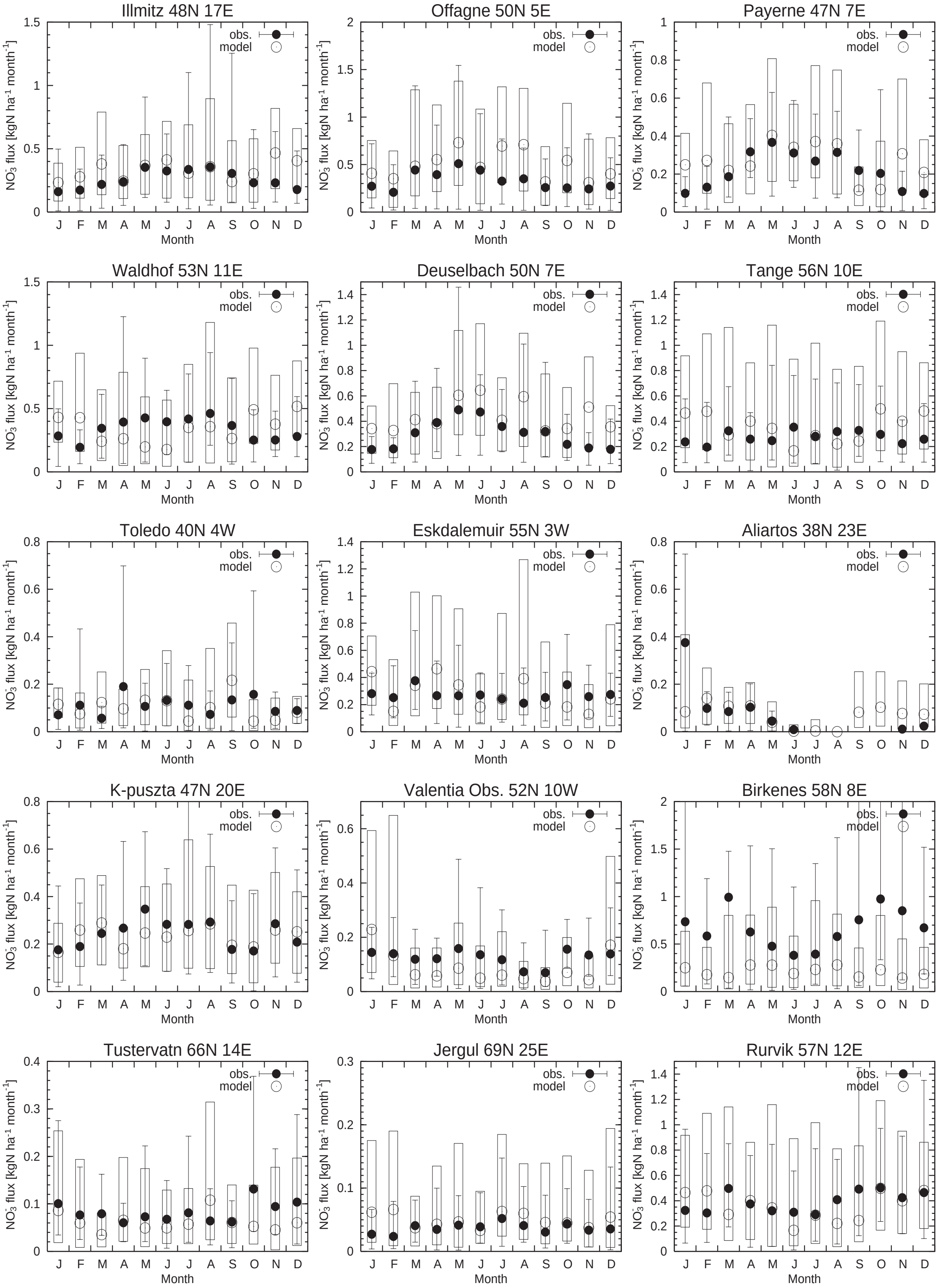

Figure 2.12. Seasonal variations of NO_3^- wet deposition flux (kgN ha^{-1} month^{-1}) observed (solid circles) and calculated (open circles with boxes showing the range) at the surface sites. The ranges of annual variation of the observation (during 1978-1995) are also shown with error bars. The observations are taken from the EMEP network.

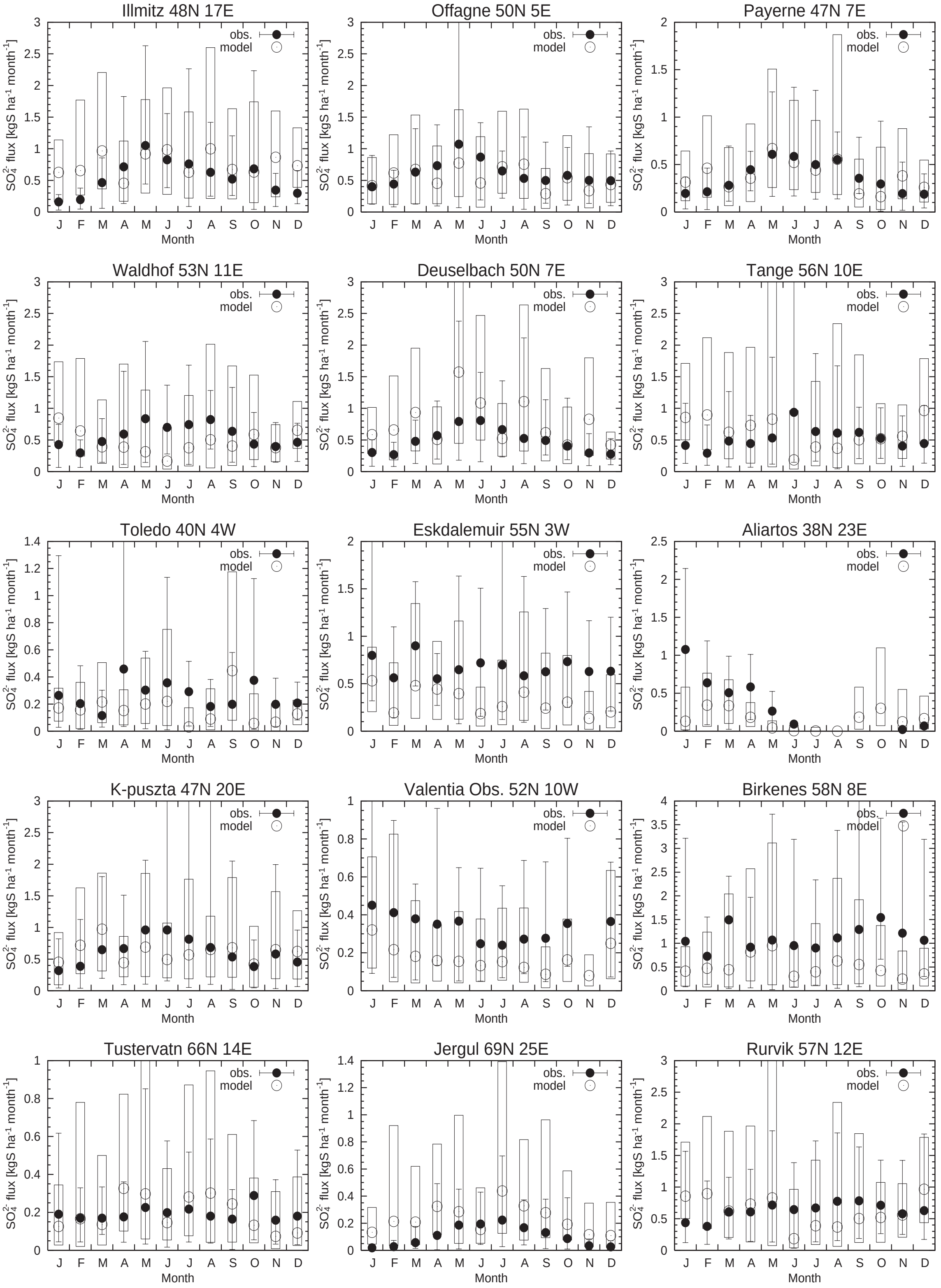

Figure 2.13. Same as Figure 2.12 but for SO_4^{2-} wet deposition flux (kgS ha^{-1} month^{-1}).

2.3 Model results and evaluation

The previous sections have described a global chemical model of the troposphere, named CHASER (CHemical AGCM for Study of atmospheric Environment and Radiative forcing). In this section, results and evaluation of the model are presented. CHASER is basically driven on-line by climatological meteorology generated by the AGCM. For simulations of a specific time period, analyzed data of wind velocities, temperature, and specific humidity as from the ECMWF are optionally used as a constraint to the AGCM. For the simulation considered in this section, horizontal wind velocities and temperature (u, v, and T) in the model are moderately nudged to those from the ECMWF with a relaxation time of one week. The model in this study adopts the horizontal resolution of T42 (approximately 2.8° longitude×2.8° latitude) , with 32 layers in the vertical from the surface to about 40 km altitude.

To validate the model capability to simulate the tropospheric photochemistry, it is necessary to evaluate the model results of ozone and species related to the ozone production and destruction (i.e., peroxy radicals, NO_x, CO, NMHCs, and reservoir species). Additionally, we need to carefully evaluate aldehydes and peroxyacetylnitrate (PAN) simulated by the model, to check the simplified chemical schemes for NMHCs adopted in the model (especially of the condensed isoprene and terpenes oxidation schemes, see section 2.2.1). The model was evaluated with several observational data sets. The data set of *Emmons et al.* [2000], a compilation made from the NASA Global Tropospheric Experiment (GTE) aircraft campaigns, is mainly used to evaluate the vertical distributions of calculated chemical species. This data set is also used for evaluation of the IMAGES model [*Müller and Brasseur*, 1995] and the MOZART model [*Hauglustaine et al.*, 1998; *Emmons et al.*, 2000]. Information about the NASA GTE observations is briefly summarized in Table 2.5. For comparison with the GTE data, model results of individual species are averaged over the regions and dates as listed in Table 2.5. It should be noted that data from campaign observations like the NASA GTE are not climatological, and that there may be some differences in meteorological conditions between the campaign observations and the climatological simulations by the model. In the evaluation of ozone and surface CO, climatological data [e.g., *Logan*, 1999; *Novelli et al.*, 1992, 1994] are used in addition to the NASA GTE data.

In this study, global tropospheric budget is calculated for some species such as CO and O_3. The budget is calculated for the region below the tropopause height determined from the vertical temperature gradient (-2 K/km) in the model. Each budget shows global annual averages of values (source and sink, etc.) calculated at each time step (typically 20 min in this study) in the model.

The results and evaluation of CO and NMHCs are presented in section 2.3.1, and reactive nitrogen oxides (NO_y) such as NO, HNO_3, and PAN in section 2.3.2. The results of HO_x and related species (formaldehyde CH_2O, acetone, and peroxides) are evaluated in section 2.3.3. Section 2.3.4 presents and evaluates the simulated ozone and the global tropospheric ozone budget calculated

Table 2.5. NASA GTE Campaign Regions and Dates

Campaign	Dates	Region Name	Latitudes	Longitudes
ABLE-3A	July 7 to Aug. 17, 1988			
		Alaska	55N-75N	190E-205E
ABLE-3B	July 6 to Aug. 15, 1990			
		Ontario	45N-60N	270E-280E
		US-E-Coast	35N-45N	280E-290E
		Labrador	50N-55N	300E-315E
PEM-WEST-A	Sept. 16 to Oct. 21, 1991			
		Hawaii	15N-35N	180E-210E
		Japan	25N-40N	135E-150E
		China-Coast	20N-30N	115E-130E
PEM-WEST-B	Feb. 7 to March 14, 1994			
		Japan	25N-40N	135E-150E
		China-Coast	20N-30N	115E-130E
		Philippine-Sea	5N-20N	135E-150E
PEM-Tropics-A	Aug. 15 to Oct. 5, 1996			
		Hawaii	10N-30N	190E-210E
		Chris.-Island	0-10N	200E-220E
		Tahiti	20S-0	200E-230E
		Fiji	30S-10S	170E-190E
		Easter-Island	40S-20S	240E-260E
PEM-Tropics-B	March 6 to April 18, 1999			
		Hawaii	10N-30N	190E-210E
		Chris.-Island	0-10N	200E-220E
		Tahiti	20S-0	200E-230E
		Fiji	30S-10S	170E-190E
		Easter-Island	40S-20S	240E-260E
TRACE-A	Sept. 21 to Oct. 26, 1992			
		S-Africa	25S-5S	15E-35E
		W-Africa-Coast	25S-5S	0E-10E
		S-Atlantic	20S-0	340E-350E
		E-Brazil	15S-5S	310E-320E
		E-Brazil-Coast	35S-25S	305E-320E
TRACE-P	March 3 to April 15, 2001			
		Japan	25N-40N	135E-150E
		China-Coast	20N-30N	115E-130E

Only campaigns and regions used for the evaluation are listed.

by the model. Simulation of sulfur species (SO_2 and sulfate) in this study is also summarized in section 2.3.5.

2.3.1 CO and NMHCs

Carbon monoxide (CO) and nonmethane hydrocarbons (NMHCs) play important roles in tropospheric chemistry, reacting with OH (controlling OH concentration) and significantly enhancing the ozone production. In this section, CO and NMHCs species (mainly of ethane and propane) simulated by CHASER are evaluated.

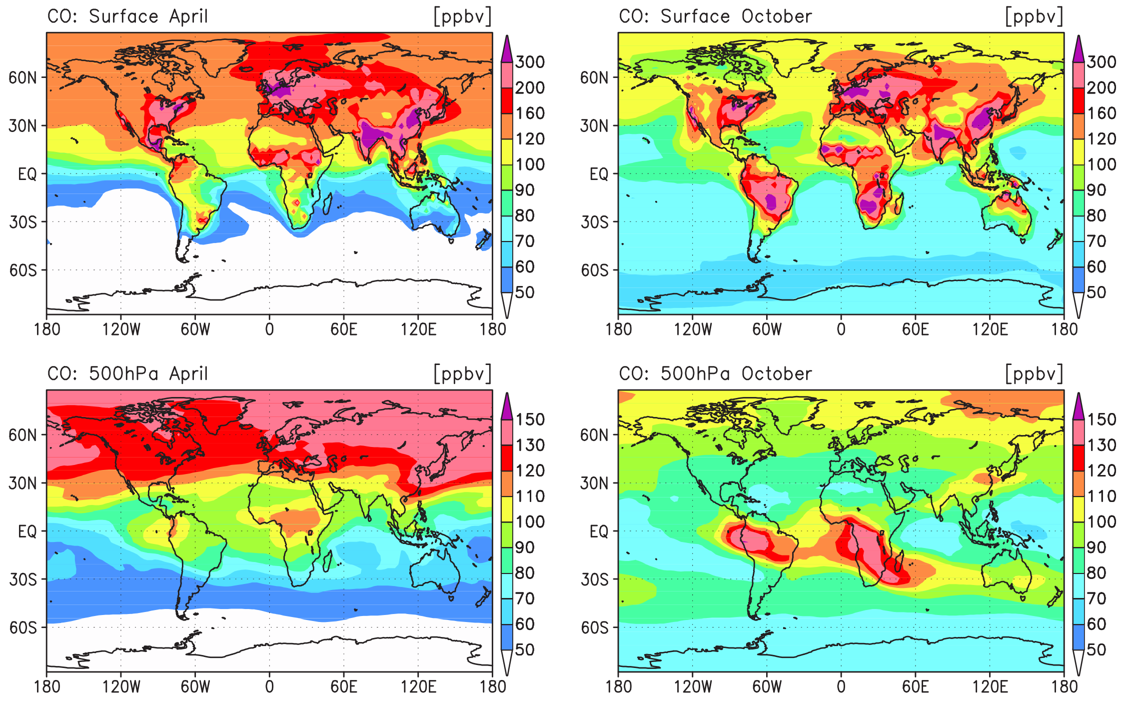

Figure 2.14. Calculated CO distributions (ppbv) at the surface and 500 hPa for April (left) and October (right).

CO

Figure 2.14 shows the calculated CO distributions at the surface and 500 hPa altitude for April and October. The CO mixing ratios calculated for April are generally higher than 100 ppbv in the northern hemisphere at both the surface and 500 hPa, with showing steep concentration gradients in the midlatitudes. At 500 hPa, two CO peaks are found in the tropics over South America and South Africa, reflecting vertical transport of CO from the surface and the CO production from oxidation of NMHCs species emitted by vegetation. The surface CO mixing ratios of 200-350 ppbv are predicted for both April and October in the industrial regions as the eastern United States, Europe, and eastern Asia. In October, high concentrations of CO (∼300 ppbv) are also calculated at the surface in South America and South Africa, associated with biomass burning emissions considered in the model. The effect of biomass burning emissions on CO is clearly seen at 500 hPa. CO emitted or produced at the surface in South America and South Africa is vertically transported, resulting in high levels of CO (120-150 ppbv) at this altitude. Relatively high CO concentrations (∼100 ppbv) are also extending over the South Atlantic, and over the Indian Ocean toward Australia like a plume.

Figure 2.15 compares the seasonal cycle of surface CO mixing ratios observed and calculated at several sites. The model generally well reproduces the observed CO seasonal variations. The seasonal variations of surface CO, characterized by spring-maximum, are associated with the seasonal

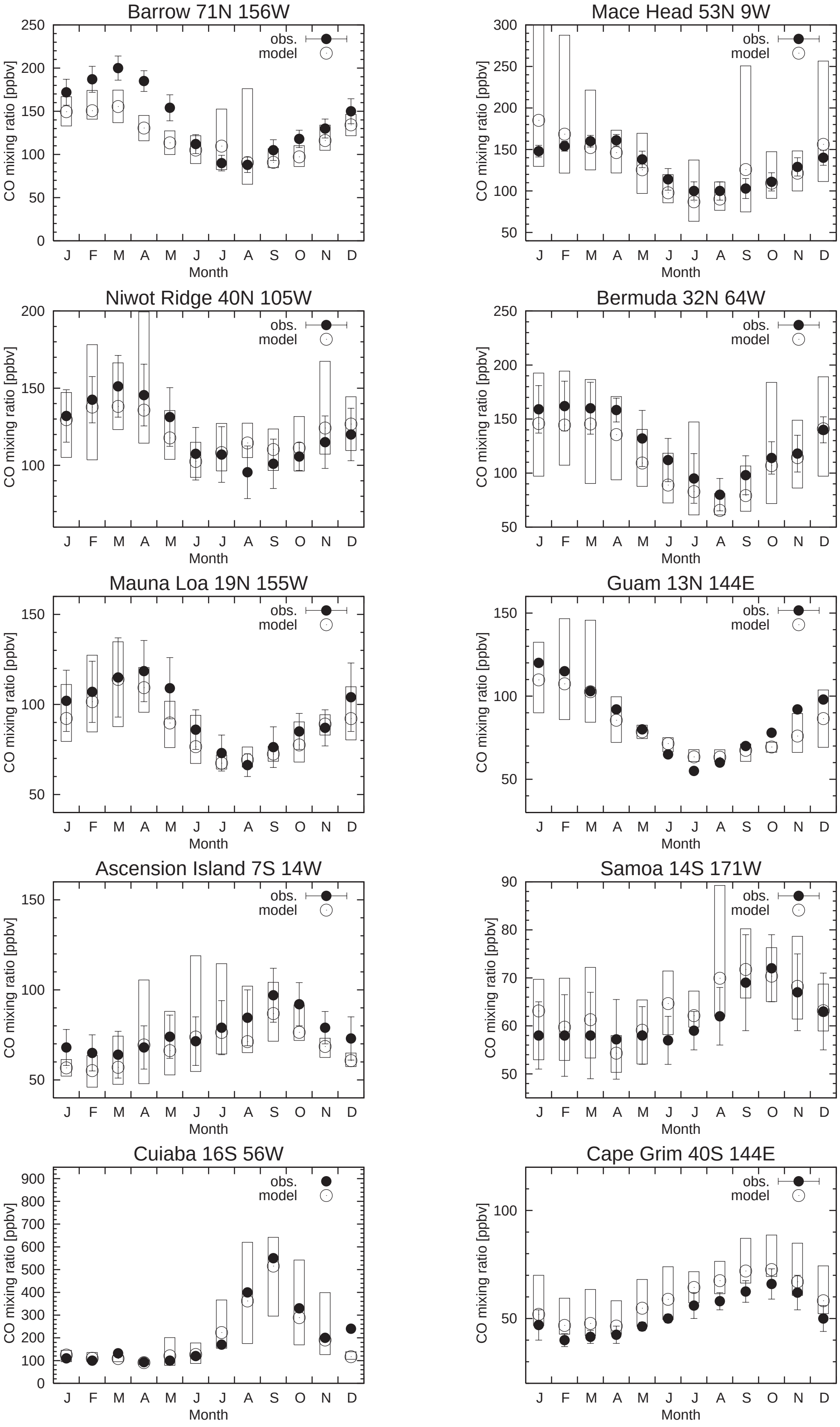

Figure 2.15. Observed (solid circles) and calculated (open circles) surface CO mixing ratios (ppbv) at several sites. Boxes indicate the range of the day-to-day variability calculated by the model. Measurements are taken from *Novelli et al.* [1992, 1994] and *Kirchhoff et al.* [1989] (for Cuiaba).

cycle of OH radical, transport of CO due to large-scale wind field and convection, and biomass burning (especially for the southern hemisphere). At Cuiaba located in the biomass burning region in South America, the seasonal cycle of surface CO has a peak in September (500-600 ppbv), much affected by biomass burning emissions. In the model, the seasonal variation of biomass burning emissions is imposed by using hot spot (fire distribution) data derived from satellites (see *Sudo et al.* [2002a] and section 2.2.2). The model appears to reproduce the observed seasonal cycle of surface CO at Cuiaba well, indicating the validity of the seasonal variation of biomass burning emissions considered in the model. A CO maximum in spring is seen at Ascension (over the tropical Atlantic) associated with biomass burning in South America and Africa, which is also captured by the model. The seasonal cycle of CO observed and simulated at Mauna Loa (spring peak) is much associated with the transport from eastern Asia (Asian outflow) as suggested by the simulation of atmospheric ^{222}Rn (see *Sudo et al.* [2002a] or Appendix 2A). At Barrow, the model underestimates the observed CO mixing ratios in spring, maybe indicating an overestimation of OH level or an underestimation of the CO surface emission in the high latitudes considered in the model.

A comparison between the calculated and the observed vertical profiles of CO over the GTE regions listed in Table 2.5 is shown in Figure 2.16. The observed CO vertical profiles are generally well reproduced by the model. In remote regions like Hawaii, Philippine-Sea, and Fiji, CO distributions are relatively uniform in the vertical with a range of 50-100 ppbv, whereas they are more variable in the source regions of biomass burning (E-Brazil and S-Africa) in the range of 100-200 ppbv. The model well captures the CO profiles observed over the Japan region during PEM-West-B, reproducing the CO increase in the lower troposphere (150-200 ppbv) due to industrial CO emissions. During TRACE-P (March to April), the observed CO profile in the China-Coast region shows increase below 5 km, owing to the combination of industrial CO emissions in China and CO transport from biomass burning in southeastern Asia (Thailand etc.). The model also calculates CO increases quite consistent with the observation in China-Coast. In the S-Atlantic region, CO levels are high in the free troposphere, especially in the upper troposphere ($>$ 8 km), much associated with transport from South Africa and South America as suggested by *Thompson et al.* [1996]. A CO plume from Africa toward South America is simulated well in 2-5 km over the W-Africa-Coast region. The model tends to overestimate CO levels in the tropical Pacific regions in some cases; Christmas-Island and Tahiti during PEM-Tropics-A. Although this may imply an underestimation of OH levels in the tropics, simulated OH concentrations in the tropical Pacific are quite consistent with the observations during the PEM-Tropics-B expedition (section 2.3.3).

Table 2.6 shows the global annual budget of tropospheric CO calculated by CHASER. The budget is calculated for the region below the tropopause height determined from the vertical temperature gradient (-2 K/km) in the model. CO has indirect sources from oxidation of CH_4 and NMHCs, as well as direct sources from surface emission (taken to be 1267 TgCO/yr in this simulation). The global chemical production of CO is estimated at 1514 TgCO/yr, showing a significant

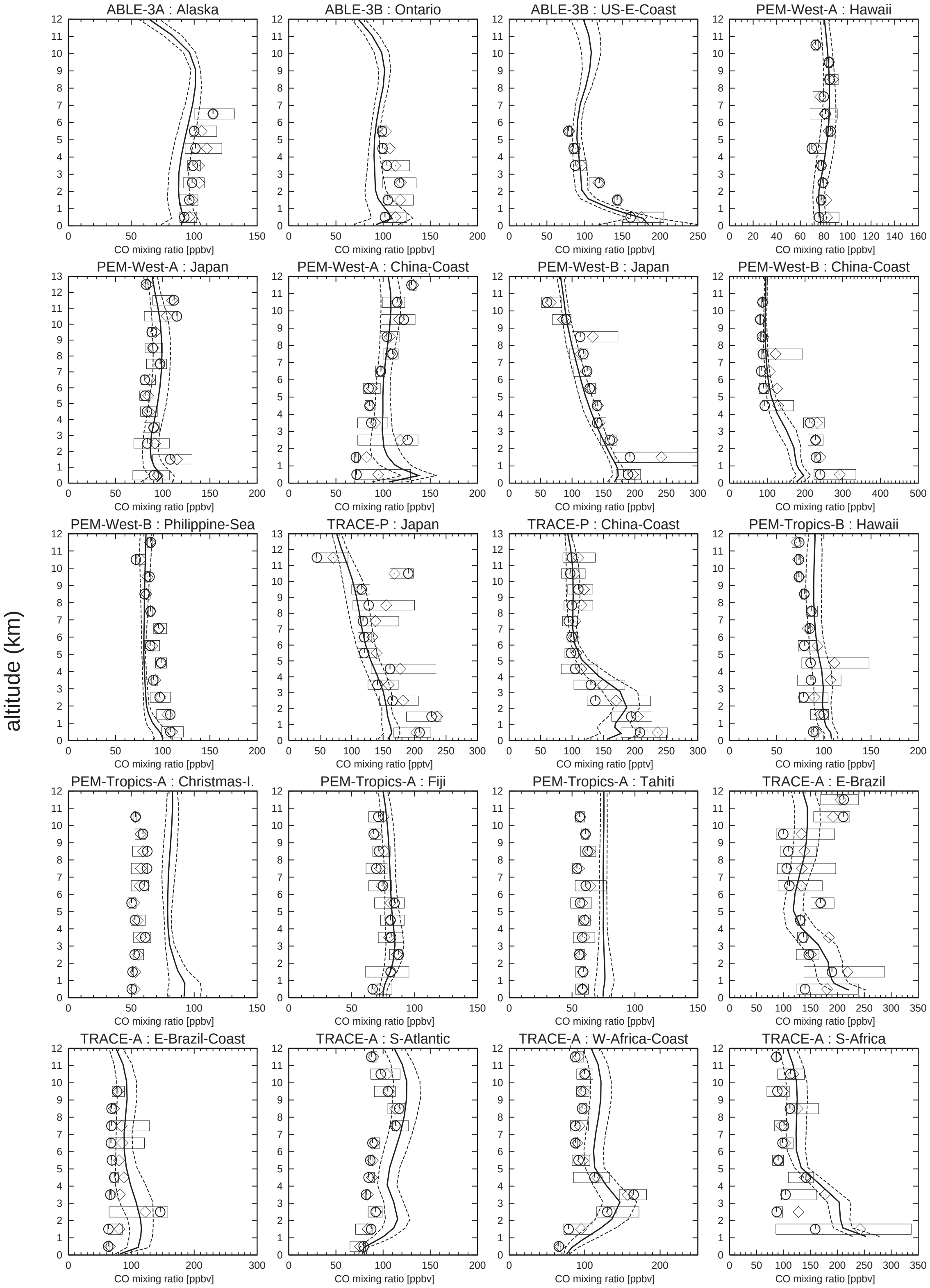

Figure 2.16. CO vertical profiles observed and calculated over the regions of GTE campaigns (listed in Table 2.5). Solid lines and dashed lines show temporal mean and ±1σ of the model calculation, respectively. The observations show mean (diamonds), median (circles), and inner 50% of the data (boxes).

Table 2.6. Global Budget of Tropospheric CO Calculated by CHASER.[a]

	Global	NH	SH
Sources	2781		
Surface emission	1267		
Chemical production	1514	844	670
$CH_2O + h\nu$	931	506	425
$CH_2O + OH$	397	243	154
Others [b]	186	95	91
Sinks	−2781		
STE [c]	−71		
Dry deposition	−139	−110	−29
Chemical loss (CO + OH)	−2571	−1582	−989
Chemical lifetime (days)	55	52	59
Burden (TgCO)	360	212	148

[a] Values (in TgCO/yr) are calculated for the region below the tropopause height in the model. NH, Northern Hemisphere; SH, Southern Hemisphere.

[b] Mainly from isoprene and terpenes oxidation.

[c] Stratosphere-Troposphere Exchange (CO flux to the stratosphere).

contribution from degradation of formaldehyde (CH_2O) and a contribution of ~13% from degradation of NMHCs. Note that the CO production from CH_2O includes oxidation processes of both CH_4 and NMHCs. The reaction with OH radical is the only chemical sink for CO and is estimated at 2571 TgCO/yr in the global troposphere by the model. The chemical lifetime of CO due to this reaction is estimated at about 1.8 months in annual average by the model, with longer lifetime (59 days) in the southern hemisphere than that in the northern hemisphere (52 days), reflecting the distribution of OH radical. This estimated global lifetime of CO, 1.8 months, is slightly shorter than the value of 2.0 months estimated by *Müller and Brasseur* [1995]; *Hauglustaine et al.* [1998]. The global CO burden is calculated as 360 TgCO (59% in HN, 41% in SH), in good agreement with recent model studies [e.g., *Müller and Brasseur*, 1995; *Hauglustaine et al.*, 1998]. The distributions of net CO chemical production P(CO)-L(CO) calculated for April are shown in Figure 2.17. At the surface, high positive production rates of 6-10 ppbv/day are calculated in South America, South Africa, etc., associated with biogenic emissions of NMHCs as isoprene and terpenes. Relatively high CO production rates (1-2 ppbv/day) are also calculated at 200 hPa over South America and South Africa, reflecting convective transport of NMHCs species from the surface. In other regions, CO is slowly destroyed by OH at rates of −0.5 to −2 ppbv/day.

NMHCs

Distributions of NMHCs species are spatially and temporally variable compared to CO, because of their relatively short lifetimes (ranging from several hours to weeks). Figure 2.18 shows

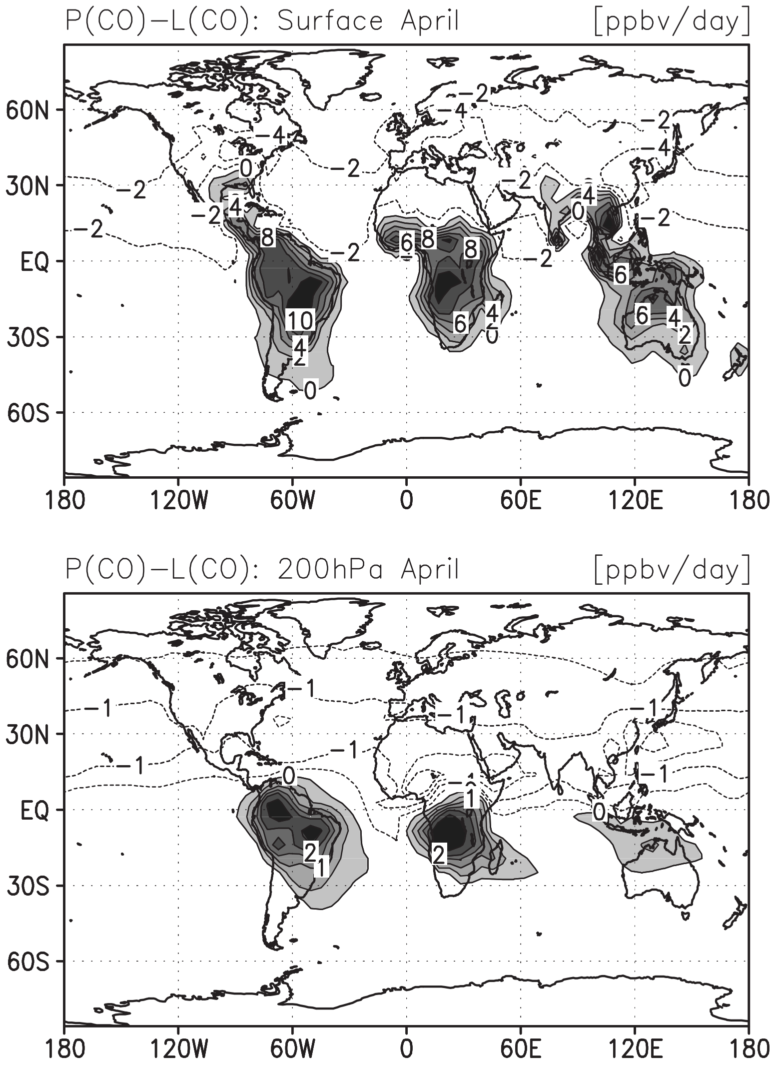

Figure 2.17. Net CO production rates (ppbv/day) calculated at the surface and 200 hPa altitude for April. Only positive areas are shaded.

the observed and the calculated seasonal cycles of surface C_2H_6 and C_3H_8. At the European site (Waldhof), the model captures the observed seasonal cycles of both C_2H_6 and C_3H_8. At Mauna Loa, the model appears to reproduce the observed C_2H_6 mixing ratios, though it slightly underestimates C_3H_8. The levels of C_2H_6 are much higher than C_3H_8 in Mauna Loa as C_2H_6 has a longer lifetime (2-3 weeks) compared to C_3H_8 (several days). The C_3H_8/C_2H_6 ratios are much less than 0.1 at Mauna Loa and 0.3-0.5 at Waldhof, indicating that the air at Mauna Loa is photochemically aged well (more than 5 days from a source region) [*Gregory et al.*, 1996] compared to Waldhof. At both sites, the calculated concentration and the temporal variability are high in winter and spring as well as CO. High temporal variabilities in winter-spring as seen in the calculated CO and NMHCs are also visible in the simulation of ^{222}Rn at the surface [*Sudo et al.*, 2002a].

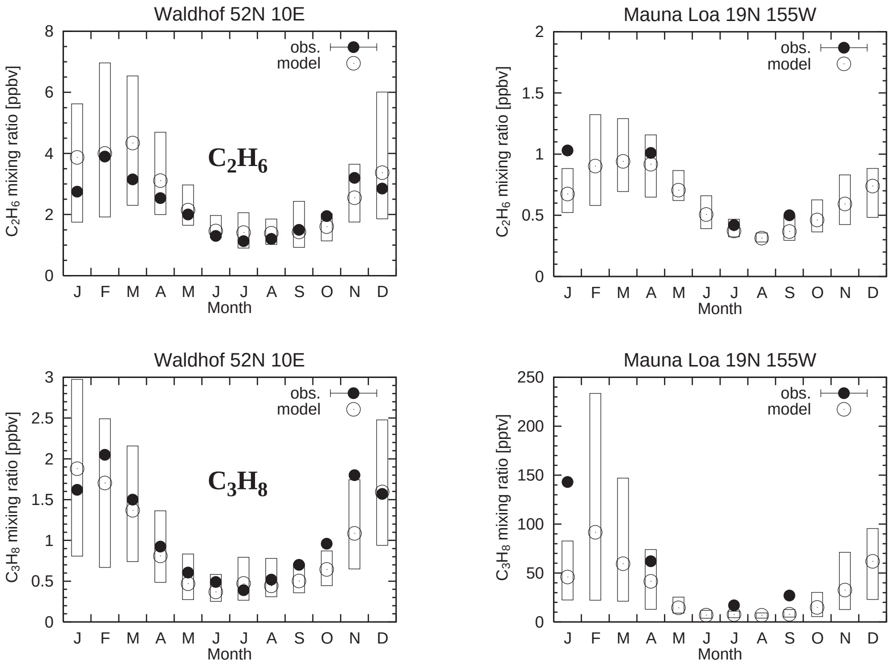

Figure 2.18. Observed (solid circles) and calculated (open circles) surface C_2H_6 (upper) and C_3H_8 (lower) mixing ratios (ppbv). Boxes indicate the range of the day-to-day variability calculated by the model. Measurements are taken from *Solberg et al.* [1996] and *Greenberg et al.* [1996] (for Mauna Loa).

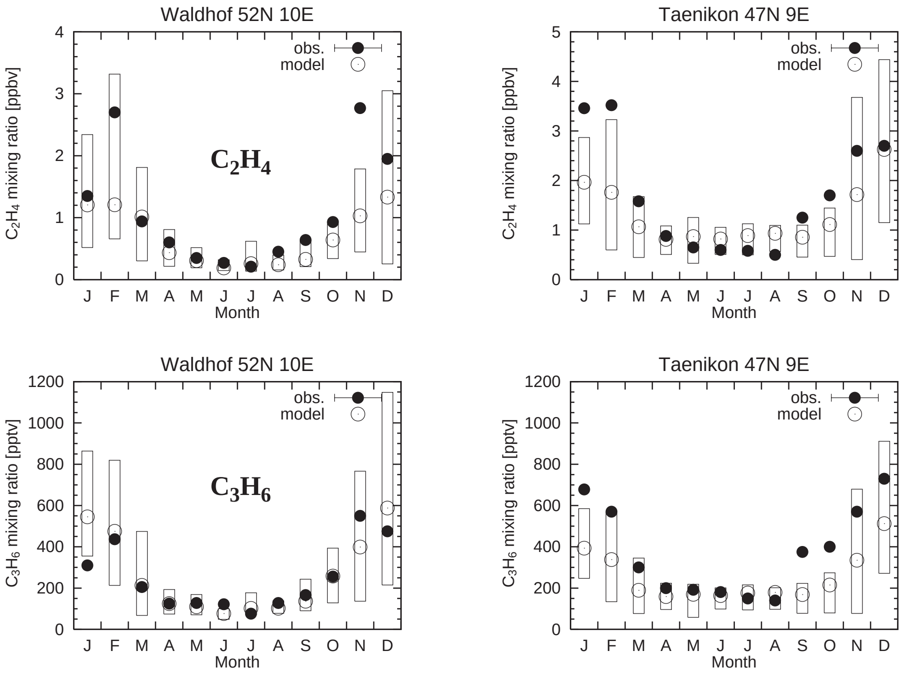

Figure 2.19. Observed (solid circles) and calculated (open circles) surface C_2H_4 (upper) and C_3H_6 (lower) mixing ratios (ppbv). Boxes indicate the range of the day-to-day variability calculated by the model. Measurements are taken from *Solberg et al.* [1996].

In Figure 2.19, the calculated and the observed seasonal cycles of surface C_2H_4 and C_3H_6 are shown for two European sites. Alkenes such as C_2H_4, C_3H_6 are destroyed by the reaction with OH radical with a lifetime of $\sim$1 day, and also by the reaction with O_3 with a lifetime of a day or several days. The model captures the observed seasonal variations of C_2H_4 and C_3H_6, reproducing well the winter maxima as with C_2H_6 and C_3H_8.

The observed and the calculated vertical profiles of C_2H_6 and C_3H_8 are compared in Figure 2.20 and Figure 2.21, respectively. In the US-E-Coast region (ABLE-3B), the model does not capture the observed levels of C_2H_6 (1-2 ppbv) and C_3H_8 (0.7-0.8 ppbv) in the lower troposphere, probably indicating an underestimation of surface emissions around this region. In the Japan and the China-Coast regions (PEM-West-B), C_2H_6 and C_3H_8 levels are higher near the surface ($C_2H_6 \sim 2$ ppbv, $C_3H_8 \sim 0.8$ ppbv), associated with considerable emission sources around these regions. In these regions, the model appears to underestimate slightly C_3H_8 near the surface, though it reproduces the profiles of C_2H_6 observed there well. During PEM-West-A (September to October), C_2H_6 and C_3H_8 levels below 5 km in the Japan and China-Coast regions are lower by a factor of 2 compared to PEM-West-B (February to March). These seasonal variations in C_2H_6 and C_3H_8 are well simulated by the model. During TRACE-P, the model well simulates the C_2H_6 profiles as well as CO (Figure 2.16). In these tropical remote regions C_2H_6 distributions are relatively uniform in the vertical ranging from 200 to 400 pptv , while C_3H_8 is more variable and shows relatively low mixing ratios (5-100 pptv) due to its short chemical lifetime. For the observations in the tropical Pacific regions (PEM-Tropics-A and B), the model tends to overestimate C_2H_6 levels, whereas it appears to reproduce generally the observed C_3H_8 profiles. The overestimation of C_2H_6 in the tropical Pacific, coinciding with the CO overestimation as described above (Figure 2.16), may indicate large transport from source regions. In the biomass burning regions (TRACE-A), the model appears to successfully simulate the vertical distributions of both C_2H_6 and C_3H_8. In the E-Brazil region, the model captures the observed positive vertical gradient in the middle-upper troposphere associated with convective transport in this region (as revealed by *Fishman et al.* [1996]). The modeled increase in C_2H_6 in the upper troposphere appears to be somewhat smaller than that by the previous CHASER version [*Sudo et al.*, 2002b], probably indicating reduced convection over South America in the model. This may come from the differences in the base AGCM version and adopted horizontal resolution between this work and the previous [*Sudo et al.*, 2002b]. The CHASER model in this study uses the CCSR/NIES version 5.6 AGCM with the T42 horizontal resolution ($\sim 2.8^\circ \times 2.8^\circ$), while the previous CHASER uses the version 5.4 AGCM with the T21 resolution ($\sim 5.6^\circ \times 5.6^\circ$). In the S-Atlantic region, levels of C_2H_6 and C_3H_8 are higher ($C_2H_6 \sim 800$ pptv, $C_3H_8 \sim 100$ ppbv) in the upper troposphere as for CO (Figure 2.16). The observed increase in C_2H_6 and C_3H_8 with altitude over the S-Atlantic region is well reproduced by the model, though the discontinuous jumping at $\sim$7 km is not represented clearly. Although the model appears to overestimate the C_2H_6 and C_3H_8 profiles observed over the W-Africa-Coast region, it simulates the increases in 2-5 km due to

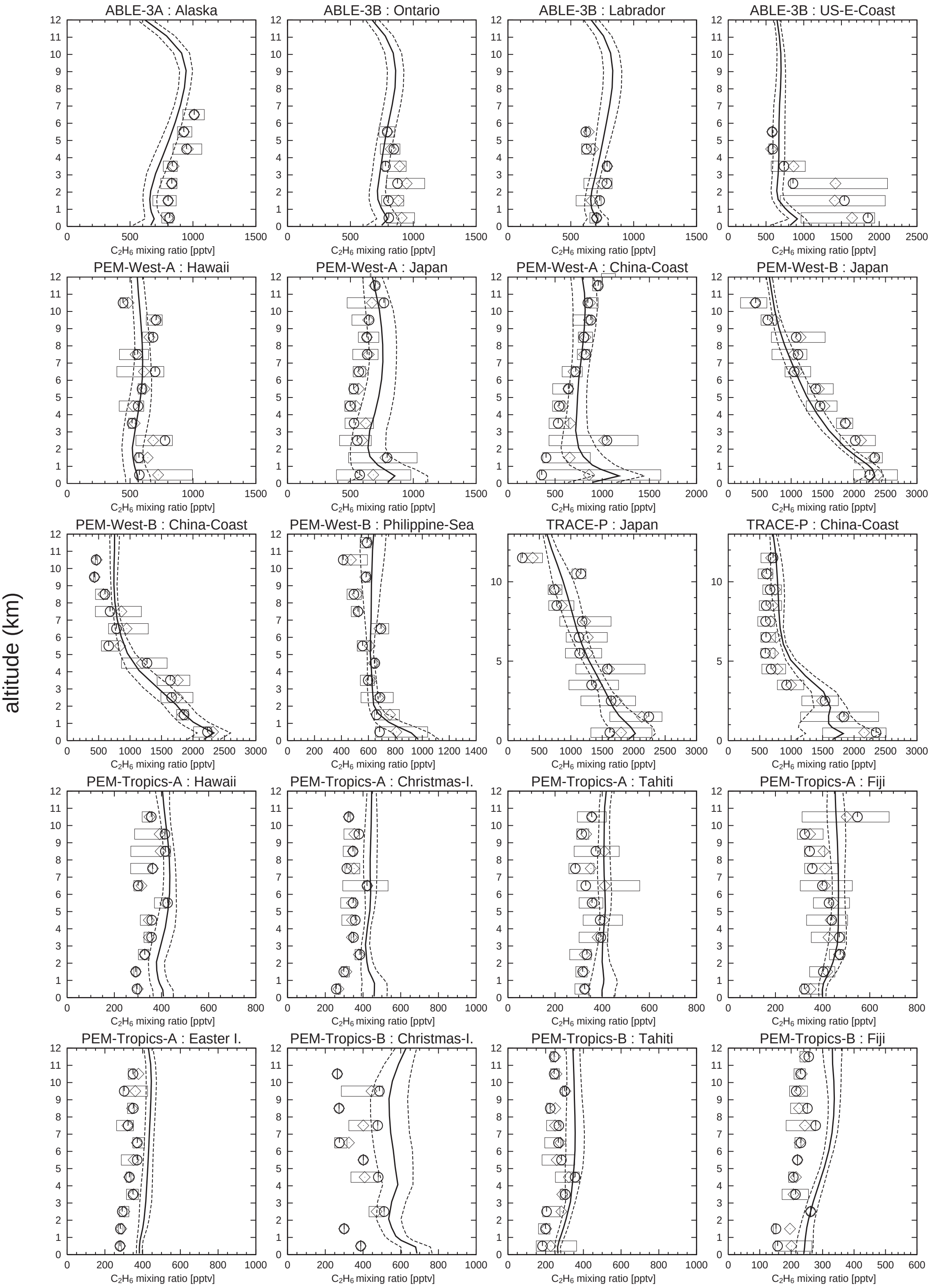

Figure 2.20. C_2H_6 vertical profiles observed and calculated over the regions of GTE campaigns (listed in Table 2.5). Solid lines and dashed lines show temporal mean and $\pm 1\sigma$ of the model calculation, respectively. The observations show mean (diamonds), median (circles), and inner 50% of the data (boxes).

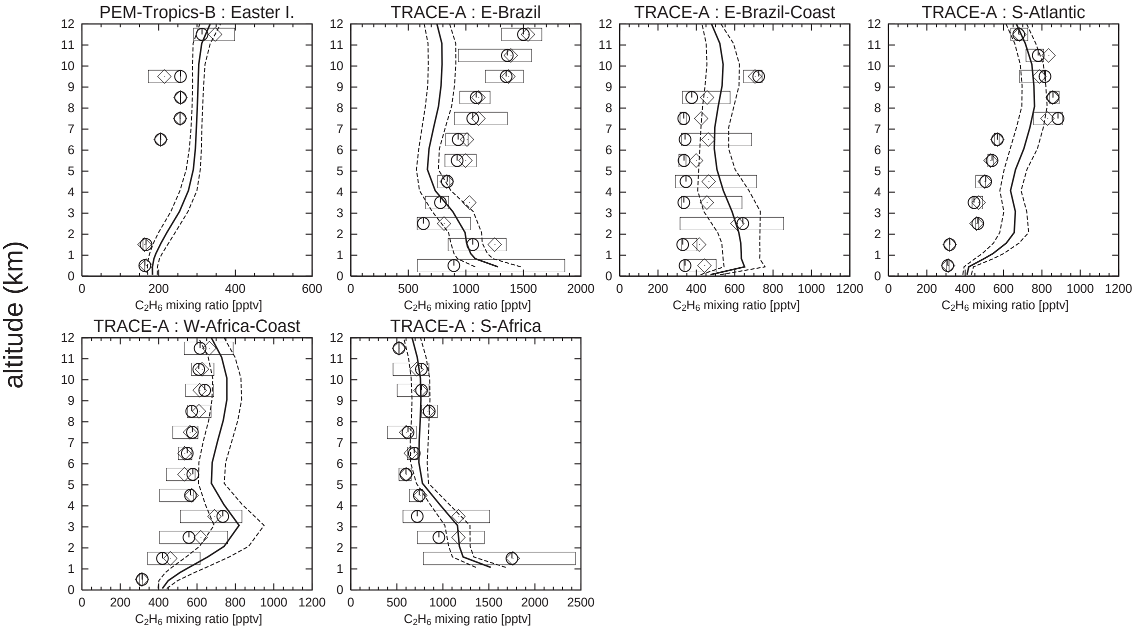

Figure 2.20. (continued).

African outflow as well as CO.

As isoprene and terpenes rapidly react with OH, O_3, and NO_3, they have much shorter lifetimes (hours), and the calculated distributions of these two NMHCs species are limited near source regions (i.e., vegetation) in the continental boundary layer. Figure 2.22 shows the distributions of isoprene calculated at the surface for January and July (24-hour average). The 24-hour averaged isoprene mixing ratios calculated in the boundary layer range from 1 ppbv to 8 ppbv in the tropical rain forests like the Amazon, in agreement with *Zimmerman et al.* [1988]. In July, the calculated mixing ratios of isoprene are 0.5-2 ppbv in temperate (deciduous) forests in the northern hemisphere, in agreement with measurements [e.g., *Martin et al.*, 1991; *Montzka et al.*, 1995]. Similarly, the terpenes distribution calculated near the surface has peaks in the tropical rain forests (1-2 ppbv), and shows high levels (0.2-1.5 ppbv) in cold-deciduous, needle-leaved forests in the northern high latitudes in July (not shown). In the model, the chemical lifetimes of isoprene and terpenes are estimated at 1.9 hour and 1.0 hour, respectively, in the annual and global average. The isoprene and terpenes mixing ratios calculated over the ocean are very low (generally equal to zero), due to their short chemical lifetimes.

2.3.2 Nitrogen species

Nitrogen oxides NO_x ($= NO + NO_2$) have a critical importance for ozone production and the HO_2/OH ratio in the troposphere. We must carefully evaluate the model results of NO_x and its reservoir species. Figure 2.23 shows the simulated NO_x distributions at the surface and 500

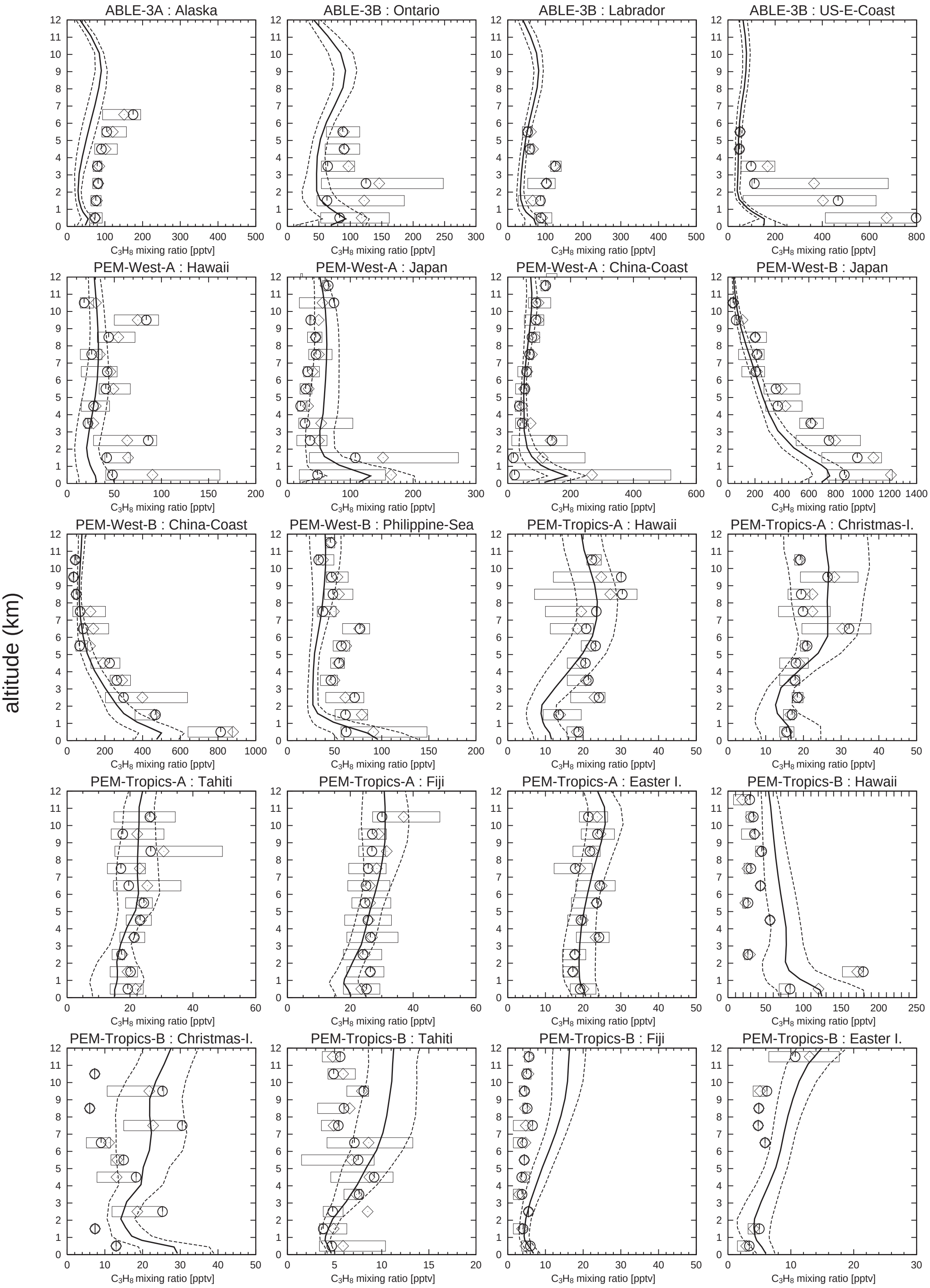

Figure 2.21. C_3H_8 vertical profiles observed and calculated over the regions of GTE campaigns (listed in Table 2.5). Solid lines and dashed lines show temporal mean and $\pm 1\sigma$ of the model calculation, respectively. The observations show mean (diamonds), median (circles), and inner 50% of the data (boxes).

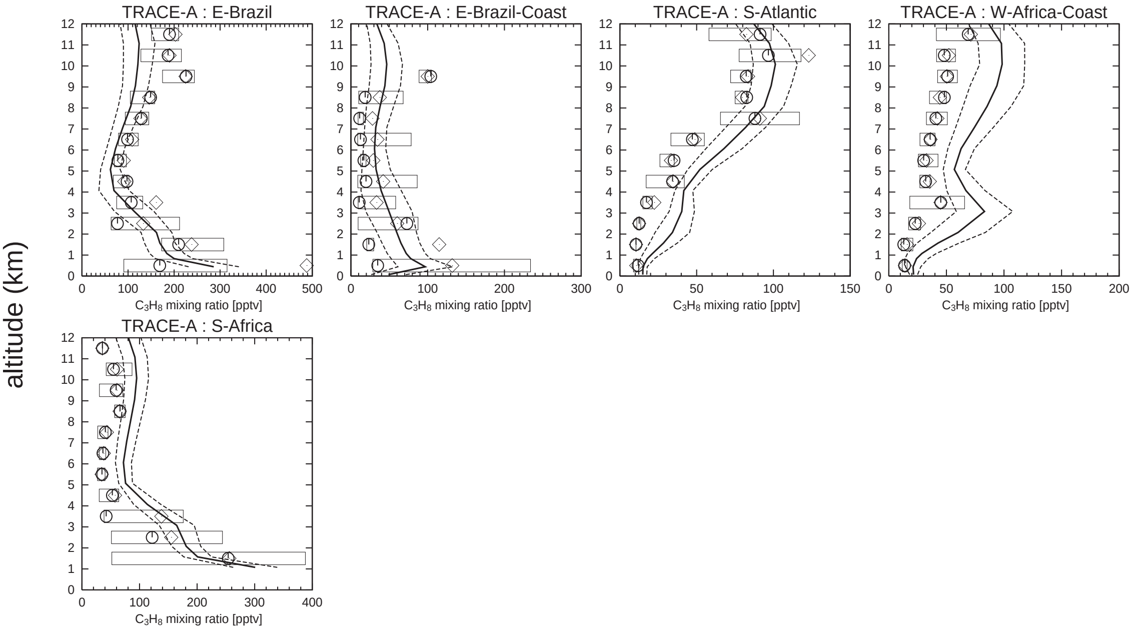

Figure 2.21. (continued).

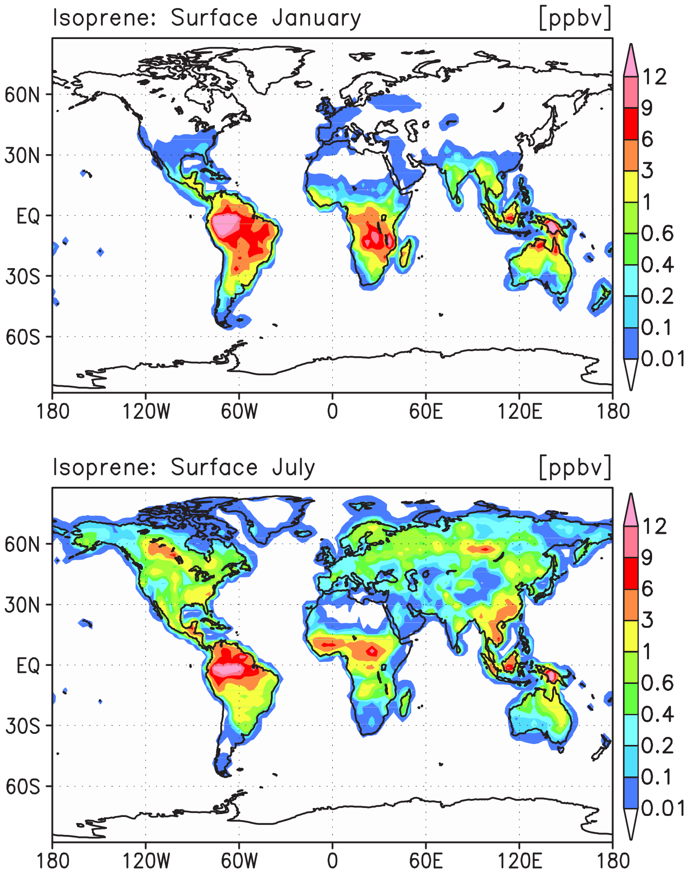

Figure 2.22. Calculated isoprene distributions (ppbv) at the surface for January and July.

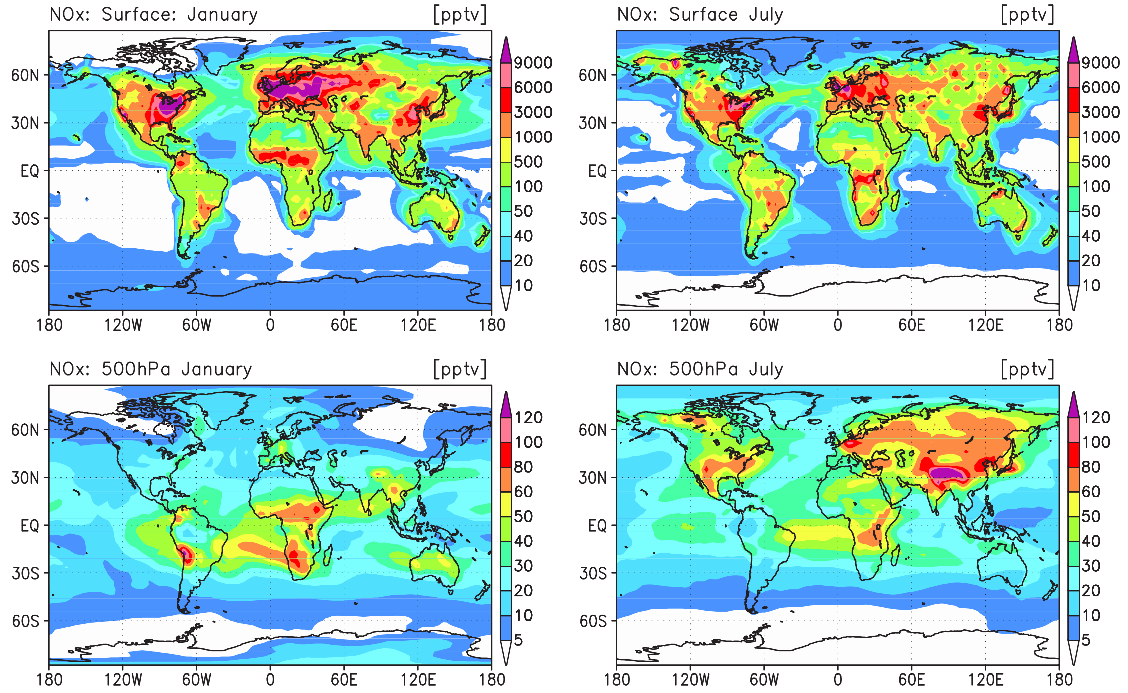

Figure 2.23. Calculated NO_x distributions (pptv) at the surface and 500hPa for January (left) and July (right).

hPa altitude for January and July. As NO_x is converted to HNO_3 by the reaction with OH on a timescale of a day near the surface, the NO_x distribution is highly limited near the continental source regions, especially in summer. Surface NO_x levels over the ocean are in the range of 10-80 pptv in winter and generally lower than 20 pptv near the surface. In July, the model calculates the NO_x mixing ratios of $\sim$3 ppbv over the eastern United States, somewhat higher than the simulation of *Horowitz et al.* [1998]. In January, the high NO_x concentrations of 5-10 ppbv are calculated in the eastern United States and Europe, reflecting a longer lifetime of NO_x. NO_x levels in those polluted regions are reduced by 30-50% compared to the previous version [*Sudo et al.*, 2002b] due to the heterogeneous reaction of N_2O_5 on aerosols (mainly sulfate in this study) which is not included in the previous version. At 500 hPa, NO_x peaks (60-100 pptv) are calculated over Africa and the Atlantic in January, associated with biomass burning in North Africa and with the lightning NO_x production. High NO_x concentration ($\sim$60 pptv) calculated over the Atlantic is also owing in the model to export from Africa and the in-situ NO_x recycling from HNO_3 and PAN. In the model, the positive net production of NO_x of 5-20 pptv/day is found in 6-12 km altitudes over the Atlantic, indicating the recycling process of NO_x. The calculation also shows a NO_x minimum (10-30 pptv) over South America (Brazil), reflecting rapid removal of HNO_3 by wet scavenging over this region during this season, and formation of PAN by the oxidation of biogenic NMHCs (mainly isoprene and terpenes). However, this NO_x minimum can be caused also by the overestimation of PAN formation by the chemical scheme of the model as described in the following. In July, the model predicts high NO_x concentrations ($>$ 60 pptv) over continents in the northern hemisphere centered around the southeastern United States and eastern Asia (60-100 pptv). These are attributed to convective transport of NO_x from the surface and to the lightning NO_x production, though the effect of the lightning NO_x may be less visible at this altitude.

The observed and calculated vertical profiles of NO over the GTE regions listed in Table 2.5 are shown in Figure 2.24. Since the data includes only measurements in daytime (solar zenith angle $< 90°$), the model results show average value of NO in daytime. In all cases, distributions of NO increase with altitude in the upper troposphere, due to the transport of stratospheric NO_x and HNO_3, the lightning NO_x production and the transport of surface emissions in convectively active regions, and increase in the lifetime of NO_x. Both the observations and calculations show high variability in the upper troposphere, reflecting the influence of stratospheric $NO_x$and lightning NO_x. The model simulates NO profiles well consistent with those observed during ABLE-3A (Alaska) and ABLE-3B (Ontario, US-E-Coast), calculating a rapid increase in the upper troposphere ($>$ 6 km) affected by stratospheric NO_x and HNO_3. The NO distributions over the polluted regions show “C-shaped” profiles. The model well simulates the observed “C-shaped” NO profile in the US-E-Coast (ABLE-3B), the China-Coast (PEM-West-B), the E-Brazil and the S-Africa (TRACE-A) regions. The model, however, overestimates the NO profiles in the Japan and China-Coast regions during TRACE-P. In the remote Pacific regions during PEM-Tropics-A and B, the model generally simulates the observed monotonic increase in NO with altitude. The NO profiles in the Hawaii region are, however, overestimated during both PEM-Tropics-A and B, due probably to the overestimation of PAN (see Figure 2.28), or possibly to overestimation of stratospheric influx of NO_y species such as NO_x, HNO_3, and N_2O_5. On the contrary, the model appears to underestimate NO above 8 km in Fiji and Tahiti during PEM-Tropics-A. The underestimations of NO in the upper troposphere over these regions may indicate the underestimation of lightning NO_x and/or biomass burning emission of NO_x in Australia. In the source regions of biomass burning (TRACE-A: E-Brazil, W-Africa-Coast, and S-Africa), the observations show “C-shaped” NO profiles, showing increase in the upper troposphere. The model appears to underestimate slightly NO levels in the upper troposphere (higher than 10 km) in these regions, with calculating NO profiles close to the observations in the lower-middle troposphere (below 10 km). Although this discrepancy appears to be caused by the underestimation of the flux of stratospheric NO_x, it can be attributed to the underestimation of lightning NO_x in the upper troposphere or the overestimation of PAN in the upper troposphere (the PAN/NO_x ratio is overestimated by a factor of 2-3 in the upper troposphere over these regions, Figure 2.29) , or possibly to the recycling of NO_x from HNO_3 on aerosols as tested in *Wang et al.* [1998b]. In the S-Atlantic region, both the observation and the calculation show a monotonic increase of NO with altitude, with the model slightly underestimating NO in the upper troposphere. The increase in the upper troposphere over S-Atlantic is related in the model to the gas-phase recycling of NO_x from HNO_3 and PAN, as well as the transport of NO_x from the

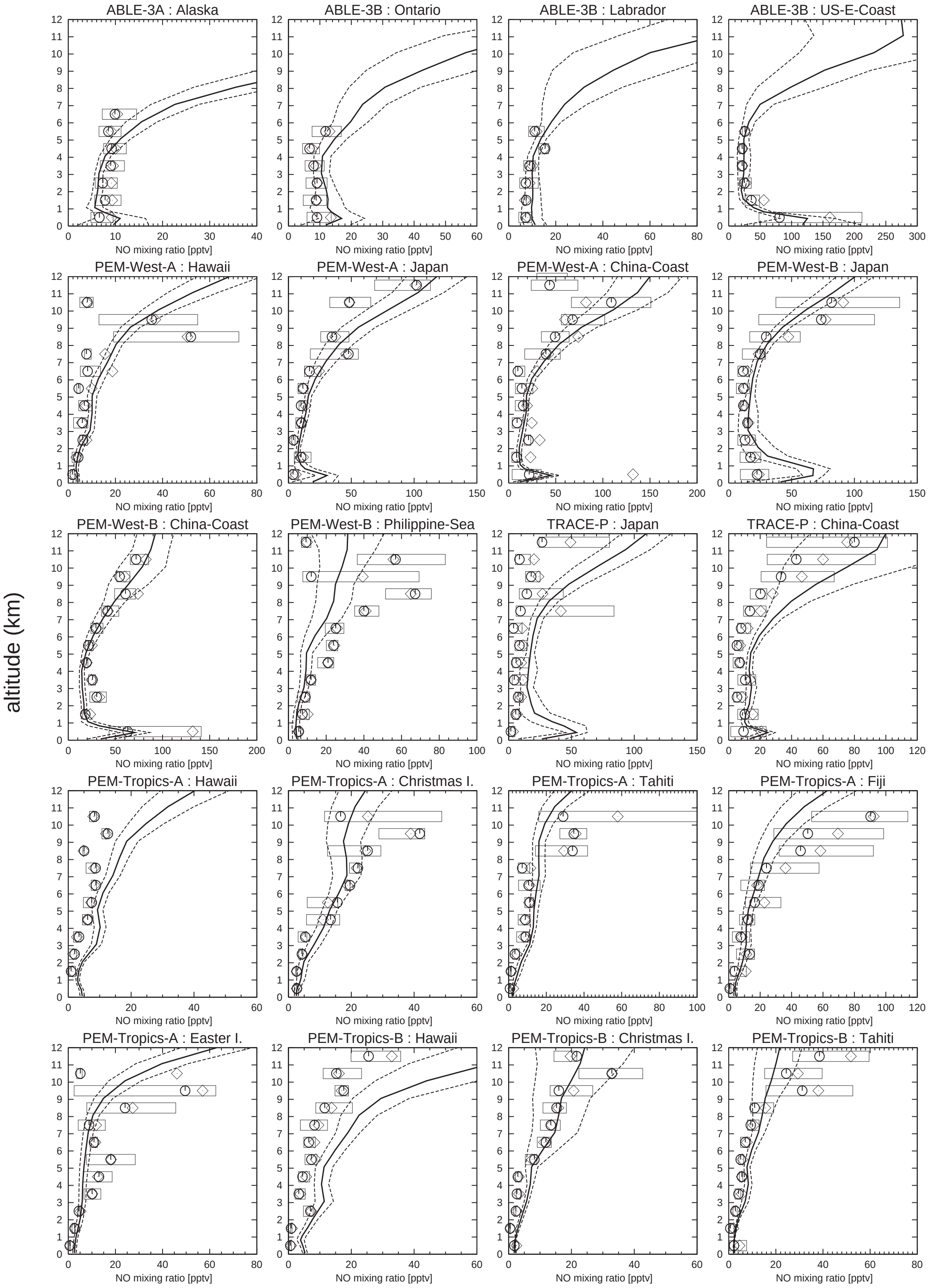

Figure 2.24. NO vertical profiles (in daytime) observed and calculated over the regions of GTE campaigns (listed in Table 2.5). Solid lines and dashed lines show temporal mean and ±1σ of the model calculation, respectively. The observations show mean (diamonds), median (circles), and inner 50% of the data (boxes).

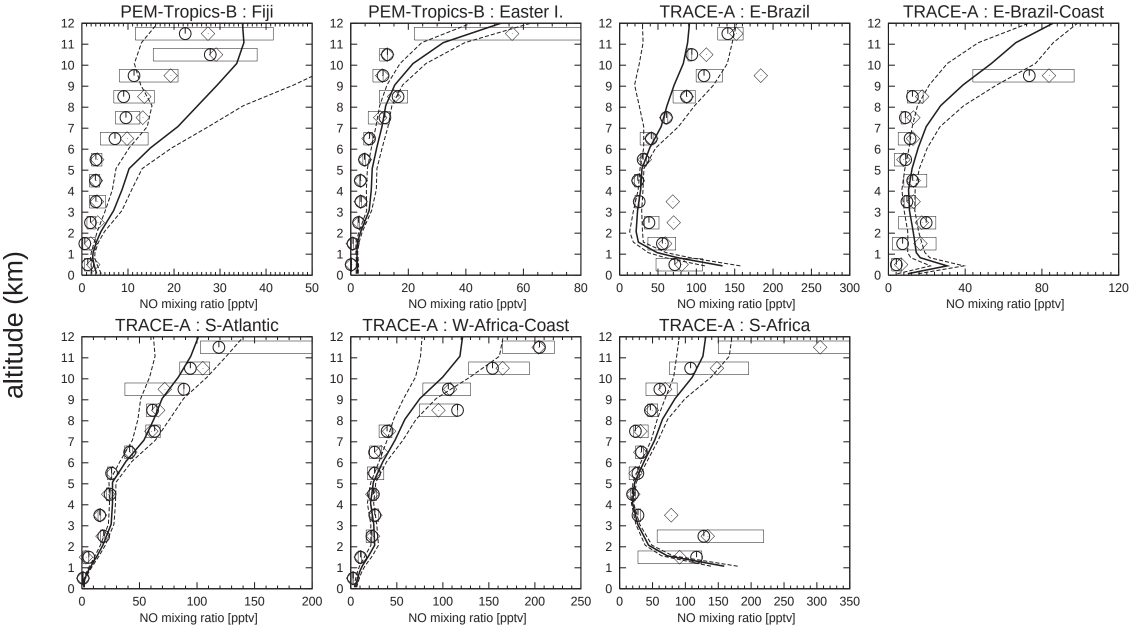

Figure 2.24. (continued).

source regions (South America and Africa). In the model, positive net production of NO_x (5-30 pptv/day) is calculated above 7 km over the Atlantic in September-October, indicating the recycling from HNO_3 and PAN exported from South America and Africa.

Figure 2.25 shows the calculated distributions of HNO_3 at the surface and 500 hPa altitude for January and July. Peaks of HNO_3 mixing ratio (higher than 2 ppbv) are calculated at the surface in the polluted areas as the eastern United States (also including California), Europe, India, China, and the biomass burning regions in both seasons. In July, the calculated HNO_3 mixing ratios in the eastern United States reach the range of 2-5 ppbv, higher than the measurements reported by *Parrish et al.* [1993] (1-2 ppbv). It should be noted that the model does not account for the conversion of HNO_3 to NO_x on aerosols (like soot) [*Hauglustaine et al.*, 1996; *Aumont et al.*, 1999; *Velders and Granier*, 2001, etc.] and particulate nitrates (NO_3^-) [e.g., *Singh et al.*, 1996] which would reduce gas-phase HNO_3. At 500 hPa, a clear maximum of HNO_3 (200-400 pptv) is calculated over the South Atlantic in January, due to the export from South America and Africa, and to sparse precipitation over this region. Low HNO_3 levels are calculated over South America (less than 40 pptv) at both the surface and 500 hPa in January. In the model, these low HNO_3 levels appear to be associated with convective precipitation during this season, and also with low NO_x levels due to strong PAN formation in the oxidation process of NMHCs emitted from vegetation. In July, a maximum of HNO_3 in the range of 400-500 pptv are calculated over the Eurasian Continent and the southern United States, associated with the lightning NO_x production and the convective transport of surface NO_x emission. A significant outflow of HNO_3 is visible over the eastern North Pacific

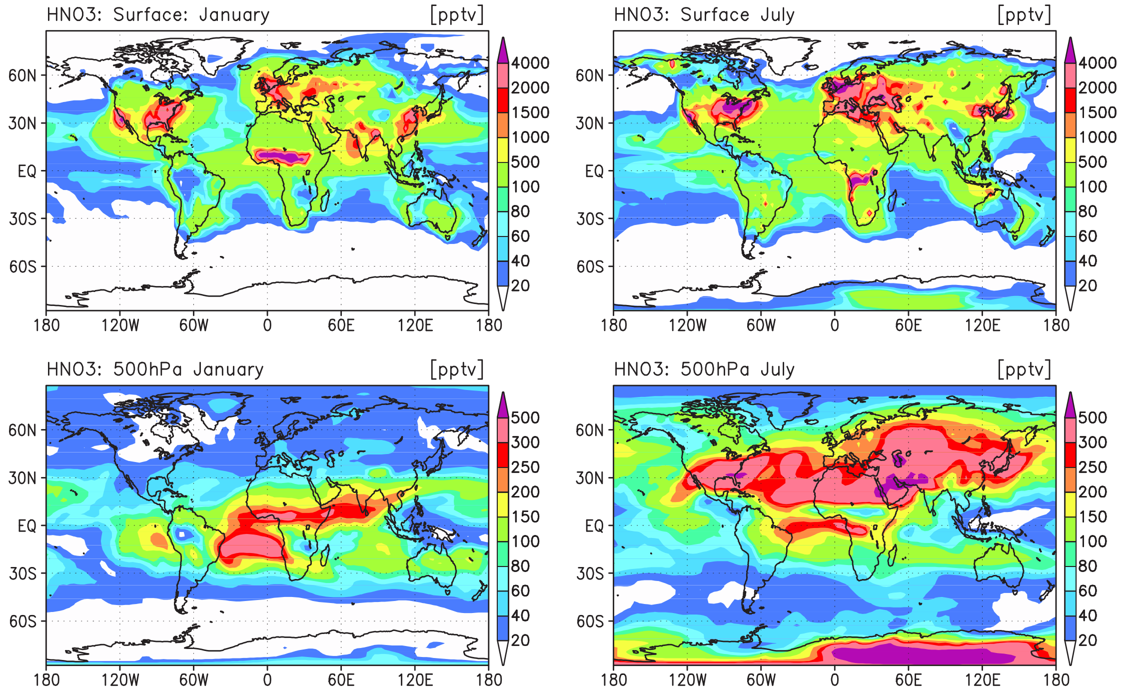

Figure 2.25. Calculated HNO_3 distributions (pptv) at the surface and 500hPa for January (left) and July (right).

including Hawaii from the western United States. This outflow, however, seems to be somewhat overestimated. HNO_3 and HNO_3/NO_x calculated at Mauna Loa are 1.5-2 times higher than the measurements by the Mauna Loa Observatory Photochemistry Experiment (MLOPEX) 1 and 2 [*Ridley and Robinson*, 1992; *Atlas and Ridley*, 1996]. High HNO_3 levels are also seen over the Antarctic continent in July, owing in the model to HNO_3 flux from the lower stratosphere associated with HNO_3 deposition due to ice particle sedimentation.

A comparison between the calculated and the observed vertical profiles of HNO_3 over the GTE regions listed in Table 2.5 is shown in Figure 2.26. In ABLE-3B (July-August), the calculated HNO_3 profiles show increase in the upper troposphere, reflecting the effect of stratospheric HNO_3. In comparison with the previous version of CHASER [*Sudo et al.*, 2002b], the model in this study calculates relatively low HNO_3 mixing ratios in the middle and upper troposphere over the Ontario, Labrador, and US-E-Coast regions, due to the improved wet deposition scheme considering deposition on ice cloud particles (see section 2.2.3). Similarly, the HNO_3 profile over the Japan region during PEM-West-B (February), which was overestimated by the previous CHASER, is well simulated in this study. A detailed evaluation of HNO_3 wet deposition flux is presented in section 2.2.3. In the tropical Pacific regions, the model generally reproduces the observed HNO_3 profiles (PEM-Tropics-A and B). The model, however, tends to overestimate lower tropospheric HNO_3 in the Hawaii region (PEM-Tropics-A and B) and the Christmas-Island and Tahiti regions

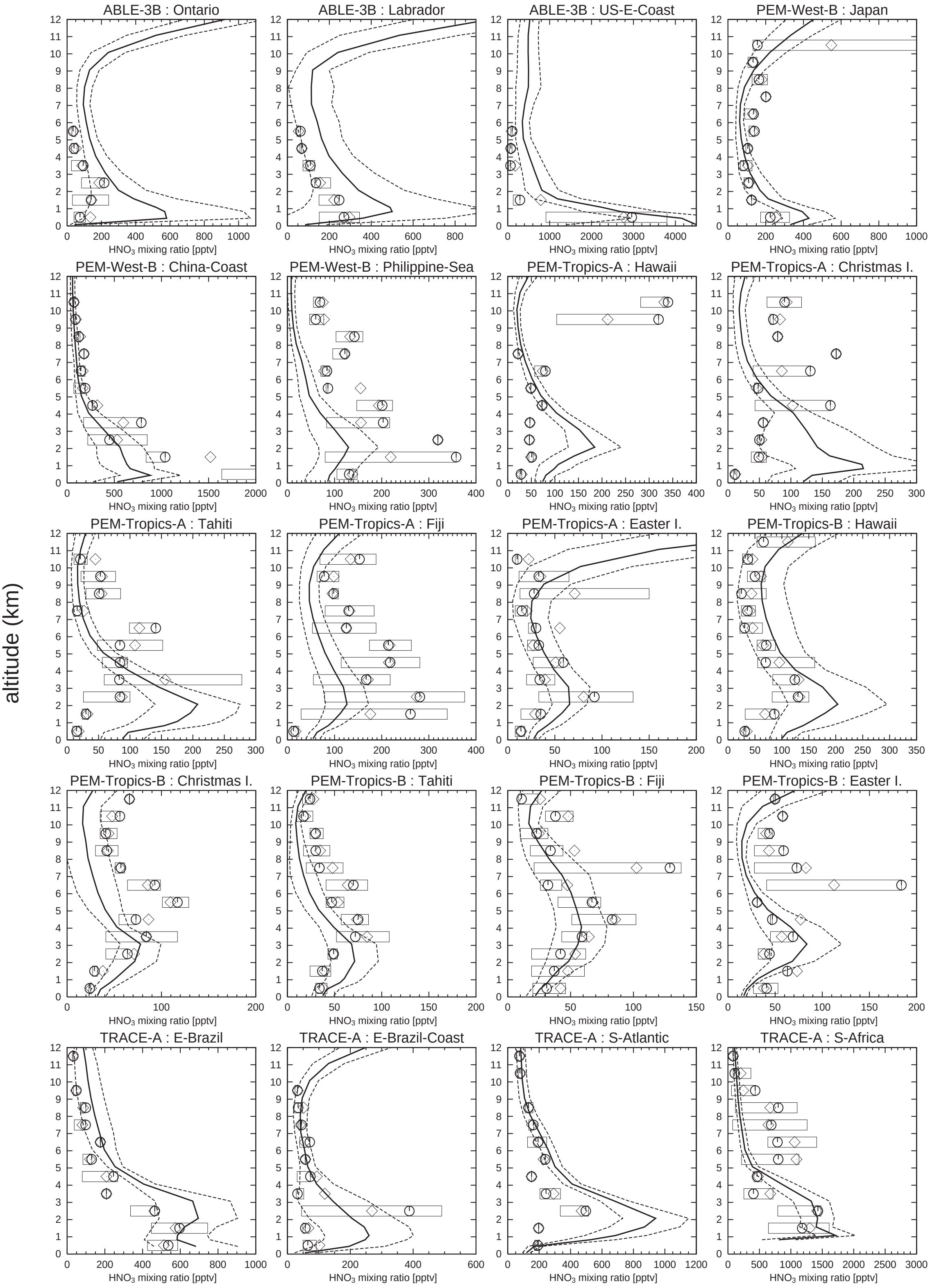

Figure 2.26. HNO$_3$ vertical profiles observed and calculated over the regions of GTE campaigns (listed in Table 2.5). Solid lines and dashed lines show temporal mean and $\pm 1\sigma$ of the model calculation, respectively. The observations show mean (diamonds), median (circles), and inner 50% of the data (boxes).

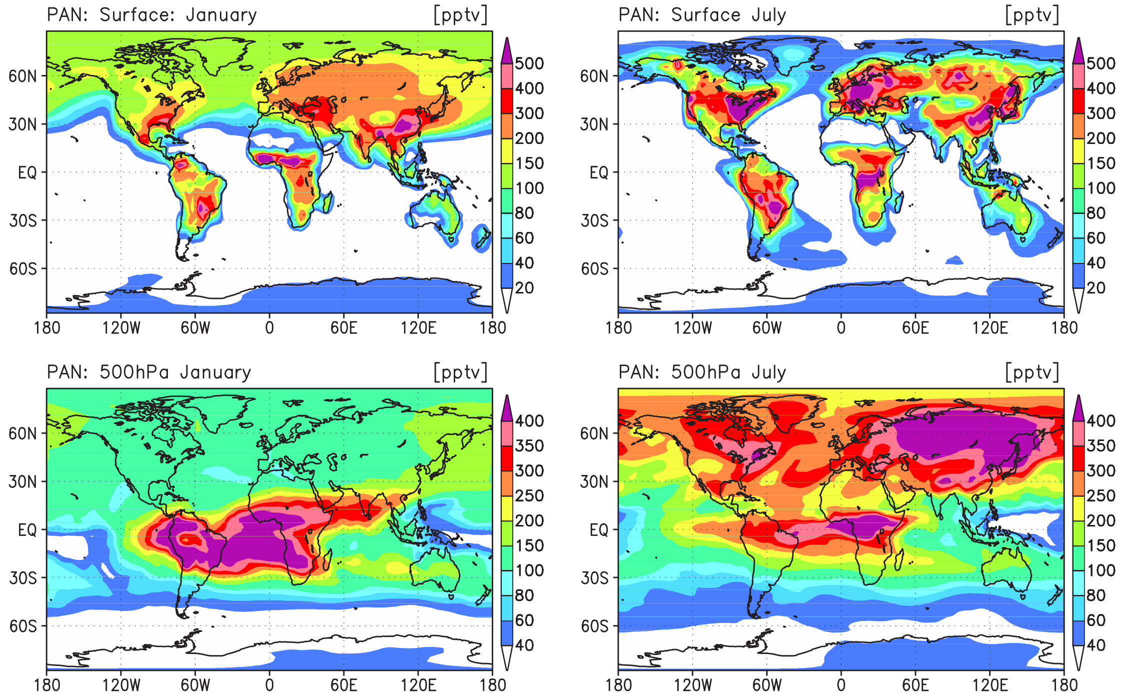

Figure 2.27. Calculated PAN distributions (pptv) at the surface and 500hPa for January (left) and July (right).

(PEM-Tropics-A). The overestimation in the Hawaii region appears to be related to too large outflow from the United States in the model. Also, HNO_3 outflow from the biomass burning regions in South America seems to result in the overestimation in the Tahiti region during PEM-Tropics-A. However, such overestimation may imply the existence of aerosol nitrates (NO_3^-) as revealed by *Singh et al.* [1996] which the model does not account for. In TRACE-A (September-October), an overestimation is found in 1-4 km over the S-Atlantic region as previous model simulations [e.g. *Wang et al.*, 1998b; *Lawrence et al.*, 1999]. The model results show that the calculated peak at about 2 km is much associated with the transport from Africa and hence the overestimation over the S-Atlantic (1-4 km) region is probably caused by the overestimation of HNO_3 in Africa as can be seen in the S-Africa region (Figure 2.26). The conversion of HNO_3 to NO on soot [*Hauglustaine et al.*, 1996; *Aumont et al.*, 1999; *Velders and Granier*, 2001, etc.] can be also a possible reason for this discrepancy. Consequently, the model results of HNO_3 and NO_x may indicate the necessity of consideration of particulate nitrates (NO_3^-) and reactions on soot affecting the HNO_3/NO_x ratio.

Peroxyacetyl nitrate (PAN) is also an important nitrogen species that acts as a source for NO_x in the remote atmosphere [*Fan et al.*, 1994; *Moxim et al.*, 1996]. PAN is formed by the reaction of NO_2 with peroxyacetyl radical and decomposes principally by thermolysis (slightly by photolysis). As peroxyacetyl radical is produced from the oxidation of NMHCs (ethane, propane, propene, acetone, isoprene, and terpenes in the model), we can validate the simplified scheme for NMHCs oxidation

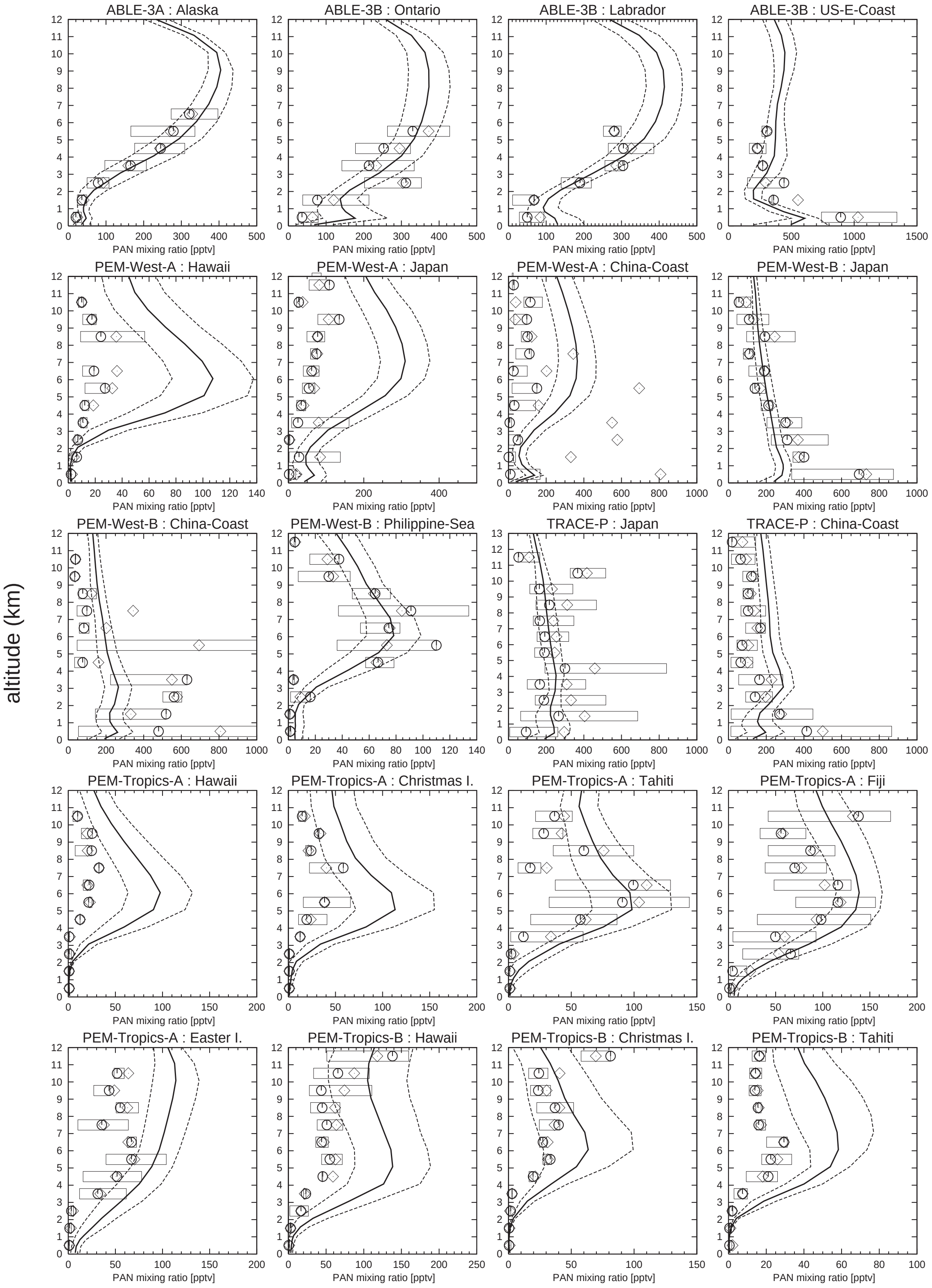

Figure 2.28. PAN vertical profiles observed and calculated over the regions of GTE campaigns (listed in Table 2.5). Solid lines and dashed lines show temporal mean and $\pm 1\sigma$ of the model calculation, respectively. The observations show mean (diamonds), median (circles), and inner 50% of the data (boxes).

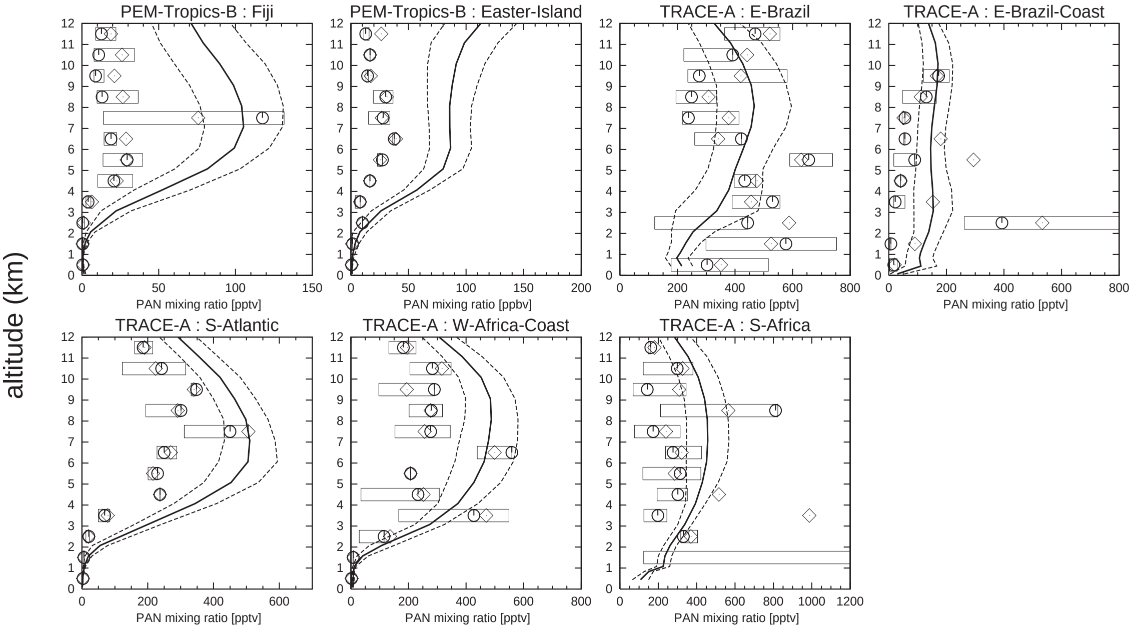

Figure 2.28. (continued).

adopted in the model by evaluating the simulation of PAN. Figure 2.27 shows the calculated PAN distributions at the surface and 500 hPa for January and July. At the surface in January, high levels of PAN (300-500 pptv) are calculated in South America and Africa associated with biogenic emissions of NMHCs over these regions. The model calculates the PAN concentrations of 150-300 pptv in the mid-high latitudes with a maximum (400-600 pptv) around India and China. In July, high concentrations of PAN (above 500 pptv) are predicted at the surface in the polluted areas (United States, Europe, eastern Asia including Japan). The model results for the eastern United States in summer are consistent with the observation of *Parrish et al.* [1993] (0.5-1.5 ppbv). At 500 hPa in January, the model calculates high levels of PAN (300-450 pptv) over South America, Africa, and the South Atlantic, associated with NMHCs emissions by vegetation and lightning NO_x over South America and Africa. The calculated high concentrations of PAN over the Atlantic contribute to the positive net production (recycling) of NO_x (5-20 pptv/day) calculated in the middle-upper troposphere over the Atlantic during this season as described above. In July, high concentrations of PAN (above 300 pptv) are calculated over continents in the northern hemisphere with a maximum (above 400 pptv) over the eastern Eurasian Continent, due to the lightning NO_x production and surface emissions of NO_x and NMHCs.

Figure 2.28 shows the calculated and the observed vertical profiles of PAN over the GTE regions. In the Alaska region during ABLE-3A (July-August), the model calculates increase of PAN with height with showing mixing ratios of 300-400 pptv in the upper troposphere, in excellent agreement with the observation. The calculated PAN profiles over the Ontario, Labrador, and US-E

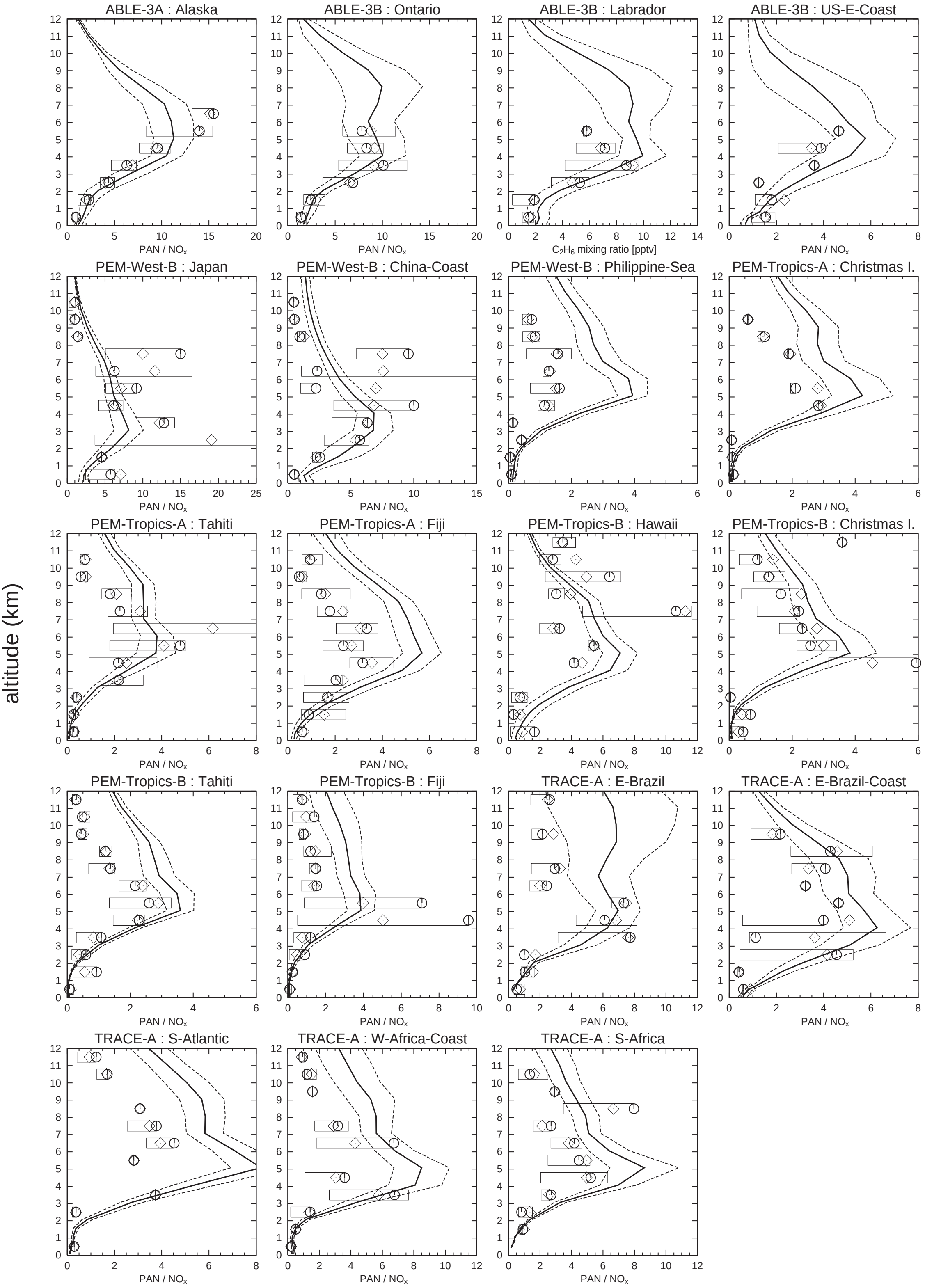

Figure 2.29. PAN/NO$_x$ ratio vertical profiles observed and calculated over the regions of GTE campaigns (listed in Table 2.5). Solid lines and dashed lines show temporal mean and $\pm 1\sigma$ of the model calculation, respectively. The observations show mean (diamonds), median (circles), and inner 50% of the data (boxes).

regions (ABLE-3B) are also consistent with the observations. In the Japan and the China-Coast regions during PEM-West-B and TRACE-P, PAN levels increase near the surface (400-800 pptv), reflecting the abundance of NMHCs (e.g., Figure 2.20, Figure 2.21) and NO_x (Figure 2.24). In the Japan region, the model well simulates the observed PAN profiles for PEM-West-B and TRACE-P, but overestimates significantly for PEM-West-A especially in the upper troposphere. The same kind of overestimation by the model appears in the Hawaii region during PEM-West-A and PEM-Tropics-A and B. The overestimation in the Hawaii region is attributed to transport from eastern Asia and the United States. For Fiji and Tahiti (PEM-Tropics-A), both the observation and the model show a peak of PAN (80-150 pptv) in 4-8 km, associated with the transport of PAN from South America, Africa, and Australia. The model, however, overestimates the PAN profiles in 4-10 km over the tropical Pacific regions during PEM-Tropics-B (March-April) by a factor of 1.5-3, maybe indicating that the condensed isoprene and terpenes oxidation scheme [*Pöschl et al.*, 2000] (see *Sudo et al.* [2002a]) or the lumped NMHCs species (ONMV, see *Sudo et al.* [2002a]) in the model produces too much peroxyacetyl radical and hence too much PAN. Similar overestimation of PAN in the tropical Pacific is seen in the simulation by the MOZART model [*Horowitz et al.*, 2002]. In the biomass burning regions (TRACE-A), the model appears to reproduce the observed profiles of PAN, simulating the rapid decrease in PAN below 3 km (nearly zero) over the S-Atlantic region and the W-Africa-Coast region, and the increase in the middle troposphere (300-500 pptv). The model, however, tends to overestimate PAN levels in the middle-upper troposphere, indicating too strong PAN formation again. Figure 2.29 shows the calculated and the observed vertical profiles of PAN/NO_x ratio over the GTE regions. The ratio is calculated in each time step in the model. The model generally reproduces the observed PAN/NO_x ratios well, calculating a peak in the middle troposphere for individual cases. The observed and calculated peaks in the middle troposphere are generally in the range of 5-10 in the polluted areas, and lower than 5 in the remote regions. An overestimation of the PAN/NO_x ratio in the Philippine-Sea region is associated with the underestimation of NO_x in this region (Figure 2.24). The calculated PAN/NO_x profile in the Hawaii region (PEM-Tropics-B) is relatively consistent with the observation, while both NO_x and PAN in this region are overestimated by the model (Figure 2.24 and 2.28). For the regions of TRACE-A, the model overestimates the PAN/NO_x ratio in the upper troposphere by a factor of 2-3, due to the underestimation of NO_x and the overestimation of PAN in these regions as described above.

The seasonal cycle of PAN calculated at the surface is also compared with the observational data for several sites [*Bottenheim et al.*, 1994; *Houweling et al.*, 1998; *Ridley et al.*, 1998] (not shown). It was found that the model overestimates PAN at Mauna Loa by a factor of 2, compared to the data of the MLOPEX [*Ridley et al.*, 1998]. For other sites, the calculated seasonal variations of PAN are consistent with observations.

The overestimation of PAN by the model in some instances may be attributed primarily to overestimation of peroxy acetyl radical (CH_3COO_2) by the simplified chemical mechanism for

Table 2.7. Global budget of NO_y species (TgN/yr) Calculated by CHASER.

	Global	NH	SH
Sources	44.3		
Surface Emission	38.8		
Lightning NO_x	5.0	2.93	2.07
Aircraft NO_x	0.55		
Sinks	−45.1	−35.5	−9.6
Wet deposition	−25.8	−19.8	−6.0
HNO_3	−25.2	−19.4	−5.8
HNO_4	−0.57	−0.39	−0.18
Dry deposition	−19.4	−15.7	−3.7
HNO_3	−13.8	−11.5	−2.3
HNO_4	−0.03	−0.023	−0.007
NO_x	−3.85	−3.05	−0.8
PANs [a]	−1.28	−0.86	−0.42
ISON [b]	−0.35	−0.21	−0.14
NALD	−0.04	−0.023	−0.017

$NO_y = NO + NO_2 + NO_3 + 2\,N_2O_5 + HNO_3 + HNO_4 + PAN + MPAN + ISON + NALD$ in the model (NALD = nitroxy acet aldehyde).

[a] PAN (peroxyacetyl nitrate) + MPAN (higher peroxyacetyl nitrates).

[b] Isoprene nitrates.

NMHCs used in the model, as mentioned above. The simulation with the previous CHASER version [*Sudo et al.*, 2002b] has suggested heterogeneous loss of some peroxy radicals (RO_2) including CH_3COO_2 on aerosols [*Jacob*, 2000] for another possibility, as RO_2 radicals formed by isoprene and terpenes oxidation are precursors of CH_3COO_2 radical. Although such heterogeneous reactions are included in this study (see section 2.2.1), there do not seem to be significant differences between this work and the previous one [*Sudo et al.*, 2002b]. Further investigation is needed to validate the uptake coefficients (γ values) for the heterogeneous reactions of RO_2 and products from those heterogeneous reactions (assumed to be peroxides ROOH) in the model (section 2.2.1).

The budget of total nitrogen species (NO_y) calculated by CHASER is shown in Table 2.7. In this simulation, the NO_y sources amount to 44.3 TgN/yr (87.5%, surface emission; 11.3%, lightning; 1.2%, aircraft). They are balanced primarily with the wet and dry deposition of HNO_3 (∼88% of the source) in the model. About 60% of the global lightning NO_x emission is calculated in the northern hemisphere. The calculated global wet deposition of HNO_3 reaches a maximum in August-September. About 80% of the global deposition loss of HNO_3 is calculated in the northern hemisphere (20% in the southern hemisphere). A slight imbalance between the total source and the total sink for NO_y (0.8 TgN/yr) is attributed to transport from the stratosphere.

2.3.3 HO_x and related species

OH radical plays a central role in the oxidation of chemical compounds (the oxidizing power of the atmosphere) and the production and destruction of ozone. OH is converted to HO_2 by the reactions with O_3, peroxides, and CO, and reversely HO_2 is converted to OH by the reactions with O_3 and NO on a timescale of minutes. HO_x ($= OH + HO_2$) is produced by the reaction of $O(^1D)$ with water vapor (H_2O) [*Levy*, 1971] and also by the oxidation of CH_4 and NMHCs. Decomposition of peroxides can be also a HO_x source in the upper troposphere [e.g., *Jaeglé et al.*, 1997; *Folkins et al.*, 1998; *Cohan et al.*, 1999]. The sinks for HO_x are the reactions of OH with CH_4, NMHCs, and HO_2, and the reactions of HO_2 with peroxy radicals to form peroxides (e.g., H_2O_2, CH_3OOH).

HO_x

Figure 2.30 shows the zonal mean concentrations (molecules cm^{-3}) of OH calculated for January and July. In January, the calculated OH distribution shows a maximum ($\sim 2.0\times10^6$ molecules cm^{-3}) in 10°S-30°S, reflecting the distributions of O_3, water vapor (H_2O), and UV radiation. This OH maximum is calculated at 2-4 km altitude, indicating the significant OH destruction by NMHCs and CO near the surface. We conducted a simulation without NMHCs chemistry. The simulation suggests that inclusion of NMHCs in the model reduces OH concentrations by a factor of 30-60% near the surface over land, as indicated by previous studies [e.g., *Wang et al.*, 1998c; *Roelofs and Lelieveld*, 2000]. In July, high concentrations of OH ($2.5\text{-}3.0\times10^6$ molecules cm^{-3}) are calculated in the northern midlatitudes in spite of the OH depletion by CO and NMHCs, as a result of high NO_x levels and enhanced O_3 over continents [*Thompson*, 1992]. Although the zonal mean OH distributions calculated for January and July are similar to those calculated by previous studies [e.g., *Müller and Brasseur*, 1995; *Wang et al.*, 1998b; *Hauglustaine et al.*, 1998], the maximum values of OH concentrations calculated in this simulation appear to be somewhat (10-30%) higher than them, probably indicating the differences in O_3 and NO_x levels. The tropospheric OH distribution presented here results in a global annual average of 1.06×10^6 molecules cm^{-3} (below 200 hPa), in good agreement with the simulations of *Spivakovsky et al.* [2000] (1.16×10^6 molecules cm^{-3}) and *Roelofs and Lelieveld* [2000] (1.00×10^6 molecules cm^{-3}). The annual and zonal mean HO_2/OH ratios calculated in the low-mid latitudes (45°S-45°N) are in the range of 50-100, and 100-600 in the high latitudes in both hemispheres below 200 hPa, much associated with the distribution of CO, O_3, and NO (not shown).

Data available for evaluation of OH and HO_2 are quite limited because of the difficulty of measuring them. We made use of the data obtained during the NASA GTE campaigns (PEM-Tropics-B and TRACE-P) for evaluation of the HO_x distribution. The PEM-Tropics-B mission provided the first extensive measurements of the OH radical in the tropical troposphere. In Figure 2.31, the OH and HO_2 vertical profiles observed and calculated for the regions of the PEM-Tropics-B and

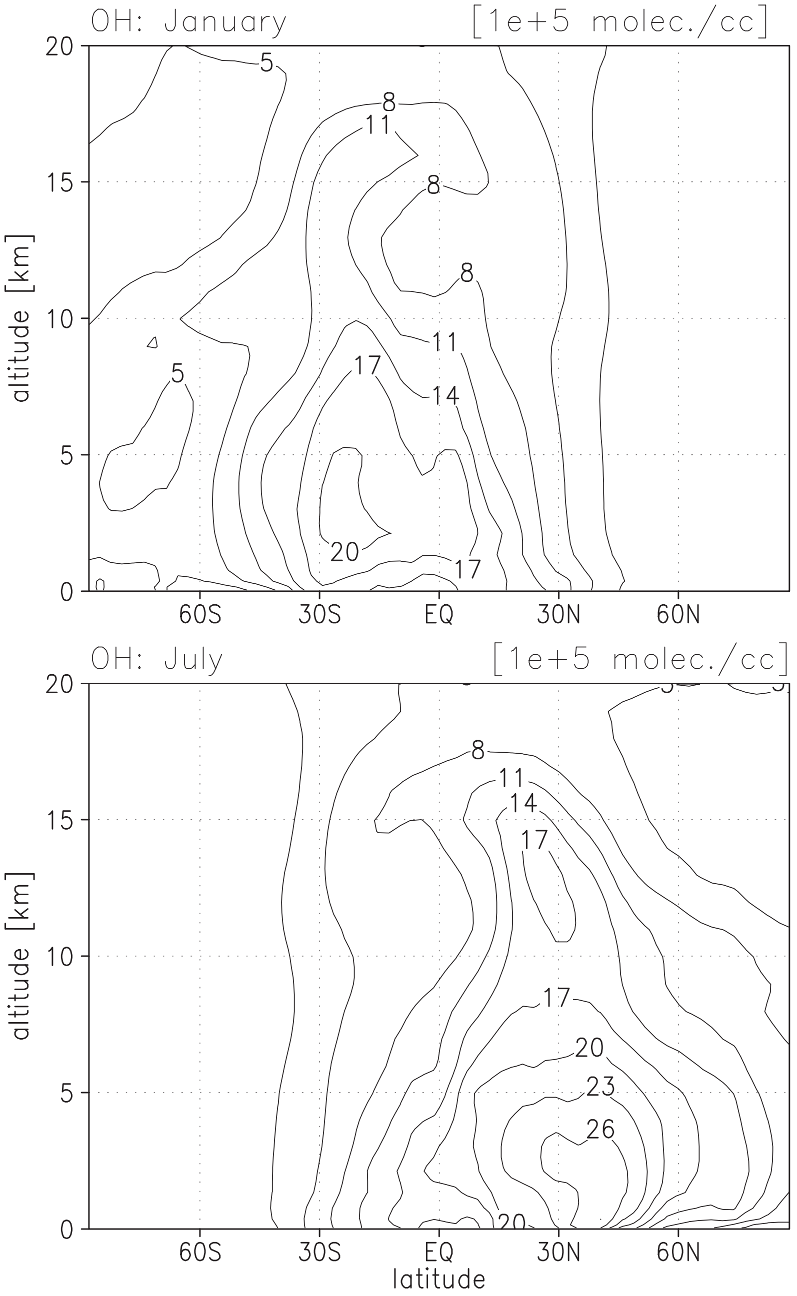

Figure 2.30. Zonal mean OH distributions (10^5 molecules cm^{-3}) calculated for January and July. Contour interval is 3 (10^5 molecules cm^{-3}).

TRACE-P expeditions are shown. The model results are again averaged over the regions in Table 2.5 and dates during the expeditions (March 6 to April 18 for PEM-Tropics-B, March 3 to April 15 for TRACE-P). Since most of the GTE flights were taken place in daytime, we display the calculated mixing ratios of OH and HO_2 in the daytime average except for the Easter-Island region during PEM-Tropics-B where the mission includes nighttime flights after sunset (We compare the 24-hour averaged model results for the Easter-Island region). In this comparison, we must

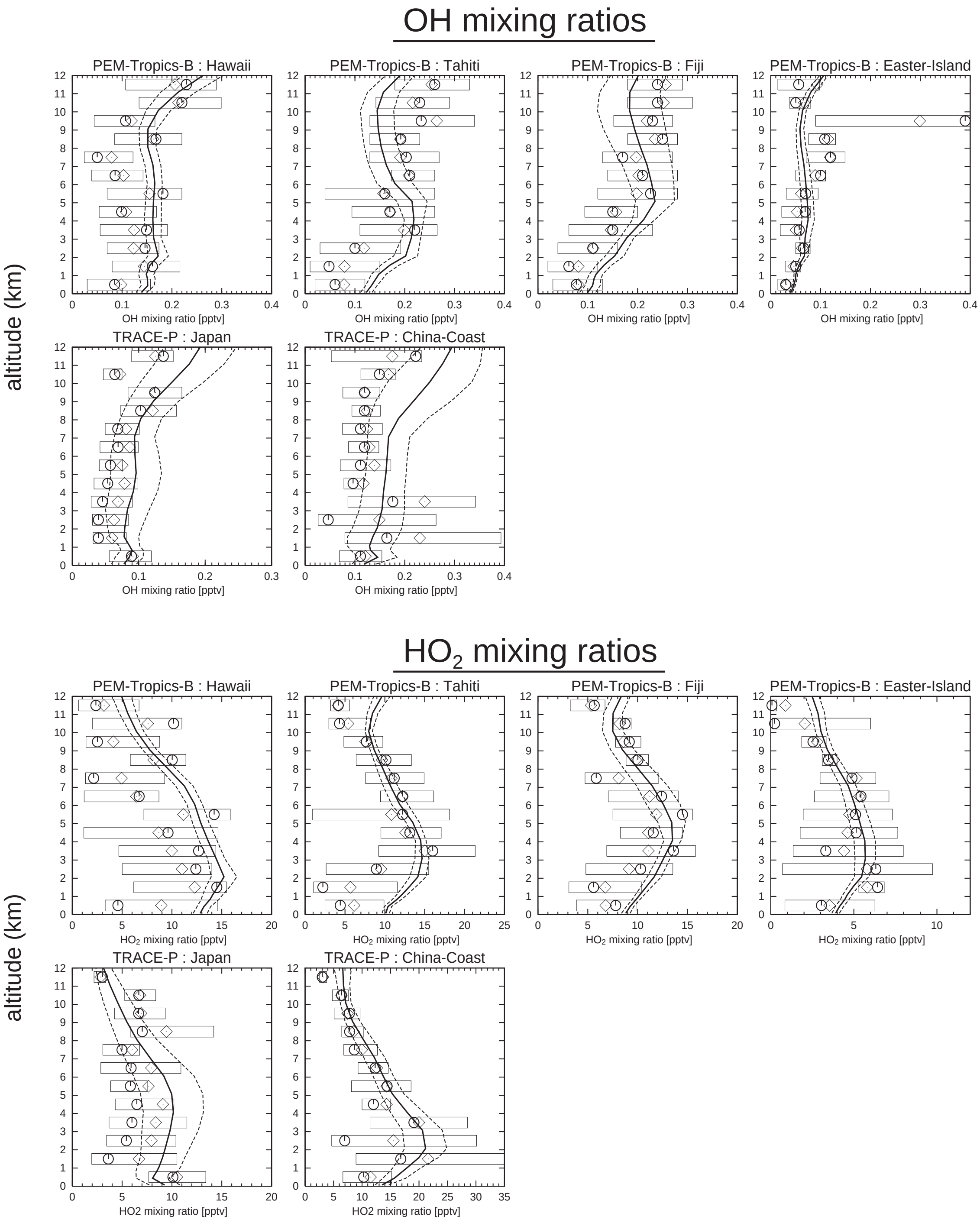

Figure 2.31. OH (upper) and HO_2 (lower) vertical profiles observed and calculated over the regions of GTE campaigns (listed in Table 2.5). The model results show mixing ratios of OH and HO_2 in the daytime average except for Easter-Island in the 24-hour average. Solid lines and dashed lines show temporal mean and $\pm 1\sigma$ of the model calculation, respectively. The observations show mean (diamonds), median (circles), and inner 50% of the data (boxes).

note again that values measured by a flight campaign are fragmentary with respect to time and space for individual altitudes, and there may be discrepancies in representation of time and space between measurements and model calculations especially for short-lived radicals such as OH and HO_2. The comparison appears to show that the calculated HO_x species are generally consistent with the measurements. Daytime mixing ratios of OH and HO_2 are in the ranges of 0.05-0.3 pptv and 5-20 pptv, respectively. In the China-Coast region during TRACE-P, the model well captures the observed HO_2 increase ($\sim$20 pptv) in 1-4 km altitudes. This HO_2 enhancement over the China-Coast region appears to be coinciding with the increase in CH_2O and acetone (Figure 2.34 and 2.35) associated with industrial emissions in China and transport from the biomass burning regions in southeastern Asia. The HO_2/OH ratio decreases in the upper troposphere, due to the increase in O_3 and NO. In the Fiji and Tahiti regions during PEM-Tropics-B, OH mixing ratios in the upper troposphere are considered to be underestimated by 20-40%. This discrepancy may be attributed to the slight overestimation of CO and the underestimation of NO in the upper troposphere over the tropical Pacific. The calculated profiles of water vapor, ozone, acetone, CH_2O (see Figure 2.34) and CH_3OOH (Figure 2.40) over Fiji and Tahiti are generally consistent with the measurements during the PEM-Tropics-B, and the HO_x production rate calculated in the upper troposphere (8-12 km) over Fiji ranges from 500 to 2000 pptv/day, in good agreement with the box model calculation for the flight 10 around Fiji during the PEM-Tropics-B experiment [*Mari et al.*, 2001]. In the Japan and China-Coast regions (TRACE-P), the modeled OH levels are 1.5-2 times higher than the observation especially in the middle-upper troposphere. This appears to originate from the overestimation of NO_x (NO) in these regions during TRACE-P as shown in Figure 2.24.

The global OH field calculated by the model is also evaluated by comparing lifetime of CH_4 (methane) and CH_3CCl_3 (metylchloroform) in the model with measurements. *Prinn et al.* [1995] derived a global lifetime of 4.9±0.3 years for CH_3CCl_3 below 200 hPa regarding OH oxidation, and obtained a global methane lifetime of 8.9±0.6 years, based on observed CH_3CCl_3 concentrations. In this simulation, the calculated global OH concentrations (below 200 hPa) lead to a global CH_3CCl_3 lifetime of 5.0 years (4.5 years in the northern hemisphere, 5.6 years in the southern hemisphere), in excellent agreement with the CH_3CCl_3 lifetime suggested by *Prinn et al.* [1995] (4.9±0.3 years). The global methane lifetime, defined as (global methane burden)/(OH destruction within the troposphere), is calculated as 9.4 years in this simulation. This estimated methane lifetime against tropospheric OH is well within the range suggested by *Prinn et al.* [1995] (0.89±0.6 years), and is also close to the recent IPCC estimate (9.6 years) [*Prather et al.*, 2001].

Figure 2.32 shows the 24-hour average distributions of HO_x production rate (pptv/day) calculated in the upper troposphere (8-13km) for January and July. As can be expected, the HO_x production in the upper troposphere is anomalously high in regions of high NMHCs level in the low latitudes. The HO_x production is high (3000-6000 pptv/day) over the tropical rainforests associated with biogenic emissions of NMHCs, being also high in July over the eastern United States and

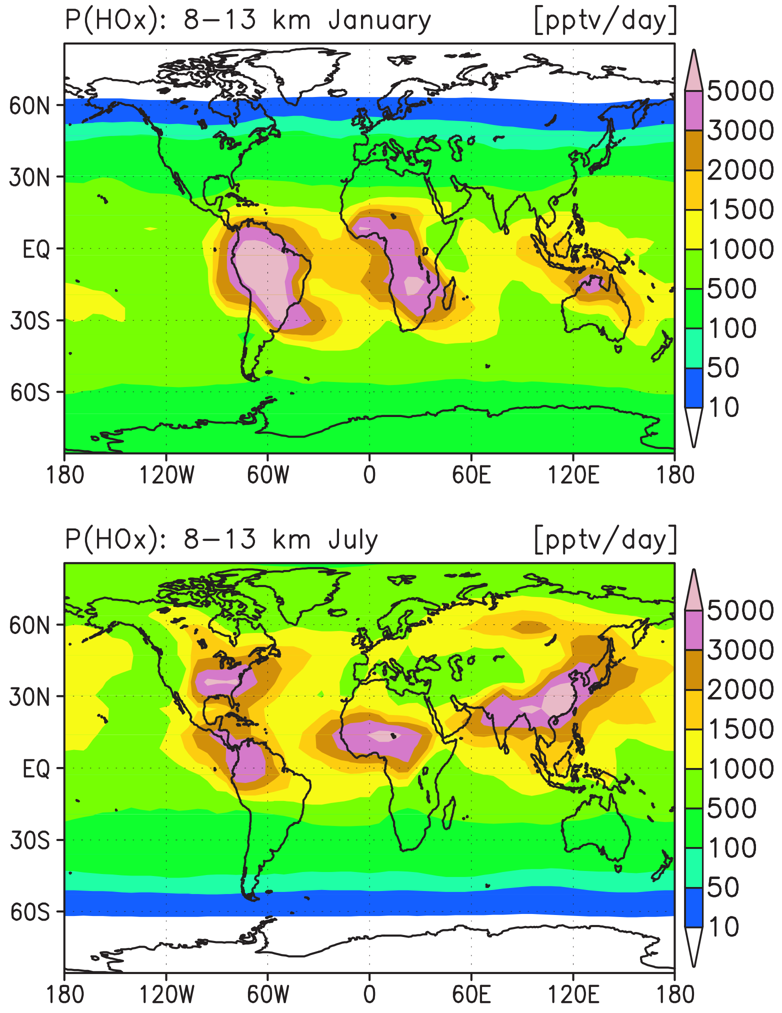

Figure 2.32. Distributions of the HO_x production term $P(HO_x)$ (pptv/day) in the upper troposphere (averaged over 8-13 km altitude) calculated for January and July.

eastern Asia (India, China) (above 3000 pptv/day). Over the ocean in the low latitudes, the calculated production rate is in the range of 500-1500 pptv/day off continents, and 1500-3000 pptv/day in the vicinity of continents (e.g., over the South Atlantic in January and over the western Pacific including Japan in July).

The global HO_x production and the mean lifetime of HO_x calculated by the model below the tropopause are presented in Table 2.8. The model calculates a global HO_x production of 215 TgH/yr corresponding to 1.3×10^{38} molecules/yr (58% in the northern hemisphere), and a global mean lifetime of 4.5 min. The differences in the production and the lifetime between the northern hemisphere and the southern hemisphere are owing to differences in the abundance of O_3 and NMHCs.

Table 2.8. Chemical Production and Lifetime of HO_x Calculated by CHASER.

	Global	NH	SH
Chemical production (TgH/yr)	214.7	124.2	90.5
Chemical lifetime (min)	4.5	3.7	5.7

TgH/yr corresponds to 6.02×10^{35} molecules/yr.

Formaldehyde and acetone

The primary source for HO_x is the photolysis of ozone followed by the reaction of $O(^1D)$ with water vapor (H_2O). In dry regions as in the upper troposphere, acetone (CH_3COCH_3) [*Singh et al.*, 1995; *Arnold et al.*, 1997; *McKeen et al.*, 1997; *Wennberg et al.*, 1998], and formaldehyde and other aldehydes produced in the oxidation of methane and NMHCs [*Müller and Brasseur*, 1999] become important HO_x sources. Figure 2.33 shows the calculated distributions of formaldehyde (CH_2O) and acetone in the upper troposphere (8-13 km average) for January and July. CH_2O decomposes by photolysis on a timescale of hours in summer and hence effectively produces HO_x. In Figure 2.33, high concentrations (100-400 pptv) of CH_2O are calculated over the regions where NMHCs are abundant (i.e., tropical rainforests, the eastern United States, eastern Asia), well correlated with the

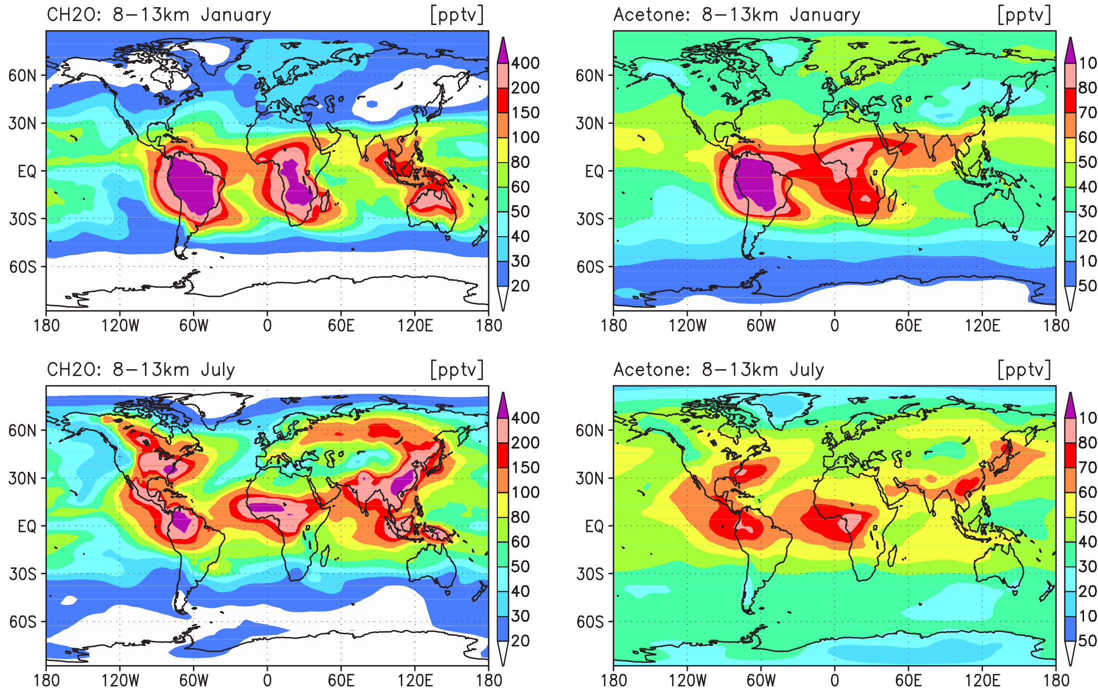

Figure 2.33. Calculated CH_2O (left) and acetone (right) distributions (pptv) in the upper troposphere (averaged over 8-13 km) for January and July.

HO_x production in the upper troposphere in Figure 2.32. Acetone similarly produces HO_x in the upper troposphere by its photolysis. As the lifetime of acetone against photolysis and OH oxidation is much longer than CH_2O (calculated global mean lifetime of acetone is 27 days), acetone can be an important source for HO_x in remote regions as well as in source regions. The distributions of acetone (Figure 2.33) indicate the contribution of acetone to the HO_x production in the upper troposphere. In this simulation, the model includes acetone emission sources of 1.02 TgC/yr from industry, 4.88 TgC/yr from biomass burning, 11.2 TgC/yr from vegetation, and 12.0 TgC/yr from ocean. The model secondarily considers the acetone source from oxidation of NMHCs (propane C_3H_8 and terpenes in this simulation, see section 2.2.1). The calculated acetone in 8-13 km is high (700-1200 pptv) over South America and Africa including the South Atlantic in January, reflecting the emissions of acetone by vegetation and biomass burning, and the photochemical production of acetone by the oxidation of propane and terpenes. A long range transport of acetone from eastern Asia and North Africa to the North Pacific is visible in January associated with the long chemical lifetime of acetone in winter ($>$ 1 month). In July, the calculated distribution of acetone in the upper troposphere (8-13 km) is somewhat similar to that of CH_2O, showing peaks ($>$ 600 pptv) over the eastern United States, eastern Asia, and the tropical rain forests.

Simulated vertical profiles of CH_2O and acetone are compared with the observations of the NASA GTE campaign in Figure 2.34 and 2.35, respectively. In Figure 2.34, the model simulates the CH_2O vertical profiles very well in the tropics observed during PEM-Tropics-B, though underestimating CH_2O in the upper troposphere over the Tahiti region. In these tropical regions, both the observation and the calculation show the CH_2O mixing ratios of 300-400 pptv near the surface and lower than 100 pptv in the upper troposphere (above 6 km). In the source regions of biomass burning (E-Brazil, S-Africa in TRACE-A), the model tends to overestimate CH_2O near the surface. In the west of African coast (W-Africa-Coast), CH_2O distribution is overestimated by the model at all altitudes, though the observed increase in the lower troposphere is simulated qualitatively. Our evaluation shows also a large overestimation of CH_2O in the South Atlantic region during the TRACE-A (not shown here). The overestimation of CH_2O over these regions may suggest that the chemical scheme for oxidation of isoprene, terpenes, and a lumped NMHCs species (ONMV, see section 2.2.1) adopted in the model produces too much CH_2O and hence too much HO_x. The CH_2O profiles observed in the Japan and China-Coast regions during TRACE-P are well reproduced by the model. In Figure 2.35 showing acetone vertical profiles, the calculated vertical distributions of acetone are well within the range of the observations. Acetone mixing ratios are in the range of 500-1000 pptv near the source regions (Japan, China-Coast in PEM-West-B and TRACE-P), and 300-500 pptv over the remote ocean as Philippine-Sea (PEM-West-B) and the central Pacific (PEM-Tropics-B). In the simulation with the previous CHASER version [*Sudo et al.*, 2002b], acetone levels in the tropical Pacific regions during PEM-Tropics-B were underestimated by a factor of 2, but are simulated relatively well in this study with including oceanic acetone emission of 12.0

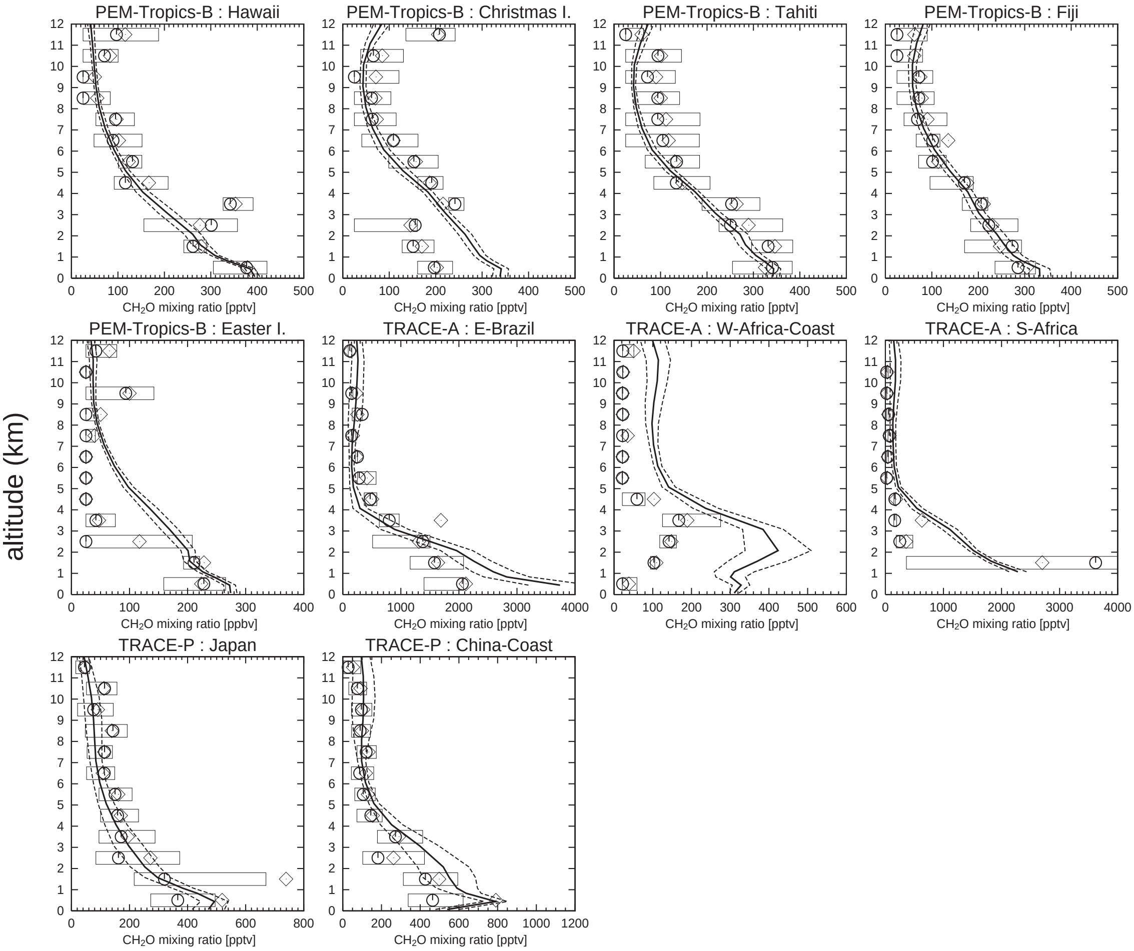

Figure 2.34. CH_2O vertical profiles observed and calculated over the regions of GTE campaigns (listed in Table 2.5). Solid lines and dashed lines show temporal mean and $\pm 1\sigma$ of the model calculation, respectively. The observations show mean (diamonds), median (circles), and inner 50% of the data (boxes).

TgC/yr. The simulated acetone mixing ratio reaches about 1500-2500 pptv in the source regions of biomass burning (E-Brazil and S-Africa). In the E-Brazil region, both the observation and the model show an increase in the upper troposphere, resulting from convective transport [*Fishman et al.*, 1996]. For the TRACE-P expedition, the model reproduces the acetone profiles observed in the Japan and China-Coast regions, simulating the increase below 5 km in China-Coast as with CO (Figure 2.16) and C_2H_6 (Figure 2.20).

To evaluate the seasonal variation of CH_2O and acetone calculated by the model, we display a comparison of seasonal cycle of CH_2O and acetone observed and calculated at the surface for an European site in Figure 2.36. The model appears to reproduce the observed seasonal variation of CH_2O, well simulating the enhancement of CH_2O ($\sim$1.5 ppbv) in summer due to production by the oxidation of methane and NMHCs. The simulated acetone at the surface is also consistent with the observation (1-1.5 ppbv), though the model somewhat underestimates acetone in summer.

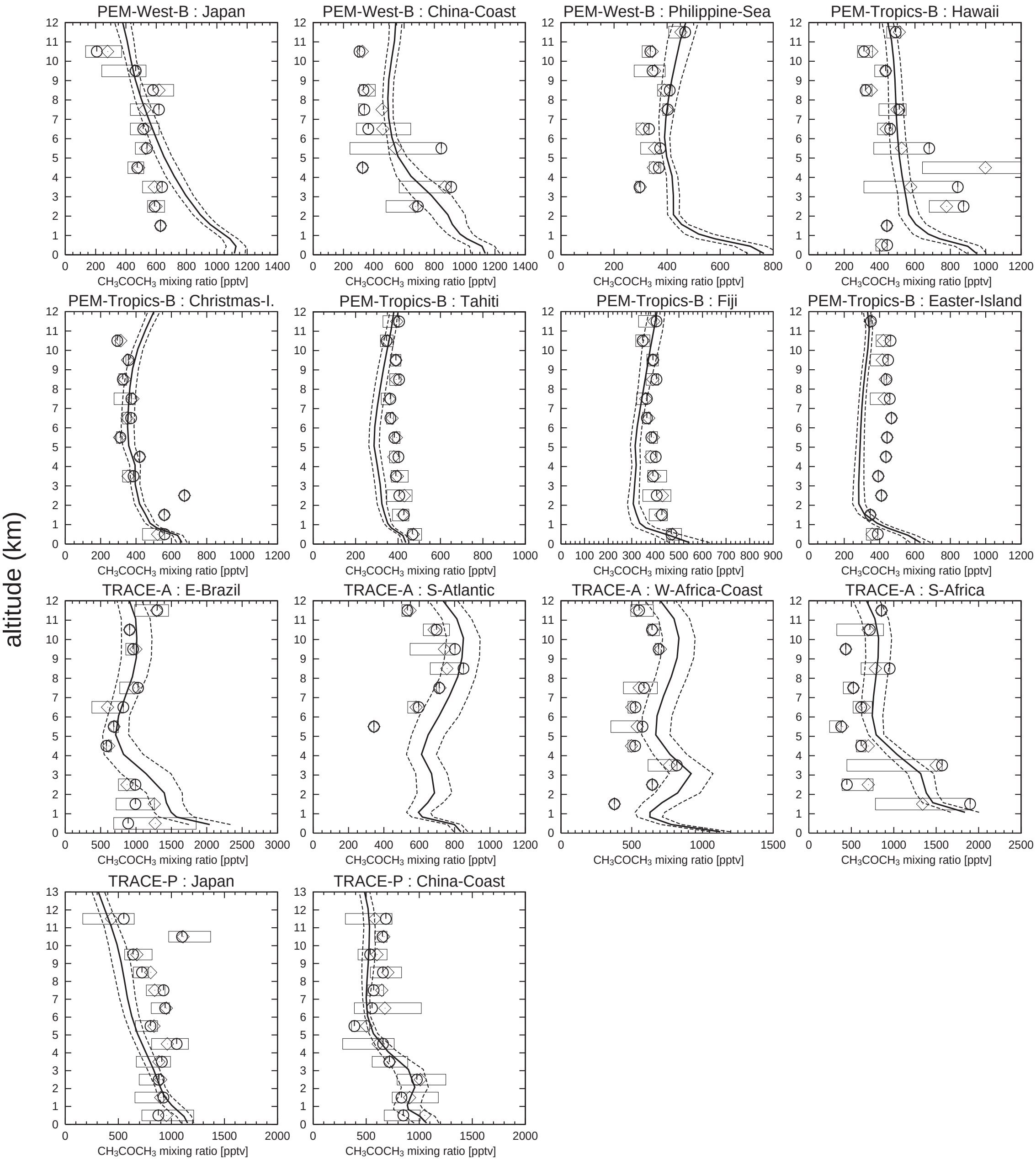

Figure 2.35. Acetone CH_3COCH_3 vertical profiles observed and calculated over the regions of GTE campaigns (listed in Table 2.5). Solid lines and dashed lines show temporal mean and $\pm 1\sigma$ of the model calculation, respectively. The observations show mean (diamonds), median (circles), and inner 50% of the data (boxes).

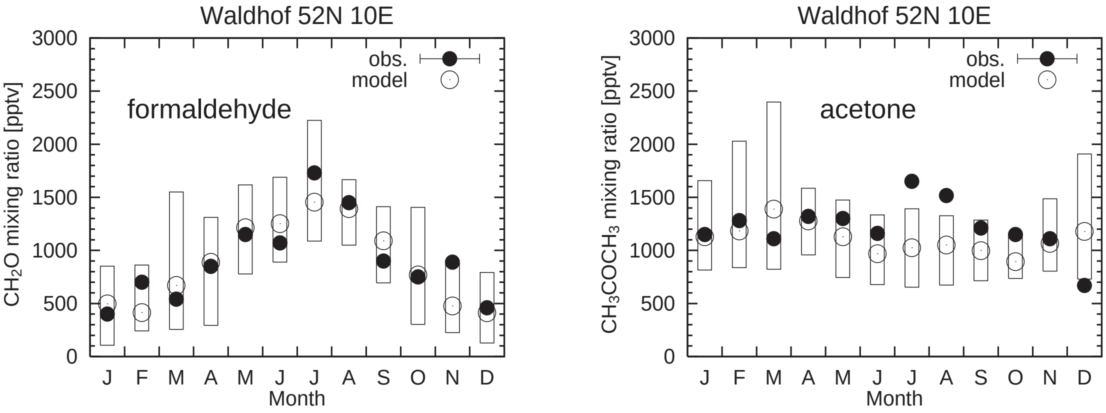

Figure 2.36. Observed (solid circles) and calculated (open circles) surface mixing ratios (pptv) of CH_2O (left) and acetone (right). Boxes indicate the range of the day-to-day variability calculated by the model. Measurements are taken from *Solberg et al.* [1996].

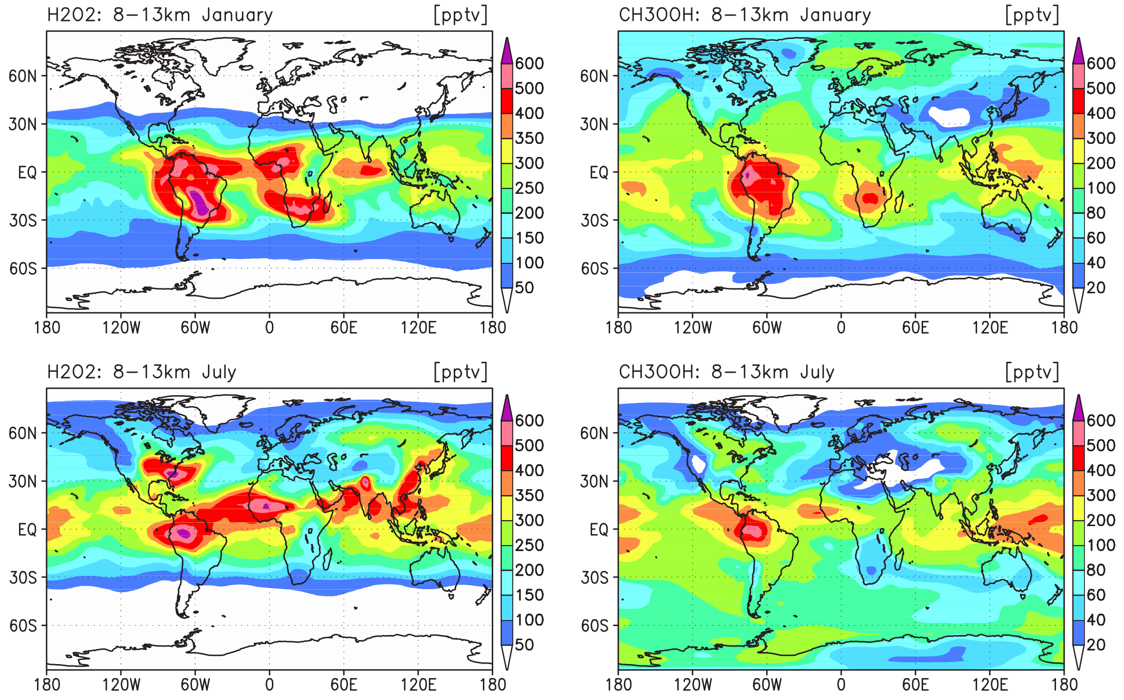

Figure 2.37. Calculated H_2O_2 (left) and CH_3OOH (right) distributions (pptv) in the upper troposphere (averaged over 8-13 km) for January and July.

Peroxides

Peroxides are produced by the reactions of HO_2 with peroxy radicals and decompose by photolysis and OH reaction. Photolysis of peroxides transported to the upper troposphere are considered to be an important HO_x source [*Jaeglé et al.*, 1997; *Folkins et al.*, 1998; *Cohan et al.*, 1999]. Peroxides are, therefore, milestones for simulating the HO_x chemistry. Additionally, H_2O_2 plays a central role in the liquid-phase oxidation of SO_2 to form sulfate (SO_4^{2-}). We focus our attention here on H_2O_2 and CH_3OOH. Figure 2.37 shows the calculated distributions of H_2O_2 and CH_3OOH in the upper troposphere (8-13 km average) for January and July. H_2O_2 and CH_3OOH in the upper troposphere are much more abundant in the tropics (100-600 pptv) than in the extra-tropics (below 100 pptv). The distributions of both H_2O_2 and CH_3OOH show correlation to the distributions of HO_x production in Figure 2.32 as CH_2O and acetone, since H_2O_2 and CH_3OOH, formed by the HO_2 reactions, produce HO_x in the upper troposphere. The high levels of H_2O_2 and CH_3OOH calculated over South America and Africa (higher than 500 pptv) are owing to in-situ production of peroxides in the upper troposphere and convective transport of H_2O_2 and CH_3OOH overcoming wet deposition of them.

Figure 2.38 shows the calculated zonal mean distributions of H_2O_2 and CH_3OOH in the annual

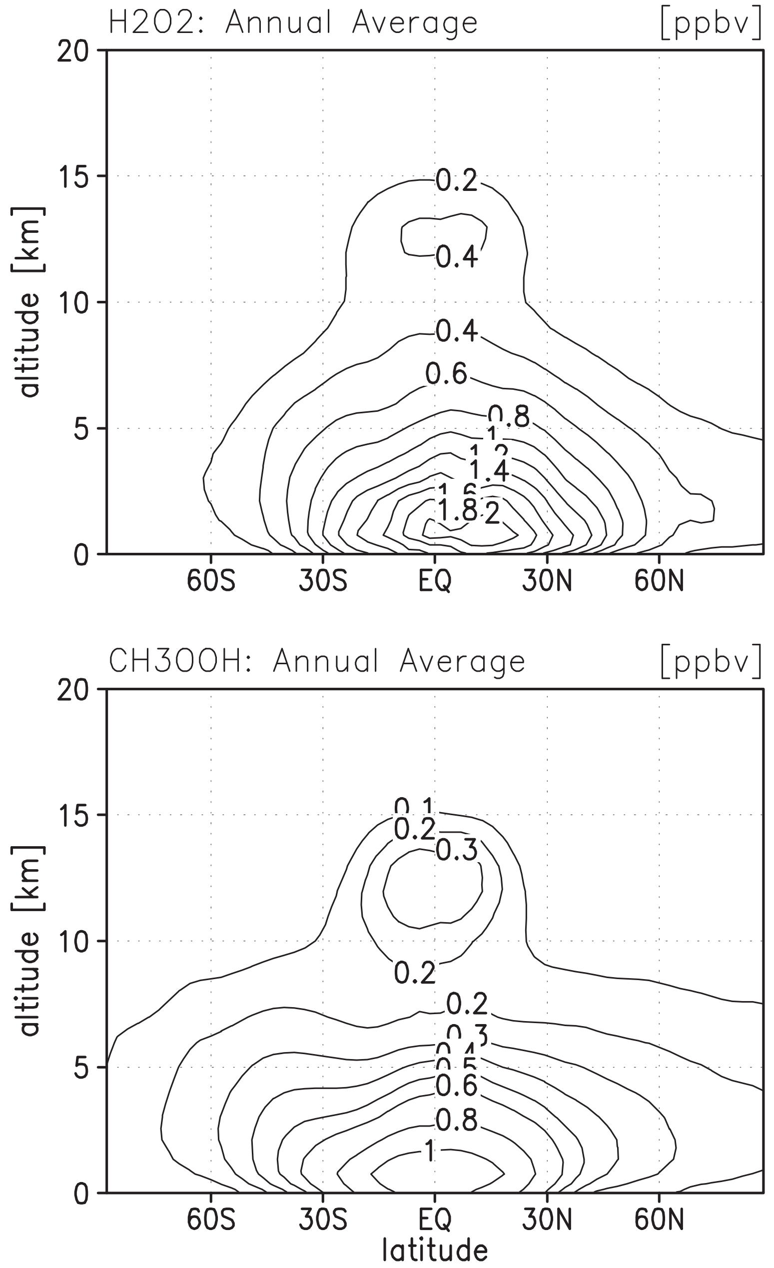

Figure 2.38. Zonal mean distributions (ppbv) of H_2O_2 and CH_3OOH in the annual average.

average. Though H_2O_2 is removed by wet deposition more efficiently than CH_3OOH, the calculated H_2O_2 concentration is generally higher than CH_3OOH as suggested by measurements [e.g., *Talbot et al.*, 1996; *Heikes et al.*, 1996]. The distributions of both H_2O_2 and CH_3OOH show a peak near the surface (∼1 km) in the tropics (H_2O_2∼ 2 ppbv, CH_3OOH∼1 ppbv). Peaks of H_2O_2 and CH_3OOH are also calculated in the tropical upper troposphere. Although these peaks seem to be consistent with convective transport of H_2O_2 and CH_3OOH in the tropics, they may be overestimated by the model because the model probably overestimates the HO_2/HO ratio due to underestimation of NO

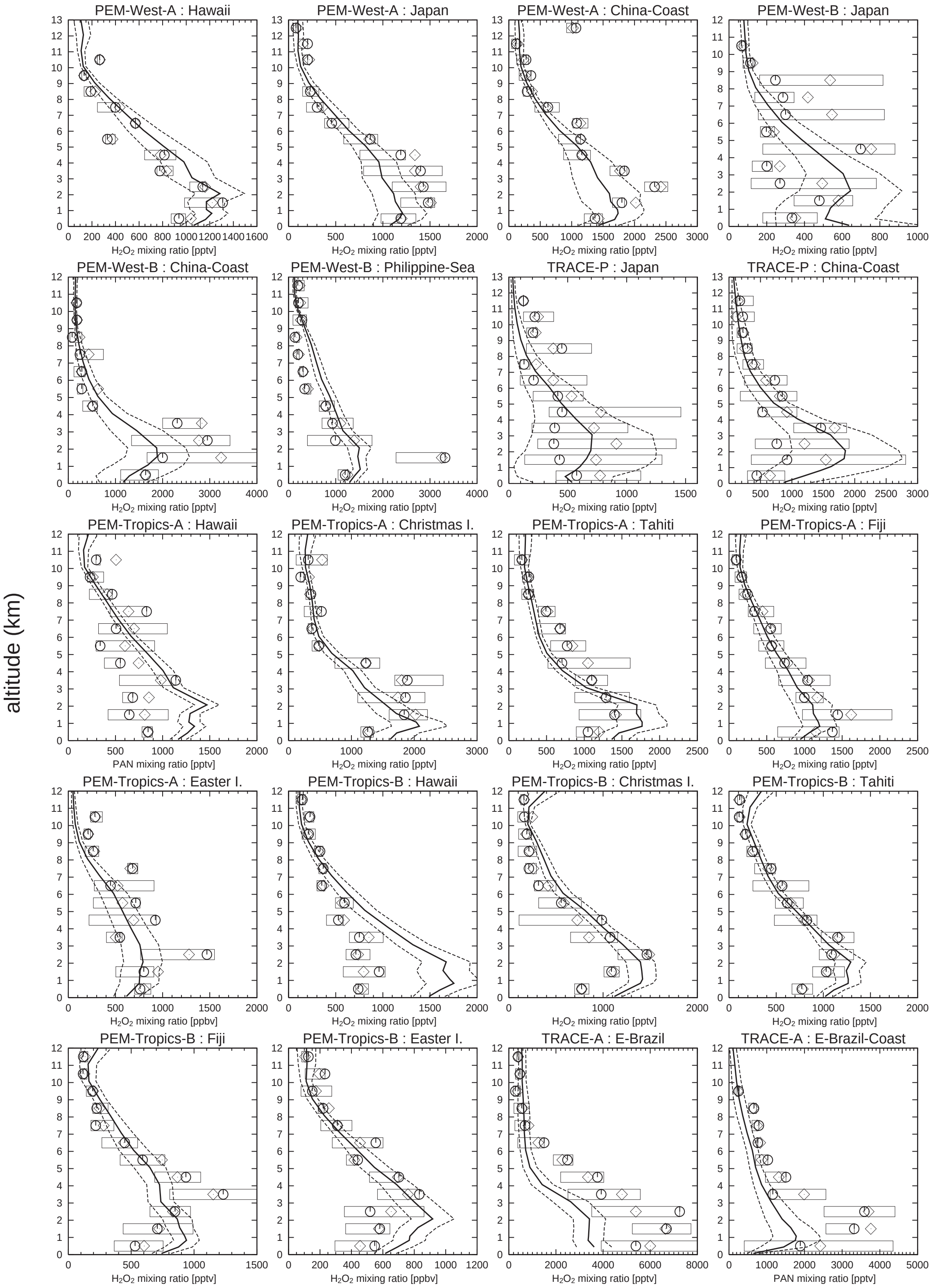

Figure 2.39. H_2O_2 vertical profiles observed and calculated over the regions of GTE campaigns (listed in Table 2.5). Solid lines and dashed lines show temporal mean and $\pm 1\sigma$ of the model calculation, respectively. The observations show mean (diamonds), median (circles), and inner 50% of the data (boxes).

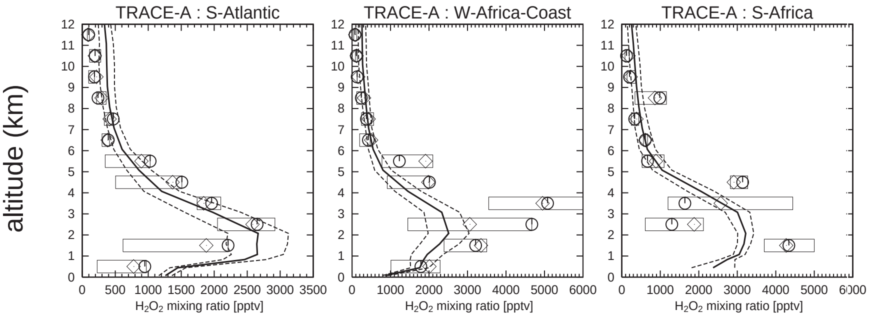

Figure 2.39. (continued).

in the tropical upper troposphere.

In Figure 2.39, the observed and the calculated vertical profiles of H_2O_2 are compared. The model reproduces the observed H_2O_2 profiles very well in most cases. In the Japan region during both PEM-West-B and TRACE-P, the observation shows high variabilities of H_2O_2 (ranging from 100 to 1000 pptv) below 9 km. The model also shows large standard deviations ($\pm 1\sigma$) over this region, calculating H_2O_2 levels well consistent with the observation. The H_2O_2 increase in 1-5 km altitudes in the China-Coast region during TRACE-P is well reproduced by the model and is resulting from the abundant HO_2 in the region (Figure 2.31). The previous CHASER version [*Sudo et al.*, 2002b] tends to overestimate H_2O_2 in the upper troposphere above 9 km in the tropical regions for PEM-Tropics-A and B. Such an overestimation appears to be reduced in this simulation by including H_2O_2 deposition on ice particles in cirrus clouds (see section 2.2.3). In the biomass burning regions in South America (E-Brazil in TRACE-A), the model underestimates the observed H_2O_2 by a factor of 2 below 5 km. This discrepancy would be reduced by considering methanol emissions from vegetation and biomass burning as suggested by *Horowitz et al.* [2002]. In the S-Atlantic region, both the observation and the model show high level of H_2O_2 ($\sim$2000 pptv) in 1-4 km altitudes, associated with the African outflow. Figure 2.40 is the same as Figure 2.39 but for CH_3OOH profiles. CH_3OOH profiles are captured well by the model as well as H_2O_2. Over the China-Coast and the Philippine-Sea regions during PEM-West-B, the model overestimates CH_3OOH in the middle-upper troposphere by a factor of $\sim$2, with showing good agreement with the observations for H_2O_2 (Figure 2.39). This may indicate overestimation of methyl peroxy radical (CH_3O_2) and hence too strong formation of CH_3O_2 by the oxidation of NMHCs around these regions. In the tropical regions (PEM-Tropics), the simulated profiles of CH_3OOH are well consistent with the observations, calculating mixing ratios of $\sim$1 ppbv near the surface and 100-300 pptv in the upper troposphere. In the biomass burning regions (TRACE-A), CH_3OOH in the upper troposphere is somewhat overestimated, though CH_3OOH in the lower-middle troposphere (500-1000 pptv) is well simulated.

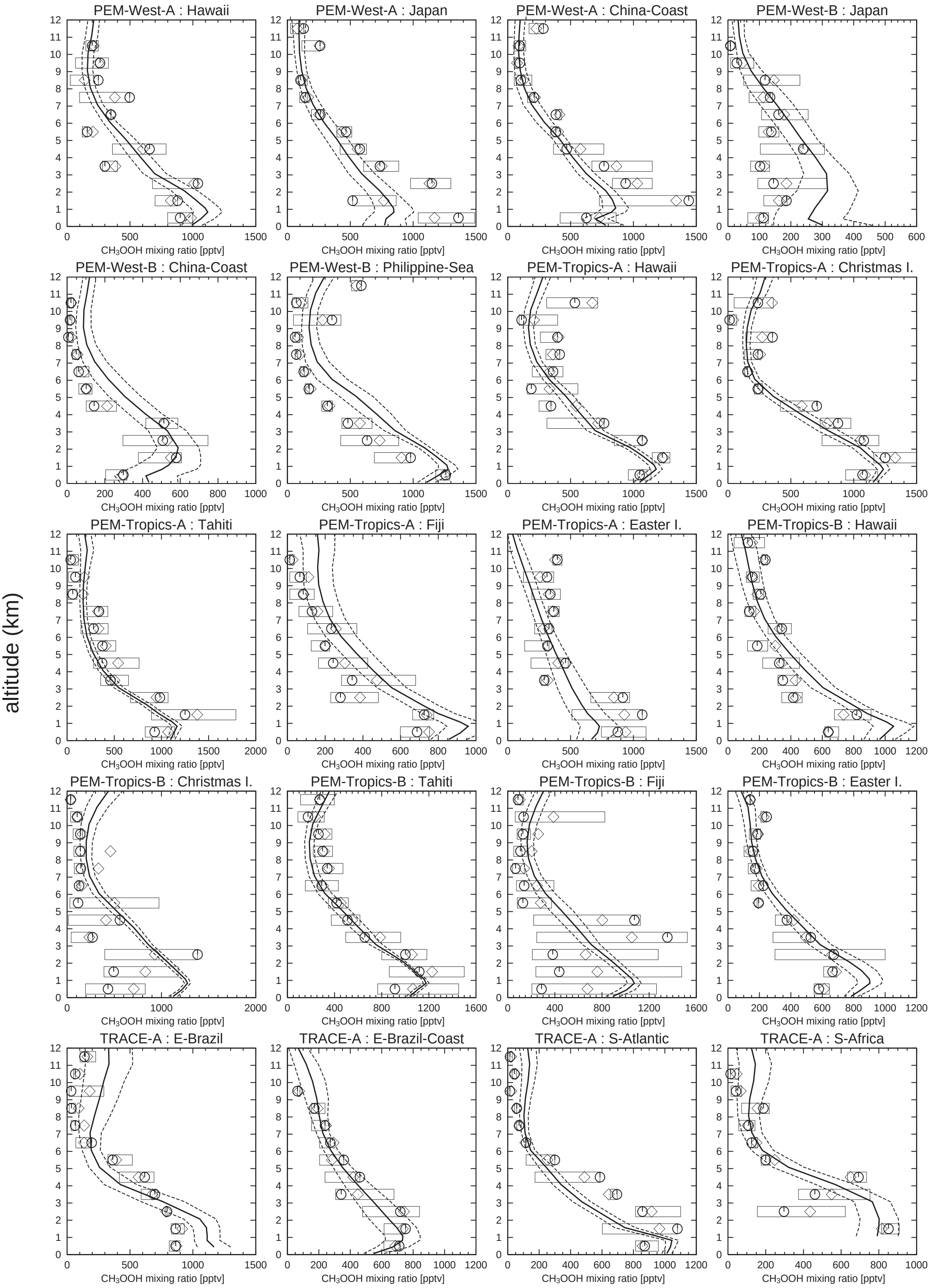

Figure 2.40. CH_3OOH vertical profiles observed and calculated over the regions of GTE campaigns (listed in Table 2.5). Solid lines and dashed lines show temporal mean and $\pm1\sigma$ of the model calculation, respectively. The observations show mean (diamonds), median (circles), and inner 50% of the data (boxes).

2.3.4 Ozone

Distributions

Figure 2.41 shows the surface O_3 distributions calculated for 4 different seasons. In January, high concentration of O_3 (50-60 ppbv) is calculated in India, owing to industrial emissions of O_3 precursors. High O_3 levels ($\sim$60 ppbv) are also seen in the biomass burning region in North Africa. O_3 concentration in the midlatitudes ranges from 30 to 40 ppbv over the ocean in the northern hemisphere, as a result of longer chemical lifetime of O_3 in winter and transport from the stratosphere. The calculated stratospheric ozone distribution at the surface indicates a 40-50% contribution by stratospheric ozone to the surface O_3 abundance in the northern midlatitudes in January. In April, the O_3 chemistry is activated in the northern hemisphere. High O_3 levels (50-65 ppbv) are predicted in eastern Asia as India, China, and Japan, affected by intense UV radiation and surface emissions by industry and biomass burning. Ozone produced in eastern Asia and Japan is transported to the western Pacific. In July, O_3 is much abundant in the United States and in the central Eurasia including Europe, ranging from 50 to 70 ppbv. High O_3 level associated with biomass burning is seen in the western edge of Africa. The effect of biomass burning on the surface O_3 is clearly visible in October over South America and Africa (50-60 ppbv). The model calculates low concentrations of O_3 (10-15 ppbv) in Amazonia through a year, resulting from strong ozone destruction by biogenic NMHCs and from strong dry deposition (deposition velocities of $\sim$1 cm s^{-1} in the model).

Similar features are also visible in the distributions of tropospheric column ozone TCO (Figure 2.42). TCO calculated by the model shows the ozone column integrated from the surface to the physically defined tropopause in the model (defined as the lowest altitude at which the vertical temperature gradient is greater than -2 K/km). Abundant tropospheric ozone in the range of 35-50 DU is calculated in the low to midlatitudes in both hemisphere due to industrial and biomass burning emissions. In July, the model calculates an O_3 peak of 45-50 DU around the Middle East, arising from transport of pollutants from the northern midlatitudes and eastern Asia and NO_x emissions from lightning as suggested by *Li et al.* [2001]. A large O_3 enhancement ($>$40 DU) is seen over the South Atlantic in October in accordance with biomass burning emissions in South America and Africa. The O_3 enhancement is also extending over the Indian Ocean ($\sim$40 DU) as a plume toward Australia. For all seasons, the model calculates an O_3 peak over the Atlantic with a minimum around the western Pacific (the wave 1 pattern) in the tropical latitudes, associated with the large-scale Walker circulation, lightning NO_x emissions, and biomass burning in the tropics. The wave 1 like pattern in zonal ozone distribution declines rapidly with latitude in the extratropics. This feature of tropical tropospheric ozone distribution is derived also by many satellite-based observations [e.g., *Fishman and Larsen*, 1987; *Fishman et al.*, 1996; *Ziemke et al.*, 1998] (see chapter 4). The model, however, tends to overestimate O_3 abundance around the North Atlantic, North Africa, and India compared to the satellite observations, especially in January to April.

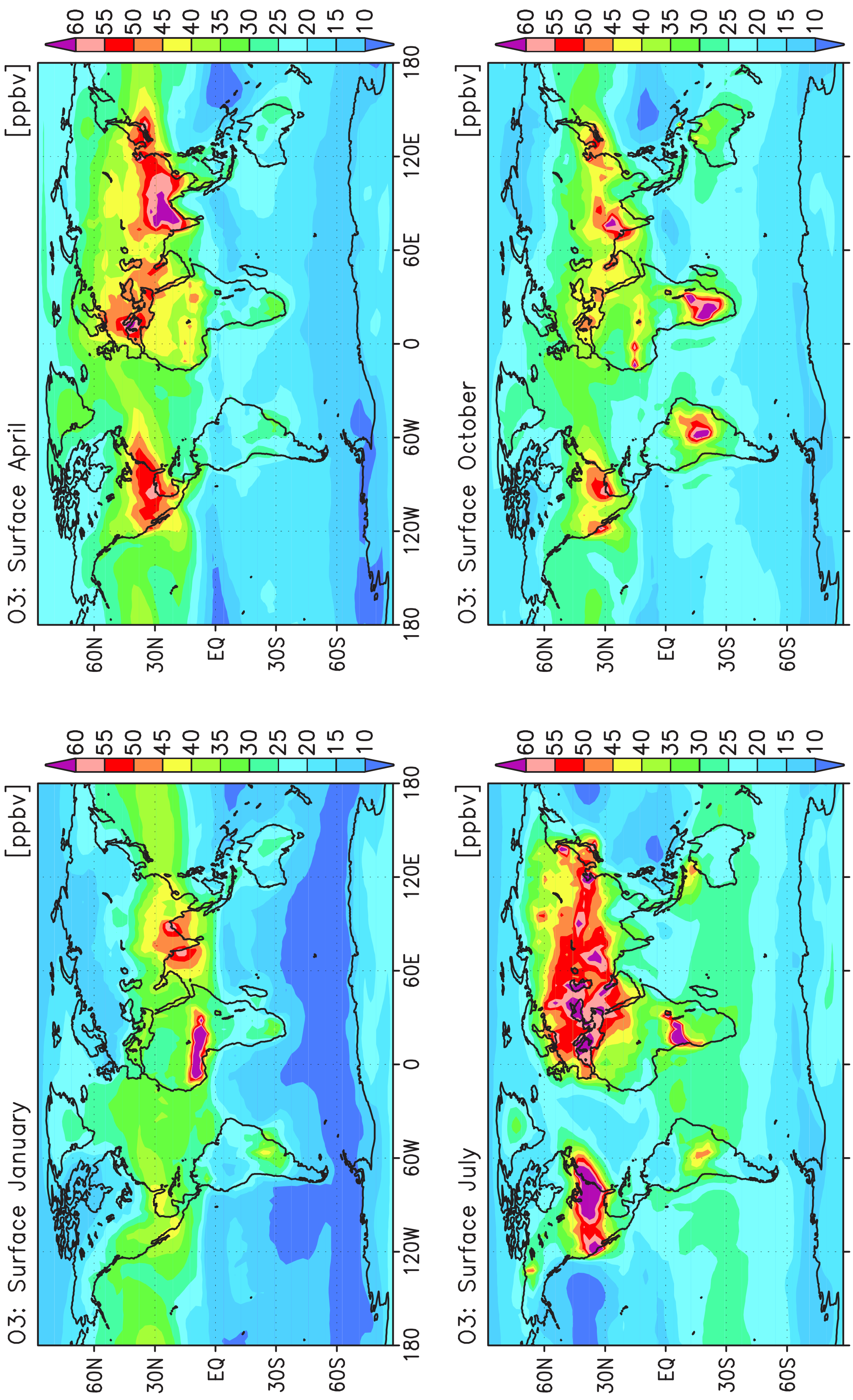

Figure 2.41. Calculated O_3 distributions (ppbv) at the surface for 4 distinct seasons (indicated).

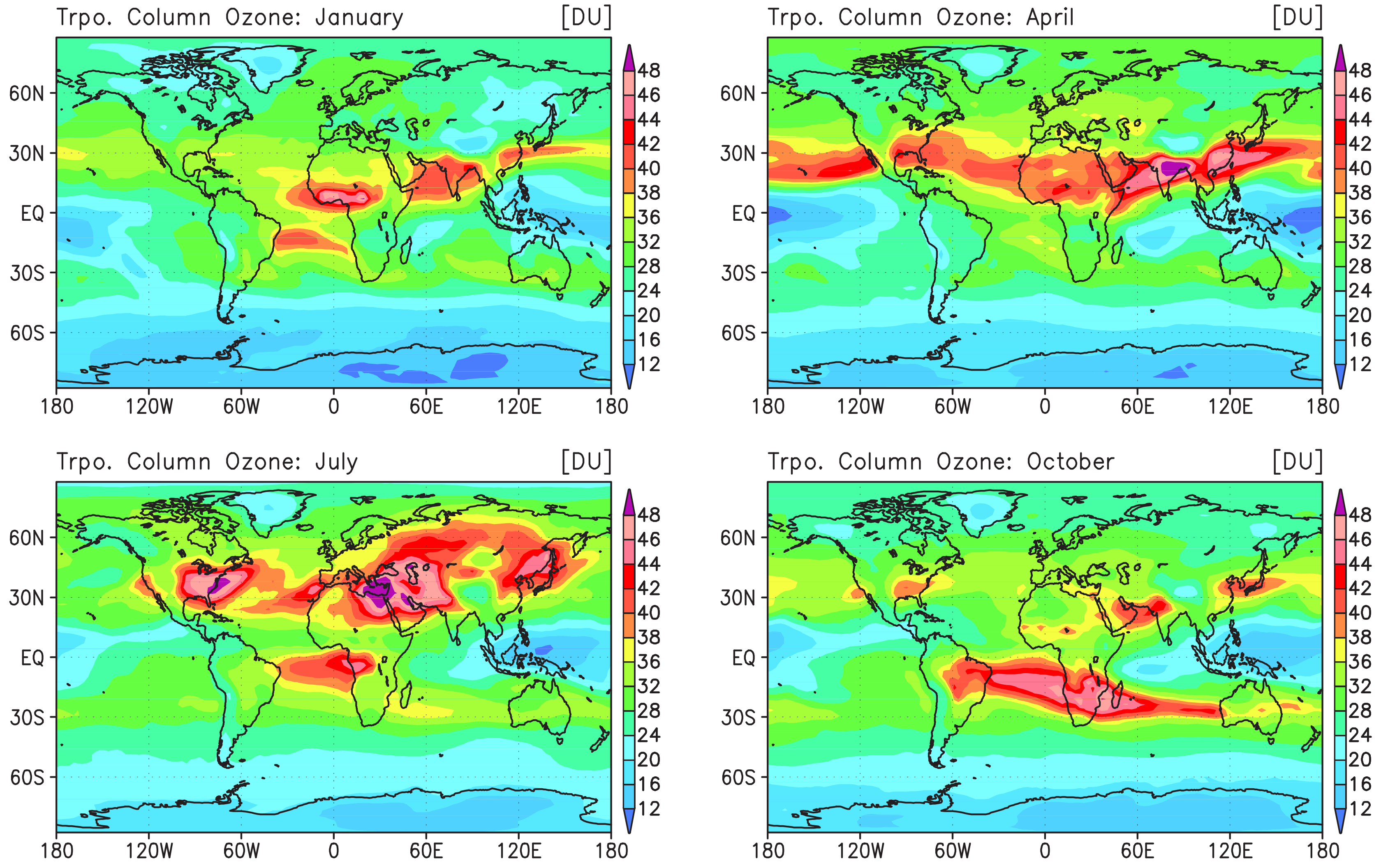

Figure 2.42. Tropospheric column ozone (TCO in Dobson Units) calculated for 4 distinct seasons (indicated).

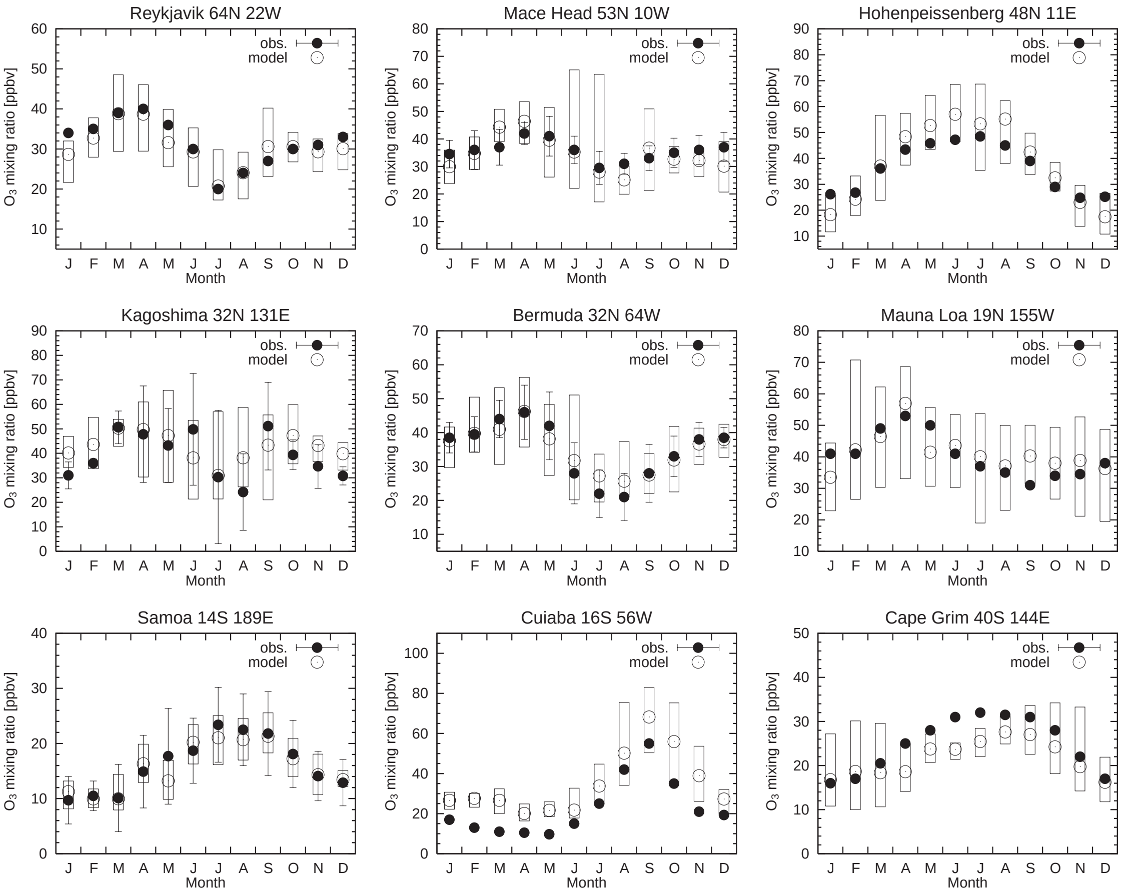

Figure 2.43. O_3 seasonal variations observed (solid circles) and calculated (open circles with boxes showing the range) at the surface for several sites. Measurements are from *Oltmans and Levy* [1994], *Kirchhoff et al.* [1989] (for Cuiaba) , and *Logan* [1999] (for Kagoshima).

Figure 2.43 compares the calculated seasonal cycle of surface O_3 with observations. The observations are mainly from *Oltmans and Levy* [1994]. The model well simulates the observed seasonal cycle of surface O_3 characterized by spring-maximum in the remote regions (Reykjavik, Mace Head, Bermuda, Mauna Loa, Samoa, Cape Grim) and summer-maximum in the polluted source regions (Höhenpeissenberg). The spring ozone peak at Bermuda is closely associated with the outflow from the United States in the model. Similarly, the peak in April at Mauna Loa is much related to the Asian outflow and to the transport of stratospheric ozone. For Cuiaba in the biomass burning region in South America, the model well reproduces the observed seasonal cycle (September maximum) associated with biomass burning as well as CO (Figure 2.15). The simulated O_3 levels in Cuiaba are, however, somewhat higher than the observation through a year, maybe indicating the underestimation of O_3 deposition velocity, or the overestimation of soil NO_x emission around Cuiaba. Similar overestimation at this site is also found in a previous modeling study [*Roelofs and Lelieveld*, 2000]. For Samoa and Cape Grim, the model reproduces the observed seasonal varia-

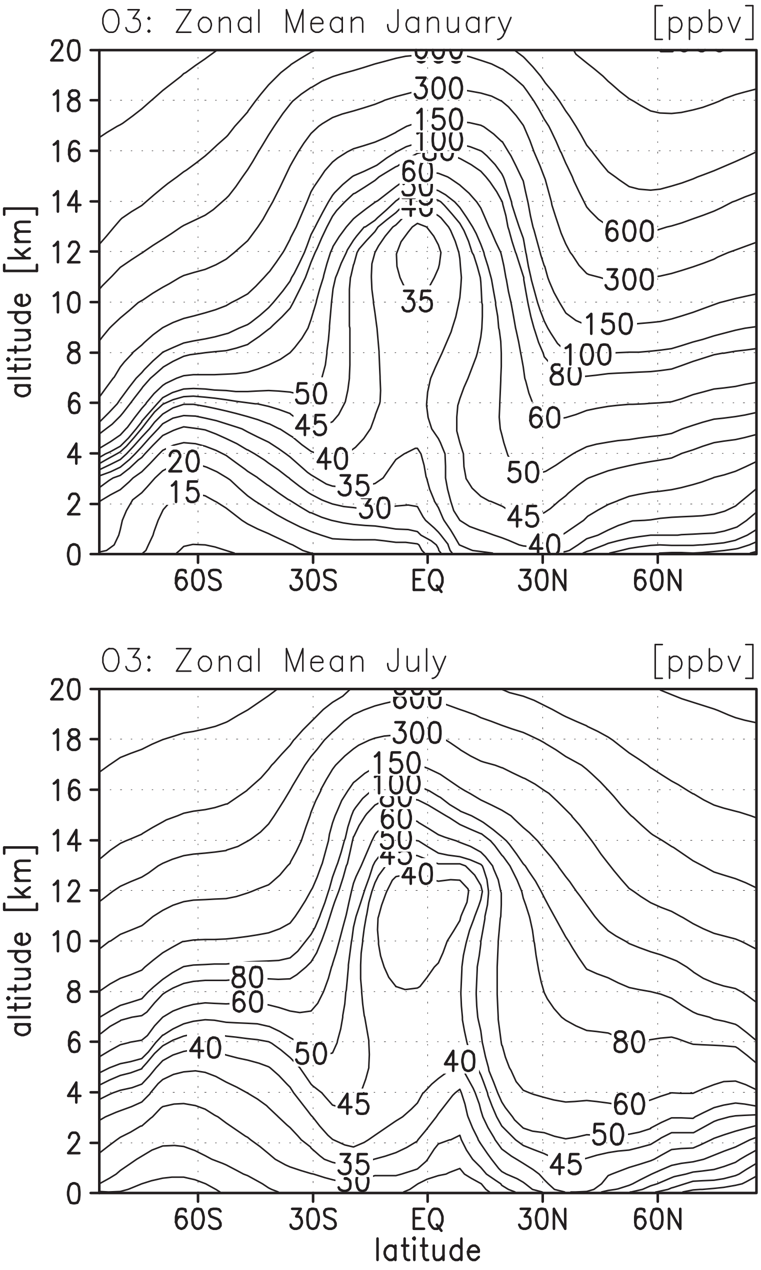

Figure 2.44. Zonally averaged ozone mixing ratios (ppbv) calculated for January and July.

tions associated with chemical lifetime of O_3 and transport from the stratosphere, though it slightly underestimates O_3 in June and July for Cape Grim.

Figure 2.44 shows the zonal mean O_3 distributions calculated for January and July. In both seasons, the model calculates low O_3 levels (30-40 ppbv) in the tropics due to short chemical lifetime of O_3 and convective activity. In January, O_3 concentration is high in the middle-upper troposphere in the northern midlatitudes, associated with transport from the stratosphere. In July, the model calculates high O_3 concentrations in the northern hemisphere through much of the troposphere, reflecting

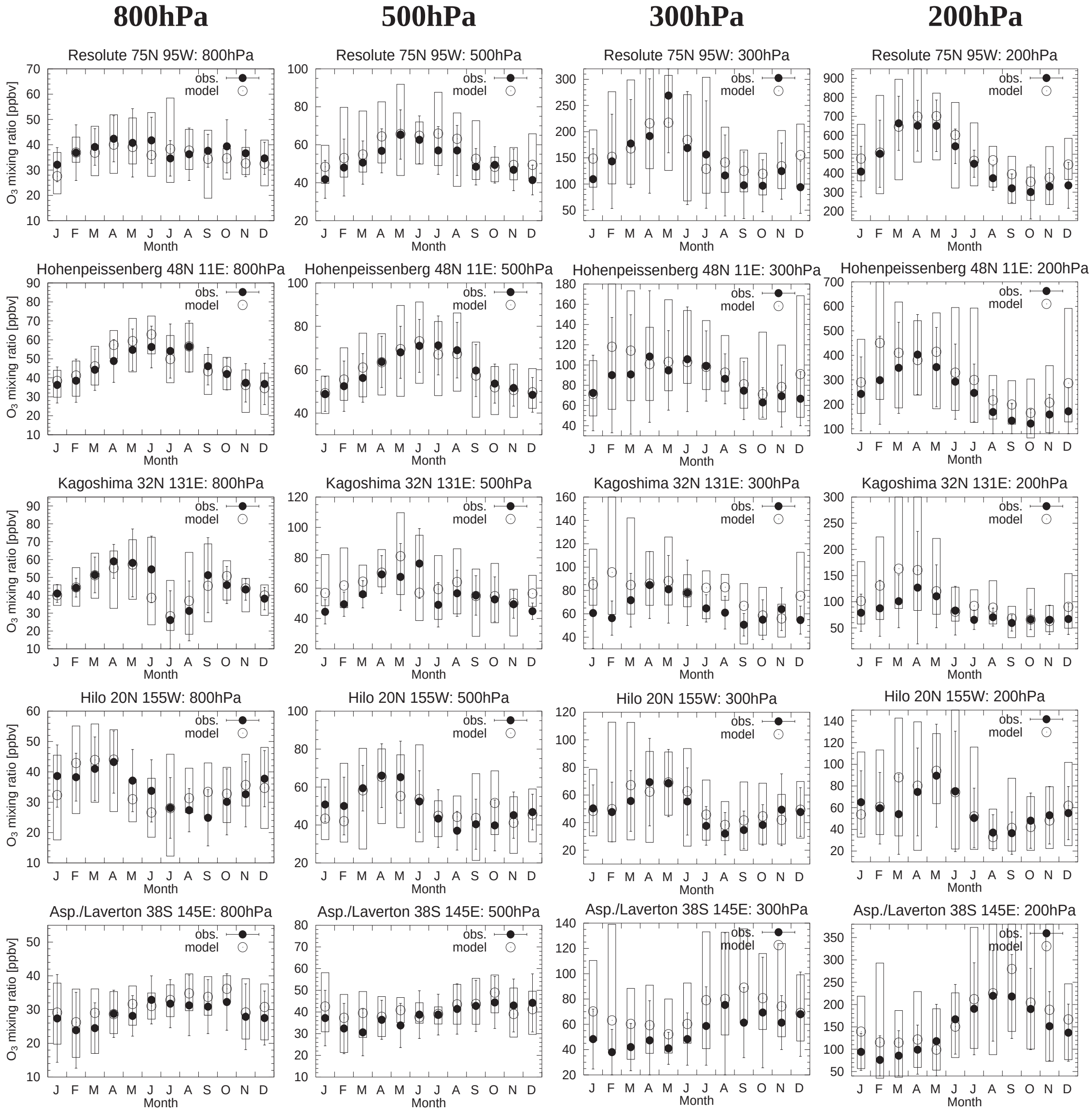

Figure 2.45. O_3 seasonal variations observed (solid circles) and calculated (open circles with boxes showing the range) at different elevations. Observations are taken from *Logan* [1999].

intensive photochemical production of O_3 in summer. In the southern hemisphere, the model calculates low mixing ratios of ozone (10-20 ppbv) near the surface in January, and calculates higher ozone concentrations (25-35 ppbv) in July associated with transport from the stratosphere.

In Figure 2.45, the seasonal variations of O_3 calculated at distinct altitudes are compared with the ozonesonde data compiled by *Logan* [1999]. The model generally well reproduces the observed seasonal cycles of O_3 at individual altitudes. At Resolute, the observed and the calculated O_3 at 200 hPa reach a peak (600-700 ppbv) in spring, associated with the stratospheric O_3 transport. Similar spring maximum is observed at 200 hPa over Höhenpeissenberg, overestimated slightly by the model, though. O_3 seasonal variation at Höhenpeissenberg shows a summer maximum from

800 hPa to 300 hPa, indicating considerable chemical production of O_3 over Europe in summer. At Kagoshima in the southern Japan, the model well captures the summertime minimum (rapid decrease in July and August) observed at 800 hPa. This minimum is associated with the shift in the airmass origin. The airmass at Kagoshima is maritime in summer and is continental in winter-spring, much influenced by the Asian outflow. At 300 and 200 hPa over Kagoshima, the model overestimates O_3 in winter by a factor of 2, indicating too much transport from the stratosphere. At Hilo, the model well reproduces the observed seasonal variations at individual altitudes, capturing spring O_3 peaks. At Laverton in the southern hemisphere, the model captures the seasonal variation of ozone observed at 200 hPa, well reproducing the ozone peak (200-250 ppbv) in spring associated with the stratospheric ozone transport, though the model overestimates the observed ozone levels at 300 hPa through a year. In winter-spring, the model tends to overestimate O_3 in the upper troposphere in the midlatitudes in both hemispheres, probably resulting from overestimation of O_3 transport from the stratosphere.

Additionally, calculated vertical profiles of O_3 are compared with the observational data [*Logan*, 1999] in Figure 2.46. The calculated profiles are generally well consistent with the observations. At Hilo, the model tends to overestimate O_3 in the upper troposphere especially in December-January-February (DJF) and March-April-May (MAM). We note that both the observation and the model show high temporal variabilities (indicated by the standard deviations) in the upper troposphere at Hilo, in winter-spring (DJF and MAM). At Natal located in the eastern coast of Brazil, the model reproduces the increase in O_3 ($\sim$70 ppbv) in 800-300 hPa in September-October-November (SON) associated with biomass burning. The model, however, appears to slightly overestimate O_3 in the middle troposphere at Natal in MAM and JJA. At Samoa, the observed seasonal cycle of ozone profile showing maximum in spring (SON) is well simulated by the model. The model well captures also the decrease of O_3 observed in the tropical lower troposphere (Naha, Hilo, Natal, and Samoa) related to the trade wind inversion in the tropics [*Heikes et al.*, 1996; *Logan*, 1999].

The calculated O_3 vertical profiles are also evaluated with the NASA GTE campaign data (Table 2.5) in Figure 2.47. In the Alaska (ABLE-3A), Ontario, and US-E-Coast regions, the calculated profiles are well consistent with the campaign measurements. The O_3 profile in the Japan region is well simulated by the model during PEM-West-A (September-October), but is overestimated significantly in the middle-upper troposphere during PEM-West-B (February-March) due to the overestimation of transport of stratospheric O_3 in the midlatitudes. A similar overestimation is also found during TRACE-P in the region. A slight overestimation of ozone is also found in the middle troposphere over the China-Coast region (PEM-West-B). This overestimation by the model can be also attributed to the overestimation of the stratospheric ozone transport, since the photochemical production rates of ozone calculated for this region during PEM-West-B are well consistent with the box model calculation constrained by the observation (see Figure 2.49). In the tropical regions (PEM-Tropics-A and B), the model well simulates the observed profiles of O_3, capturing

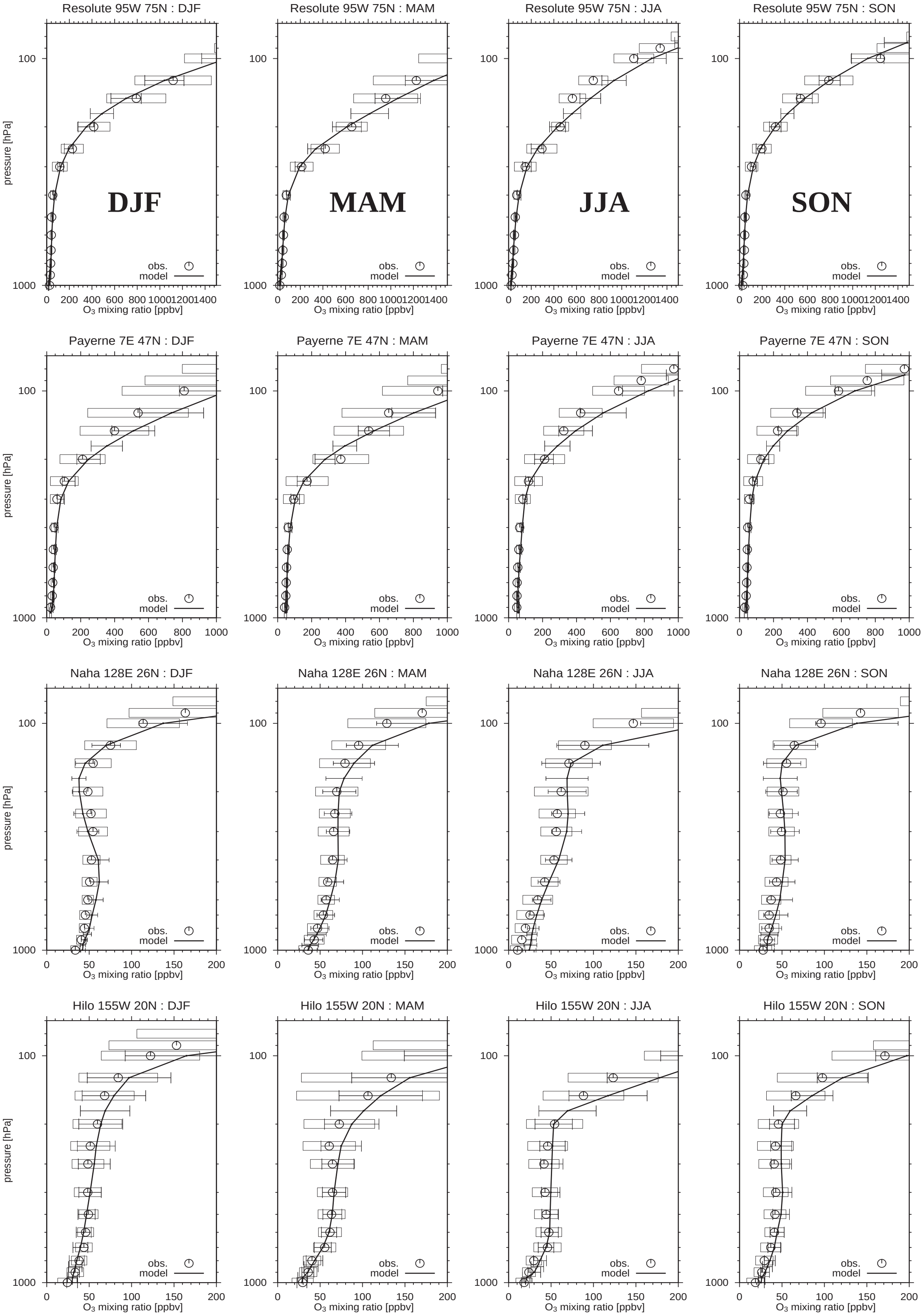

Figure 2.46. O_3 vertical profiles observed (open circles) and calculated (solid lines with $\pm\sigma$ bars) at several stations for 4 different seasons. Boxes show the standard deviations of observations. Observations are taken from *Logan* [1999].

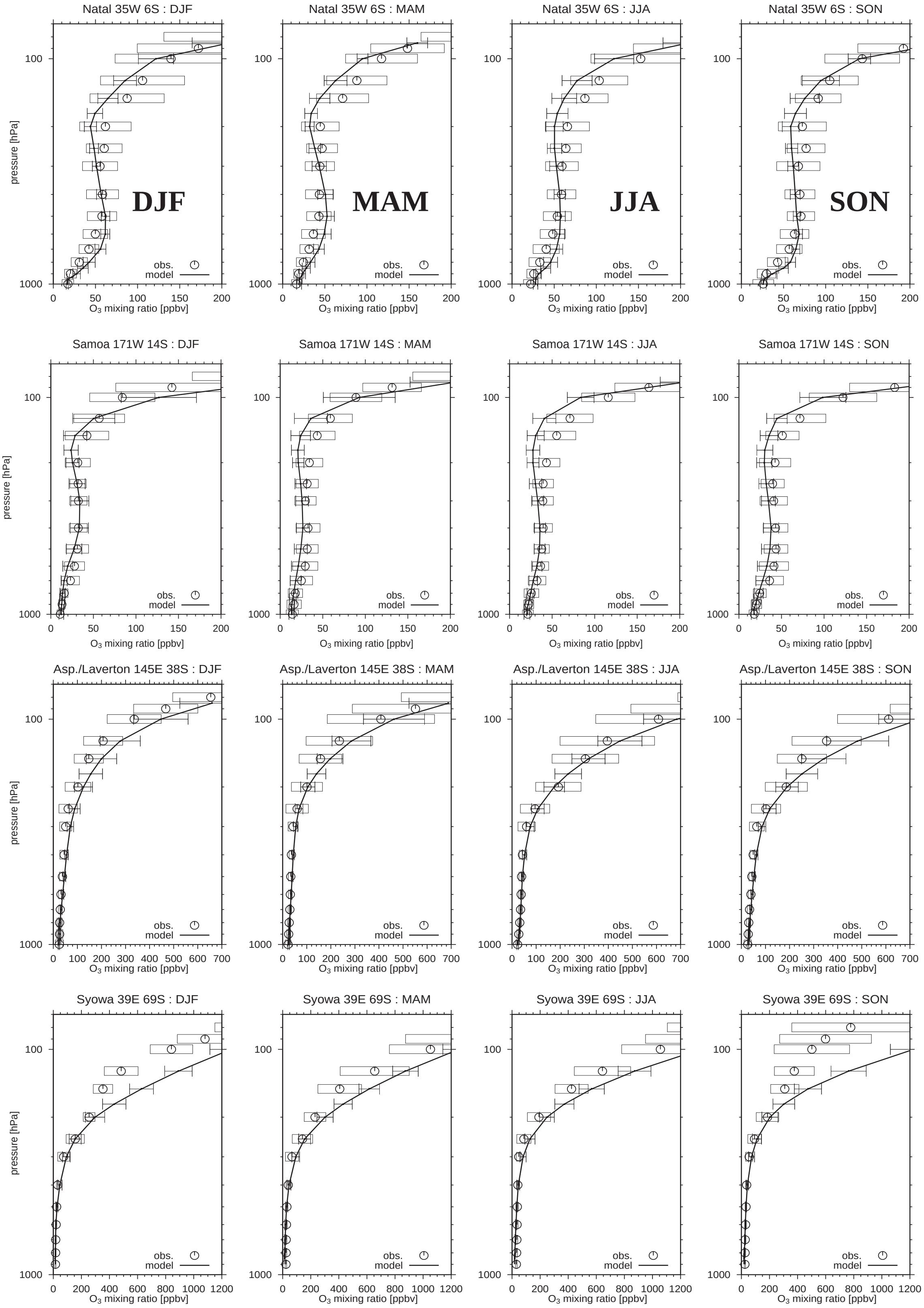

Figure 2.46. (continued).

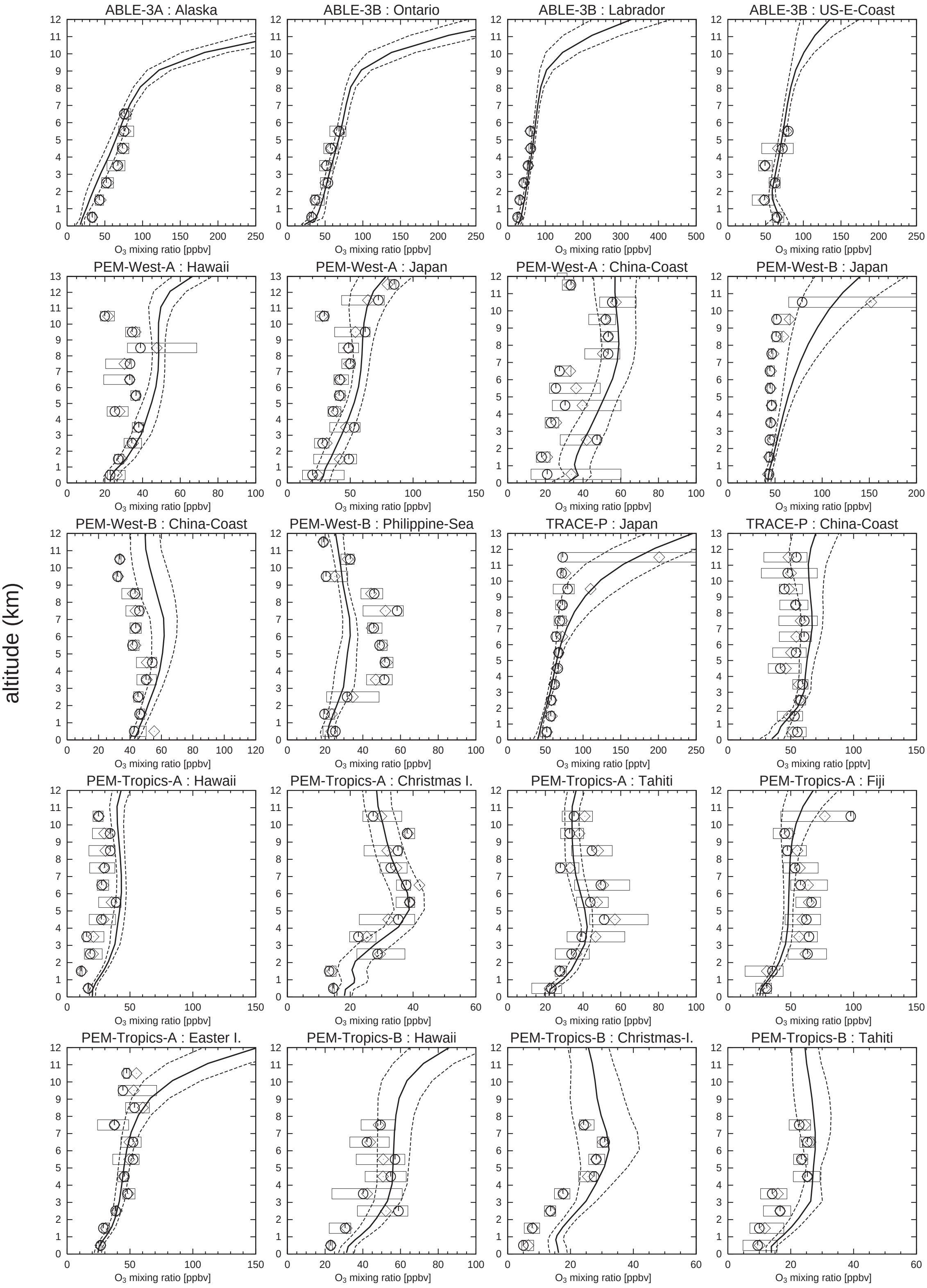

Figure 2.47. O_3 vertical profiles observed and calculated over the regions of GTE campaigns (listed in Table 2.5). Solid lines and dashed lines show temporal mean and $\pm 1\sigma$ of the model calculation, respectively. The observations show mean (diamonds), median (circles), and inner 50% of the data (boxes).

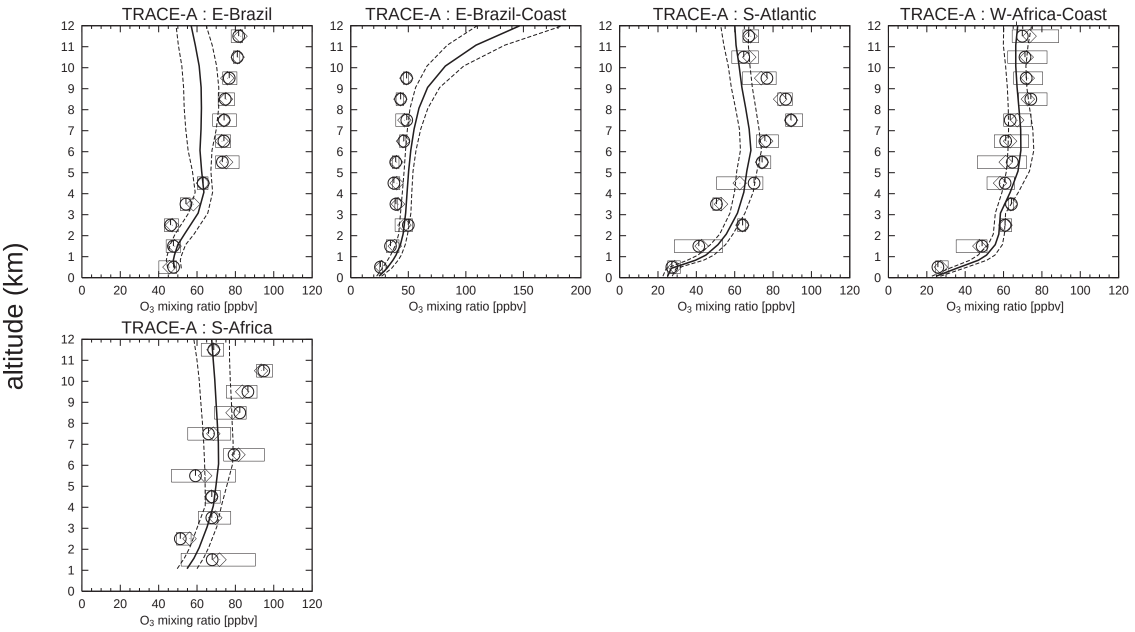

Figure 2.47. (continued).

the rapid decrease in 0-5 km. For TRACE-A, the model reproduces the enhanced O_3 levels in the middle-upper troposphere due to biomass burning in South America and Africa. The model, however, underestimates the O_3 increase above 5 km over the E-Brazil region, probably caused by the underestimation of NO_x in the upper troposphere over this region (Figure 2.24). A rapid decrease in O_3 concentrations near the surface ($\sim$20 ppbv at the surface) is also well simulated by the model for the S-Atlantic region and the W-Africa-Coast region.

Budget

There are two kind of sources for tropospheric ozone. One is the transport of ozone associated with the stratosphere-troposphere exchange (STE), and the other is the in-situ photochemical production in the troposphere due to the reaction of NO with peroxy radicals and the subsequent photolysis of NO_2. Loss of tropospheric ozone is mainly by photochemical destruction due to the reaction of atomic oxygen (singlet) $O(^1D)$ with water vapor ($O(^1D)$ + H_2O) and the subsequent reactions (i.e., O_3 + OH and O_3 + HO_2), and by dry deposition at the surface. Transport of ozone to the stratosphere associated with the STE is also loss of tropospheric ozone.

Figure 2.48 shows the distributions of the 24-hour averaged net chemical production $P(O_y)-L(O_y)$ calculated at the surface and in the upper troposphere (8-13km average) for January and July. O_y is the conventionally defined odd oxygen family and indicates $O_3 + O(^1D) + NO_2 + 2NO_3 + 3N_2O_5 + PAN + MPAN + 2HNO_3 + HNO_4 + ISON + NALD$ in this simulation (ISON=isoprene nitrates, NALD=nitrooxy acetaldehyde, see section 2.2.1). The budget of O_y is

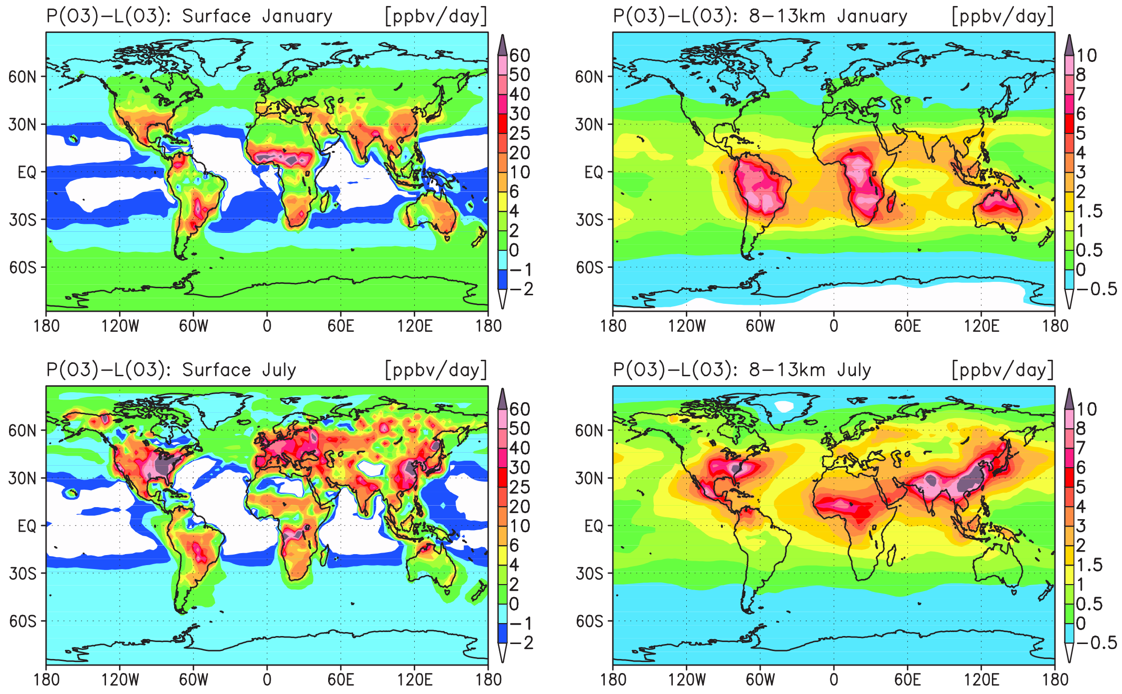

Figure 2.48. Calculated distributions of the net chemical production of ozone (ppbv/day) at the surface (left) and in the upper troposphere (8-13 km) (right) for January and July.

almost identical to that of ozone. The model calculates intensive ozone production in the polluted areas at the surface for both seasons. In January, ozone production rates of 30-50 ppbv/day are calculated over North Africa, associated with biomass burning. The model predicts relatively strong ozone production (6-15 ppbv/day) in the southern United States and eastern Asia, and also calculates positive production (0-2 ppbv/day) in the northern high latitudes (45-60°N) in spite of reduced UV radiation. In July, the net ozone production at the surface is most intense in the eastern United States, Europe, and eastern Asia (30-70 ppbv/day) owing to industrial emissions of ozone precursors. The net ozone production over the ocean is generally negative (ozone destruction). In the upper troposphere, the model calculates positive net ozone production through much of the low-mid latitudes. In January, high ozone production rates (3-8 ppbv/day) are calculated over South America, Africa, and the northern Australia, due to lightning NO_x and convective transport of biogenic emissions of NMHCs. Strong ozone production (∼8 ppbv/day) over North Africa is associated with convective transport of biomass burning emissions. The net ozone production calculated for July also displays the effect of surface emissions, convective transport, and lightning NO_x on the ozone budget in the upper troposphere. Intensive ozone production (8-10 ppbv/day) is calculated over the southern United States and eastern Asia extending over the western Pacific including Japan (2-5 ppbv/day).

Ozone production and loss rates have been calculated for several of the aircraft campaigns, us-

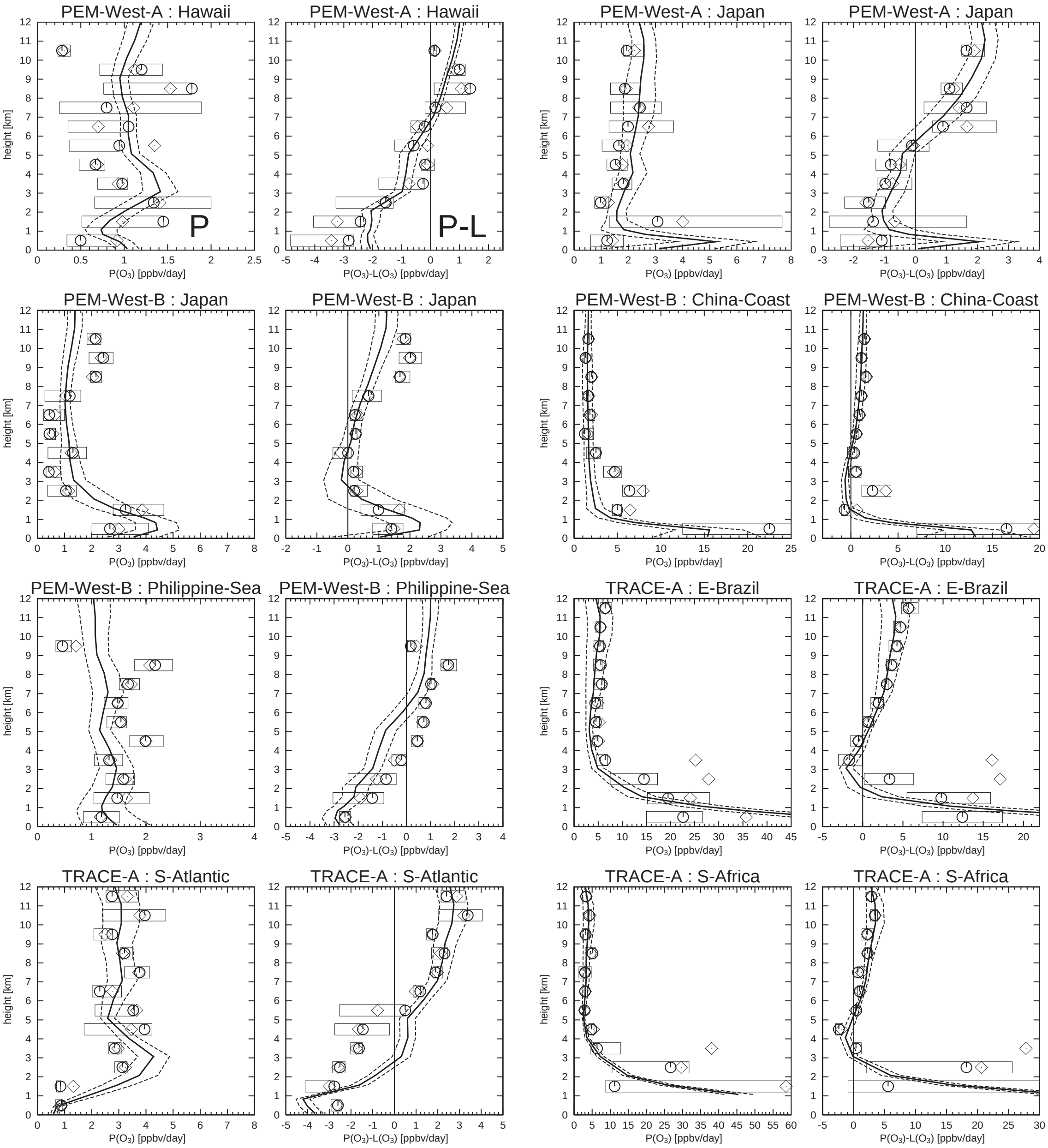

Figure 2.49. Vertical profiles of the ozone production P(O_3) and the net production P(O_3)-L(O_3) derived from observations and calculated by CHASER over the regions of GTE campaigns (listed in Table 2.5). Solid lines and dashed lines show temporal mean and $\pm 1\sigma$ of the model calculation, respectively. The observations show mean (diamonds), median (circles), and inner 50% of the data (boxes).

ing photochemical box (0-dimensional) models constrained by observations [e.g., *Crawford et al.*, 1996, 1997; *Schultz et al.*, 1999]. We compare the calculated ozone production rates with these observation-derived ozone production rates. Figure 2.49 shows the vertical profiles of the ozone chemical production P(O_y) and the net chemical production P(O_y)-L(O_y) derived from the GTE campaign measurements [*Crawford et al.*, 1996, 1997] and calculated by CHASER. The values show the 24-hour averaged ozone production and net production. In Hawaii (PEM-West-A), the calculated P(O_y) ranges from 0.5-1.5 ppbv/day, well within the range of the constrained box model calculation (BMC, hereafter). The calculated net ozone production P(O_y)-L(O_y) is also consistent with the BMC, well reproducing the net ozone production (0-1.5 ppbv/day) above $\sim$7 km. In the Japan region during PEM-West-A (September-October), the model well simulates the ozone production (1.5-3 ppbv/day) in the free troposphere, and also reproduces the decrease in the net production below 7 km (net ozone destruction) reflecting the shorter lifetime of ozone in the lower troposphere. The ozone production near the surface is, however, overestimated by a factor of 5. During the PEM-West-B expedition (February-March), the model calculates vertical profiles consistent with the BMC over the Japan region below 8 km for both P(O_y) and P(O_y)-L(O_y). The model does not capture the high rates of ozone production and net production ($\sim$2 ppbv/day) in the upper troposphere above 8 km. In the China-Coast region, the model well simulates profiles of P(O_y) and P(O_y)-L(O_y), calculating high net ozone production rates ($\sim$2 ppbv/day) in the upper troposphere. Intense ozone production near the surface (15-20 ppbv/day) is also reproduced. In the Philippine-Sea region, the net ozone production appears to be underestimated by 1-2 ppbv/day, though the calculated ozone production P(O_y) is well consistent with the BMC (1-2 ppbv/day). This may indicate the overestimation of water vapor leading to overestimation of ozone loss over this region. Over the source regions of biomass burning (E-Brazil and the S-Africa), the high production rates (3-5 ppbv/day) in the upper troposphere derived by the BMC are also reproduced by CHASER. The profiles of ozone production P(O_y) show almost constant rates (3-5 ppbv/day) in the free troposphere above 3 km with high rates in the boundary layer (15-50 ppbv/day). Both the BMC and CHASER calculations display steep decrease in the net ozone production with altitude in the boundary layer and increase in the free troposphere, with showing slight negative rates above the top of boundary layer (3-5 km). Over the S-Atlantic region, ozone production rates calculated in the upper troposphere ($\sim$2 ppbv/day) are consistent with the BMC. The net ozone production rates in 2-6 km altitudes are, however, overestimated by CHASER by 1-2 ppbv/day, caused partly by the overestimation of ozone production in 2-4 km, and also by the underestimation of water vapor over the South Atlantic (not verified).

In Table 2.9, the global annual budget of tropospheric ozone (O_y) calculated by the model is presented. The model calculates a global ozone chemical production of 4746 TgO_3/yr (62% in the northern hemisphere). The reactions of NO with HO_2 and CH_3O_2 are main production , contributing to the total ozone production for 64% and 22%, respectively. The remainder (14% of the total ozone production) is due to the reactions of NO with peroxy radicals formed by the oxidation of NMHCs. The reaction of HO_2 with CH_3COO_2 also makes a slight contribution to the ozone production in the model. The simulation with the previous version of CHASER [*Sudo et al.*, 2002b] suggested that heterogeneous reactions (uptake) of HO_2 and peroxy radicals (RO_2) formed by oxidation of isoprene and terpenes [e.g., *Walcek et al.*, 1997; *Horowitz et al.*, 1998; *Jacob*, 2000]

Table 2.9. Global Budget of Tropospheric O_y Calculated by CHASER.

	Global	NH	SH
Sources	5277.4		
Net STE [a]	531.4		
Chemical production	4746.0	2925.2	1820.8
HO_2 + NO	3045.6		
CH_3O_2 + NO	1051.4		
$C_2H_5O_2$ + NO	29.7		
$C_3H_7O_2$ + NO	7.1		
$CH_3COCH_2O_2$ + NO	18.0		
$HOC_2H_4O_2$ + NO	31.4		
$HOC_3H_6O_2$ + NO	8.6		
CH_3COO_2 + NO	206.8		
CH_3COO_2 + HO_2	54.4		
ISO_2 [b] + NO	138.4		
$MACRO_2$ [c] + NO	149.1		
Sinks	−5277.4	−3155.5	− 2121.9
Dry deposition	−898.6	−583.3	−315.3
Chemical loss	−4378.8	−2572.2	−1806.6
$O(^1D) + H_2O$	−2497.0		
$O_3 + HO_2$	−1236.4		
O_3 + OH	−558.2		
$CH_4 + O(^1D)$	−1.0		
$C_2H_4 + O_3$	−4.9		
$C_3H_6 + O_3$	−3.7		
$C_5H_8 + O_3$	−38.2		
MACR + O_3	−17.3		
$C_{10}H_{16} + O_3$	−20.5		
Net chemical production	367.2	353.0	14.2
O_y chemical lifetime (days)	25	24	27
Burden (TgO_3)	323	171	152

Budgets (in TgO_3/yr) are calculated for the region below the tropopause height in the model.

[a] Stratosphere-Troposphere Exchange (net O_3 flux from the stratosphere).

[b] Peroxy radicals from isoprene (C_5H_8) + OH

[c] Peroxy radicals from methacrolein (MACR) + OH

Table 2.10. Net Ozone Production in the Boundary Layers and the Free Troposphere[a]

	Global	NH	SH	Tropics[b]
Free troposphere	357.2	216.3	140.9	171.6
Boundary Layer	10.0	137.1	−127.1	−136.6

Values are calculated in TgO_3/yr.

[a] Vertical regions of the boundary layers are defined as the five lowermost layers in the model (surface to approximately 750 hPa).

[b] 15°S to 15°N.

may reduce the O_3 production in polluted areas and hence the global O_3 production. However, this study, including such heterogeneous reactions (section 2.2.1), does not seem to display significant differences in the global ozone budget from the previous CHASER simulation. The ozone chemical production calculated in this simulation, 4746 TgO_3/yr, is on the higher side of the range suggested by many of the previous modeling studies (4550 TgO_3/yr, *Müller and Brasseur* [1995]; 3609 TgO_3/yr, *Lelieveld and van Dorland* [1995]; 3206 TgO_3/yr, *Roelofs and Lelieveld* [1995]; 3415 TgO_3/yr, *Roelofs et al.* [1997]; 4300 TgO_3/yr, *Wang et al.* [1998b]; 3018 TgO_3/yr, *Hauglustaine et al.* [1998]; 4375 TgO_3/yr, *Roelofs and Lelieveld* [2000]). However, much larger ozone production (5258 TgO_3/yr) is estimated by the updated version of the MOZART model [*Horowitz et al.*, 2002]. The global chemical loss of tropospheric ozone is calculated as 4379 TgO_3/yr (59% in the northern hemisphere), contributing for 83% to the total ozone sink (5277 TgO_3/yr). The chemical loss of ozone is mainly by $O(^1D) + H_2O$ (55%), $O_3 + HO_2$ (28%), and $O_3 + OH$ (14%) in the model. The ozone loss by the reactions with NMHCs (as C_2H_4, C_3H_6, isoprene, and terpenes) is important for the ozone budget in the boundary layer over the tropical rain forest (especially in Amazonia and Africa) where biogenic emissions of NMHCs are abundant. Consequently, the calculated net ozone chemical production (difference between the production and the loss) is 367.2 TgO_3/yr (96% in the northern hemisphere). The net ozone production is also highly variable according to individual studies, ranging from 73 TgO_3/yr [*Roelofs and Lelieveld*, 2000] to 550 TgO_3/yr *Müller and Brasseur* [1995]. Although the reason for this variability is unclear, it is attributed partly to the difference in the model domain (i.e., tropopause height) considered for the budget analysis in the models. The net ozone production calculated for the northern hemisphere shows two peaks in late spring (April-May, reaching 500 TgO_3/yr) and late summer (August-September, 400-500 TgO_3/yr). In the southern hemisphere, the calculated net ozone production is positive during the dry season including the biomass burning season (June-October, 100-200 TgO_3/yr). Dry deposition at the surface is also a sink for tropospheric ozone and calculated as 899 TgO_3/yr (65% in the northern hemisphere) by the model, in good agreement with the recent studies (890 TgO_3/yr [*Wang et al.*, 1998b], 898 TgO_3/yr [*Hauglustaine et al.*, 1998], 857 TgO_3/yr [*Horowitz et al.*, 2002]), The net ozone flux associated with the Stratosphere-Troposphere Exchange (STE) is estimated at 531.4 TgO_3/yr in this simulation, contributing for 10% to the total ozone source. This value is in the middle of the range of previous studies (ranging from 391 TgO_3/yr [*Hauglustaine et al.*, 1998] to 846 TgO_3/yr [*Berntsen and Isaksen*, 1997a]) and is relatively close to the simulation of *McLinden et al.* [2000] with their developed Synoz (synthetic ozone) method (475 TgO_3/yr). The tropospheric ozone burden is calculated as 323 TgO_3 (53% in the northern hemisphere). The photochemical lifetime of ozone is estimated at 25 days in the global and annual average. Slightly longer lifetime is found in the southern hemisphere (27 days), reflecting less abundant HO_x concentration in the southern hemisphere (see Section 2.3.3). In both hemispheres, the averaged photochemical lifetime of ozone is about 40 days in winter and about 15 days in summer. The photochemical lifetime of ozone calculated in the tropical boundary layer is generally in the range of 6-15 days, with showing anomalously short lifetimes of 2-3 days over the tropical rain forests like Amazonia associated with the strong ozone destruction by the reactions with NMHCs.

Table 2.10 shows the calculated net ozone production in the free troposphere and the boundary layers in the model. In the global total, ozone production is much more efficient in the free troposphere, indicating 97% contribution to the total net ozone production. In the northern hemisphere, ozone production within the boundary layer also contributes significantly ($\sim$ 40%), reflecting intense industrial emissions in the midlatitudes. On the contrary, ozone destruction (-127 TgO_3/yr) is calculated in the southern hemispheric boundary layer, canceling the ozone production in the free troposphere (141 TgO_3/yr). The calculated net ozone production in the tropics is much similar to that in the southern hemisphere.

2.3.5 SO_2 and sulfate

In this study, SO_2 oxidation to form sulfate is also simulated by CHASER and is used for the heterogeneous reactions in the model. The model calculates the sulfate formation process using the distributions of H_2O_2, O_3, and OH computed on-line in the chemistry component of CHASER. Figure 2.50 shows the annually averaged distributions of SO_2 and sulfate calculated at the surface. The model calculates high SO_2 mixing ratios ($\sim$10 ppbv) around the industrial regions in the northern midlatitudes (United States, Europe, and eastern Asia). Relatively high SO_2 levels ($\sim$1 ppbv) are also visible in South America and Africa, due partly to biomass burning. In accordance with SO_2, sulfate concentrations are high in the United States, Europe, and China, reaching 5-10 μg m^{-3}.

Figure 2.51 and 2.52 compare seasonal variations observed and calculated at European sites (the EMEP network) for SO_2 and sulfate, respectively. The model generally appears to reproduce the observed SO_2 levels well for most cases. Both the observation and calculation show winter maxima with minima in summer, reflecting the OH seasonality. The model calculation, however, tends to overestimate SO_2 levels in summer by 50-100%. It should be noted here that this study does not account for seasonal variation of residential SO_2 emissions as from stoves, using constant emissions through a year. Inclusion of such seasonal variation of SO_2 emission would reduce surface SO_2 levels in summer. In the case of sulfate, the model generally captures the observed levels, but appears to overestimate the observation in some cases, calculating summer maxima inconsistent with the observation. This model defect may be related to the SO_2 overestimation in summer coming from lack of seasonal variation of residential SO_2 emissions in the model as described above. Additionally, it is also possible that the liquid-phase reactions with H_2O_2 and O_3 are underestimated due in the model to low pH values (i.e., high $[H^+]$ levels) in cloud drops around Europe. Since dissolution of SO_2 into cloud drops and subsequent liquid-phase oxidation by aqueous-phase O_3 are much controlled by the pH values in cloud drops, it is necessary to evaluate further the simulated pH in clouds. Figure 2.53 shows a comparison between the observed and

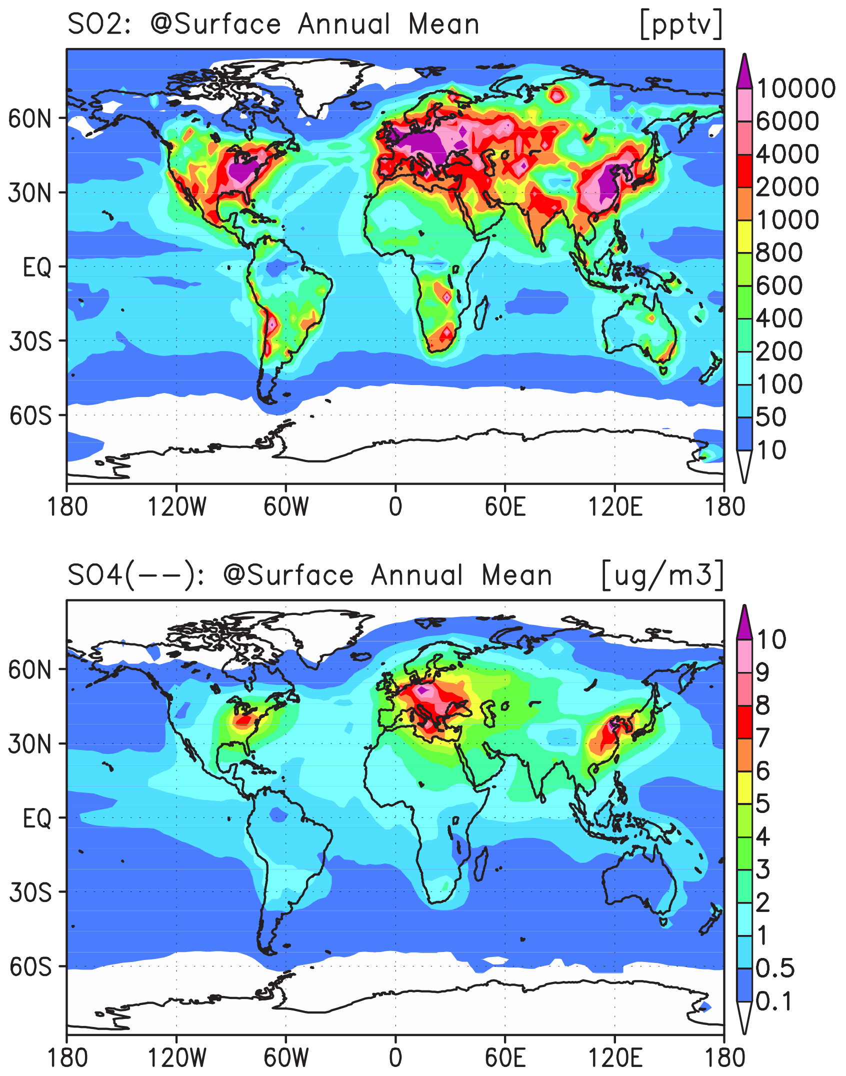

Figure 2.50. SO_2 and sulfate (SO_4^{2-}) distributions calculated at the surface (in annual means).

calculated sulfate mixing ratios for several remote sites. The calculations are well consistent with the observations, reproducing summer sulfate maxima associated with the seasonal variation of SO_2 oxidation with OH and DMS emissions in the remote ocean. However, the model overestimates sulfate levels at Cape Grim (42°S,145°E) by a factor of 2-3 through the year. Since Cape Grim is generally downwind of cities in eastern Australia, this may suggest that the model overestimates SO_2 oxidation and/or underestimates sulfate deposition around the area.

The calculated SO_2 and sulfate vertical distributions are also compared to the NASA GTE observations. Figure 2.54 shows a comparison with the TRACE-P expedition (March-April) as an example. In this Figure, the modeled profiles appear to be consistent with the observation, well simulating the observed increases near the surface due to considerable SO_2 emissions in China.

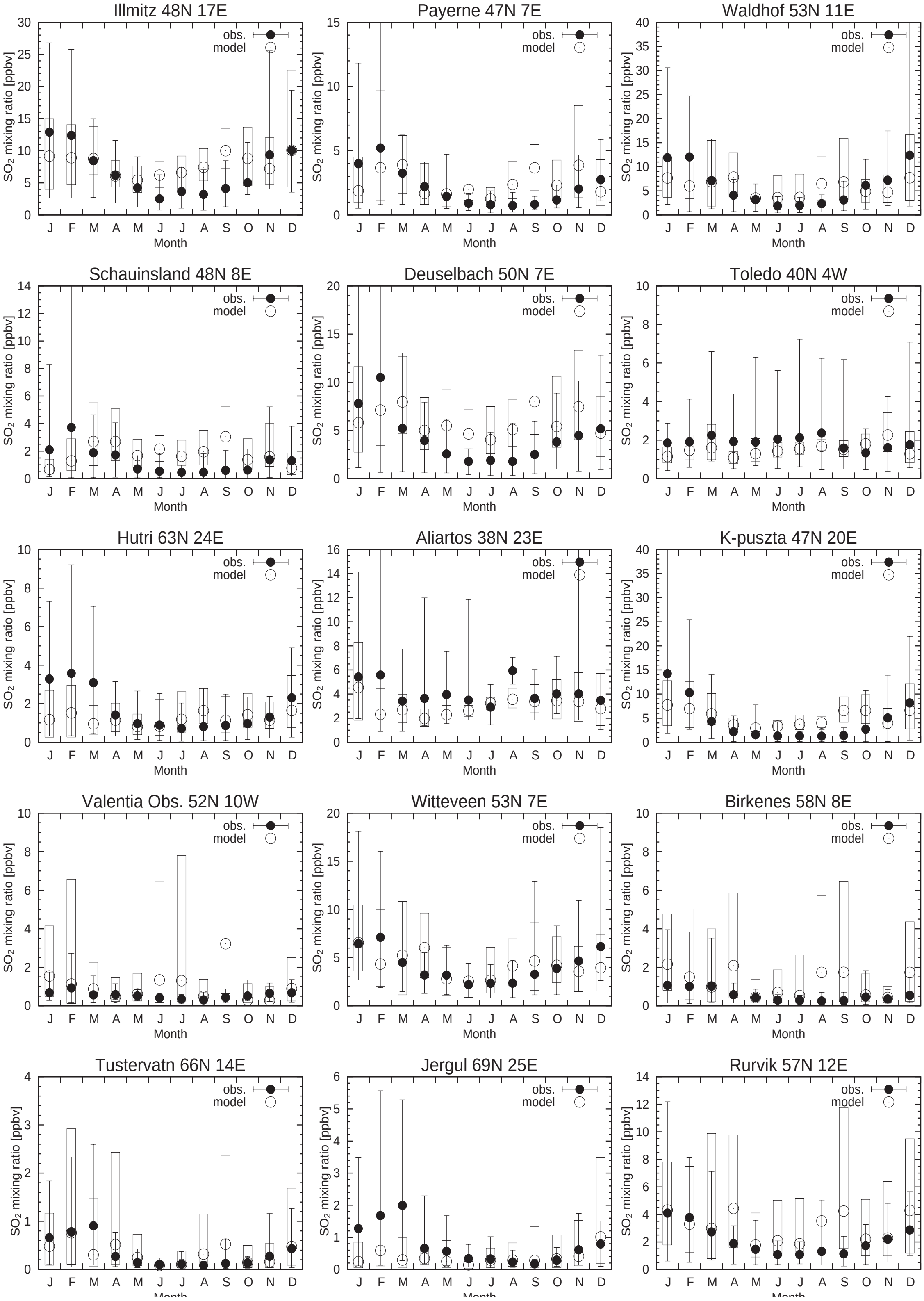

Figure 2.51. SO_2 seasonal variations observed (solid circles) and calculated (open circles) at the surface. Boxes indicate the standard deviations of day-to-day calculations. The ranges of annual variation of the observation (during 1978-1995) are also shown with error bars. The observations are taken from the EMEP network.

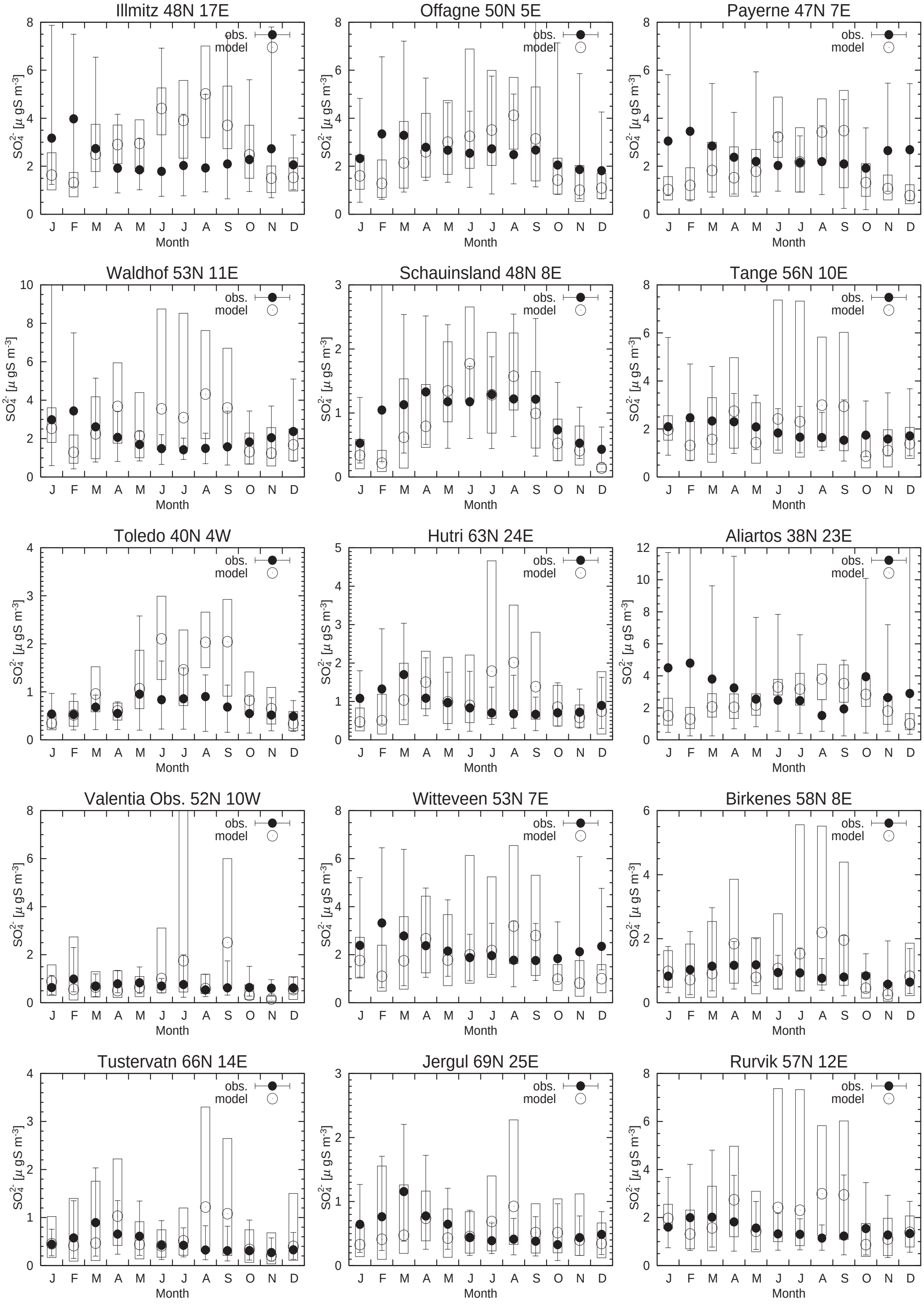

Figure 2.52. Same as Figure 2.51 but for sulfate (SO_4^{2-}).

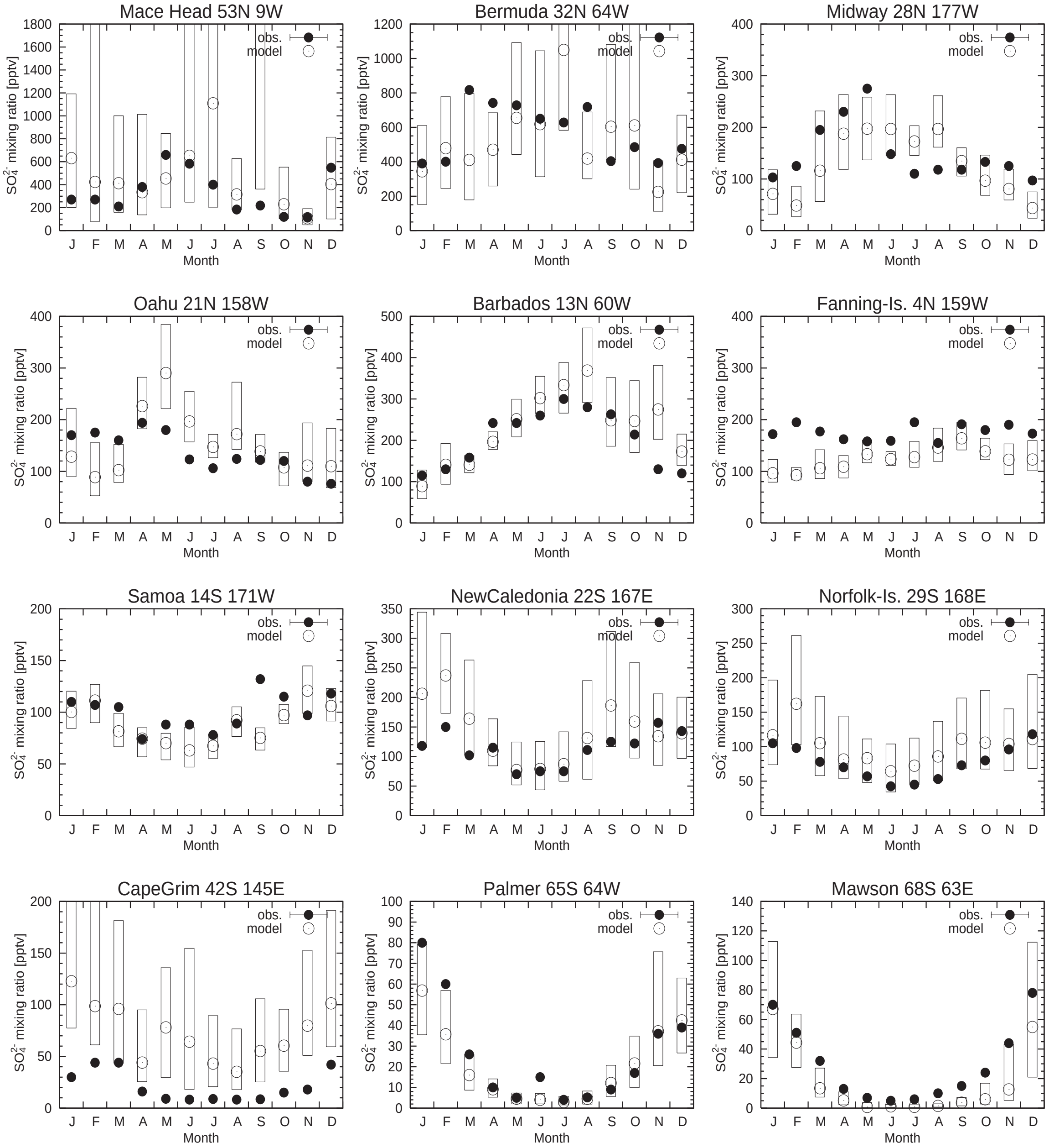

Figure 2.53. Sulfate (SO_4^{2-}) mixing ratios (pptv) observed (solid circles) and calculated (open circles) at several remote locations. Boxes indicate the range of day-to-day calculations.

The model, however, tends to overestimate the upper tropospheric SO_2, possibly implying an underestimation of liquid water content in the upper troposphere over those regions. The same kind of SO_2 overestimation by the model is found in the tropical upper troposphere during PEM-Tropics-B (not shown). The underestimation of sulfate in the free troposphere in the Japan region may suggest inconsistent wet deposition of sulfate (see section 2.2.3 for detailed description of the adopted

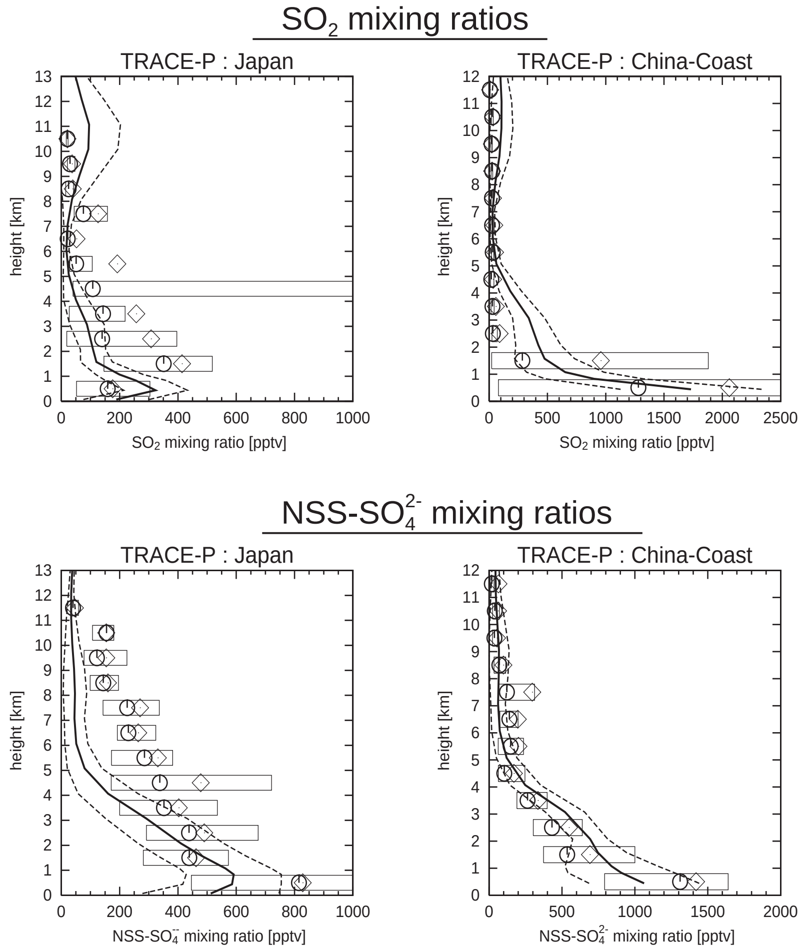

Figure 2.54. SO_2 and SO_4 (sulfate) vertical profiles observed and calculated over the regions of GTE campaigns (listed in Table 2.5). Solid lines and dashed lines show temporal mean and $\pm 1\sigma$ of the model calculation, respectively. The observations show mean (diamonds), median (circles), and inner 50% of the data (boxes).

Table 2.11. Global Budget of Sulfate Aerosol Calculated by CHASER[a]

	Global	NH	SH
Source(chemical prod.)	50.34	40.26	10.08
SO_2 + OH (gas-phase)	14.24	11.94	2.30
S(IV) + O_3 (liq.-phase)	10.80	8.82	1.98
S(IV) + H_2O_2 (liq.-phase)	25.30	19.50	5.80
Sink	−50.52	−40.54	−9.98
Dry deposition	−4.40	−3.53	−0.87
Wet deposition	−46.12	−37.01	−9.11
Burden(TgS)	0.56	0.43	0.13

[a] Budgets are calculated in TgS/yr

deposition scheme and evaluation of sulfate wet deposition flux around Europe).

The global budget of sulfate in this simulation is presented in Table 2.11. About 70% of the total sulfate formation occurs in liquid phase. As the reactions with aqueous-phase O_3 decline with the pH values in cloud drops, the model calculates higher contribution by the reaction with aqueous-phase H_2O_2 (70% of the liquid-phase formation). The model calculates sulfate formation predominantly in the northern hemisphere ($\sim$80%) as a result of intense SO_2 emissions from industry in the northern midlatitudes. The calculated global sulfate formation is balanced mainly with wet deposition (90%), and with dry deposition (10%). Reflecting predominant abundance of sulfate in the northern hemisphere (77% of 0.56 TgS), 80% of the total sulfate wet deposition is calculated in the northern hemisphere, leading to acid rain as illustrated in Figure 2.9. The sulfate budget calculated here are generally consistent with the simulation with the CCSR/NIES aerosol model [*Takemura et al.*, 2000]. This study, however, calculates a larger sulfate formation from the liquid-phase reactions with O_3 and H_2O_2, with a larger (by 10-20%) sulfate burden relative to the simulation of *Takemura et al.* [2000]. This appears to come from the difference in the schemes for liquid-phase oxidation of SO_2 between this work and *Takemura et al.* [2000]. The study of *Takemura et al.* [2000] simulates SO_2 liquid-phase oxidation using the monthly averaged H_2O_2 and O_3 distributions calculated by the previous version of CHASER, whereas this study uses H_2O_2 and O_3 distributions computed on-line in the model.

2.4 Conclusions

This chapter has described and evaluated a global chemical model of the troposphere, named CHASER (CHemical AGCM for Study of atmospheric Environment and Radiative forcing). The CHASER model, developed in the framework of Center for Climate System Research/National Institute for Environment Studies (CCSR/NIES) atmospheric general circulation model (AGCM) [*Numaguti*, 1993; *Numaguti et al.*, 1995], is aimed to study the tropospheric photochemistry and its influences on climate. CHASER is basically driven on-line by climatological meteorology generated by the AGCM to account for interactions between meteorological fields and tropospheric chemistry. The model includes a detailed simulation of tropospheric O_3-HO_x-NO_x-CH_4-CO, NMHCs, and sulfur chemistry calculating the concentrations of 54 chemical species with 139 reactions (gas/liquid phase and heterogeneous) in this study. The sulfate (SO_4^{2-}) formation process is simulated in this study using concentrations of H_2O_2, O_3, and OH computed on-line in the model. Detailed schemes for the dry/wet deposition and emission processes are also implemented in the model. The wet deposition scheme in the previous version of CHASER [*Sudo et al.*, 2002a] has been improved to simulate the deposition process on ice cloud (cirrus) particles and reversible below-cloud scavenging process in this study (section 2.2.3). With the improved wet deposition scheme, the model is capable to simulate the liquid/ice-phase concentrations of individual species dissolved in precipitation. Also, the heterogeneous reactions of N_2O_5 and peroxyradicals (RO_2) (from unsaturated hydrocarbons), not considered in the previous CHASER version [*Sudo et al.*, 2002a], are newly included in this study. The model considers emission sources for NO_x (44.3 TgN/yr including lightning NO_x of 5 TgN/yr), CO (1267 TgCO/yr), and NMHCs (including isoprene, 400 TgC/yr and terpenes, 102 TgC/yr). In CHASER, NO_x emissions from lightning are parameterized in the CCSR/AGCM convection, based on *Price and Rind* [1992] and *Price et al.* [1997]. SO_2 and DMS emissions (79.4 and 15 TgS/yr, respectively) are also included for the sulfate simulation in the model. Seasonal variation of biomass burning emissions is simulated using the satellite derived hot-spot data (from ATSR and AVHRR). The sulfate simulation is reflected on-line on the heterogeneous reaction process in the model, but is not coupled with the AGCM radiation component for now. For this study, the T42 horizontal resolution ($\sim$2.8°×2.8°) is chosen with 32 vertical layers from the surface to about 40 km altitude. The basic time step for the dynamical and physical processes in the model is 20 min. The chemistry component (chemical reaction) is evaluated with a constant time step of 10 min in this study.

In the detailed evaluation of the model results (section 2.3), the CHASER calculations show excellent agreement with observations in most cases for important trace gases such as CO, NMHCs, NO_y species, HO_x and related species (formaldehyde, acetone, and peroxides) as well as for ozone. The model computes a CO source of 1514 TgCO/yr from oxidation of methane and NMHCs, larger than the surface emissions (1267 TgCO/yr) considered in this study. The calculated chemical production of CO is most significant in the tropical rainforests, resulting from the NMHCs oxidation process. The model tends to overestimate CO and C_2H_6 in the central Pacific, suggesting too large transport from the United States and the biomass burning regions in South America. The CO and NMHCs distributions observed in the biomass burning related regions (South America, Atlantic, and Africa, during TRACE-A of the NASA GTE) are well reproduced by the model, but appear to be underestimated in the upper troposphere over South America (Brazil) compared also to the previous version of CHASER [*Sudo et al.*, 2002b]. This is attributed probably to the differences in the meteorological fields (particularly convection) generated by the AGCM between this work and the previous [*Sudo et al.*, 2002b]. In the evaluation of the modeled nitrogen species (NO_y), the model appears to simulate well NO_x, HNO_3, and PAN distributions as observed. Simulation of HNO_3 is improved relative to the previous version [*Sudo et al.*, 2002b] with the new wet deposition scheme in this study. The model generally well reproduces the observed PAN distributions, but tends to overestimate middle-upper tropospheric PAN abundances in remote regions as the central Pacific. Though the model in this study includes heterogeneous reactions of unsaturated peroxy radicals (RO_2) which are suggested for a possible cause of PAN overestimation by *Sudo et al.* [2002b], those heterogeneous reactions do not seem to reduce such PAN overestimation in this study. Further investigation, however appears to be needed to check the sensitivity to such heterogeneous RO_2 reactions. In addition, the simplified reaction scheme for NMHCs oxidation adopted in the model must be also evaluated. In this study, the simulated HO_x species ($= OH + HO_2$) are also evaluated in detail. The model appears to calculate OH and HO_2 distributions much close to the observations during the PEM-Tropics-B and TRACE-P expeditions. The global methane lifetime against the tropospheric OH reaction, an useful measure for OH abundance in the troposphere, is estimated at 9.4 years in this study (the IPCC estimate is 9.6 years). The simulated distributions of important HO_x related species such as formaldehyde, acetone, and peroxides (H_2O_2 and CH_3OOH) are quite consistent with observations. Since peroxides are strongly coupled with HO_x, the agreement between the calculated and the observed peroxides in this study appears to mean successful simulation of HO_x. The ozone distributions simulated in this study are generally in excellent agreement with a number of observations, well capturing the seasonal variation of ozone in both polluted and remote locations. The observed ozone enhancements associated with biomass burning are well simulated by the model. The model, however, tends to overestimate upper tropospheric ozone in the midlatitudes in both hemisphere, which implies overestimation of stratospheric influx of ozone in the midlatitudes. This study also compares the simulated ozone production rates with those derived from observations (Figure 2.49). The model well simulates ozone production as derived from observations, capturing the contrast between the free troposphere and the boundary layer. The calculated global budget of tropospheric ozone shows a chemical production of 4746 TgO_3/yr (with a net production of 367 TgO_3/yr), well within the range suggested by the previous works (3206 TgO_3/yr, *Roelofs and Lelieveld* [1995] to 5258 TgO_3/yr, *Horowitz et al.* [2002]). The simulation shows much more efficient ozone production in the free troposphere, calculating a global net ozone production of 357 TgO_3/yr in the free troposphere with 10 TgO_3/yr in the boundary layer. The estimated net stratospheric O_3 influx is 531.4 TgO_3/yr, consistent with the previous studies (300-800 TgO_3/yr). However, this estimated value (531.4 TgO_3/yr) may be overestimated, since the model in this study tends to overestimate upper tropospheric O_3 in the midlatitudes as described above. Further development of transport scheme is necessary to improve the representation of cross-tropopause transport of ozone in CHASER. In the evaluation of the sulfate simulation by CHASER, the model appears to simulate SO_2 and sulfate distributions generally well, but tends to overestimate surface SO_2 and sulfate levels observed in European sites especially during summer, probably indicating the need of considering seasonal variation of residential SO_2 emissions in the model. The calculated global sulfate burden is 0.56 TgS in this simulation, $\sim$10% larger than the simulation of *Takemura et al.* [2000]. This study also calculates the contribution by sulfate wet deposition to precipitation pH together with nitrates wet deposition (Figure 2.9, page 30). The simulated sulfate and nitrates wet deposition fluxes in Europe show good agreements with the observation from the EMEP network (Figure 2.10 to 2.13). In this study, the model consider oceanic DMS emission in a much simple way ignoring the distributions of planktonic bacteria. DMS oxidation mechanism is also simplified in this study. Future version of CHASER will include detailed reaction mechanism of DMS [e.g., *Lucus and Prinn*, 2002] for a better simulation of sulfate.

As a consequence, this study suggests that the present version of CHASER, newly developed in this study, is well capable to simulate tropospheric chemistry involving ozone with detailed schemes for chemical and physical processes. Future model development will be focused on improvement of the transport scheme in the model. Also, more detailed aqueous-phase chemistry will be included in future versions of CHASER.

Appendix 2A: Evaluation of transport and deposition processes

Evaluation: Transport process

Transport is one of the most important processes to simulate the atmospheric photochemistry. Emitted or chemically produced species undergo advection by large-scale wind field and subgrid vertical transport by diffusion and moist convection. In CHASER, advective transport is simulated by a 4th order flux-form advection scheme of the monotonic van Leer [*van Leer*, 1977], except for the vicinity of the poles (the flux-form semi-Lagrangian scheme of *Lin and Rood* [1996] is used for a simulation of advection around the poles), with vertical transport associated with moist convection (updrafts and downdrafts) simulated by the cumulus convection scheme in the CCSR/NIES AGCM.

It is necessary to validate the model capability for simulations of transport. For this purpose, we have conducted a simple simulation of the distribution of atmospheric radon (^{222}Rn). Radon is emitted from the earth's surface (mainly from land surface) and decays radioactively with a lifetime of 5.5 days. Surface emission of radon considered here is generally based on *Jacob et al.* [1997]. In *Jacob et al.* [1997], radon emission from land surface is set 1.0 atoms cm^{-2} s^{-1} uniformally. Some simulation studies based on this radon emission scenario, however, show an underestimation of the simulated radon concentrations at Mauna Loa by a factor of 2-3 compared to observations, with showing relatively good agreement of simulations with observations at other sites [*Jacob et al.*, 1997; *Brasseur et al.*, 1998]. Although there is a possibility that an insufficient transport in the simulations causes this discrepancy on one side, it can be attributed to a higher emission rate of radon in eastern Asia as suggested by *Mahowald et al.* [1997]. To take this into account, emission rate in eastern Asia (10°S-55°N, 100°E-160°E) is tentatively increased by a factor of 2 in this simulation.

Figure 2A.1 shows the simulated radon distributions for June-July-August (JJA). As can be seen in zonal mean distribution (upper panel), radon is vertically transported from the surface up to the tropopause height associated with convective activities in the northern hemisphere. Horizontal distribution of radon in the upper troposphere can be seen in the lower panel of Figure 2A.1. Outstanding high concentrations over eastern Asia are due to the doubled emission rate in this region. Transport of radon from northern America and Africa to over the Atlantic is seen. Moreover, long range transport of radon from eastern Asia appears to reach the eastern Pacific region including western America. Figure 2A.2 compares the simulated and the observed radon vertical profiles in western America (California) for June and JJA conditions. The model appears to reproduce the observed radon vertical distribution in the middle-upper troposphere well. The radon maximum

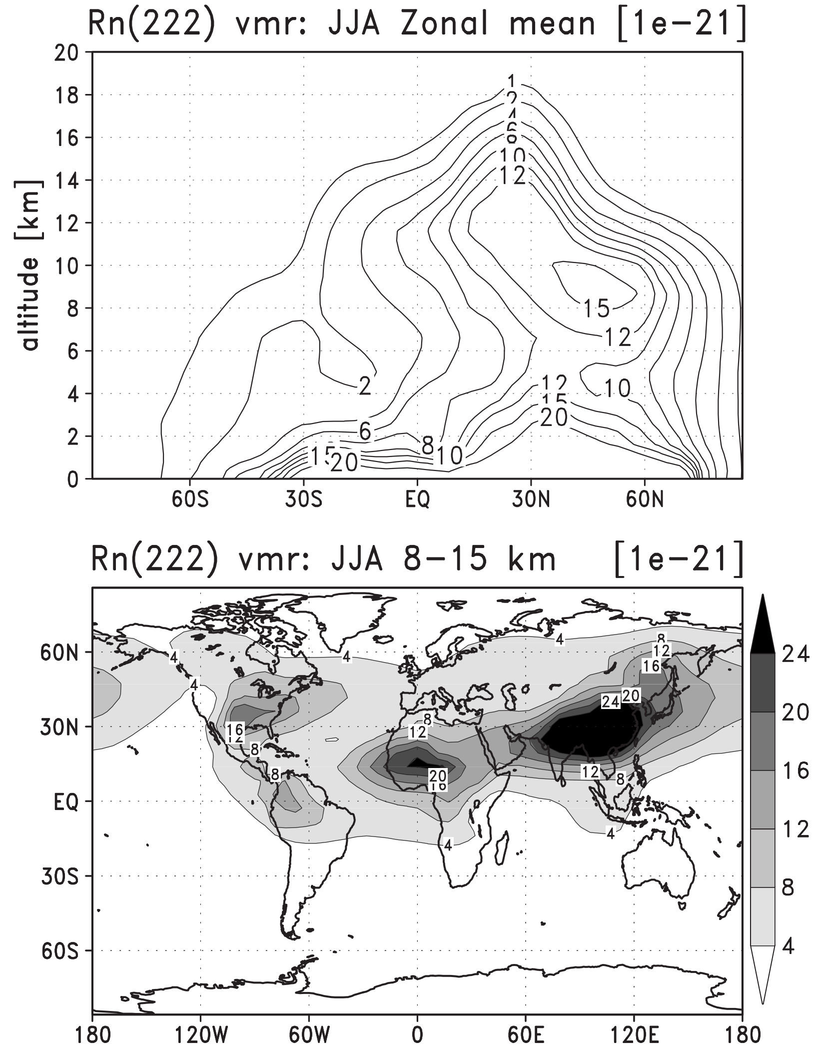

Figure 2A.1. Calculated distributions (volume mixing ratio) of radon for June-July-August. The distribution in the upper panel is zonally averaged, and averaged over 8-15 km altitude for the lower panel

seen at 8-10 km altitude is much associated with long range transport from eastern Asia, according to *Stockwell et al.* [1998]. This feature is clearly seen in Figure 2A.3 showing the cross sectional distribution of calculated radon over 36°N for June. It can be seen that the radon distribution in the middle-upper troposphere is largely affected by transport from eastern Asia through much of the eastern Pacific and western America. In Figure 2A.2, radon concentration is slightly underestimated by the model in 1-3 km altitudes, whereas it is overestimated at the surface. This may indicate an insufficient mixing between the planetary boundary layer and the lower troposphere. Figure 2A.4 shows a comparison of calculated and observed seasonal variations of surface radon at several sites. The model appears to reproduce observed radon seasonal cycle well. Both the concentration and the time variability of calculated surface radon are generally high in winter time when vertical transport of emitted radon is not efficient due to low convective activity. The seasonal

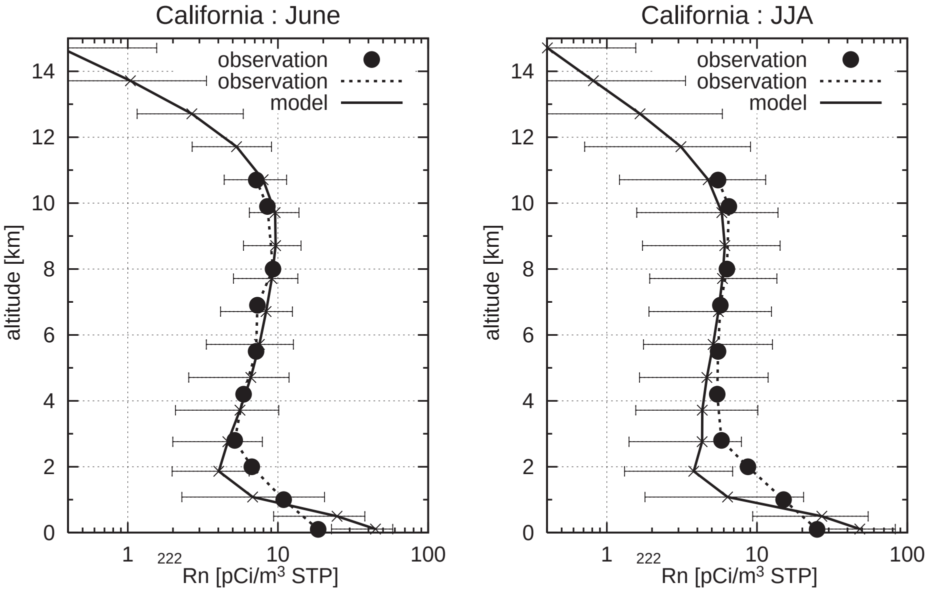

Figure 2A.2. Calculated (solid lines) and observed (solid circles and dashed lines) radon vertical profiles in California (37.4°N, 122°W). The values are June average (left panel) and June-July-August average (right panel). Error bars with calculated profiles show the range. Observation is from *Kritz et al.* [1998].

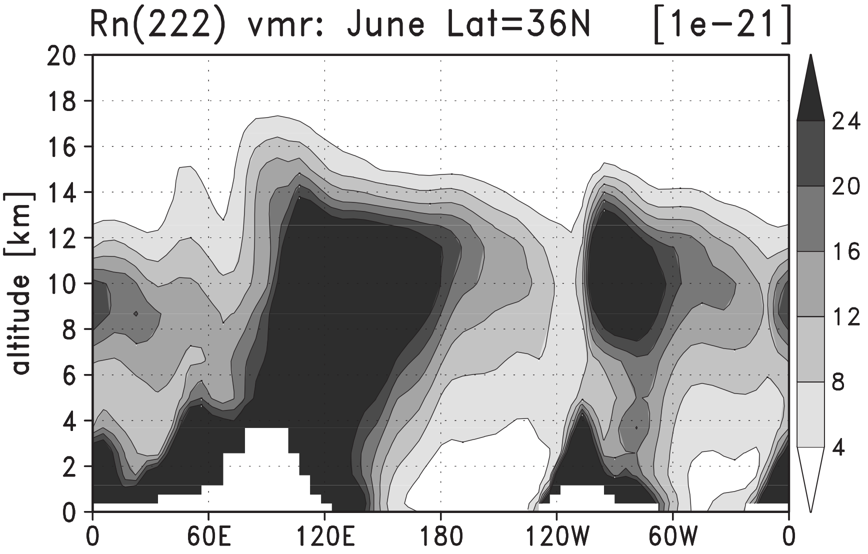

Figure 2A.3. Calculated distribution (volume mixing ratio) of radon in June for 36°N.

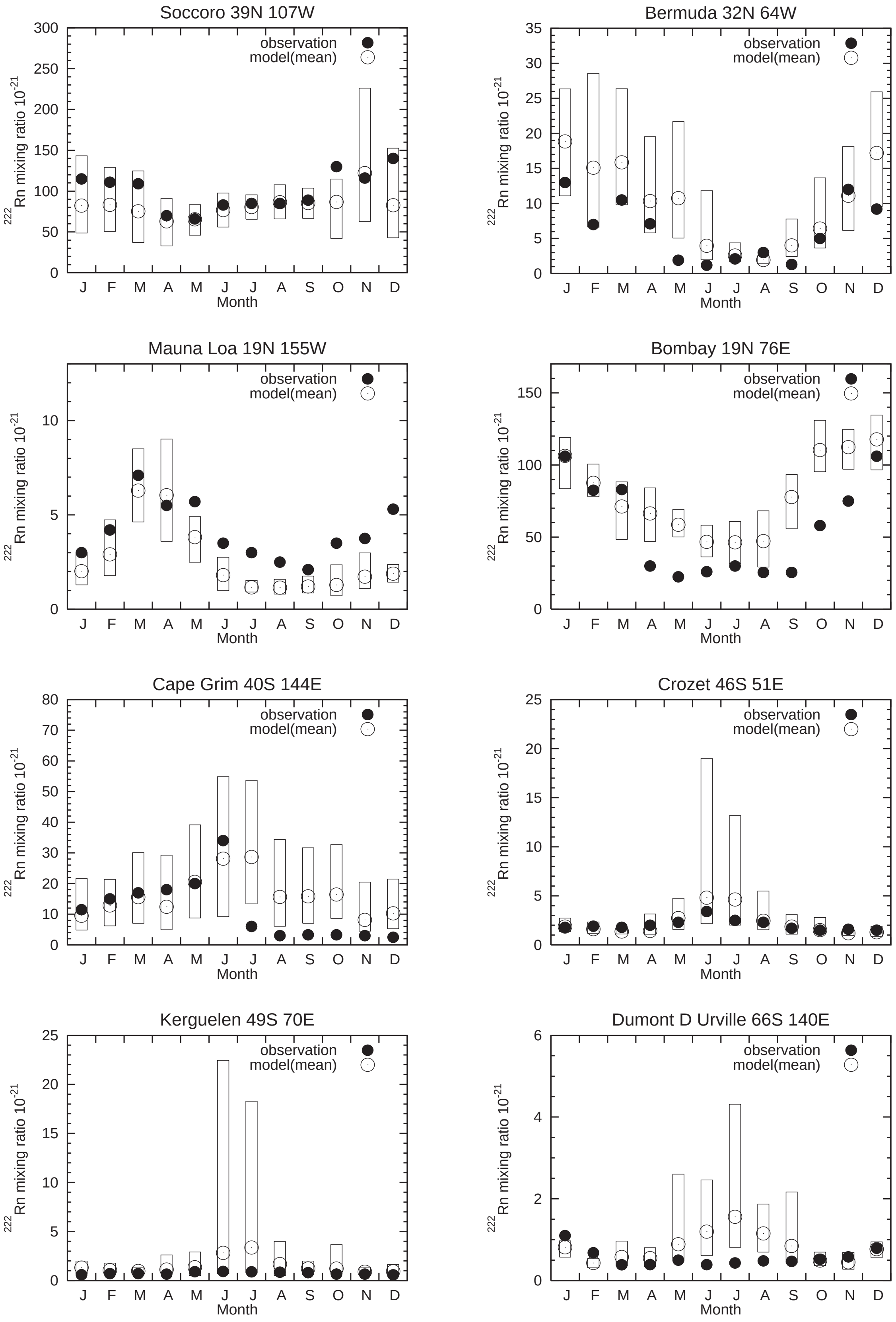

Figure 2A.4. Calculated (open circles) and observed (solid circles) surface radon (^{222}Rn) seasonal variations. Boxes show the range of calculated values.

cycle of spring-maximum at Mauna Loa is also well reproduced with the doubled radon emission in eastern Asia.

Evaluation: Deposition process

For an evaluation of the wet deposition scheme as described in section 2.2.3, we have conducted a simulation using atmospheric lead (^{210}Pb) as a tracer. This simulation has been performed as an extension of the simulation of ^{222}Rn described right above, since ^{210}Pb is produced by radioactive decay of ^{222}Rn. ^{210}Pb produced from ^{222}Rn, believed to stick to aerosol surfaces rapidly, was assumed to efficiently removed by wet deposition with the same scavenging lifetime for HNO_3 as in many other simulations [*Balkanski et al.*, 1993; *Lee and Feichter*, 1995; *Rehfeld and Heimann*, 1995; *Brasseur et al.*, 1998]. Note that the reemission process below clouds as described in section 2.2.3 is not considered in this ^{210}Pb simulation. The dry deposition velocity of ^{210}Pb at the surface is taken to be 0.2 cm s^{-1} over land surface and 0.05 cm s^{-1} over sea surface, following *Balkanski et al.* [1993].

Figure 2A.5 shows a comparison of the mixing ratios of ^{210}Pb calculated and observed at the surface. The seasonal variations of ^{210}Pb are well reproduced by the model for all sites. For Mauna Loa, calculated values are in good agreement with the observation because of our augmentation of radon emission in eastern Asia (see above). Although Figure 2A.5 indicates that the model successfully simulates the wet deposition process, it should be noted that there may be uncertainties in the surface emission of radon adopted here and precipitation simulated by the AGCM.

Appendix 2B: Aqueous-phase reactions in the model

In this study, the model includes liquid-phase oxidation of SO_2 in cloud drops, considering the tendency for S(IV), the sum of $SO_2(aq)$, HSO_3^-, and SO_3^{2-} in liquid-phase (Table 2B.1). The hydrogen ion concentration $[H^+]$ in cloud drops, needed for the A1 and A2 reactions, is given as:

$$[H^+] = f_n \times ([NO_3^-] + [SO_4^{2-}] + [HSO_3^-] + [SO_3^{2-}]) \qquad (2B.1)$$

using the neutralizing factor f_n to consider neutralization by cations, and the liquid-phase concentrations (eq l^{-1}) of NO_3^-, SO_4^{2-}, HSO_3^-, and SO_3^{2-}. In this study, f_n has been taken to be 0.1-0.2 to simulate $[H^+]$ close to observations. The gas/liquid partitioning for "SO_2(g) $\leftrightarrow$ S(IV)", "O_3(g) $\leftrightarrow$ O_3(aq)", and "H_2O_2(g) $\leftrightarrow$ H_2O_2(aq)" is determined from the effective Henry's law constants H for SO_2, O_3, and H_2O_2. In the case of SO_2(g) $\leftrightarrow$ S(IV), H is calculated depending on $[H^+]$ as:

$$H(SO_2) = 1.2 \exp\left[3200\left(\frac{1}{T} - \frac{1}{298.15}\right)\right] \cdot \left(1 + \frac{K_1}{[H^+]} + \frac{K_1 K_2}{[H^+]^2}\right) \qquad (2B.2)$$

with the K_1 and K_2 the equilibrium constants for SO_2(aq) $\leftrightarrow$ HSO_3^- and HSO_3^- $\leftrightarrow$ SO_3^{2-} listed in Table 2B.1. This shows that dissolution of SO_2 in liquid-phase is highly limited by the $[H^+]$ level (i.e., pH), decreasing as pH in cloud drops becomes lower.

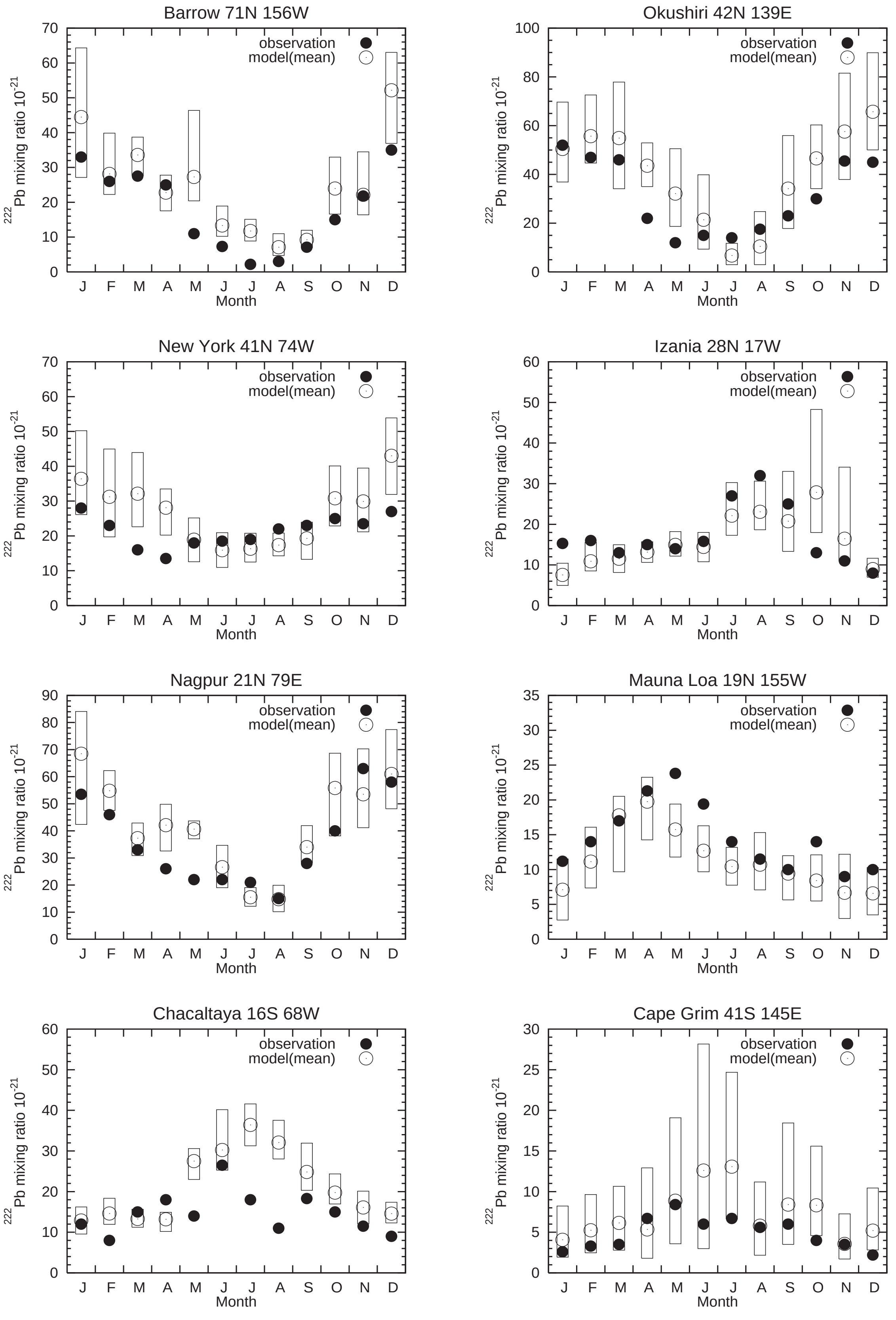

Figure 2A.5. Seasonal variations of calculated (solid circles) and observed (solid circles) surface lead (^{210}Pb). Boxes show the range of calculated values.

Table 2B.1. Aqueous-phase Oxidation of S(IV).

No.	Reaction	Rate[a]
A1	$S(IV) + O_3(aq) \rightarrow SO_4^{2-}$	$k_{A1} = \dfrac{k_1 + \frac{k_2K_1}{[H^+]} + \frac{k_3K_1K_2}{[H^+]^2}}{1 + \frac{K_1}{[H^+]} + \frac{K_1K_2}{[H^+]^2}}$, $k_1 = 2.4E+4$, $k_2 = 3.7E+5 \exp(-5500(1/T-1/298.15))$, $k_3 = 1.5E+9 \exp(-5300(1/T-1/298.15))$, $K_1{}^b = 1.7E-2 \exp(-2090(1/T-1/298.15))$, $K_2{}^c = 6.0E-8 \exp(-1120(1/T-1/298.15))$
A2	$S(IV) + H_2O_2(aq) \rightarrow SO_4^{2-}$	$k_{A2} = \dfrac{k_4[H^+]}{(0.1 + [H^+])\left(1 + \frac{[H^+]}{K_1} + \frac{K_2}{[H^+]}\right)}$ $k_4 = 5.2E+6 \exp(-2750(1/T-1/298.15))$

References: *Hoffmann and Calvert* [1985].

[a] K_{A1} and K_{A2} are in l mol^{-1} s^{-1}.

[b] Equilibrium constant for $SO_2(aq) \leftrightarrow HSO_3^-$

[c] Equilibrium constant for $HSO_3^- \leftrightarrow SO_3^{2-}$

To consider time integration of aqueous-phase reactions as listed in Table 2B.1, the model evaluates tendencies of bulk-phase (gas+liquid) concentrations in clouds. The tendency of a bulk-phase concentration C_i due to aqueous-phase reactions is given by:

$$\frac{dC_i}{dt} = P_i - \beta_i C_i = P_i^l L - \beta_i^l \frac{H_i RT \cdot L}{1 + H_i RT \cdot L} C_i \qquad (2B.3)$$

with L the liquid water content, P^l the production rate in aqueous-phase (per unit volume of water), and β^l the loss rate for aqueous-phase concentrations due to aqueous-phase reactions. This tendency applies for SO_2, O_3, H_2O_2, and SO_4^{2-} with respect to the A1 and A2 reactions in this study. The tendency equations for those species are iteratively solved employing an implicit scheme (EBI scheme) with a time step of 10 min as with gas-phase reactions in the model.

Chapter 3

Radiative Forcing from Tropospheric Ozone

3.1 Introduction

Tropospheric ozone is a significant greenhouse gas that absorbs both longwave (terrestrial) and shortwave (solar) radiation [*Wang et al.*, 1980; *Lacis et al.*, 1990]. There is observational evidence that tropospheric ozone has increased since preindustrial times, particularly in the northern mid-latitudes [*Staehelin et al.*, 1994; *Marenco et al.*, 1994]. Increase in tropospheric ozone has been also demonstrated by model studies with increasing emissions of ozone precursor gases [*Crutzen and Zimmermann*, 1991; *Levy et al.*, 1997; *Wang and Jacob*, 1998d]. Estimates of the global mean radiative forcing from tropospheric ozone increase since preindustrial times range from 0.2 to 0.6 W m^{-2} [*Houghton et al.*, 1995], relatively wide compared to those of most other greenhouse gases. This wide range of estimates can be attributed primarily to spatially inhomogeneous distribution of tropospheric ozone, coming from short chemical lifetime of ozone in the troposphere (weeks). Accurate knowledge of the changes in ozone distribution, therefore, has a critical importance in investigation of the radiative forcing from anthropogenic ozone. Since observations of tropospheric ozone are quite limited particularly for preindustrial times, the ozone increase and associated radiative forcing are generally estimated by models. However, it should be noted that two-dimensional models [e.g., *Hauglustaine et al.*, 1994; *Forster et al.*, 1996] have tended to overestimate ozone abundances, since such models artificially diffuse NO_x emissions, increasing the ozone production efficiency [*Liu et al.*, 1987; *Kanakidou and Crutzen*, 1993]. We should note also that several studies [e.g., *Roelofs and Lelieveld*, 1995; *Lawrence et al.*, 1999] ignore the NMHCs chemistry which contributes largely to ozone formation, leading to an underestimation of the ozone radiative forcing. These defects in several studies can also cause the wide range of estimates of the radiative forcing from tropospheric ozone.

In this study, the radiative forcing from tropospheric ozone increase is estimated with a chemistry coupled GCM, named CHASER. The CHASER model simulates tropospheric chemistry involving ozone formation and destruction “on-line” based on a atmospheric general circulation model developed at the Center for Climate System Research, University of Tokyo and National Institute for Environmental Studies (CCSR/NIES AGCM). The model well reproduces observed distributions of ozone and precursors [*Sudo et al.*, 2002b], with a detailed simulation of O_3-HO_x-NO_x-CH_4-CO and NMHCs chemistry in the model [*Sudo et al.*, 2002a] (see also chapter 2). The global aerosol model of *Takemura et al.* [2000], also based on the CCSR/NIES AGCM, has estimated single-scattering albedo and radiative forcing of various aerosols [*Takemura et al.*, 2002]. *Takemura et al.* [2002] have also evaluated the cloud radiative forcing for shortwave and longwave radiation simulated by the CCSR/NIES AGCM, using the satellite observations by the Earth Radiation Budget Experiment (ERBE).

3.2 Model description and experiments

In this study, the global tropospheric ozone change and associated radiative forcing since preindustrial times are calculated with the CHASER model [*Sudo et al.*, 2002a] based on the CCSR/NIES AGCM. CHASER, driven on-line by climatological meteorology generated by the AGCM, calculates the chemistry and radiation processes interactively, considering the short-term correlations between meteorological variables (e.g.,temperature) and chemical fields such as ozone distributions in the AGCM. The model simulates detailed O_3-HO_x-NO_x-CH_4-CO and NMHCs chemistry on-line with a time step of 10 min (section 2.2.1), and includes also detailed dry/wet deposition schemes. The CHASER model version adopted in this study is basically identical to that described in the previous chapter (chapter 2). This version of CHASER, based on the CCSR/NIES AGCM, version 5.6, newly includes an improved wet deposition scheme, heterogeneous reactions on aerosols for N_2O_5 and several peroxyradicals RO_2, and also the sulfate formation process (section 2.2.1), compared to the previous version [*Sudo et al.*, 2002a]. Although the sulfate formation process is available in the present model, it is not coupled for now with the radiation calculation in the AGCM, so that estimation of the sulfate radiative forcing is not possible in this study. Sulfate formation is, however, included in this study to take into account the impact of the changes in sulfate distribution since preindustrial times on the heterogeneous reactions on aerosols considered in the model. The changes in sulfate distribution simulated in this study are also compared to the simulation with the CCSR/NIES aerosol model [*Takemura et al.*, 2002]. For this study, the horizontal resolution of T42 ($2.8^\circ \times 2.8^\circ$) is adopted with 32 layers to about 40 km altitude. Detailed description and evaluation of the model are shown in chapter 2.

To estimate the ozone increase since preindustrial times, simulations of present-day and preindustrial ozone distributions have been performed. The present-day simulation follows chapter 2 using emissions described in section 2.2.2 (NO_x, 44.3 TgN/yr; CO, 1267 Tg/yr; NMHCs, 668 TgC/yr; SO_2, 79.41 TgS/yr; DMS, 14.93 TgS/yr, as a total). Methane (CH_4) is not transported in this study, but is fixed to 1.77 ppmv (NH) and 1.68 ppmv (SH) for the present-day simulation (as in chapter 2) and to 0.7 ppmv globally for the preindustrial simulation. All anthropogenic emissions are shut off except for biomass burning emissions, which are reduced to 10% of their present-day values, following *Mickley et al.* [1999]. Natural emissions from vegetation, ocean, and soils for the preindustrial simulation are the same as for present-day except for soil NO_x emission, which is reduced to 40% of 5.5 TgN/yr (2.2 TgN/yr), following *Mickley et al.* [2001]. The meteorological fields generated by the AGCM in the present-day and preindustrial simulations are exactly the same in this study. Therefore, lightning NO_x emission and DMS emission from ocean, which are parameterized with the meteorological variables in the AGCM, are identical in both simulations (lightning NO_x, 5 TgN/yr; DMS flux, 15 TgS/yr). Note that oceanic emission of acetone as described in section 2.2.2 is not taken into account in the simulations. Note also that this study does not consider the changes in stratospheric ozone distribution since preindustrial times. In both the simulations, concentrations of O_3, NO_x, HNO_3, and N_2O_5 in the stratosphere (above 20 km altitude) are prescribed in the same manner, using zonal mean satellite data from the Halogen Occultation Experiment project (HALOE) and monthly averaged output data from a three-dimensional stratospheric chemical model [*Takigawa et al.*, 1999].

The CCSR/NIES AGCM adopts a radiation scheme based on the k-distribution and the two-stream discrete ordinate method [*Nakajima and Tanaka*, 1986]. The scheme considers the absorption and scattering by gases (H_2O, CO_2, N_2O, CH_4, O_3, and HFCs), aerosols and clouds, and the effect of surface albedo. A detailed description of the radiation scheme adopted in the AGCM is given by *Nakajima et al.* [1995]. Ozone in the troposphere absorbs the radiation in 9.6-14 μm in the infrared and the Huggins bands (310-400 nm) and the Chappuis bands (400-800 nm) in the ultraviolet and visible. For the CHASER calculations, the original wavelength resolution between 290 nm and 800 nm in the AGCM has been improved. The radiative process is evaluated every three hours in the model. In both the present-day and preindustrial simulations, radiative budgets of longwave and shortwave are calculated on the basis of the ozone distributions simulated on-line. The ozone radiative forcing is then obtained as the difference in the radiative fluxes at the tropopause between the present-day and preindustrial simulations. Since the model in this study uses the same meteorological fields for present-day and preindustrial, it estimates the “instantaneous” radiative forcing, with no feedback to the climate in the AGCM. Some previous studies [*Roelofs et al.*, 1997; *Berntsen and Isaksen*, 1997a; *Haywood et al.*, 1998] have calculated the “adjusted” radiative forcing, in which the stratospheric temperatures are permitted to relax to equilibrium following the radiative perturbation. The difference between instantaneous and adjusted forcings appears to be 10-20% [*Berntsen and Isaksen*, 1997a; *Haywood et al.*, 1998].

3.3 Tropospheric ozone changes since preindustrial times

Figure 3.1 displays surface ozone distributions calculated in the preindustrial simulation for January and July. For both seasons, calculated surface ozone levels are 10-30 ppbv lower than those in the present-day simulation. Low ozone levels of $<$10 ppbv are widely distributed over the ocean in the summer hemisphere. In July, relatively high concentrations (25-30 ppbv) are seen over the Eurasian Continent with a peak around the Middle East, resulting from lightning NO_x formation

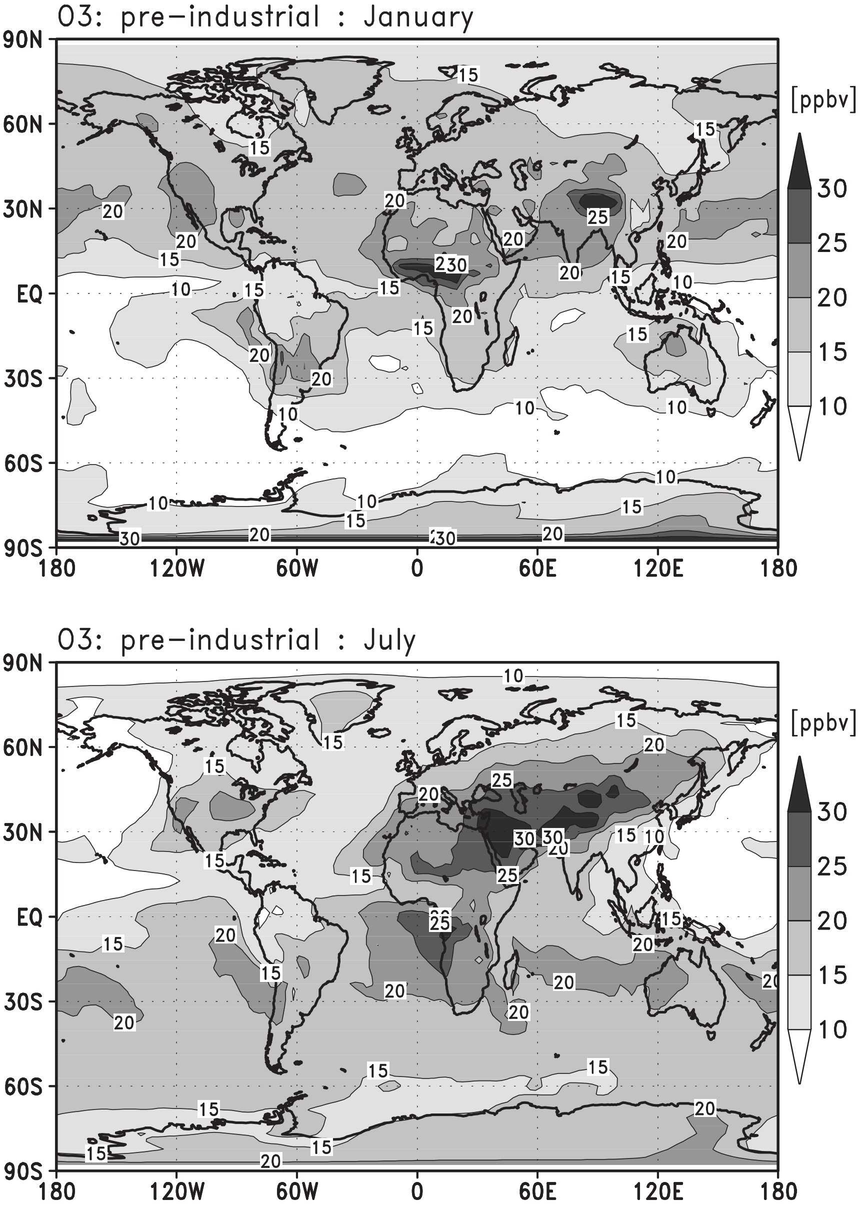

Figure 3.1. Surface ozone distributions (in January and July) simulated for preindustrial times.

and NO_x emission from soils over the continent. The same kind of feature of ozone distribution in summer is seen also in the present-day simulation. In the present-day simulation, ozone level in the industrial areas (especially in the United States and Europe) is high, reaching 50-80 ppbv in summer, whereas it is ∼20 ppbv in the preindustrial simulation. The figure also shows ozone formation associated with biomass burning in North/South Africa in January/July, although biomass burning emissions of ozone precursors are reduced to 10% of the present-day values. However, ozone enhancements calculated during the biomass burning season appear to be overestimated by 50-100%, in comparison with observations at several sites in the southern hemisphere, as in other preindustrial simulations [e.g., *Mickley et al.*, 2001]. This may indicate that biomass burning emis-

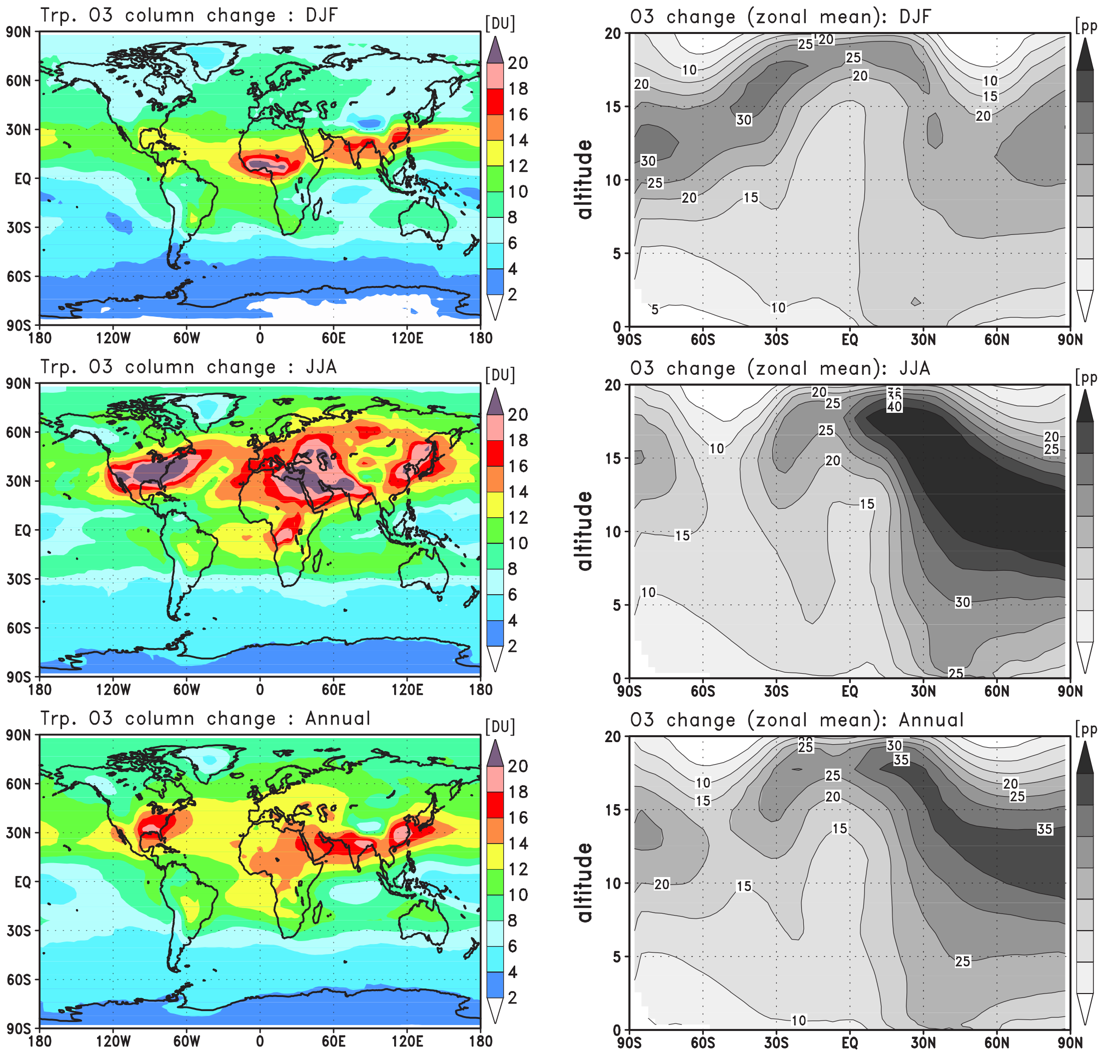

Figure 3.2. Simulated changes (increases) in tropospheric column ozone (left, in Dobson Units) and zonal mean ozone distributions (right) since preindustrial times for DJF, JJA, and annual means.

sions considered for preindustrial times (10% of the present-day) are still too large. *Mickley et al.* [2001] also suggested less efficient lightning NO_x formation and larger biogenic NMHCs emissions relative to the present-day for other factors of the overestimation of preindustrial ozone by models.

Figure 3.2 shows the differences in tropospheric ozone distribution between the preindustrial and the present-day simulations. On the annual average, tropospheric column ozone (TCO) increases more than 10 DU through much of the northern hemisphere since preindustrial times. Particularly large increases (>15 DU) are calculated around the United States and middle to eastern Asia, reflecting the considerable increases in anthropogenic emissions. For JJA, increase in TCO is most significant in the United States, the Middle East, and eastern Asia including Japan, reaching ∼20 DU (∼ a double increase). The ozone increase in the Middle East is caused by transport

Table 3.1. Global Budget of Tropospheric Ozone Calculated in the Present-day and Preindustrial Simulations

	Present-day	Preindustrial
Sources	5336	2946
Net STE[a]	652	689
Chemical production	4684	2257
HO_2 + NO	2948	1332
CH_3O_2 + NO	1047	485
others	689	440
Sinks	−5336	−2946
Dry deposition	−958	−476
Chemical loss	−4378	−2471
$O(^1D)$ +H_2O	−2548	−1518
O_3 + HO_2	−1202	−487
O_3 + OH	−537	−385
others	−91	−81
Net chemical production	306	−214
Chemical lifetime (days)	25	29
Burden(TgO_3)	311	197

Budgets are calculated in TgO_3/yr
[a] Stratosphere-Troposphere Exchange.

of pollutants from the northern midlatitudes and eastern Asia and NO_x emissions from lightning as suggested by *Li et al.* [2001]. In the vertical, large ozone increases are calculated in the upper troposphere and the tropopause region through a year. In particular, ozone level increases more than 40 ppbv around the tropopause in JJA, associated with the emission increases in the northern midlatitudes and with high ozone production efficiencies in the upper troposphere. Ozone increases of 15-20 ppbv are also calculated in the upper troposphere in the southern hemisphere, due mainly to the increase in biomass burning emissions.

Global budgets of tropospheric ozone in the preindustrial and the present-day simulations are compared in Table 3.1. In-situ chemical ozone production in the preindustrial simulation (2257 TgO_3/yr) is approximately doubled in the present-day simulation (4687 TgO_3/yr), owing principally to enhancement of the reactions of NO with HO_2 and CH_3O_2 which are the main chemical sources for ozone. Chemical ozone destruction due to reactions with H_2O, OH, and HO_2 increases by about 80% in the present-day simulation, whereas other reactions, mainly with NMHCs such as isoprene, increase by only 10%. The calculated net chemical production of ozone is positive (306 TgO_3/yr) in the present-day simulation, but negative (-214 TgO_3/yr) in the preindustrial one, indicating net destruction of ozone from the stratosphere. Averaged chemical lifetime of ozone is slightly longer in the preindustrial simulation, reflecting the differences in HO_x (OH+HO_2) abundance. The slight difference in net stratospheric ozone influx associated with the Stratosphere-Troposphere Exchange

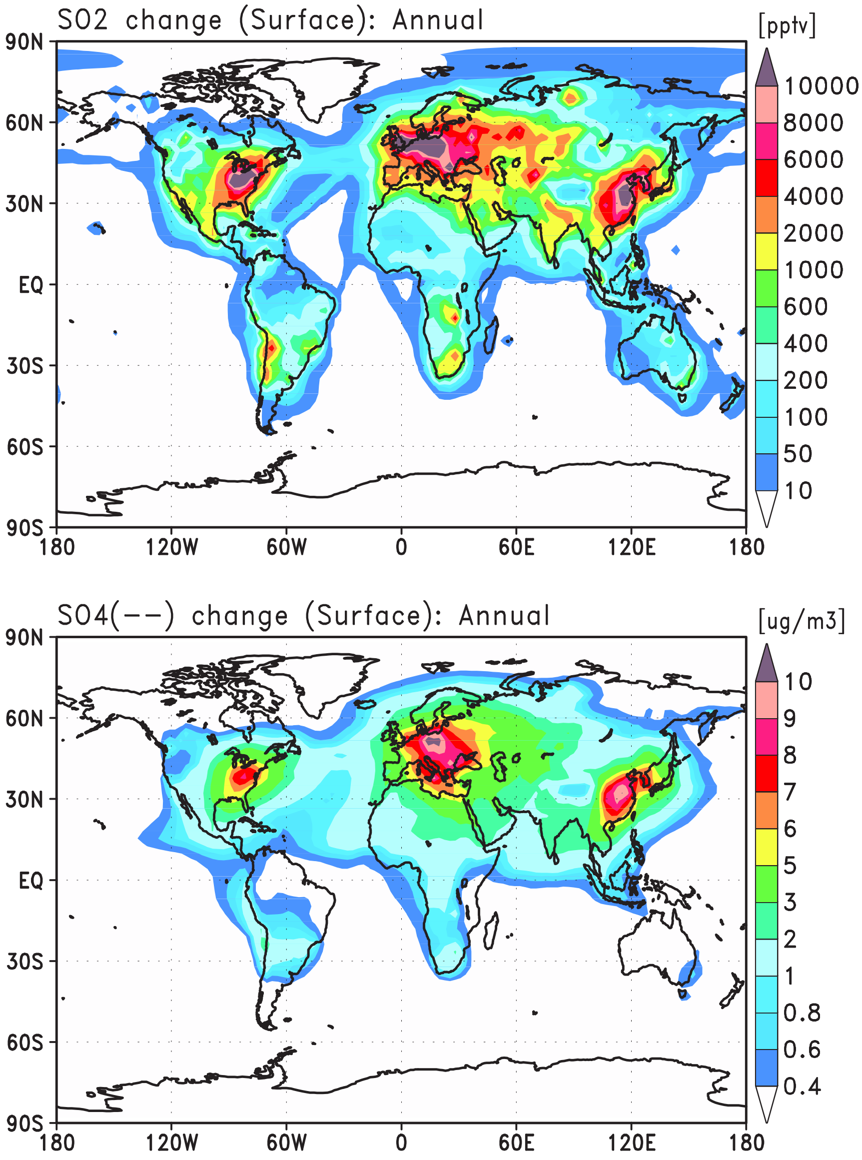

Figure 3.3. Changes in SO_2 (pptv) and sulfate (μg m^{-3}) distributions (annual means) since preindustrial times calculated at the surface.

(STE) between the preindustrial and the present-day simulations is attributed to the larger ozone abundance in the troposphere (i.e., larger ozone flux to the stratosphere) in the present-day simulation. The calculated burden of tropospheric ozone increases from 197 TgO_3 in preindustrial to 311 TgO_3 in present-day, corresponding to 10.4 DU increase in TCO. This estimated ozone increase is a little larger than 9.4 DU in the simulations of *Forster et al.* [1996] and *Berntsen and Isaksen* [1997a], and 7.9 DU by *Haywood et al.* [1998], but 20% smaller compared to 12.6 DU in *Mickley et al.* [1999]. The differences in natural emissions such as lightning NO_x emission and biogenic NMHCs emissions among the individual models are possible candidates for such variability in estimates of the ozone increase since preindustrial times, as tested by *Mickley et al.* [2001].

Table 3.2. Global Budget of Sulfate Aerosol Calculated in the Present-day and Preindustrial Simulations

	Present-day	Preindustrial
Source(chemical prod.)	53.19	11.94
SO_2 + OH (gas-phase)	13.20	2.10
S(IV) + O_3 (liq.-phase)	12.60	2.97
S(IV) + H_2O_2 (liq.-phase)	27.39	6.87
Sink	-52.90	-11.80
Dry deposition	-4.90	-1.10
Wet deposition	-48.00	-10.70
Burden(TgS)	0.61	0.15

Budgets are calculated in TgS/yr

In this study, the sulfate formation process is also simulated for preindustrial times and present-day. Figure 3.3 shows the calculated changes in SO_2 and sulfate (SO_4^{2-}) distributions at the surface. Significant increases in SO_2 ($>$5 ppbv) are calculated in the United States, Europe, and China with increases in sulfate ($>5\ \mu$g m^{-3}), in accordance with the SO_2 emission increases. Sulfate formation increases from 12 TgS/yr in preindustrial to 53.2 TgS/yr in present-day (Table 3.2). The efficiency of sulfate formation by liquid-phase reactions (per one molecule of SO_2) is, however, higher in the preindustrial simulation, due to lower $[H^+]$ levels (i.e., higher pH) in cloud drops relative to the present-day simulation (see Appendix 2B, page 106 for the calculation of $[H^+]$ in cloud drops in the model). As a result, increase in SO_2 oxidation in liquid-phase (by a factor of 4.2) is less significant than that in gas-phase oxidation (by a factor of 6.3) in this study. Dry and wet deposition of sulfate also increases by a factor of 4-5 in the present-day simulation, in accordance with the increase in sulfate burden in the global troposphere from 0.15 TgS for preindustrial to 0.61 TgS for present-day ($+$0.46 TgS). *Takemura et al.* [2002] have simulated the changes in sulfate distribution to estimate the direct radiative forcing from anthropogenic sulfate, using a global aerosol model which is also based on the CCSR/NIES AGCM like CHASER. The simulation of *Takemura et al.* [2002] has calculated a sulfate increase of 0.4 TgS (from 0.1 TgS to 0.5 TgS) since preindustrial times, 15% smaller than in this study. However, the sulfate increase estimated by *Takemura et al.* [2002] can be underestimated, since they don't consider an on-line simulation of H_2O_2 and O_3 in the liquid-phase reactions, using monthly mean distributions of H_2O_2, O_3, and OH. *Takemura et al.* [2002] have estimated the direct (shortwave) radiative forcing from sulfate as -0.44 W m^{-2} with a sulfate increase of 0.4 TgS. Assuming a linear correlation between the sulfate radiative forcing and the sulfate increase, the sulfate increase calculated in this study leads to a sulfate shortwave forcing of -0.51 W m^{-2} on the simplest analogy of the study of *Takemura et al.* [2002].

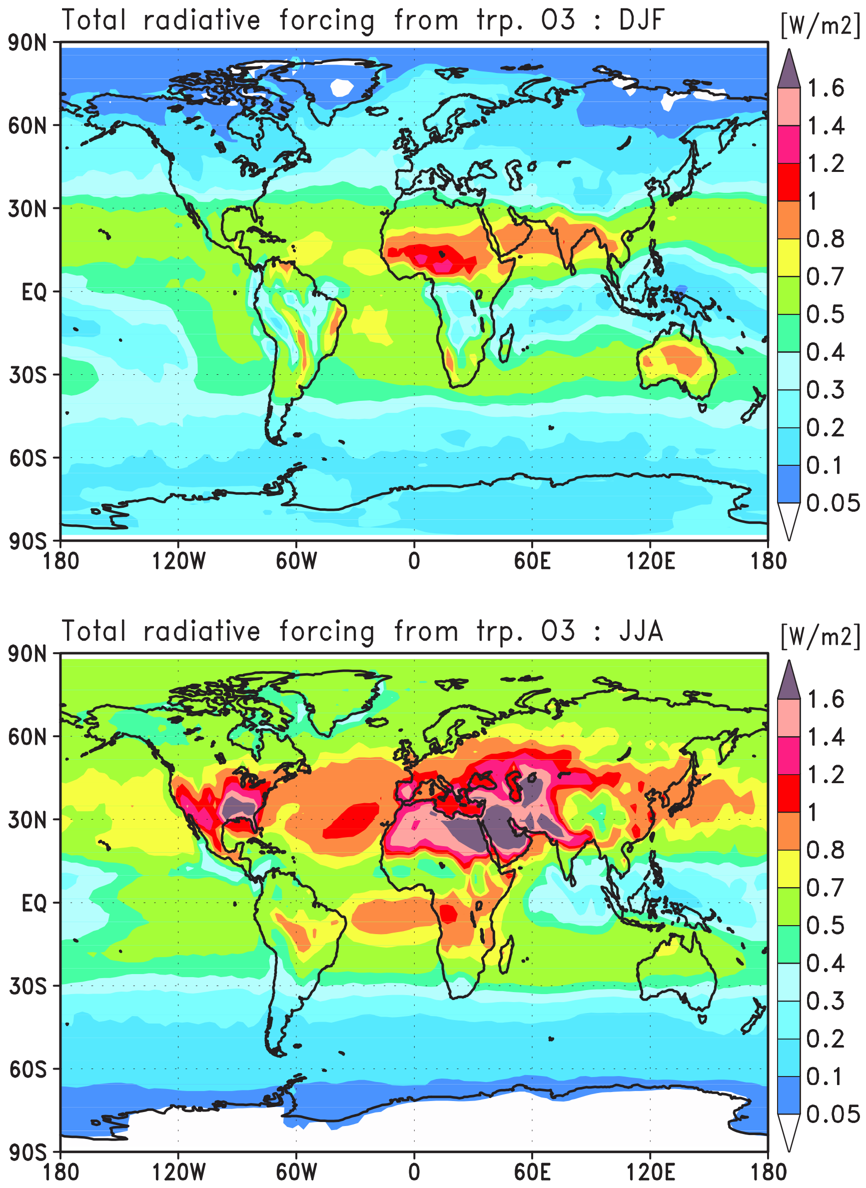

Figure 3.4. Total (longwave + shortwave) radiative forcing from anthropogenic ozone for DJF and JJA. Values are calculated for whole-sky conditions.

3.4 Radiative forcing

The radiative forcing from anthropogenic ozone is evaluated using the CCSR/NIES AGCM on the basis of the ozone distributions in the preindustrial and the present-day simulations described in the previous section. The forcing is defined as the difference in net flux of longwave and shortwave radiation at the tropopause between the preindustrial and present-day simulations. Figure 3.4 displays the calculated total radiative forcing from tropospheric ozone for whole-sky conditions. In DJF, ozone forcing of $\sim$0.5 W m^{-2} is calculated in the lowlatitudes in both hemispheres (EQ-30°) with relatively strong forcing ($>$ 0.8 W m^{-2}) in South Africa and India due to the increases in biomass burning and industrial emissions. In JJA, the model calculates significant forcings over the United Sates, North Africa, and the Middle East reaching 1.5 W m^{-2}, comparable with the CO_2 forcing [*Houghton et al.*, 1995]. Strong ozone forcing ($>$0.8 W m^{-2}) is also seen in the remote oceans as the western North Pacific and the Atlantic, resulting from the ozone increase associated with transport of pollution from the industrial regions (eastern Asia and the United States, etc.). Forcings of 0.8 W m^{-2} over the South Atlantic, Africa, and South America in JJA are attributed to the increase in biomass burning emissions.

In Figure 3.5, the calculated radiative forcing from tropospheric ozone is shown for longwave and shortwave radiation separately. The shortwave radiative forcing from tropospheric ozone means absorption of out-going shortwave radiation (reflected on the Earth's surface, clouds, aerosols, etc.) by ozone. The calculated longwave ozone forcing is generally much larger than the shortwave forcing, contributing by $\sim$80% to the total forcing. The calculated shortwave radiative forcing is much depending on the distributions of clouds and surface albedo. The shortwave radiative forcing shows a peak ($>$0.16 W m^{-2}) over North Africa and the Middle East, owing to high reflectivities in the deserts. Relatively strong shortwave forcings of 0.12-0.14 W m^{-2} are also calculated over the northern highlatitudes (around the North Pole) due to ice albedo.

Figure 3.6 shows the zonal mean radiative forcing from anthropogenic ozone as a function of latitude. The model calculates two peak values of longwave and total forcing in the midlatitudes in both hemisphere, reflecting the emission increases in the industrial regions. In the southern hemisphere, the increase in biomass burning emissions (South America and Africa, in particular) also contributes largely to the calculated forcings. In JJA, the calculated ozone forcing ranges from 0.6 to 1 W m^{-2} through much of the northern hemisphere, larger than the estimated CH_4 forcing (approximately 0.5 W m^{-2}). The contribution from shortwave radiative forcing is most significant in the highlatitudes in the summer hemisphere, showing shortwave forcing of 0.2-0.3 W m^{-2} in the northern highlatitudes in JJA. The zonal mean radiative forcing distributions as shown in Figure 3.6 are generally consistent with those by *Roelofs* [1999] and *Mickley et al.* [1999], but show slightly larger peak values in the northern midlatitudes reaching 0.8 or 1.0 W m^{-2}. Also, *Mickley et al.* [1999] calculate strong shortwave ozone forcings of $\sim$0.7 W m^{-2} around the North Pole in JJA, much larger than in this study.

It should be noted that estimation of the longwave and shortwave forcings from tropospheric ozone is much influenced by cloud representation in models [*Roelofs*, 1999; *Mickley et al.*, 1999]. Figure 3.7 and 3.8 show the radiative forcing from ozone calculated for whole-sky and clear-sky conditions. The shortwave ozone forcing displays a high sensitivity to the cloud distributions in the AGCM, with larger values in whole-sky conditions. According to the study of *Takemura et al.* [2002], the CCSR/NIES AGCM tends to overestimate the shortwave radiative forcing from clouds in the tropical latitudes by $\sim$20% in comparison with the observation of ERBE (Earth Radiation Budget Experiment). Therefore, it is possible that the shortwave radiative forcing from tropo-

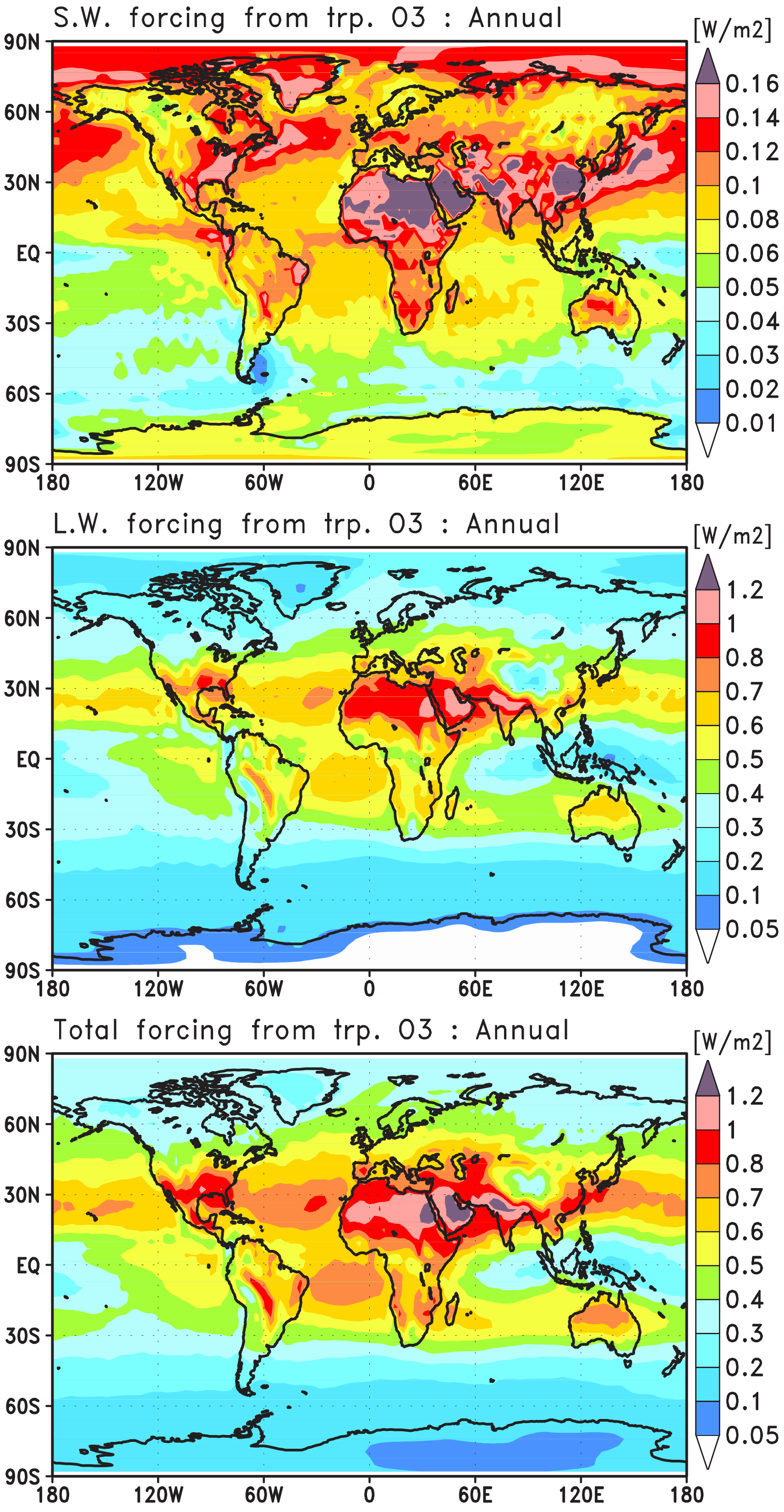

Figure 3.5. Longwave (L.W.) and shortwave (S.W.) radiative forcing from anthropogenic ozone for whole-sky conditions on an annual average.

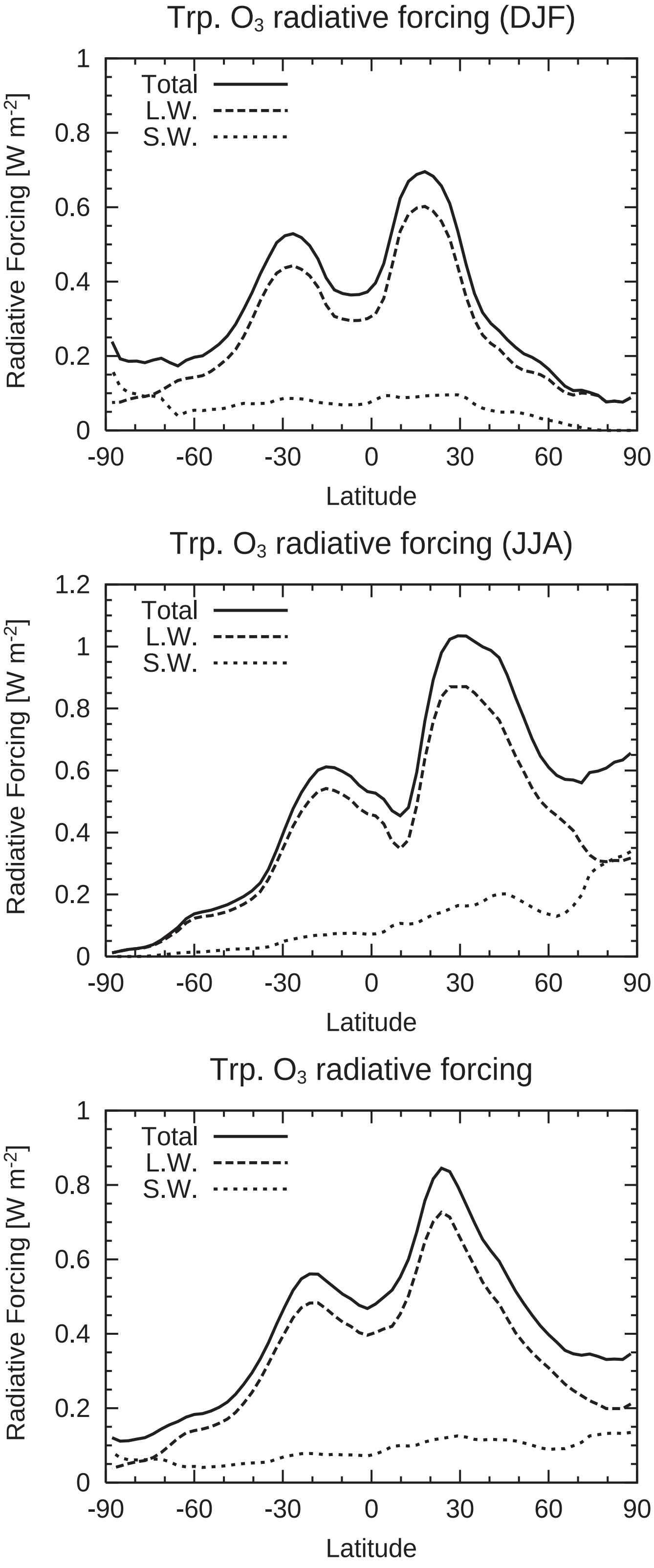

Figure 3.6. Zonal mean radiative forcing from tropospheric ozone on DJF (upper), JJA (middle), and annual averages (bottom). Plots are for whole-sky conditions.

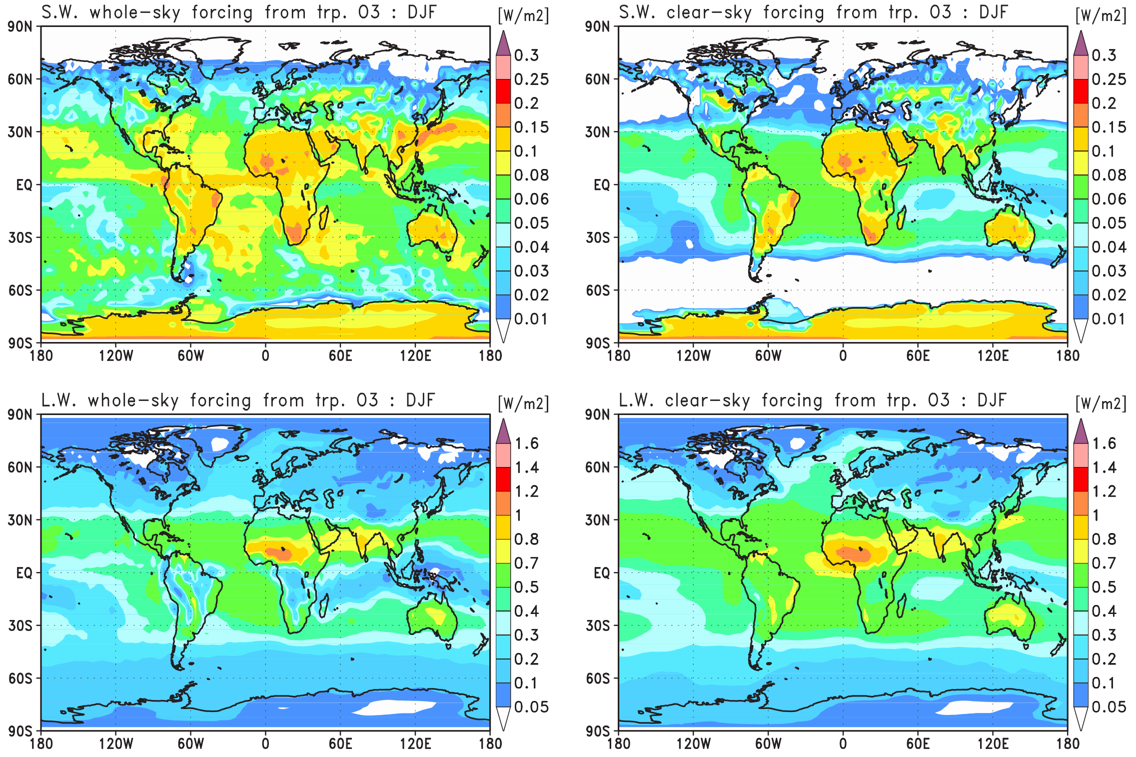
S.W. whole−sky forcing from trp. O3 : DJF

S.W. clear−sky forcing from trp. O3 : DJF

L.W. whole−sky forcing from trp. O3 : DJF

L.W. clear−sky forcing from trp. O3 : DJF

Figure 3.7. Longwave (L.W.) and shortwave (S.W.) radiative forcing from anthropogenic ozone for DJF. Values are calculated for whole-sky (left) and clear-sky (right) conditions.

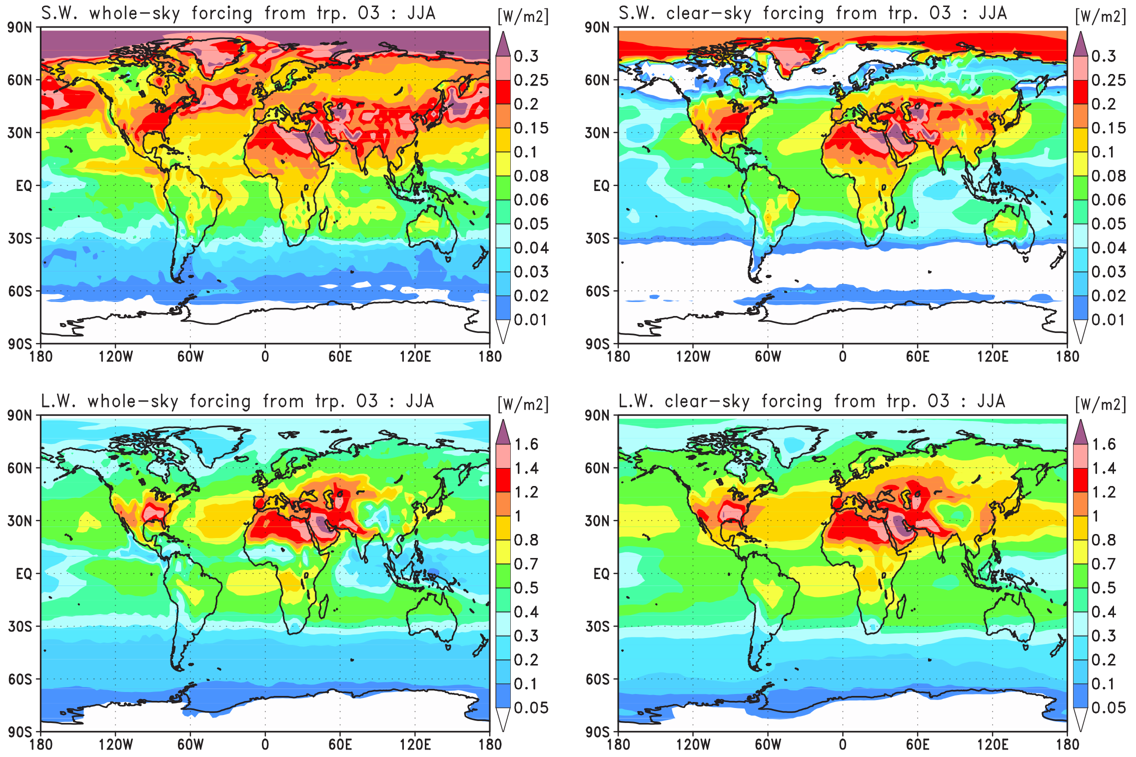
S.W. whole−sky forcing from trp. O3 : JJA

S.W. clear−sky forcing from trp. O3 : JJA

L.W. whole−sky forcing from trp. O3 : JJA

L.W. clear−sky forcing from trp. O3 : JJA

Figure 3.8. Same as Figure 3.7 but for JJA.

Table 3.3. Radiative Forcing from Tropospheric Ozone Calculated at the Tropopause (W m^{-2})

	whole-sky			clear-sky		
	Global	N.H.	S.H.	Global	N.H.	S.H.
Long wave	0.402	0.485	0.319	0.498	0.609	0.386
Short wave	0.085	0.107	0.063	0.053	0.069	0.037
Total	0.487	0.592	0.382	0.551	0.678	0.423

spheric ozone in the lowlatitudes may be overestimated in this study under whole-sky conditions with clouds. Since clouds absorb the longwave radiation around 9.6 μm (in the ozone absorption band), larger longwave ozone forcing is calculated for clear-sky conditions.

The global and annual mean radiative forcing from anthropogenic ozone is summarized in Table 3.3. The shortwave forcing contributes by less than 10% to the total forcing in the clear-sky condition, but by 17% in the whole-sky condition. Due to absorption of longwave radiation by clouds, the longwave forcing is 20% larger in the clear-sky condition relative to the whole-sky condition. The total (longwave + shortwave) ozone radiative forcing is 0.06 W m^{-2} larger in the clear-sky condition compared to the whole-sky condition, in good agreement with the previous studies (0.05-0.1 W m^{-2}). The total forcing in the northern hemisphere is 55% larger than in the southern hemisphere, reflecting the differences in the ozone increase between the hemispheres, also consistent with the previous studies (NH/SH $=$ 1.5-2).

The calculated global mean ozone radiative forcing is compared with the previous studies in Table 3.4. Forcings greater than 0.5 W m^{-2} are estimated by *Hauglustaine et al.* [1994], *Marenco et al.* [1994], and *Mickley et al.* [2001]. *Hauglustaine et al.* [1994] may overestimate the ozone forcing, since they use a two-dimensional model which tends to overestimate ozone abundances [*Liu et al.*, 1987; *Kanakidou and Crutzen*, 1993]. *Mickley et al.* [2001] reduced NO_x emissions from lightning and increased biogenic emissions of NMHCs in their preindustrial simulations, to improve the preindustrial ozone simulation, and obtained the largest ozone forcing of 0.72-0.80 W m^{-2}. Although the ozone forcing estimated in this study (0.49 W m^{-2}) appears to be on the higher side of the range suggested by the previous studies, the ozone forcing may be possibly still underestimated since ozone concentrations in preindustrial times are overestimated by $\sim$50% compared to observations in this study as in *Mickley et al.* [2001]. The normalized radiative forcing (per 1DU ozone increase) is 0.047 W m^{-2} DU^{-1} in this study, somewhat larger than the average of the previous studies (0.035-0.040 W m^{-2} DU^{-1}), but close to the study of *Roelofs and Lelieveld* [2000] which calculates 0.049 W m^{-2} DU^{-1}.

Table 3.4. Comparison of Global Mean Ozone Radiative Forcing with the Previous Studies

	Global mean radiative forcing (W m^{-2})
Hauglustaine et al. [1994]	0.55
Marenco et al. [1994]	0.62
Chalita et al. [1996]	0.28
Forster et al. [1996]	0.30
Berntsen and Isaksen [1997a]	0.28-0.30
Haywood et al. [1998]	0.35
Mickley et al. [1999]	0.44
Roelofs [1999]	0.37
Roelofs and Lelieveld [2000]	0.35
Mickley et al. [2001]	0.72-0.80
This work	0.49

3.5 Conclusions

The global radiative forcing from (anthropogenic) tropospheric ozone has been evaluated using the CHASER model based on the CCSR/NIES AGCM. CHASER includes a detailed simulation of O_3-HO_x-NO_x-CH_4-CO and NMHCs chemistry in the model [*Sudo et al.*, 2002a], and reproduces well the observed tropospheric ozone distributions in the present-day atmosphere [*Sudo et al.*, 2002b] (see also chapter 2). In this study, global tropospheric ozone increased from 197 TgO_3 in preindustrial times to 311 TgO_3 in present-day, corresponding to a 10.4 DU increase in tropospheric column ozone. The calculated radiative forcing from anthropogenic ozone is most significant in the northern midlatitudes with showing peak values larger than 1 W m^{-2} over around the Middle East. The model estimates peak ozone forcings of > 1.5 W m^{-2}, comparable with the estimated CO_2 forcing, over the United States and the Middle East in summer. Strong ozone forcing of 0.5-0.8 W m^{-2} is also calculated in the low to midlatitudes in the southern hemisphere owing to the increase in biomass burning emissions. The global and annual mean ozone radiative forcing is estimated at 0.49 W m^{-2} (0.40 longwave, 0.085 shortwave), with a normalized forcing of 0.047 W m^{-2} DU^{-1}. The calculated ozone forcing in the northern hemisphere is 0.59 W m^{-2} on an annual average, larger than the CH_4 forcing. This study, however, appears to overestimate the preindustrial ozone abundances by $\sim$ 50% as suggested by *Mickley et al.* [2001], possibly indicating an underestimation of the ozone radiative forcing in this study. The overestimation of preindustrial ozone by the model may arise from too large biomass burning emissions in the preindustrial simulation, which are taken to be 10% of the present rates. Given the still large uncertainty in the preindustrial ozone distributions, further investigation on the preindustrial atmosphere including natural emissions such as lightning NO_x and biogenic NMHCs is needed for an accurate estimate of the radiative forcing from tropospheric ozone. Since both the distribution of ozone and the radiative forcing are largely affected by meteorological variables such as temperature, clouds, and water vapor, the representation of meteorological fields in the AGCM also needs to be further evaluated. This study evaluates the instantaneous radiative forcing from ozone with no feedback to the climate in the model. But in fact, ozone increase should be coupled with climate. We will investigate the climate effect of the ozone increase as a next step.

This study also simulates the changes in sulfate distributions, with a scheme coupled with ozone chemistry. The model shows a significant increase in sulfate from 0.15 TgS to 0.61 TgS since preindustrial times due to the SO_2 emission increase, corresponding roughly to a sulfate direct forcing of -0.51 W m^{-2} in view of the simulation of *Takemura et al.* [2002] which is also based on the CCSR/NIES AGCM. This estimated sulfate forcing nearly cancels the calculated ozone forcing 0.49 W m^{-2}, leading to a combined forcing of -0.02 W m^{-2} as in *van Dorland et al.* [1997]. However, actual calculation of the sulfate radiative forcing based on the sulfate changes calculated in this study is necessary for an accurate estimate. Further evaluation of the sulfate simulation (e.g., DMS emissions in the model) is also required especially for preindustrial times as with the ozone simulation. Those are issues for further investigation. In addition, the future model version will incorporate the direct and indirect climate effects of individual aerosols and will simulate the fully coupled ozone-aerosols-climate system.

Chapter 4

Tropical Tropospheric Ozone and its Changing Process

4.1 Introduction

The tropics is the most photochemically active region in the troposphere, characterized by convective transport and precipitation, by richness of water vapor, and by large emissions of ozone precursor gases (nitrogen oxides NO_x, carbon monoxide CO, and hydrocarbons) from vegetation and biomass burning associated with forest and savanna fires, and from lightning (for NO_x). *Fishman and Larsen* [1987] was the first attempt to derive the tropical tropospheric ozone distribution (in column total) with a residual method which combines Stratospheric Aerosol and Gas Experiment (SAGE) stratospheric column ozone with total ozone mapping spectrometer (TOMS) total ozone measurements. Their study, though poor data sampling of SAGE (an occultation measuring instrument), revealed an anomalous zonal pattern in tropospheric column ozone in the tropics (zonal wavenumber 1 pattern) with a peak in the south Atlantic and a minimum around the western Pacific (around 140°E to the date line). This characteristic pattern in the tropical ozone distribution is also captured by many recent studies using more refined methods [*Jiang and Yung*, 1996; *Kim and Newchurch*, 1996; *Hudson and Thompson*, 1998; *Ziemke et al.*, 1998; *Thompson and Hudson*, 1999; *Chandra et al.*, 2002b]. Their studies and most of recent studies generally conclude that the zonal wavenumber 1 structure in the tropical column ozone is likely to be related to either natural meteorological conditions in the tropics (e.g., Walker circulation) or photochemical production of ozone associated with biomass burning and biogenic emissions of ozone precursors and NO_x emissions from lightning [e.g., *Fishman et al.*, 1996; *Thompson et al.*, 1996; *Martin et al.*, 2002].

It has been found that the tropical tropospheric ozone (O_3) distribution characterized by a zonal wavenumber 1 pattern [e.g., *Fishman and Larsen*, 1987; *Ziemke et al.*, 1998] fluctuates strongly correlated with the El Niño Southern Oscillation (ENSO) [*Shiotani and Hasebe*, 1994; *Chandra et al.*, 1998; *Ziemke and Chandra*, 1999; *Thompson and Hudson*, 1999]. In El Niño events, changes in sea surface temperature (SST) cause a shift in the convection pattern of the equatorial Pacific, leading to an increase in rainfall and water vapor (H_2O) over the eastern Pacific and a decrease over the western Pacific and Indonesia. During the 1997-1998 ENSO, positive anomalies in tropospheric column ozone (10-20 Dobson units, DU) were observed in the tropical western Pacific and Indonesia by ozone soundings [*Fujiwara et al.*, 1999, 2000] and satellite-based methods [*Chandra et al.*, 1998; *Ziemke and Chandra*, 1999], whereas anomalies observed in the eastern Pacific are negative (4-8 DU) [*Chandra et al.*, 1998], in a phase as appeared during other ENSO events in the past [*Ziemke and Chandra*, 1999]. In Indonesia, the observed positive anomalies (i.e., increase) in tropospheric column ozone during the 1997-1998 ENSO may be primarily attributed to photochemical ozone production associated with the large emissions of ozone precursors by the extensive forest fires in Sumatra and Borneo during August to October 1997 [*Sawa et al.*, 1998; *Fujiwara et al.*, 1999; *Thompson et al.*, 2001]. However, changes in meteorological conditions in Indonesia during this ENSO event (downward motion, suppressed convection, and dryness) can also be significant contributors to the large-scale ozone increase in Indonesia and the western Pacific as suggested by *Chandra et al.* [1998].

In this study, we have evaluated the meteorological impact of the 1997-1998 El Niño on the tropical tropospheric ozone distribution, using a global chemical model. The 1997-1998 El Niño , the strongest ENSO event of the century, provided us a good opportunity to study the relationship between tropical meteorological conditions and the tropical ozone distribution through the convection pattern changes. Furthermore, this El Niño event was also a good chance to evaluate the model capability to simulate changes in the ozone distribution and related photochemistry due to natural meteorological changes. *Hauglustaine et al.* [1999] assessed the effect of the 1997 Indonesian fire emissions on the ozone increase in Indonesia during the 1997-1998 ENSO, using a global chemical model. Though their simulation reproduces the ozone increase in the vicinity of the emission source region in Indonesia as observed, the large-scale ozone increase extending outside the Indonesian region and the large-scale ozone decrease in the eastern Pacific are not simulated because their simulation does not account for the meteorological changes of the 1997-1998 El Niño .

In this chapter, tropical tropospheric ozone distributions simulated by a global chemical model (CHASER) are evaluated with satellite-based observations (section 4.3). Then, section 4.4 discusses the meteorological impact of the 1997-1998 El Niño on the tropical tropospheric ozone distributions simulated by the CHASER model, with section 4.5 presenting conclusions.

4.2 Model description and simulations

In this study, a three-dimensional global chemical model, named CHASER, has been employed to simulate the tropical tropospheric ozone distributions. This model, developed in the framework of the Center for Climate System Research/National Institute for Environmental Studies (CCSR/NIES) atmospheric general circulation model (AGCM), is aimed at studying tropospheric photochemistry and its influences on climate. CHASER simulates a detailed O_3-HO_x-NO_x-CH_4-CO and NMHCs chemistry on-line in the CCSR/NIES AGCM and includes also detailed dry/wet deposition schemes.

Detailed description and evaluation of CHASER are presented in *Sudo et al.* [2002a, b]. The model accounts for emission sources for ozone precursor gases including NO_x (43.8 TgN/yr including 5 TgN/yr from lightning), CO (1227 Tg/yr), and nonmethane hydrocarbons (ethane, propane, ethene, propene, acetone, isoprene, terpenes, and a lumped species). Lightning NO_x emissions are calculated in the convection scheme of the AGCM, according to *Price and Rind* [1992]. CHASER considers wet deposition due to convective precipitation and large-scale precipitation as well as dry deposition. In the model, in-cloud and below-cloud scavenging processes are considered separately. For the simulation presented in section 4.3 in the following, the newest version of CHASER has been used, which includes an improved wet deposition scheme, heterogeneous reactions on aerosols for N_2O_5 and several peroxyradicals RO_2, and also the sulfate formation process (see section 2.2), which are not implemented in the previous version [*Sudo et al.*, 2002a]. The model version used in the simulation in section 4.4 (on the El Niño impact on the tropical ozone distributions) is exactly identical to the previous version of CHASER [*Sudo et al.*, 2002a]. The horizontal resolution is opted to be T42 ($\sim 2.8^\circ \times 2.8^\circ$) for the simulation of section 4.3, whereas it is T21 ($\sim 5.6^\circ \times 5.6^\circ$) for the simulation in section 4.4. In both the simulations (section 4.3,4.4), the model adopts a vertical resolution with 32 layers from the surface up to about 40 km altitude. The model uses a σ coordinate system in the vertical and has a vertical resolution of 1 km in the free troposphere and much of the lower stratosphere.

In the simulation of the ozone changes observed during the 1997-1998 El Niño event (section 4.4), the model results are evaluated, using tropical anomalies (October 1997 minus October 1996) in tropospheric column ozone (TCO) derived by a satellite-based method (convective-cloud differential, CCD technique) [*Chandra et al.*, 1998]. We have set up a simulation for 2 years, 1996 and 1997, for a direct comparison with *Chandra et al.* [1998]. To reproduce the meteorological conditions in 1996 and 1997, we used analyzed data of wind velocities and temperature from the European Center for Medium-Range Weather Forecasts (ECMWF) as a constraint to the dynamical component of the model, in addition to sea surface temperature (SST) data for 1996 and 1997. The model is nudged by using the daily ECMWF data with a relaxation time of 1 day. The nudged model generally well reproduces the tropical water vapor distributions in 1996 and 1997 from the ECMWF observations. To evaluate the meteorological impact of the El Niño only, the effect of the 1997 Indonesian fires is not taken into account in this simulation, and the same surface emission rates in Indonesia are used for 1996 and 1997 in the model.

4.3 Tropical ozone distribution

Many of the current techniques for deriving tropospheric ozone from satellite measurements are based on the tropospheric ozone residual (TOR) method, which derives tropospheric column ozone (TCO) by subtracting concurrent measurements of stratospheric column ozone (SCO) from total column ozone measured by the TOMS instrument [*Fishman and Larsen*, 1987]. The study of

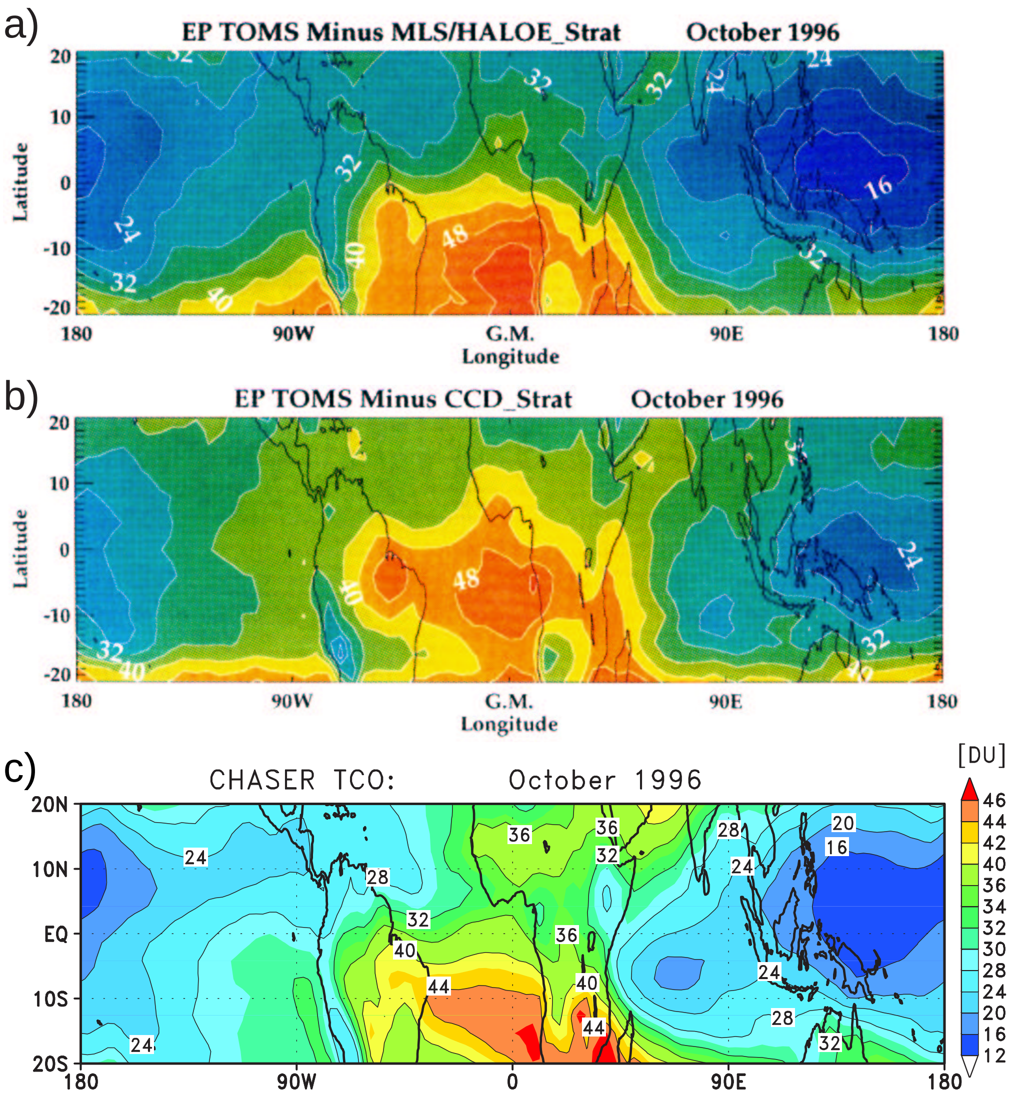

Figure 4.1. Tropical tropospheric column ozone (in Dobson Units) for October 1996 derived from satellite observations (a and b) and calculated by CHASER (c). The observations are from (a) the MLS/HALOE assimilation and (b) the CCD (Convective Cloud Differential) technique with the TOMS observations [*Ziemke et al.*, 1998].

Ziemke et al. [1998] introduced two TOR methods with the TOMS observations; the TOMS/MLS residual and TOMS/CCD (convective cloud differential) residual. In their TOMS/MLS residual, SCO is determined using the MLS ozone measurements and Halogen Occultation Experiment (HALOE) ozone data, while the TOMS/CCD uses high reflecting convective cloud scenes ($R>0.9$) near the tropopause in the tropical Pacific region and assumes that the SCO is zonally invariant in the tropical latitudes (10°N and 10°S). Figure 4.1 compares the tropical TCO simulated by CHASER with the TOMS/MLS and TOMS/CCD TCO [*Ziemke et al.*, 1998] for October 1996. TCO calculated by the model shows the O_3 column integrated from the surface to the tropopause defined as the lowest altitude at which the vertical temperature gradient is greater than -2 K/km in the model. The

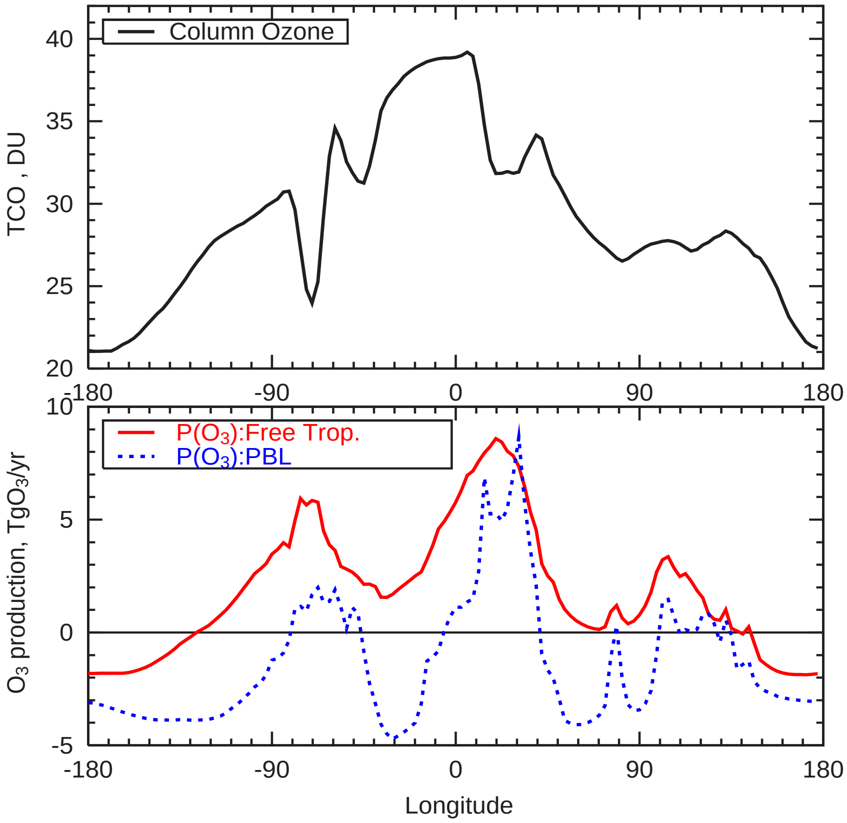

Figure 4.2. Annual mean tropospheric column ozone (DU) averaged over the tropics (15°S-15°N), and net ozone production calculated in the free troposphere (solid) and in the boundary layer (PBL:dotted) as a function of longitude. The vertical regions of the boundary layers are defined to extend from the surface to 700 hPa altitude in the model. Ozone production is shown as a budget within individual model grids (2.8°×2.8°) in 15°S-15°N.

model appears to reproduce the zonal wave 1 pattern in TCO as observed, calculating large ozone enhancement (>40 DU) over the region encompassing the South Atlantic and a minimum over the western Pacific (15-20 DU). Both the observations and the model display the effect of outflow from African biomass burning regions over the South Indian Ocean. Low TCO values over mountainous regions like Andes are topographically induced. The differences between the model and the observations increase with latitudes. However, it should be noted that the both observations tend to overestimate TCO in higher latitudes (>10°), since the TOMS/MLS may have greater errors in the estimation of SCO outside the tropics, and the TOMS/CCD method is basically valid only within the tropics. The model calculates a large TCO (∼40 DU) near India and the Middle East, which is not seen in the observed TCO. The same kind of discrepancy appears also for other seasons and is most significant in DJF season over the region encompassing North Africa and India (not shown), in a situation similar to the simulations of *Martin et al.* [2002] and *Chandra et al.* [2002a]. Since ozonesonde measurements are not available for that region, the cause of such discrepancies between models and satellite-based observations is not clear for now.

The origin of the wave 1 pattern in TCO as seen in Figure 4.1 is attributed to upper tropospheric ozone formation from lightning NO_x and biomass burning coupled with the large-scale Walker Circulation [*Thompson et al.*, 1996; *Martin et al.*, 2002]. Ozone production is enhanced also by intense biogenic emissions of NMHCs (isoprene, terpenes, etc.) from the tropical rainforests like Amazonia. Figure 4.2 shows the zonal distributions of annual mean tropical TCO and ozone production on the annual basis calculated by CHASER (15°S-15°N). The annual mean TCO shows a peak (35-40 DU) over the region encompassing South America, the Atlantic, Africa, showing minimum of $\sim$20 DU around the dateline (180°E). The zonal TCO distribution appears to be correlated with ozone production in the free troposphere. Net ozone production in the free troposphere is positive except over the Pacific where a TCO minimum is calculated, with large production over the land areas (South America, Africa, and Indonesia) where lightning NO_x and biomass burning emissions are intense. In the boundary layers, positive production of ozone is highly limited over the land surface due to efficient ozone destruction over the oceans. In the marine boundary layers, the model calculates ozone chemical lifetime of one or two weeks in the tropics, in agreement with observations [*Jacob et al.*, 1996; *Thompson et al.*, 1996]. Emissions of ozone precursors in South America and Africa are transported to the upper troposphere by large-scale air motion and convection [*Fishman et al.*, 1996] and cause large ozone production over the wide area including the Atlantic along with the Walker circulation. Large ozone destruction calculated in the boundary layers over the Atlantic indicates transport of chemically produced ozone from South America and Africa, and subsidence of upper tropospheric ozone associated with the Walker circulation.

4.4 Meteorological impact of the 1997-1998 El Niño event

As shown in the above, tropical tropospheric ozone distributions are well correlated with meteorological fields such as the large-scale Walker circulation and convection. In the following, the observed large-scale changes in tropical tropospheric ozone during the 1997-1998 El Niño are simulated by CHASER to reveal the relationship between tropical meteorology and tropical tropospheric ozone. The CHASER model version used in this simulation is identical to *Sudo et al.* [2002a] with the T21 horizontal resolution (5.6°×5.6°). For comparison to the observations in 1996 and 1997, zonal wind velocities and temperature in the model are nudged to those from the ECMWF data in 1996 and 1997. Note again that the increase in biomass burning emissions due to the 1997-1998 Indonesian forest fires is not included in this simulation.

4.4.1 Impact on the ozone distribution

Figure 4.3 shows a comparison between observed and simulated anomalies (October 1997 minus October 1996) in TCO (DU). The observed anomalies are derived from Earth Probe (EP) Total Ozone Mapping Spectrometer (TOMS) using the convective-cloud differential (CCD) technique

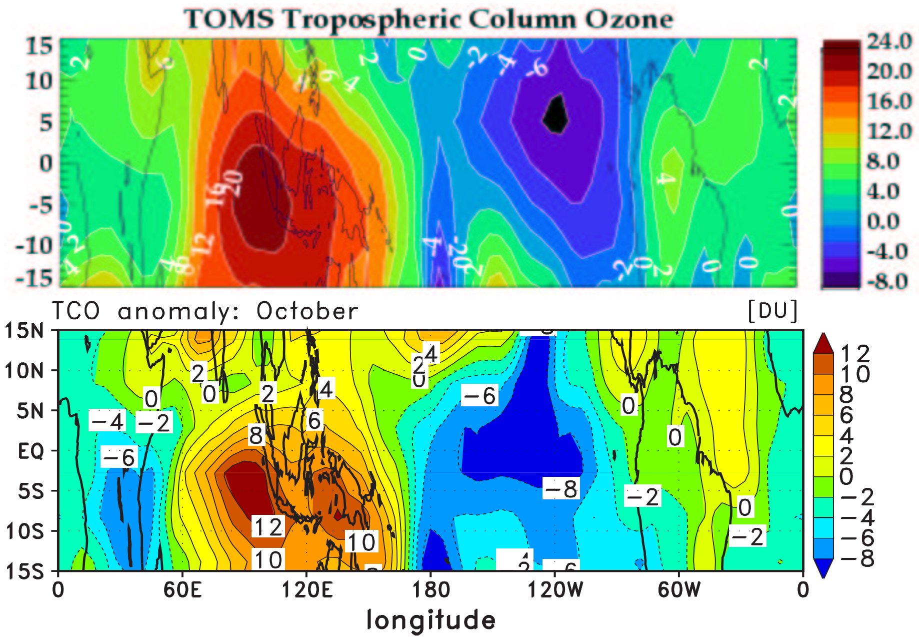

Figure 4.3. Observed and calculated tropical anomalies (1997 minus 1996) in TCO showing the effects of El Niño (1997). (Top) EP TOMS CCD TCO for October (DU) [*Chandra et al.*, 1998], (bottom) model results for October. The model results show TCO anomalies due to meteorological effects only.

[*Chandra et al.*, 1998]. TCO calculated by the model shows the O_3 column integrated from the surface to the tropopause defined as the lowest altitude at which the vertical temperature gradient is greater than -2 K/km in the model. The simulated TCO anomalies in October show an asymmetrical dipole structure centered around the date line with positive anomalies in the western Pacific and Indonesia and negative anomalies in the eastern Pacific, well reproducing the observed changes in TCO in October 1997. The simulated negative anomaly (decrease) in TCO ranges from 2 DU to 8 DU through much of the eastern Pacific, in good agreement with the observed values. The simulation also shows positive TCO anomalies (increase) of 10-12 DU in Indonesia and the Indian Ocean. The peak values of the observed O_3 increase (16-20 DU) are higher than the simulated values (10-12 DU) by 6-8 DU. This underestimation of the simulation may be attributed to the effect of the Indonesian fire emissions [*Fujiwara et al.*, 1999; *Hauglustaine et al.*, 1999; *Thompson et al.*, 2001]. However, it is interesting to note that both the observations and the simulation show a peak over the eastern Indian Ocean and the edge of Sumatra, demonstrating the considerable importance of the El Niño induced meteorological changes for the observed O_3 increase over this region. The observations also show positive anomalies (2-4 DU) over South America, reflecting the effect of changes in the zonal circulation (Walker circulation). Although these observed positive anomalies in South America are not clearly seen in the model results for October, similar positive anomalies (4-8 DU) are calculated by the model over South America in November (not shown).

4.4.2 Implications from simulation

Figure 4.4(a) shows the simulated changes (October 1997 minus October 1996) in the vertical distribution of O_3 averaged over 10°S-10°N. As expected from Figure 4.3, an asymmetrical dipole structure is seen over 60°E-100°W, strongly anti-correlated with the changes in vertical wind velocity and convective cloud mass flux computed in the model with the Arakawa-Schubert convection scheme (Figure 4.4(b)). 70-90% of the simulated TCO changes (Figure 4.3, bottom) comes from O_3 changes below 10 km as shown in Figure 4.4(a). The important factors controlling the O_3 increase over the Indonesian region (70°E-170°E) are downward motion associated with the zonal convergence in the upper troposphere, suppressed convection, and dryness as suggested by *Chandra et al.* [1998]. Anomalous convergence in the upper troposphere prevents produced upper tropospheric ozone from spreading out of the region. And, downward motion, together with suppressed convection, brings O_3 produced in the upper troposphere down, causing O_3 in the lower-middle troposphere to increase. Additionally, the dryness, leading to a longer lifetime for O_3, seems to contribute to the simulated O_3 increase over this region. Since H_2O is the main cause of O_3 loss in the low to middle troposphere [e.g., *Kley et al.*, 1996], the simulated chemical lifetime of ozone increases by 60-100% in the middle troposphere over 70°E-170°E as shown in Figure 4.4(d), anti-correlated with the specific humidity changes of Figure 4.4(c). In the Indonesian region, the chemical lifetime of ozone at 5 km altitude is prolonged typically from $\sim$10 days in October 1996 to $\sim$25 days in October 1997 in the model. The O_3 increase ($>$20 ppbv) in the upper troposphere (higher than 12 km) over the Indonesian region appears to be also associated with the downward motion and suppressed convection leading to less efficient vertical transport of low O_3 air masses from the surface, and possibly to subsidence of stratospheric O_3. These processes are reversed where there is upward motion, enhanced convection, and H_2O increase (170°E-90°W). Upward motion and enhanced convection advect low O_3 and high H_2O upward, resulting in lower O_3 (-5 to -15 ppbv) over this region (Figure 4.4(a)).

Moreover, the simulation indicates that the photochemical O_3 production process is also affected by the El Niño . Here, we focus our attention on the peak region of ozone increase over 10°S-0°. Figure 4.5(a) and (b) show longitude-altitude cross sections (10°S-0°) of the net chemical production (P-L) of O_3 (ppbv/day) simulated for October 1996 and 1997, respectively. In 1997, the O_3-producing area (P-L$>$0) is enlarged downward to 3-4 km over Indonesia. The net O_3 production at $\sim$5 km over Indonesia increases by 1-1.5 ppbv/day, changing from negative (sink) in 1996 to positive (source) in 1997. This enhancement in the net O_3 production in the middle troposphere is due to the H_2O decrease as discussed above and also to increases in O_3 precursors such as nitrogen oxides NO_x ($NO+NO_2$) and carbon monoxide CO (Figure 4.5(c) and (d)) in the low to middle troposphere. The NO_x changes below 8 km appear to be caused by changes in the efficiency of wet deposition of HNO_3 associated with precipitation pattern changes, and also by changes in the NO_x removal by OH (hydroxyl radical) due to H_2O changes. The HNO_3 lifetime against wet

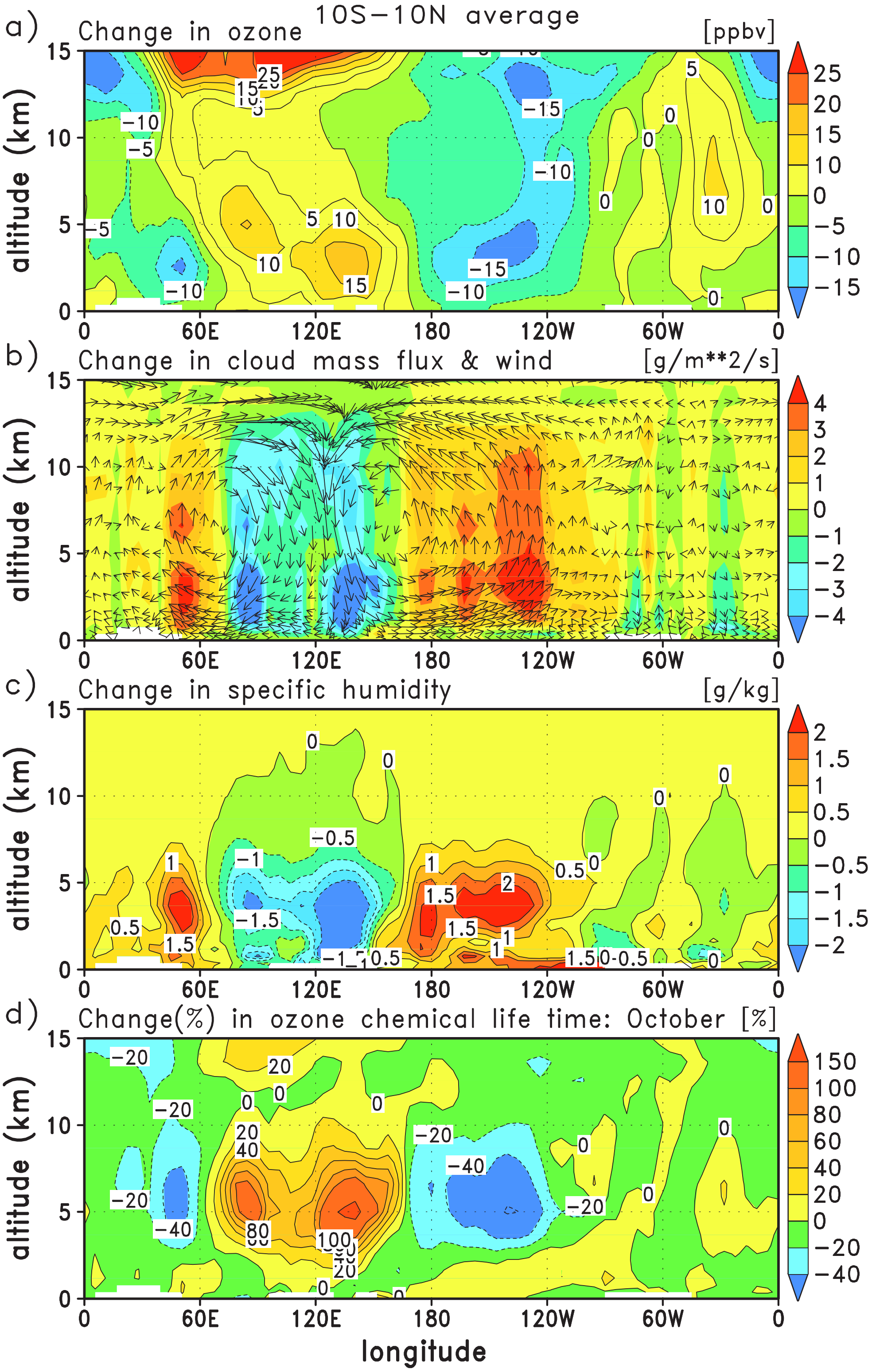

Figure 4.4. Longitude-altitude cross section of simulated anomalies in (a) ozone (ppbv), (b) convective cloud mass flux (g m^{-2} s^{-1}) and wind vector of zonal and vertical velocity (vertical velocity is scaled up by a factor of 1000), (c) specific humidity (g kg^{-1}), and (d) chemical lifetime of ozone (%) averaged over 10°S-10°N. The differences are shown as October 1997 minus October 1996.

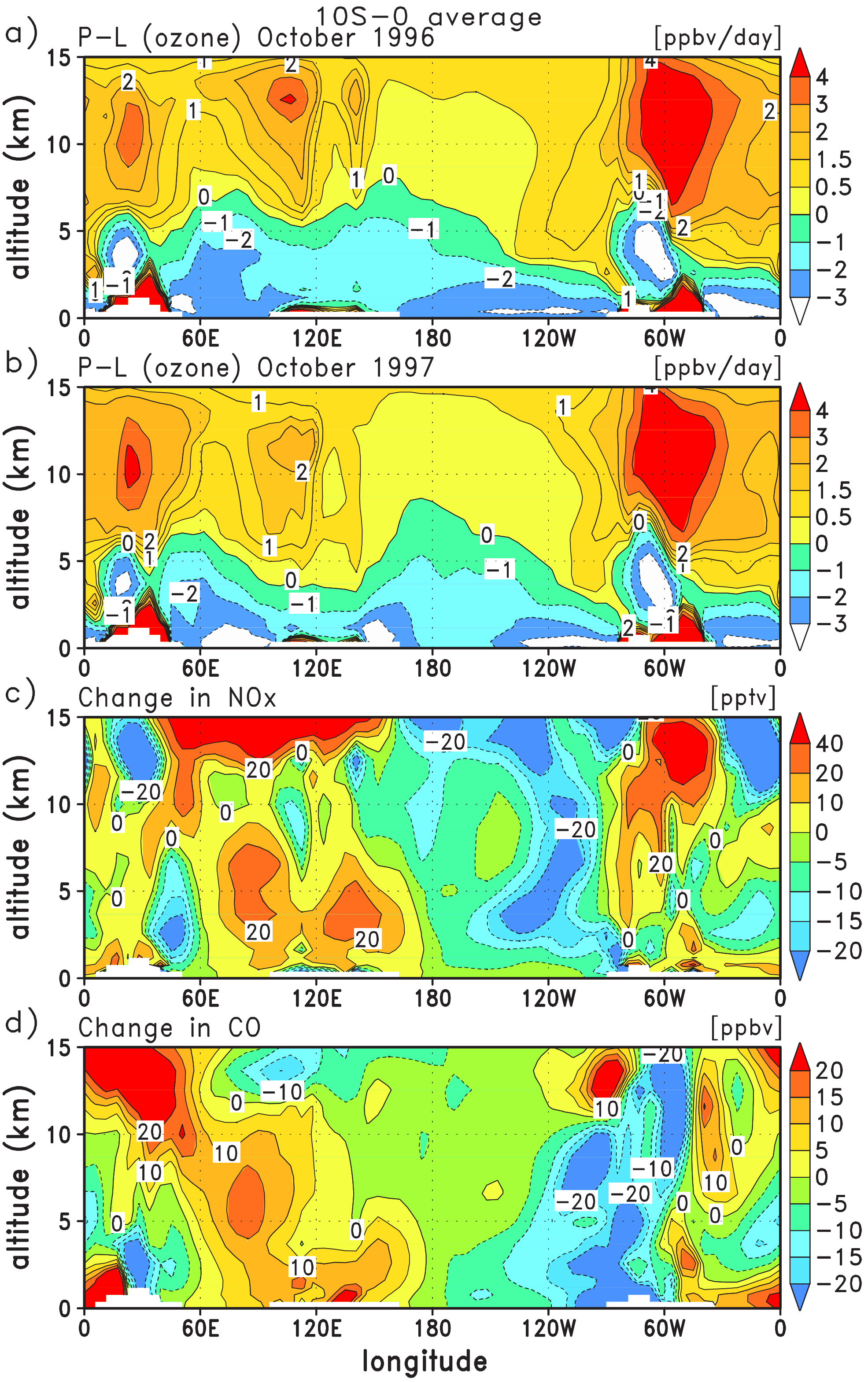

Figure 4.5. Longitude-altitude cross section (10°S-0°) of net chemical ozone production (ppbv/day) simulated (a) for October 1996 and (b) for October 1997, and simulated anomalies in (c) NO_x, and in (d) CO. The anomalies are shown as October 1997 minus October 1996.

deposition averaged over the Indonesian region is prolonged from ∼1 day in October 1996 to 3-5 days in 1997, leading to an increase in HNO_3 by 200-500%. NO_x increases in the upper troposphere (above 12 km) over 70°E-170°E may be due to subsidence of stratospheric NO_x. A slight NO_x decrease (5-10 pptv) at 6-12 km over ∼110°E may be attributed to a decrease in lightning NO_x production over Indonesia due to suppressed convection in the model. In the case of CO, the simulated increases (>10 ppbv) in the lower troposphere over 70°E-170°E appear to be due to suppressed convection and downward motion (Figure 4.4(b)). Figure 4.5(d) also shows CO increases in the middle troposphere over 60°E-120°E. These CO increases appear to be associated with a longer lifetime for CO due to reduced OH levels, and also with enhanced transport from South Africa owing to the changes in the circulation pattern in the tropics as illustrated in Figure 4.4(b). It should also be noted that the net O_3 production in the upper troposphere (>12 km) over Indonesia is weaken in October 1997 by 20-40% (Figure 4.5(b)) in spite of the NO_x increase in this region (c). This arises from decreases in other O_3 precursors such as HO_x ($OH+HO_2$), CO, and hydrocarbons in the model as shown in Figure 4.5(d). In October 1997, upward transport of CO, hydrocarbons, and HO_x precursors such as formaldehyde, acetone, and peroxides to the upper troposphere over the Indonesian region is not efficient due to suppressed convection and downward motion in this region. In the model, HO_x decreases by 50-70% in the Indonesian upper troposphere in October 1997.

4.5 Conclusions

In this study, tropical tropospheric ozone distributions simulated by the CHASER model are compared to those by satellite-based observations using tropospheric ozone residual methods with the TOMS observations. The model well reproduces the zonal wave 1 pattern in tropical TCO, a peak over the Atlantic and a minimum over the Pacific, as observed. The simulation shows that the wave 1 in tropical TCO comes primarily from upper tropospheric ozone production from lightning NO_x emission and biogenic and biomass burning emissions particularly in South America and Africa. The net ozone production calculated in the tropical free troposphere shows positive peaks around South America, Africa, and the Atlantic, with showing negative production (destruction) over the Pacific. The large-scale Walker circulation also appears to contribute much to the wave 1 in TCO. The differences between the observed and modeled TCO distributions increase with latitude especially in the region encompassing North Africa, the Middle East, and India as in the simulation of *Chandra et al.* [2002a] and *Martin et al.* [2002]. Further development of the observational method for deriving tropospheric ozone in higher latitudes outside the tropics [e.g., *Chandra et al.*, 2002b] is expected to contribute to a better comparison with models.

The meteorological impact of the 1997-1998 El Niño on the tropical tropospheric ozone distribution has been also investigated using CHASER in this study. To evaluate the El Niño induced meteorological impact alone, the effect of the 1997 Indonesian fires is ignored intentionally in this simulation. The simulation generally well reproduces the observed ozone anomalies (increase and decrease) in October 1997, though the peak values in the ozone anomaly over the Indonesian region are underestimated by the model due to lack of consideration of the 1997 Indonesian fire emissions. The key factors controlling the simulated ozone changes are (1) the downward/upward motions associated with the zonal convergence/divergence in the upper troposphere, (2) the suppressed/enhanced convection, and (3) the associated water vapor (H_2O) changes in the tropics.

In the simulation, 70-90% of the calculated change in tropospheric column ozone is caused by O_3 changes below 10 km altitude. The simulation shows that the O_3 increases below 10 km over the Indonesian region are related also to enhanced O_3 production in the middle troposphere due to increase in NO_x and other O_3 precursors associated with meteorological changes such as suppressed convection, downward motion, dryness, and reduced precipitation in this region. Transport of the O_3 precursors from African biomass burning into this region also appears to enhance in 1997, owing to changes in the Walker circulation. As the previous study of *Chandra et al.* [1998] suggests, O_3-producing air mass appears to increase in this region in the model, due to the increase in precursor and largely prolonged ozone chemical lifetime (by a factor of $\sim$2). On the contrary, in the upper troposphere over Indonesia, simulated O_3 production decreases by 20-40% owing to reduced injection of O_3 precursors associated with suppressed convection and downward motion in the region. Consequently this model simulation suggests that the effect of the 1997 Indonesian fire (not considered in this study) on O_3 production is most significant in the lower troposphere (especially in the boundary layer), and is less significant in the upper troposphere.

The above simulations of tropical ozone distributions imply that tropospheric ozone and related chemistry are significantly controlled by natural meteorological conditions such as large-scale and convective transport, and water vapor distributions. They also suggest an importance of climate change in predicting the future tropospheric chemistry.

Chapter 5

Future Distributions of Tropospheric Ozone and Sulfate Aerosol

5.1 Introduction

Ozone (O_3) in the troposphere plays key roles in both the climate system and the atmospheric environment. Tropospheric ozone itself is a significant greenhouse gas absorbing both terrestrial and solar radiation [*Wang et al.*, 1980; *Lacis et al.*, 1990], and also strongly controls the chemical lifetimes of other greenhouse gases, CH_4 and HFCs, through formation of hydroxy radical OH (oxidizing capacity of the atmosphere). In contrast with the beneficial role of stratospheric ozone, tropospheric ozone is highly reactive and destructive, causing considerable damages on vegetation including agricultural crops and the human health. In addition, tropospheric chemistry involving ozone has a critical importance in formation of sulfate aerosol which has also large impacts on climate [*Houghton et al.*, 1996] and the atmospheric environment, especially acid deposition [*Langner and Rodhe*, 1991]. Many previous studies have suggested that tropospheric ozone increases significantly since preindustrial times, in accordance with dramatical increases in anthropogenic emissions especially in the northern hemisphere [*WMO*, 1990; *Crutzen and Zimmermann*, 1991; *Staehelin et al.*, 1994; *Marenco et al.*, 1994; *Levy et al.*, 1997; *Wang and Jacob*, 1998d]. Increases in tropospheric ozone are also estimated to have caused a global mean radiative forcing of 0.3-0.6 W m^{-2} since preindustrial times [*WMO*, 1999; *Mickley et al.*, 2001, etc.], comparable with the estimated CH_4 forcing 0.5 W m^{-2} [*Houghton et al.*, 1995]. Since the contribution from both O_3 and CH_4 increases to the total radiative forcing is of the same magnitude as from CO_2 increase (1.6 W m^{-2}), tropospheric ozone and CH_4 are expected to have a large importance in the future climate system.

Although future CH_4 and HFCs concentrations depend primarily on direct emissions, tropospheric ozone chemistry, involving OH abundances, also has a large 'indirect' impact on those concentrations, strongly controlling chemical lifetimes of CH_4 and HFCs in the atmosphere. For instance, increases in carbon monoxide (CO), together with increases in CH_4 itself, cause OH decreases which lead to a longer CH_4 lifetime (indirect warming) [*Prather*, 1994], while increasing concentrations of NO_x and/or O_3 oppositely enhance OH and lead to a shorter CH_4 lifetime (indirect cooling) [*Johnson et al.*, 1999; *Wild et al.*, 2001b]. Such indirect effects of tropospheric chemistry have been shown to make a significant contribution to the total radiative forcing [*Hauglustaine et al.*, 1994; *Johnson and Derwent*, 1996; *Fuglestvedt et al.*, 1996; *Daniel and Solomon*, 1998; *Wild et al.*, 2001b]. CH_4 concentrations, in turn, control tropospheric chemistry, largely determining OH levels and ozone production in the troposphere. We should, therefore, evaluate both CH_4 and tropospheric ozone chemistry concurrently with considering interactions between them, for an accurate future prediction. Similarly, formation of sulfate aerosol which has also important direct (sunlight scattering) and indirect (cloud condensation nuclei, CCN) climate effects is much controlled by tropospheric chemistry (mainly by O_3, H_2O_2, and OH), so that evaluation coupled with tropospheric chemistry is needed to assess the future sulfate distribution and its impact on climate.

Future tropospheric ozone appears to depend largely on emissions of precursor gases (NO_x, CO, and hydrocarbons) [*van Dorland et al.*, 1997] as well as CH_4. Future emission increases are expected particularly in developing countries located in the low latitudes [*Intergovernmental Panel on Climate Change (IPCC)*, 2001]. As the impact of emission changes on the global ozone distribution is most significant in the low latitudes as in southeastern Asia due to high ozone production efficiency and rapid intercontinental transport of ozone and precursors [*Wild and Akimoto*, 2001a], the predicted emission increases in developing countries in the low latitudes are likely to have a large importance for future ozone distributions. However, the effect of future climate change should be also taken into account for future ozone distributions, since tropospheric chemistry involving ozone formation and destruction is much affected by meteorological conditions such as water vapor, temperature, clouds, and atmospheric dynamics [*Thompson et al.*, 1989; *Fuglestvedt et al.*, 1995; *Johnson et al.*, 1999; *Grewe et al.*, 1999; *Stevenson et al.*, 2000; *Johnson et al.*, 2001]. For example, the simulation study of *Johnson et al.* [2001] suggested that future tropospheric ozone increases owing to emission changes may be reduced due to water vapor increases associated with climate change. Their simulation also indicated reduction in future CH_4 increases by climate change. The impact of changes in meteorological conditions has also been suggested in a simulation of El Niño induced tropospheric ozone changes [*Sudo and Takahashi*, 2001] (chapter 4). The simulation has revealed the critical roles of water vapor distribution, convection, and large-scale circulation in the tropical ozone distributions.

This study simulates future tropospheric ozone and sulfate distributions for the next hundred years to 2100 using a coupled chemistry general circulation model (GCM), named CHASER. Ozone and sulfate aerosol in the troposphere, having much short residence times relative to other principal greenhouse gases, are controlled by emissions of precursors and also by meteorological conditions (climate) as described above. Both effects of emission changes and climate change are evaluated in this study. In this study, emission changes and climate change are considered following the IPCC SRES (Special Report on Emission Scenarios) A2 scenario (a ‘high’ case). This study simulates future climate change and tropospheric chemistry involving ozone and sulfate for every ten years from 1990 to 2100 (time-slice simulations). CH_4, not transported in the model in this study, is prescribed by time-integrating the global CH_4 tendency associated with emission based on the SRES A2 scenario and with CH_4 lifetime determined from the calculated OH abundances for every ten years. The simulations in this study do not consider likely future changes in hydrocarbon emissions from vegetation and stratospheric ozone abundances, but evaluate changes in lightning NO_x emissions due to climate change (warming) as suggested by *Price and Rind* [1994]. The CHASER model, employed in this study, has been developed in the framework of the Center for Climate System Research (CCSR), University of Tokyo/National Institute for Environmental Studies (NIES) atmospheric GCM (AGCM). *Takemura et al.* [2002] have simulated future distributions of aerosols including sulfate with the CCSR/NIES aerosol model [*Takemura et al.*, 2000] for the next fifty years to 2050. Their study, however, considers emission changes only, using fixed meteorological conditions and concentrations of O_3, H_2O_2 and OH as prescribed in a present-day simulation. Since the present version of CHASER simulates the sulfate formation process on-line, the chemical impact of changes in O_3, H_2O_2, and OH on sulfate formation is also examined in this study.

The following sections begin with the description of the CHASER model and experiments (section 5.2). This section describes the emission scenario, experimental methodology, and future climate predicted by the CCSR/NIES GCM. Section 5.3 discusses the simulated future ozone changes (section 5.3.1), time evolution of CH_4 (section 5.3.2), sulfate changes (section 5.3.3), and future acid deposition of NO_3^- and SO_4^{2-} (section 5.3.4). Conclusions from this study are presented in section 5.4.

5.2 Model description and experimental setup

5.2.1 Global chemical model

This study employs the CCSR/NIES coupled chemistry model CHASER [*Sudo et al.*, 2002a], developed in the framework of the CCSR/NIES atmospheric GCM (AGCM) [*Numaguti*, 1993; *Numaguti et al.*, 1995]. CHASER, driven on-line by meteorology generated by the AGCM, calculates the chemistry and radiation processes interactively, considering the short-term correlations between meteorological variables (e.g.,temperature) and chemical fields such as ozone distributions in the AGCM. The model simulates detailed O_3-HO_x-NO_x-CH_4-CO and NMHCs chemistry on-line with a time step of 10 min (section 2.2.1), and includes also detailed dry/wet deposition schemes (section 2.2.3). The CHASER model version adopted in this study is basically identical to that described in the previous chapter (chapter 2). This version of CHASER, based on the CCSR/NIES AGCM, version 5.6, newly includes an improved wet deposition scheme, heterogeneous reactions on aerosols for N_2O_5 and several peroxyradicals RO_2, and also the sulfate formation process (section 2.2.1), compared to the previous version [*Sudo et al.*, 2002a]. The new wet deposition scheme adopted in the present CHASER includes deposition on ice (for HNO_3 and H_2O_2 in this study) and reversible scavenging process below clouds to enable the prediction of liquid-phase concentrations of species dissolved in precipitation (section 2.2.3). Sulfate formation due to gas and liquid phase oxidation of SO_2 and DMS is simulated in the model, using concentrations of O_3, H_2O_2, and OH computed on-line in the model. The pH values ($[H^+]$) in cloud drops, necessary for the calculation of the liquid-phase reactions of SO_2, are estimated with aqueous-phase concentrations of NO_3^-, HSO_3^-, SO_3^{2-}, and SO_4^{2-} in cloud drops in the model (Appendix 2B, page 106). Note that the model version does not consider sulfate radiative forcing on climate in the AGCM, only simulating sulfate distributions. Sulfate simulation is implemented and used for the heterogeneous reactions considered in the model, but not linked to the AGCM radiation component in this version.

For this study, the horizontal resolution of T42 ($2.8^\circ \times 2.8^\circ$) is adopted with 32 layers to about 40 km altitude ($\sim$ 1km vertical resolution in the lower stratosphere and the upper troposphere). The model calculates the concentrations of 53 chemical species with 139 reactions (photolytic, gas/liquid-phase, and heterogeneous) from the surface to about 20 km altitude. The concentrations of stratospheric O_3, NO_x, HNO_3, and N_2O_5 above 20 km altitude are prescribed using monthly averaged output data from a three-dimensional stratospheric chemical model [*Takigawa et al.*, 1999]. For the O_3 distribution ($>$ 20 km), the data of *Takigawa et al.* [1999] were scaled by using zonal mean satellite data from the Halogen Occultation Experiment project (HALOE) [*Russel et al.*, 1993; *Randel*, 1998]. In this study, CHASER considers emission sources for NO_x, CO, NMHCs, SO_2, and DMS, including lightning NO_x emissions linked to the AGCM convection with the parameterization of *Price and Rind* [1992] and *Price et al.* [1997] (see section 2.2.2). Note that oceanic emissions of acetone as described in section 2.2.2 are not considered in this study.

In CHASER, advective transport is simulated by a 4th order flux-form advection scheme of the monotonic van Leer [*van Leer*, 1977], except for the vicinity of the poles. For a simulation of advection around the poles, the flux-form semi-Lagrangian scheme of *Lin and Rood* [1996] is used. Vertical transport associated with moist convection (updrafts and downdrafts) is simulated in the framework of the cumulus convection scheme (the prognostic Arakawa-Schubert scheme) in the AGCM. In the boundary layer, equations of vertical diffusion and surface emission and deposition fluxes are solved implicitly. The transport process in CHASER is evaluated in *Sudo et al.* [2002a] (also in Appendix 2A).

In the detailed model evaluation (*Sudo et al.* [2002b] and section 2.3), good agreements between the CHASER calculations and observations are found for O_3 and precursor species including HO_x radicals in a present-day simulation. The global CH_4 lifetime estimated by the present-day simulation with CHASER is 9.4 years, well within the range of the recent estimates [e.g., *Prather et al.*, 2001]. Detailed description and evaluation of the present model version of CHASER are shown in chapter 2.

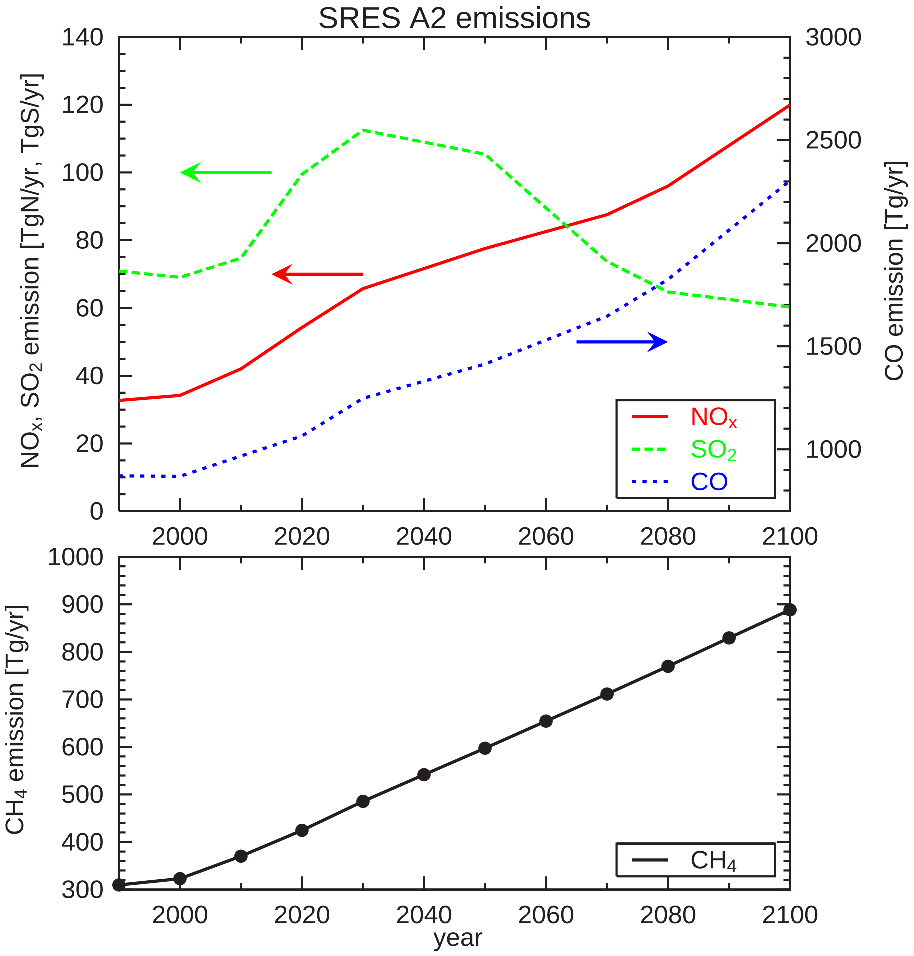

Figure 5.1. Future global anthropogenic emissions of NO_x (TgN/yr), CO (Tg/yr), SO_2 (TgS/yr), and CH_4 (Tg/yr) prescribed by the IPCC SRES A2 scenario.

5.2.2 Emissions

In this study, future emissions of precursor gases are prescribed following the IPCC SRES A2 scenario [*IPCC, 2001*]. The SRES scenario provides the spatial and temporal evolution of anthropogenic emissions of NO_x, CO, CH_4, non-methane hydrocarbons NMHCs, and SO_2. The scenario A2, a high case, has high population growth, moderate, regionally heterogeneous income and technology developments, and generates large emissions increases. The scenario shows highest emissions growth in the third world, with modest growth or reduction in emissions from the developed world.

The CHASER model, used in this study, considers surface emissions of NO_x, CO, NMHCs (C_2H_6, C_2H_4, C_3H_8, C_3H_6, acetone, isoprene, and terpenes), SO_2 and DMS (dimethylsulfide). All anthropogenic emissions from industry and biomass burning for the future simulations in this study are prescribed depending on the A2 scenario. Seasonal variation of biomass burning emissions, not included in the SRES scenarios, is imposed using the hot spot distributions derived from Advanced

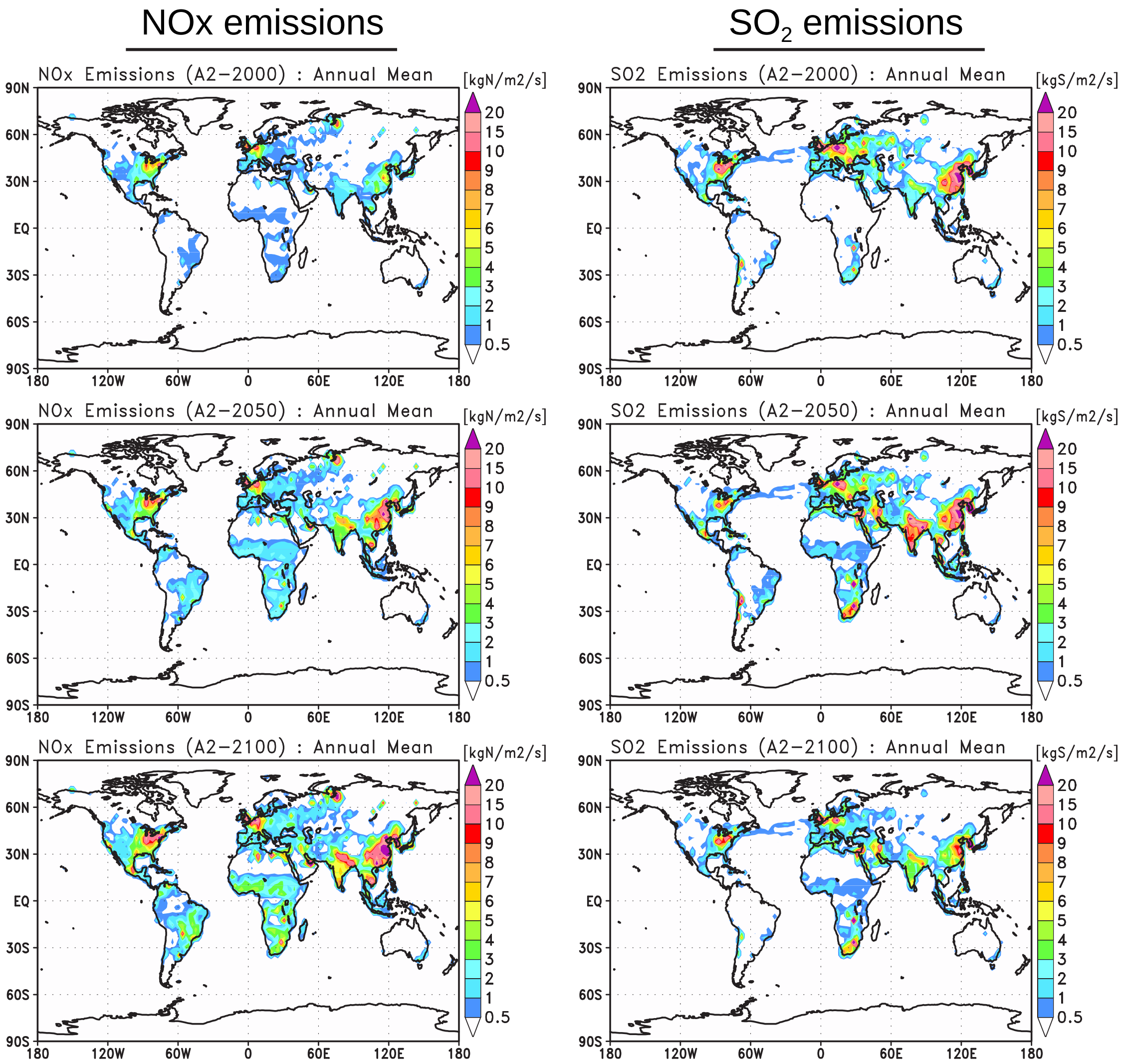

Figure 5.2. Annual mean anthropogenic emission rates of NO_x and SO_2 prescribed by the A2 scenario for 2000, 2050, 2100.

Very High Resolution Radiometer (AVHRR) and Along Track Scanning Radiometer (ATSR) [*Arino et al.*, 1999] as in present-day simulations (see section 2.2.2). Since the SRES scenario only predicts the total amount of NMHCs emissions, future emissions of individual NMHCs species considered in this study are given using the ratio of total NMHCs emission for every future time period to that for 1990. Individual NMHCs emissions for 1990 in the simulation are identical to those described in section 2.2.2. Changes in NO_x emissions from aircraft are also prescribed, using NASA inventories [*Penner et al.*, 1999]. Figure 5.1 shows the global anthropogenic emissions of NO_x, CO, SO_2, and CH_4 prescribed by the A2 scenario to 2100. In this scenario, NO_x , CO, and CH_4 emissions increase almost linearly, leading to treble emissions in 2100 relative to 1990, while SO_2 emission decreases after a peak during 2030-2050, being lower in 2100 than 1990. According to the A2 scenario, emission increases are most significant in eastern Asia (Figure 5.2). NO_x emissions in India, Thailand, and China increase more than three times in 2050 and 5-10 times in 2100 relative to 2000. Large increases are also seen in South America and Africa associated with industry and biomass burning. NO_x emissions in the developed countries (United States and Europe) increase moderately (+20-50% in 2100). In the case of SO_2, strongest emission growth is predicted in India in 2050 with increases by a factor of $\sim$5, whereas SO_2 emissions in the United States, Europe, and China decline slowly in this scenario. Natural emissions from vegetation, soil, ocean, and volcanos are specified as in *Sudo et al.* [2002a] (section 2.2.2) except for acetone emissions from ocean, which are not included in this study. Lightning NO_x emissions, parameterized with the AGCM convection, are adjusted to be 5 TgN/yr in the simulation without climate change (EXP1, see below, section 5.2.3), but are predicted on-line in the simulation with climate change (EXP2) to account for the warming effect on convection [*Price and Rind*, 1994].

5.2.3 Experiments

In this study, future simulations for the 21st century are performed, focusing on tropospheric ozone and sulfate distributions. The simulations employ the global chemical model CHASER driven on-line by the CCSR/NIES atmospheric GCM (described above). Future simulations are conducted depending on the SRES A2 scenario in this study. The model uses the horizontal resolution of T42 ($\sim 2.8^\circ \times 2.8^\circ$) with 32 layers in the vertical through the simulations in this study. Since this adopted spatial resolution, relatively higher than the previous studies [*Stevenson et al.*, 2000; *Johnson et al.*, 2001], appears to require much computational time for a long-term simulation as considered in this study, the future simulations are opted to be performed for every ten years from 1990 to 2100 (time-slice simulation) in this study. The model is time-integrated for two years including one year spin-up with respect to individual years of 1990, 2000, 2010, $\cdots$, 2100.

To evaluate impacts of emission change and of climate change independently, this study conducts two experiments; a control experiment (Exp1) and a climate change experiment (Exp2). In the control experiment (Exp1), the GCM simulates present-day meteorological conditions, but in the second experiment (Exp2) it simulates climate change using greenhouse gases evolving with the IPCC SRES A2 scenario. In the latter (Exp2), other forcing factors such as sea surface temperatures (SST) and sea ice distributions are also prescribed by the transient simulations with the CCSR/NIES coupled atmosphere-ocean GCM [*Emori et al.*, 1999; *Nozawa et al.*, 2001] (with no flux adjustment) for the SRES A2 scenario. Anthropogenic trace gas emissions of CO, NO_x, CH_4, NMHCs, and SO_2 in both experiments are prescribed by the SRES A2 scenario as described above (section 5.2.2). In Exp2, lightning NO_x emissions are prognostically calculated, but are adjusted to 5 TgN/yr in Exp1 as mentioned above. In Exp2, concentrations of CO_2, N_2O, and HFCs for the GCM radiation computation are prescribed by the SRES A2 scenario, while calculated O_3 distributions are used on-line. In the case of CH_4, global concentrations are predicted depending on the

A2 CH_4 emissions and chemical lifetimes for every decades. In specific, global CH_4 burden in the troposphere T_{CH_4} (Tg) for the next decade is calculated by time-integrating the following tendency:

$$\frac{dT_{CH_4}}{dt} = \underbrace{(E_a + E_n)}_{source} - \underbrace{(\beta_c + \beta_s + \beta_d) \cdot T_{CH_4}}_{sink} \tag{5.1}$$

with E_a the anthropogenic CH_4 emission (Tg/yr) specified by the SRES A2 scenario, E_n the natural CH_4 emission, β_c, β_s, and β_d the loss rates (yr^{-1}) due to the reaction with tropospheric OH, transport to the stratosphere, and deposition at the surface, respectively. In this study, natural emission E_n is taken to be 256 Tg/yr [*Prather et al.*, 2001] (kept constant from 1990 to 2100). The chemical loss rate β_c is given using global OH concentrations and temperatures calculated for every decades. The loss rate due to other loss processes $(\beta_s + \beta_d)$ is opted to be 1.5×10^{-2} (yr^{-1}) corresponding to a lifetime of 66 years [*Prather et al.*, 2001]. Predicted burden T_{CH_4} is converted to global CH_4 mixing ratios for the radiation and chemistry calculations in the next decade simulation. The conversion considers the CH_4 contrast between the northern and southern hemispheres, assuming 5% larger CH_4 burden in the northern hemisphere. In both Exp1 and Exp2, this procedure to predict CH_4 concentrations is repeated for every decades from 2000 to 2100 with updating E_a and β_c. The CH_4 time-integration begins with a global mean concentration of 1.7 ppmv in 1990 in this study.

Note that the sulfate simulation in the model, not linked to the GCM radiation calculation, is not reflected on climate forcing in the GCM in Exp2. Neither Exp1 nor Exp2 considers future changes in stratospheric ozone abundances, using the same stratospheric ozone distributions as prescribed in a present-day simulation as described above.

5.2.4 Future climate

In the climate change experiment (Exp2), future climate change is simulated with greenhouse gases and other forcings (SST and sea ice distributions) derived from the SRES A2 scenario and the CCSR/NIES coupled ocean-atmosphere GCM [*Nozawa et al.*, 2001] as described above. It should be noted that the CCSR/NIES coupled ocean-atmosphere GCM, which is used to derive future SST and sea ice distributions in this study, has high climate sensitivity in future climate change (global warming) experiments and tends to generate surface temperature increases larger than other models [*Nozawa et al.*, 2001]. Figure 5.3 shows the increases in global mean surface temperature predicted in Exp2 in this study. The model predicts a global mean temperature increase of $\sim$5 (K) in 2100. Note that this simulation, being time-slice, may display some differences in future climate from a transient simulation as [*Nozawa et al.*, 2001]. It is, however, possible that the temperature changes calculated in this study as shown in Figure 5.3 may be overestimated due to the high climate sensitivity of the CCSR/NIES coupled ocean GCM (i.e., overestimation of SST increases). Temperature increase predicted in the troposphere is most significant in the low latitudes, reaching $+10$ (K) in the upper troposphere in 2100 (Figure 5.4). In the simulation, larger temperature increases in the low latitudes intensify the Hadley Circulation and thereby subtropical

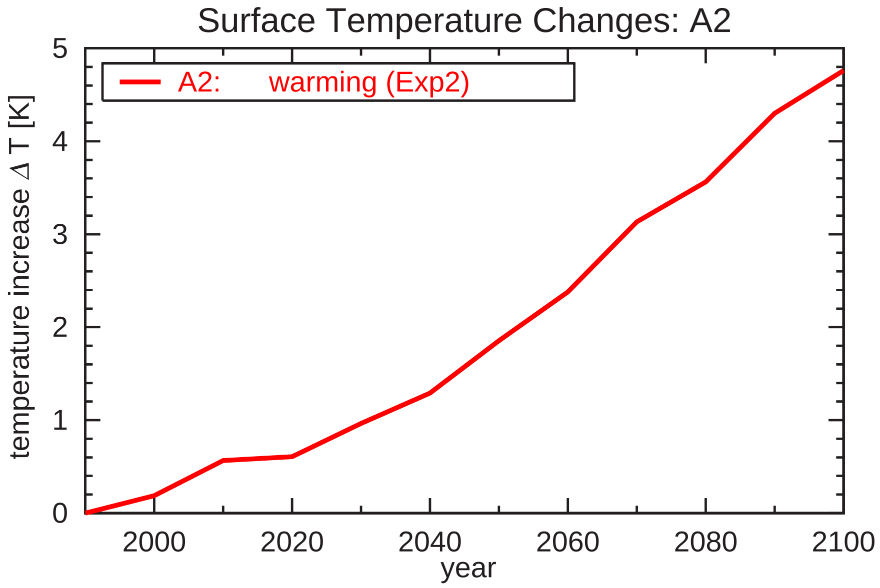

Figure 5.3. Simulated increases in the global mean surface temperature with the SRES A2 scenario.

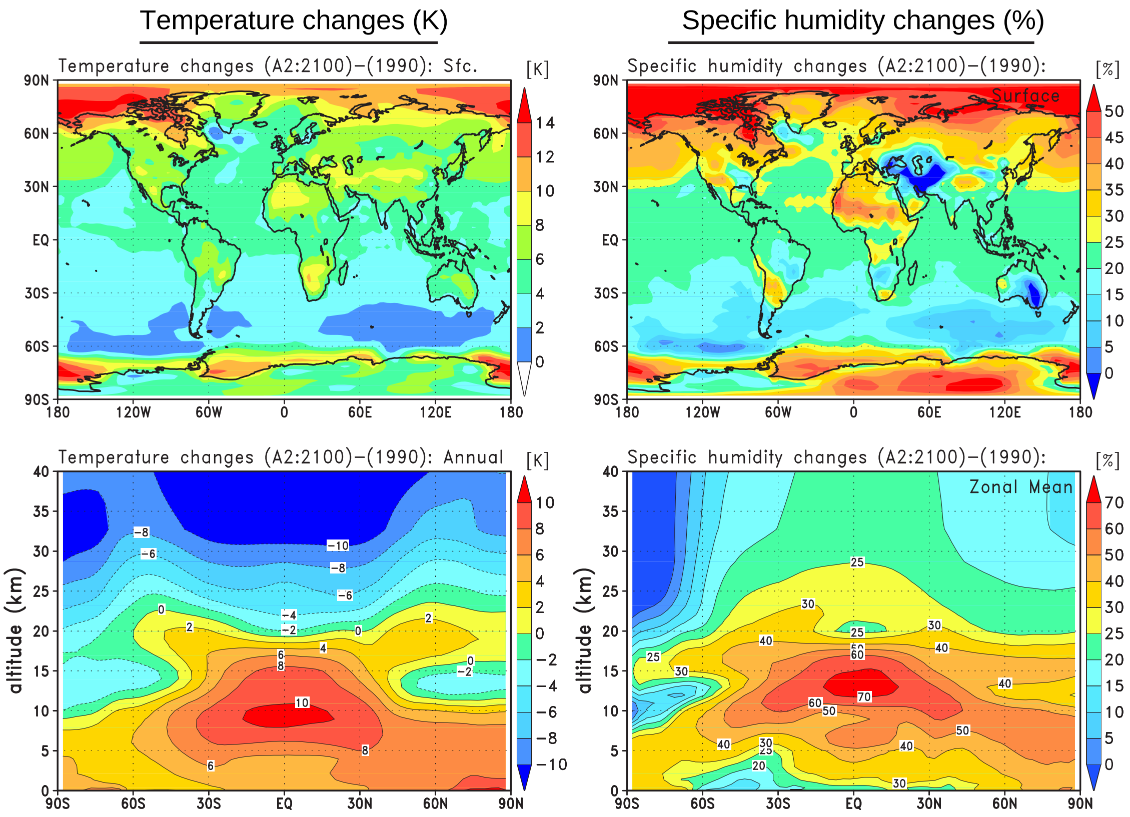

Figure 5.4. Simulated changes in annual mean temperatures (K) and specific humidities (%) in 2100 relative to 1990 with the SRES A2 scenario. (Top): surface, (bottom): zonal mean.

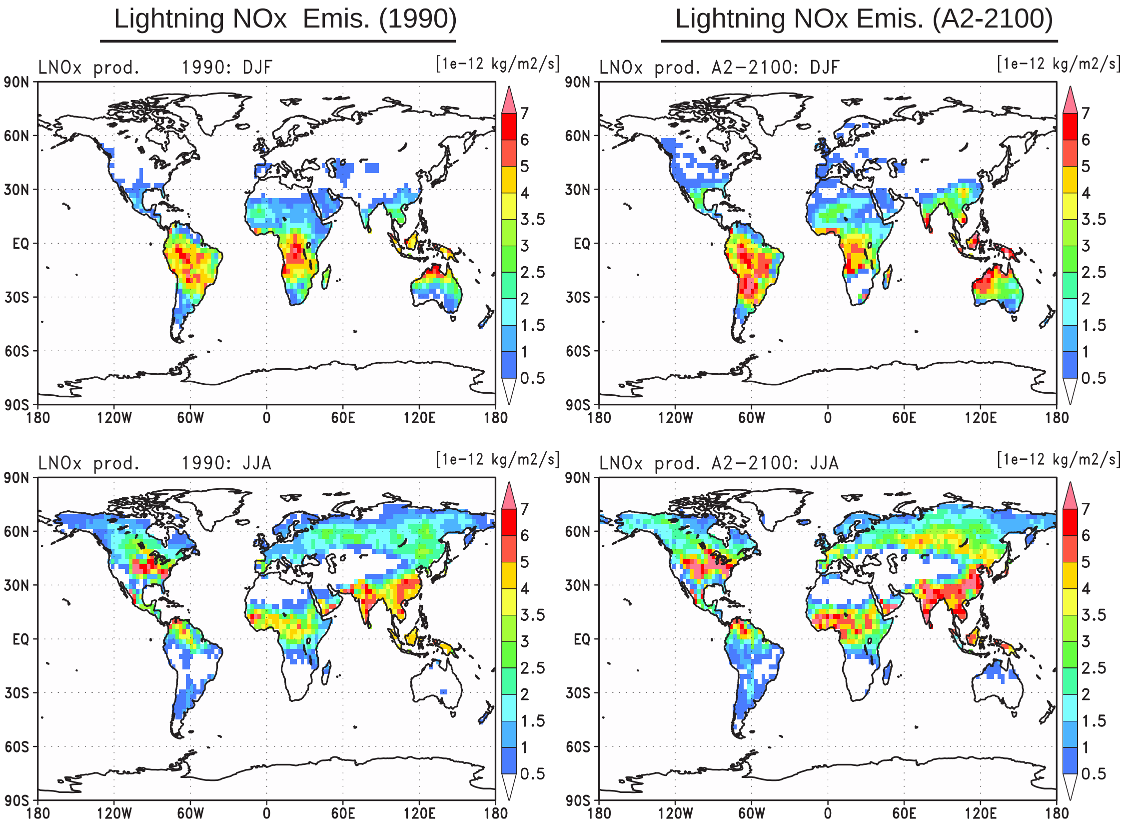

Figure 5.5. Lightning NO_x emissions calculated for 1990 and 2100 with the SRES A2 scenario in DJF and JJA. Values are in column total for each grid.

jet. On the contrary, temperature decreases (cooling) are predicted in the stratosphere (above 20 km) as seen in Figure 5.4. At the surface in 2100, temperature increases of 5-15 (K) are predicted through much of the northern hemisphere with larger increases in the high latitudes (>60°N) due to reduction or disappearance of ice. In accordance with the temperature increases, water vapor also increases particularly in the upper troposphere (+50-70%). The model predicts water vapor increases also in the stratosphere (<20%).

Although moist convection may be expected to be enhanced due to increases in temperature and water vapor, the simulation for 2100 predicts reduction of 10-30% in convective cloud mass flux below 8 km altitude relative to the simulation for 1990. However, convective cloud-top heights in the model become higher as tropospheric temperatures increase. As a result of the rise in cloud-top height, NO_x emissions from lightning increase in Exp2, since the lightning NO_x emission efficiency parameterized with the GCM convection [*Price and Rind*, 1992; *Price et al.*, 1997] is much sensitive to the cloud-top height rather than the cloud scale (i.e., mass flux). Figure 5.5 is an example to show the differences in lightning NO_x emissions due to climate change in the model. Lightning NO_x emissions calculated in 2100 are generally larger than those in 1990 in both summer and winter. Large increases of +50-100% are found in the monsoon regions as southeastern Asia and the high latitudes over the Eurasian Continent in summer. In global and annual total, NO_x emission from lightning increases from 5 TgN/yr in 1990 to 6.1 TgN/yr in 2100 (+21%), indicating a ∼4% change for every 1 K global warming. This appears to be consistent with the sensitivity experiments of *Price and Rind* [1994] which suggest 5-6% changes in lightning frequency for every 1 K global warming/cooling. It should be noted that several studies have suggested also a link between aerosol concentrations and lightning frequency. *Lyons et al.* [1998] measured increased cloud-to-ground lightning in air contaminated with smoke from Mexican forest fires. *Westcott* [1995] found that the frequency of cloud-to-ground lightning increased 40-85% downwind of many cities relative to upwind. Those may suggest another possibility of lightning NO_x increasing in the future atmospheres.

5.3 Results and discussion

5.3.1 Ozone

Distributions

Figure 5.6 shows the distributions of surface O_3 and tropospheric column O_3 simulated for 2000, 2050, and 2100 in Exp1 with no climate change. Surface O_3 levels, generally lower than 50 ppbv in 2000, increase in accordance with the SRES A2 scenario. Particularly large O_3 increases are predicted in the region encompassing India and the Middle East. Annual mean O_3 concentrations around India increase from ∼50 ppbv in 2000 to 60-70 ppbv in 2050, and to 80-90 ppbv in 2100. Surface O_3 increases are also calculated in North America in the low latitudes including Mexico (+20 ppbv in 2100 relative to 2000). In eastern Asia including India and China, the number of days with daily averaged O_3 levels higher than the environmental standard for O_3 (usually =60 ppbv) of the year increases largely in each grids toward 2100. For example, the number of days of high surface O_3 levels above 60 ppbv calculated around India and China increases from 30-60 days/yr in 2000 to 100-180 days/yr in 2050, and to 210-320 days/yr in 2100. O_3 pollution around these regions (also including North America in the low latitudes) is most significant in spring to summer. Increases in O_3 production in those areas also influence O_3 levels in the remote oceans. Over the oceans in the northern hemisphere, surface O_3 levels, ranging from 25-35 ppbv in 2000, increase by ∼5 ppbv in 2050, and by ∼10 ppbv in 2100. Similarly, increases in O_3 production in South America and South Africa appears to contribute largely to the O_3 increases in the southern midlatitudes. It should be noted that surface O_3 in Australia increases despite the emission reduction in Australia in this A2 scenario, being subject to large-scale transport of O_3 pollution. Significant increase is also seen in tropospheric column O_3. Large column O_3 changes are predicted in the low to midlatitudes particularly in the northern hemisphere, with peak increases extending over the Middle East, India, and North Africa (+10 DU in 2050 and +20 DU in 2100). Column O_3 in other remote regions also

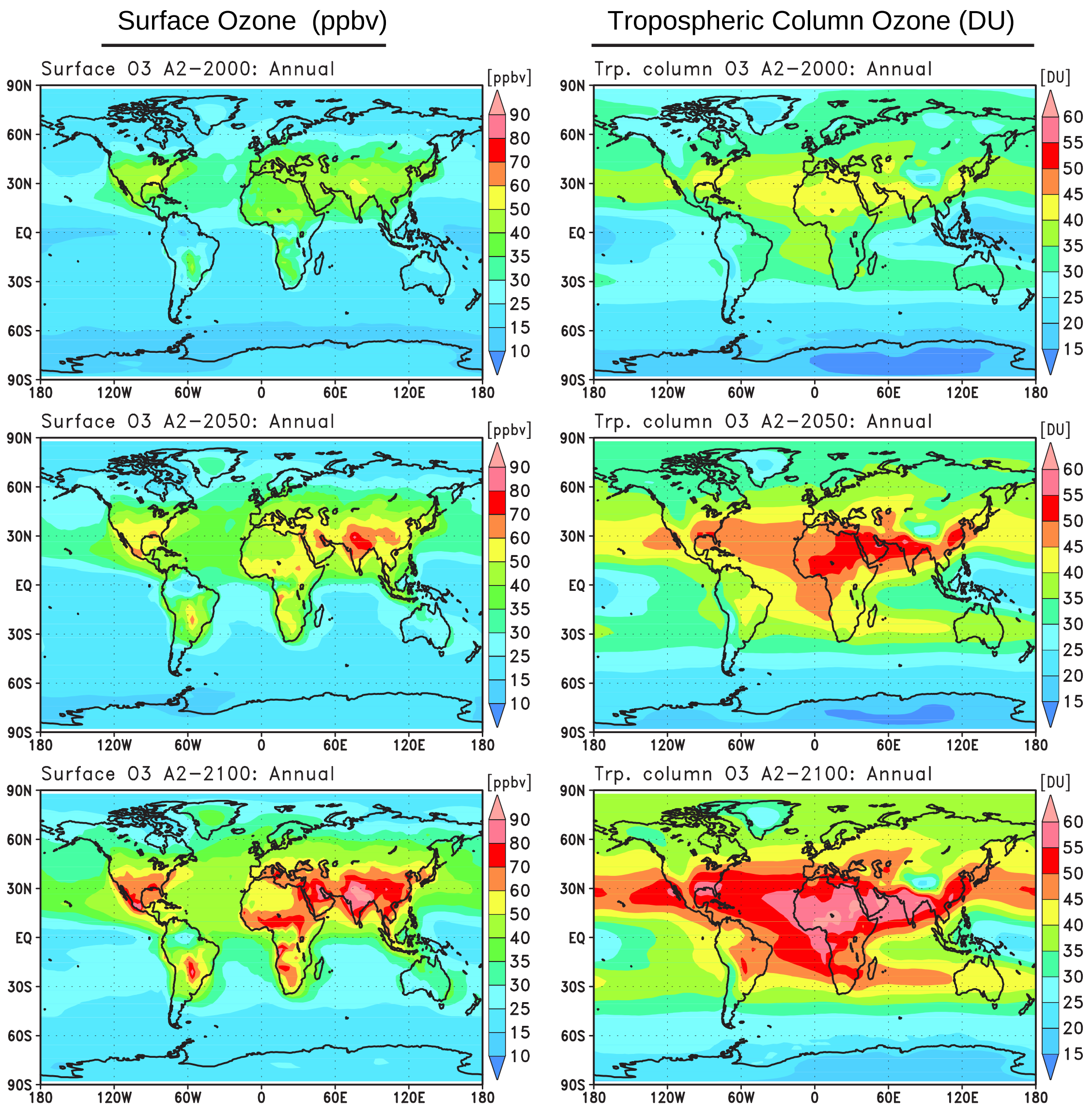

Figure 5.6. Distributions of surface ozone and tropospheric column ozone simulated for 2000, 2050, and 2100 with the SRES A2 scenario in Exp1 (no climate change).

increases 20-30% in 2050 and ∼50% in 2100. In the southern hemisphere, the O_3 plume over the Indian Ocean from Africa toward Australia is largely enhanced (+10-15 DU in 2100)

Figure 5.7 shows the zonal mean ozone concentrations for 1990 to 2100 predicted in Exp1 (control) and Exp2 (climate change, warming). Exp1 calculates linear O_3 increases in all cases leading to +40-50% in 2100, whereas Exp2 displays some differences particularly after around 2050. At 800hPa, O_3 increases predicted in Exp1 are reduced 10-20% after 2050 in Exp2, due to increases in water vapor associated with warming in Exp2. This kind of reduction in O_3 increase is also seen at 500hPa in the northern hemisphere. However, Exp2 predicts larger O_3 increases for 500hPa in the southern hemisphere and for 300hPa relative to Exp1. The O_3 increases in the upper troposphere

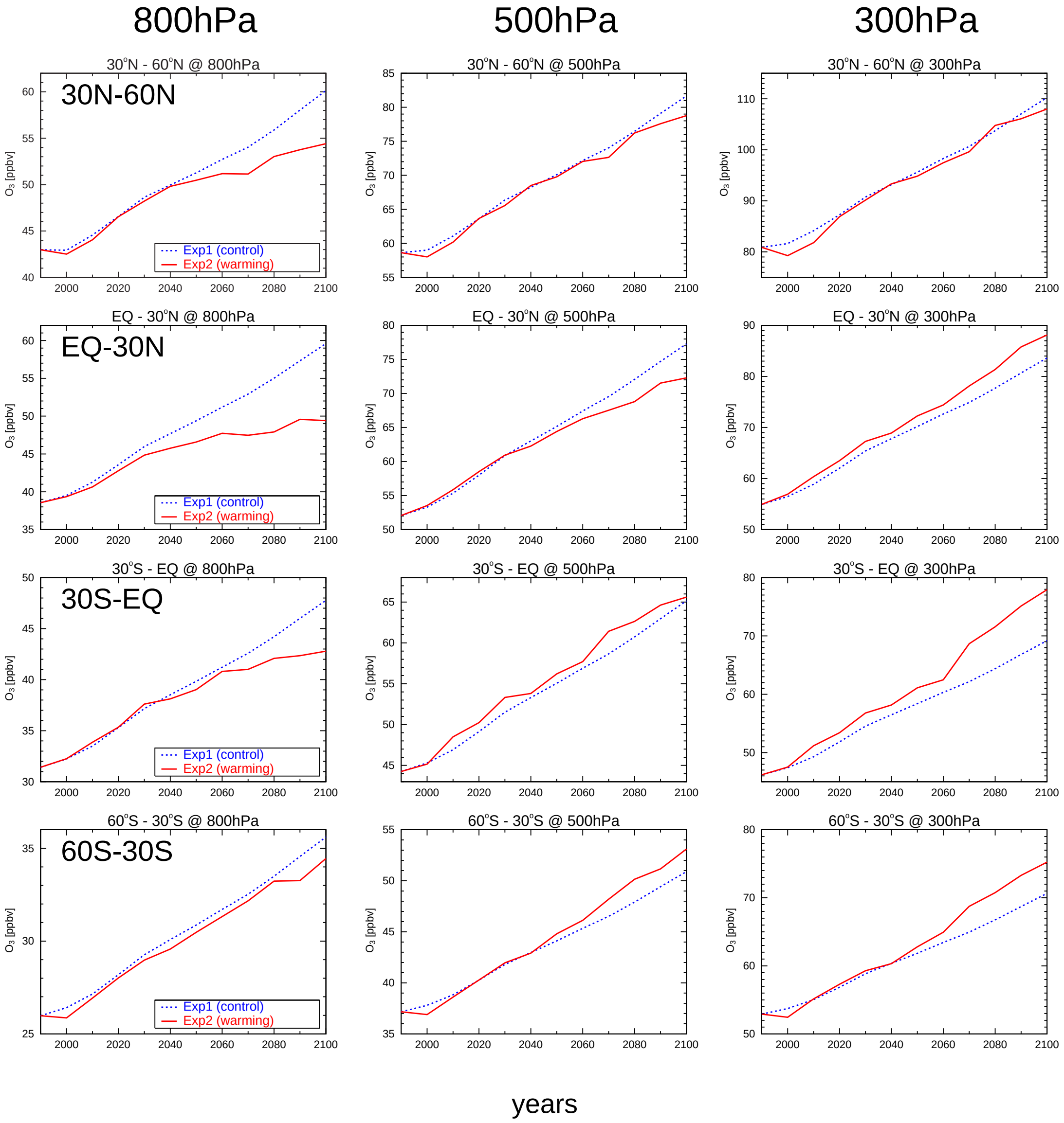

Figure 5.7. Zonal annual mean ozone mixing ratios (ppbv) calculated at 800, 500, 300 hPa for four latitudinal bands (indicated) with the SRES A2 scenario (1990-2100) in Exp1 (dashed) and Exp2 (solid).

in Exp2 appear to be much related to enhanced transport of O_3 from the stratosphere in accordance with warming in the model. The Hadley Circulation and subtropical jet intensified by warming in the model as described in the previous section appear to enhance the stratosphere-troposphere exchange, causing additional O_3 increases in the middle-upper troposphere in Exp2. In global, the increases in stratospheric O_3 input associated with warming nearly compensate for the reduction in O_3 increases due to water vapor increases in Exp2, resulting in almost the same evolution of global tropospheric O_3 burden as in Exp1 (Figure 5.8). In the region of EQ-30°N, Exp2 calculates slight reduction in O_3 burden increases after around 2050 relative to Exp1, reflecting enhanced O_3 destruction due to water vapor increases in the lower-middle troposphere. In Figure 5.9, the effects

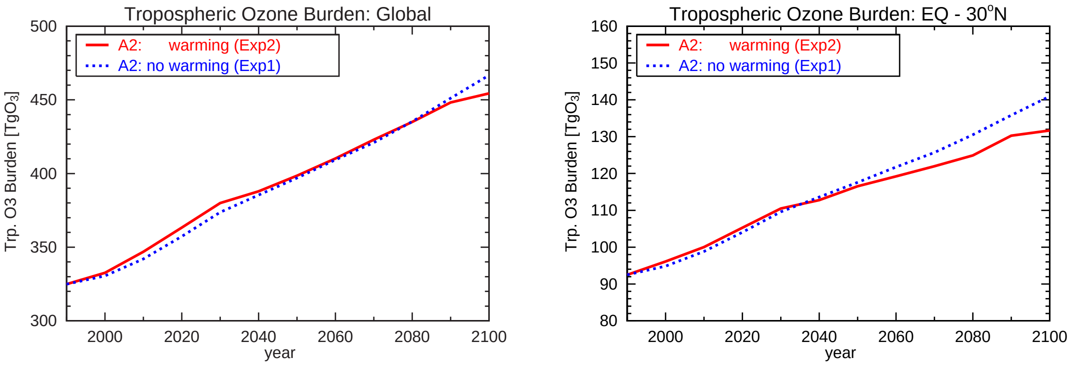

Figure 5.8. Tropospheric ozone burden (TgO_3) calculated for (left) global and (right) EQ to 30°N with the SRES A2 scenario (1990-2100) in Exp1 and Exp2.

of global warming on the surface O_3 distributions are shown (as the differences between Exp1 and Exp2) for 2050 and 2100. Surface O_3 levels in the remote oceans generally decrease 10-30% in 2100 due to enhanced O_3 destruction by water vapor in Exp2. However, it should be noted that O_3 concentrations in the polluted areas as in eastern Asia (particularly around Japan), South America, and Africa increase 5-10% in Exp2 for both 2050 and 2100, resulting from enhanced ozone production owing to temperature and water vapor increases. Increases in lightning NO_x emissions as described in the previous section may also contribute to the O_3 increases in those regions in Exp2. Figure 5.10 shows the differences in O_3 seasonal variations in 2100 between Exp1 and Exp2 for Kagoshima and Hilo. At Hilo, O_3 levels in 2100 increase by 15-20 ppbv relative to 2000 through the year in Exp1, but in the same range as in 2000 due to enhanced O_3 destruction by water vapor in Exp2. On the contrary, additional O_3 increases are calculated at Kagoshima in Exp2 compared to Exp1, showing $\sim$20 ppbv increase during May and June. Such additional O_3 increases due to warming in Exp2 appear to be related to the O_3 production enhancement in China and Japan.

Budgets

Table 5.1 summarizes the global ozone budgets calculated for 2000, 2050, and 2100 in Exp1 and Exp2. In Exp1, global chemical O_3 production increases from 4780 TgO_3/yr in 2000 to 6393 TgO_3/yr (+34%) in 2050 and to 7940 TgO_3/yr (+66%) in 2100, leading to a net chemical O_3 production of 740 TgO_3/yr (+144%). In accordance with the increases in O_3 production, tropospheric O_3 burden increases by 23% in 2050 and 44% in 2100, reaching 467 TgO_3. Dry deposition of O_3 increases by 46 % in 2100 compared to 2000. In Exp2 with climate change, both chemical production and destruction are more enhanced relative to Exp1. Large differences in net chemical O_3 production are calculated between Exp1 and Exp2 especially for 2100, showing a net O_3 destruction (-4.7TgO_3/yr) in Exp2. The significant reduction in net O_3 production is attributed to water vapor increases and enhanced O_3 transport from the stratosphere associated with warming in the model

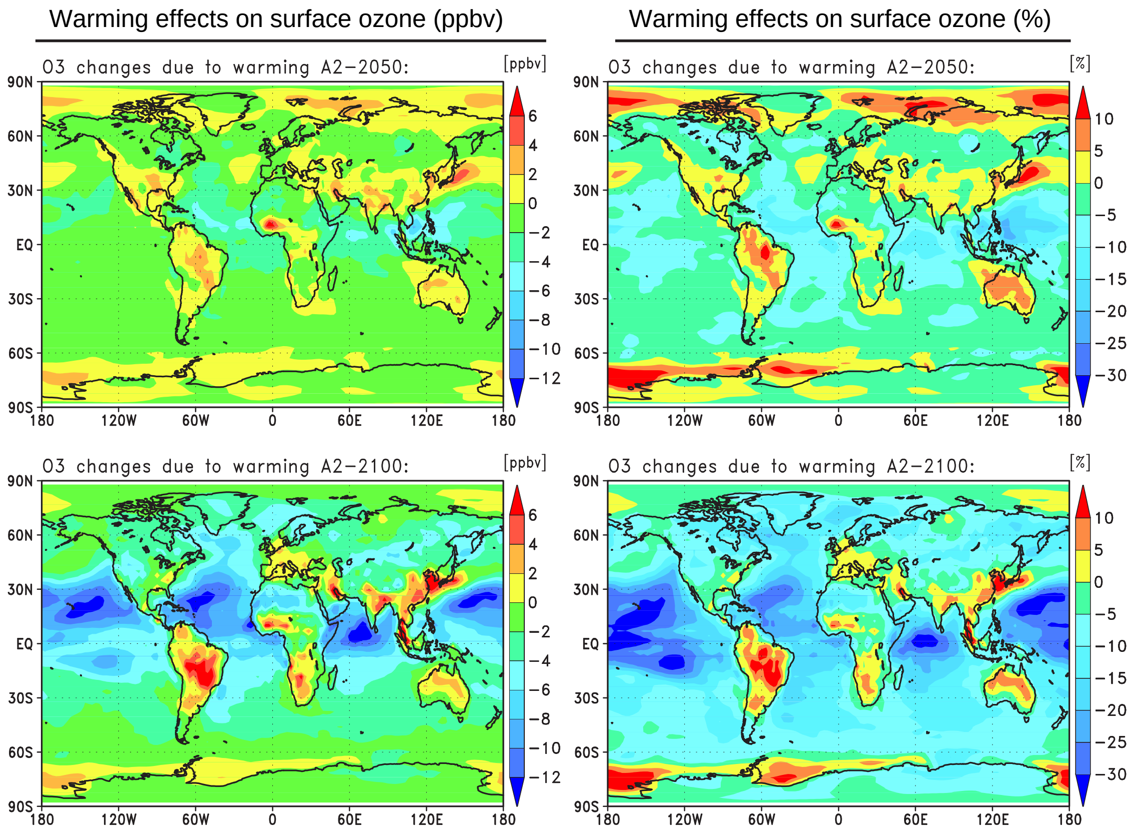

Figure 5.9. Surface ozone changes due to climate change (warming effect) in (left) mixing ratio (ppbv) and (right) percentage. Changes are shown as the differences between Exp1 and Exp2.

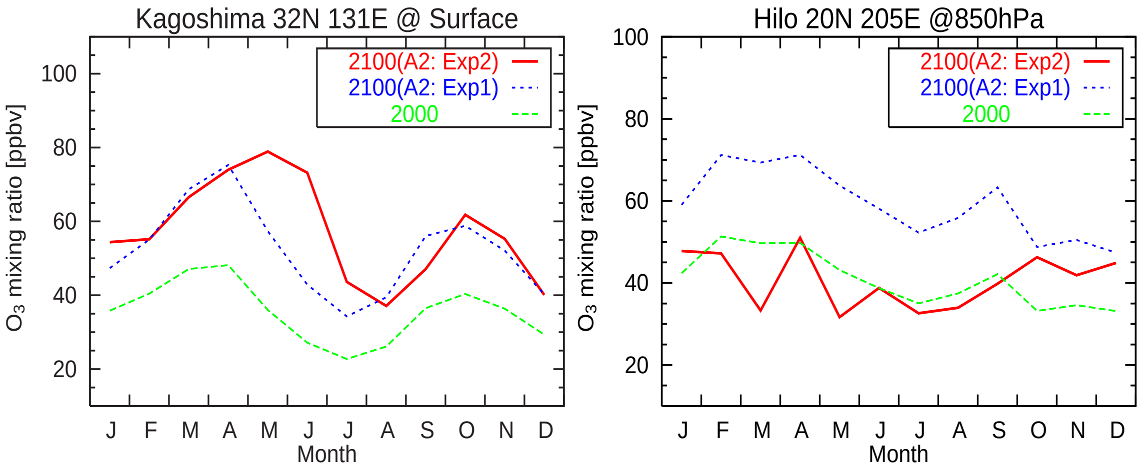

Figure 5.10. Seasonal variations of O_3 (at the surface for Kagoshima and 850hPa for Hilo) for 2100 simulated in control (Exp1) and climate change (Exp2) experiments with the SRES A2 scenario and for 2000.

Table 5.1. Global ozone budget (TgO_3/yr) for control (Exp1) and climate change (Exp2) experiments for 2050 and 2100 with the SRES A2 and for 2000

		Exp1: control		Exp2: climate change	
	2000	2050	2100	2050	2100
Sources	5392.9	6976.3	8540.9	7167.9	9425.5
Net STE[a]	613.1	583.8	601.3	700.6	1277.9
Chemical production	4779.8	6392.5	7939.6	6467.3	8147.6
HO_2 + NO	3013.3	4079.1	5148.9	4101.8	5180.0
CH_3O_2 + NO	1067.2	1471.2	1833.9	1503.5	1940.6
Others	699.3	842.2	956.8	862.0	1027.0
Sinks	-5392.9	6976.3	-8540.9	-7167.9	-9425.5
Dry deposition	-916.6	-1169.7	-1341.4	-1136.8	-1273.2
Chemical loss	-4476.3	-5806.6	-7199.5	-6031.1	-8152.3
$O(^1D)$+ H_2O	-2548.8	-3236.8	-3885.9	-3396.1	-4633.1
O_3 + HO_2	-1251.2	-1788.0	-2506.4	-1819.3	-2576.5
O_3 + OH	-579.6	-675.9	-680.1	-709.4	-819.8
Others	-96.7	-105.9	-127.1	-106.3	-122.9
Net chemical production	303.5	585.8	740.1	436.1	-4.7
Burden (TgO_3)	324.9	397.0	466.7	398.5	454.4

[a] Stratosphere-Troposphere Exchange (net O_3 flux from the stratosphere).

Table 5.2. Net ozone production (TgO_3/yr) for control (Exp1) and climate change (Exp2) experiments for 2100 with the SRES A2 and for 2000, calculated for four latitude ranges.

	30N-60N	EQ-30N	30S-EQ	60S-30S
2000				
Free Troposphere				
500hPa-Tropopause	159.0	412.6	340.5	45.3
800hPa-500hPa	-60.8	-311.7	-216.9	-58.0
Boundary Layer (< 800hPa)	189.4	-64.1	-72.7	-20.6
Exp1-2100: no climate change				
Free Troposphere				
500hPa-Tropopause	174.5	597.2	496.1	51.3
800hPa-500hPa	-110.5	-472.2	-321.1	-89.8
Boundary Layer (< 800hPa)	342.3	131.6	4.9	-15.7
Exp2-2100: climate change				
Free Troposphere				
500hPa-Tropopause	144.4	436.3	379.1	9.0
800hPa-500hPa	-183.1	-674.9	-512.9	-125.0
Boundary Layer (< 800hPa)	341.3	188.8	54.5	-18.5

as described above. In fact, Exp2 predicts significant increases in O_3 input from the stratosphere, calculating an increase of about 660 TgO_3/yr ($\sim$ a double increase) in 2100 relative to 2000. The enhancement in stratospheric O_3 input in Exp2 comes principally from intensification of the Hadley Circulation and subtropical jet to enhance the stratosphere-troposphere exchange in the model. In addition, stratospheric circulation as the Brewer-Dobson Circulation appears to intensify and contribute to downward transport of stratospheric O_3 toward the troposphere. However, it should be noted that the CHASER model, used in this study, tends to overestimate the stratospheric O_3 influx, showing overestimation of upper tropospheric O_3 (see section 2.3.4), and that climate change simulated in this study may be overestimated due to the high climate sensitivity of the CCSR/NIES GCM as described above. It is, therefore, possible that both the predicted increases in stratospheric O_3 input and enhancement in O_3 destruction by water vapor increases may be overestimated in this experiment (Exp2). A transient future simulation of *Johnson et al.* [2001] also shows a slight increase in stratospheric O_3 input due to warming effect, calculating a $\sim$17% increase in 2100 relative to 2000. Their simulation, however, adopts relatively low spatial resolution particularly in the vertical, having only nine layers to 100 hPa with $5^\circ \times 5^\circ$ in the horizontal. As a result of the enhanced stratospheric O_3 input compensating for the additional lower tropospheric O_3 destruction, Exp2 calculates tropospheric O_3 burden changes similar to those in Exp1 (+40% in 2100 relative to 2000) as mentioned above.

In Table 5.2, net ozone production for 2100 calculated in Exp1 and Exp2 are compared for different altitude and latitude ranges. Exp1 calculates increases of 45% in net O_3 production above 500 hPa in the low latitudes (30°S-30°N) relative to 2000, with increases of 40-50% in net O_3 destruction in 800-500 hPa. Significant increases in O_3 production are also seen in the boundary layers in the northern hemisphere. Net O_3 destruction below 800 hPa in EQ-30°N in 2000 turns to be net production in 2100 showing an increase of $\sim$200 TgO_3/yr. In comparison with Exp1, Exp2 calculates reduction in O_3 production in the middle-upper troposphere (above 500 hPa) with enhancement in O_3 destruction in 800-500 hPa particularly in the low latitudes where significant increases in temperature and water vapor are predicted. The changes in net O_3 production above 800 hPa are also linked to the increases in O_3 input from the stratosphere. It should be noted that Exp2 predicts larger O_3 production below 800 hPa (boundary layers) in the low latitudes (30°S-30°N) compared to Exp1. This difference arises from the enhanced O_3 production in the polluted regions in the low latitudes due to increases in temperature and water vapor, overcoming efficient O_3 destruction in the remote areas in Exp2.

Figure 5.11 shows the three-dimensional distributions of net O_3 production for June simulated for 2000, 2050, and 2100 in Exp1. The isosurfaces show the areas of high O_3 production (>3 ppbv/day) from the surface to 20 km altitude. Efficient O_3 production is calculated in the upper troposphere over the United States, Africa, and eastern Asia in each year. The impact of emission changes appears to be largest over eastern Asia including India and Himalayas. The high O_3 pro-

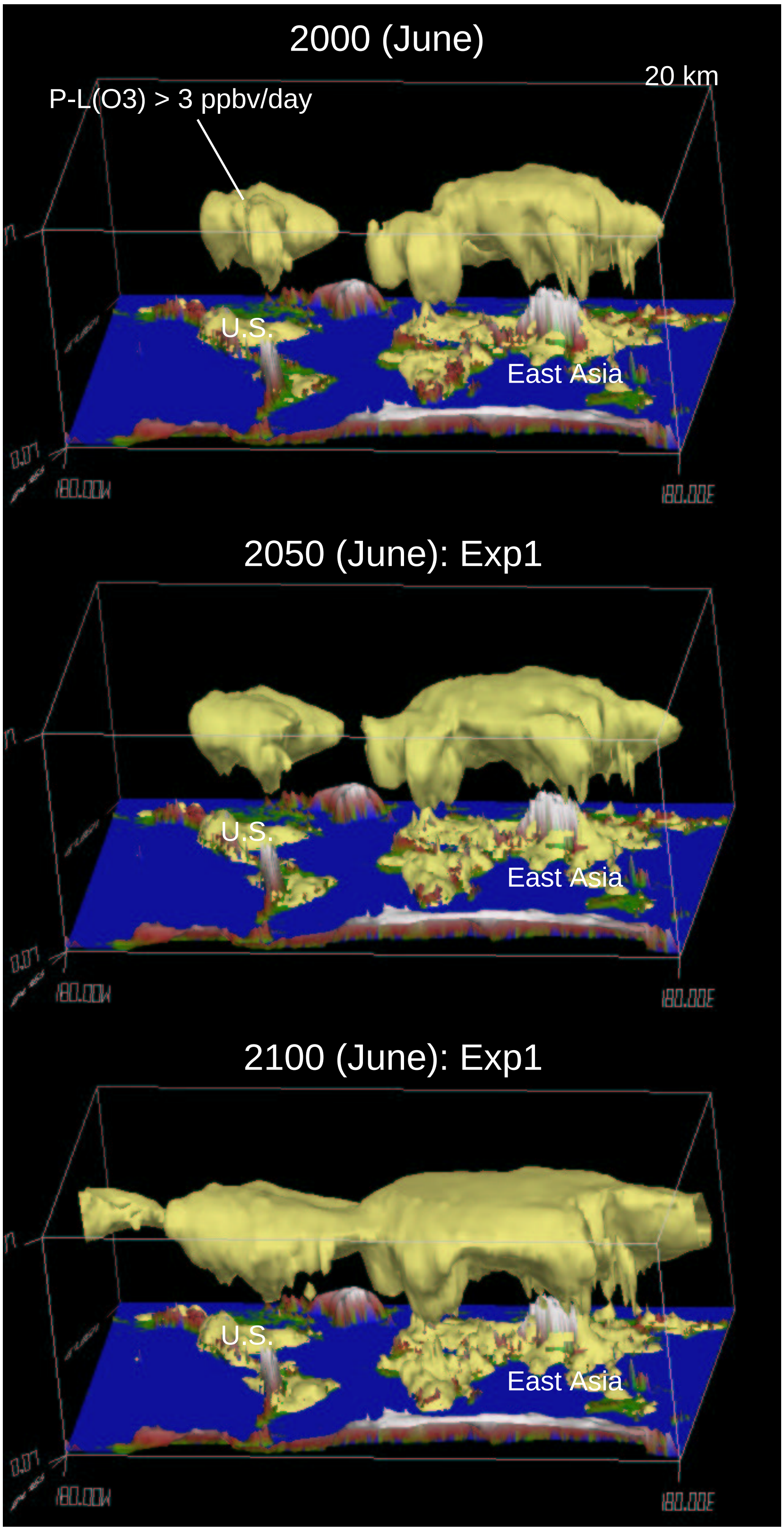

Figure 5.11. High O_3 production areas (>3 ppbv/day) in June simulated for 2000, 2050, and 2100 in Exp1 (no climate change) with the SRES A2 scenario. The O_3 production areas are shown as isosurface of 3 ppbv/day O_3 production.

duction area extending over eastern Asia increases in both the horizontal and vertical toward 2050 and 2100, reaching the United States in 2100 due to rapid intercontinental transport of precursors across the Pacific as suggested by *Wild and Akimoto* [2001a]. Similarly, O_3 production over North America in the low latitudes (including Mexico) appears to reach Europe and Africa in 2100. Net O_3 production in 8-15 km altitudes over southeastern Asia (mostly India and China) for June increases from $\sim$10 ppbv/day in 2000 to 15-20 ppbv/day in 2050 and to 30-40 ppbv/day in 2100 (not shown).

5.3.2 Methane and global OH field

As mentioned above, this study predicts CH_4 concentrations for every ten years from 1990 to 2100 using the SRES A2 emission for CH_4 and OH concentrations calculated for individual decades, and therefore considers the interaction between CH_4 and tropospheric chemistry with a time step of ten years. Figure 5.12 shows the global mean tropospheric CH_4 concentrations for 1990 to 2100 with global OH concentrations and chemical lifetime of CH_4 against OH. In Exp1, CH_4 concentration increases to $\sim$4 ppmv in 2100 with higher increase rates after around 2040, due to the emission increase (shown in Figure 5.1) and to increases in CH_4 chemical lifetime associated with OH depletion. Global mean OH concentration in Exp1 decreases from 1.06 $\times 10^6$ molecules cm^{-3} in 2000 to 0.84 $\times 10^6$ molecules cm^{-3} (-20%) in 2100, causing the prolonged CH_4 lifetime of 11.4 years in 2100 (+24% relative to 2000). The OH decreases in Exp1 originate from increases in both CO and CH_4 itself. CO, significantly controlling OH levels, increases by a factor of 2-3 through much of the troposphere in 2100 relative to 2000 as well as CH_4. However, OH near the surface in polluted locations increases due to enhanced O_3 and NO_x levels (not shown). In Exp2, predicted OH concentrations show less significant changes, due to water vapor increases during the course of the simulation compared to Exp1, with a slight decrease of -5% in 2100. Accordingly, CH_4 lifetime is also relatively invariant showing a slight decrease (6%) in 2100. For the relative decreases in CH_4 lifetime in Exp2, temperatures increases (as seen in Figure 5.4), enhancing the CH_4 + OH reaction, also contribute largely. Consequently, CH_4 increases calculated in Exp1 are reduced by 10-20% after around 2050 in Exp2, showing a CH_4 concentration of 3.3 ppmv in 2100. It is possible that this study, predicting CH_4 only for every decade, may include some errors due to ignoring variations on short time-scales. The results in this study, however, appear to be consistent with the transient simulations of *Johnson et al.* [2001] which calculate 10-15% reduction in CH_4 increases due to climate change (warming) for the SRES A2 scenario.

Figure 5.13 shows the zonal mean OH distributions for 2000, and for 2050 and 2100 in Exp1 and Exp2. Exp1 shows monotonic OH decreases ($\sim$20% in 2100) through the entire troposphere as mentioned above. On the contrary, Exp2 predicts OH distributions similar to those in 2000. OH levels for 2100 in the tropical upper troposphere increase compared to those in 2000, resulting from the large increases in water vapor as shown in Figure 5.4.

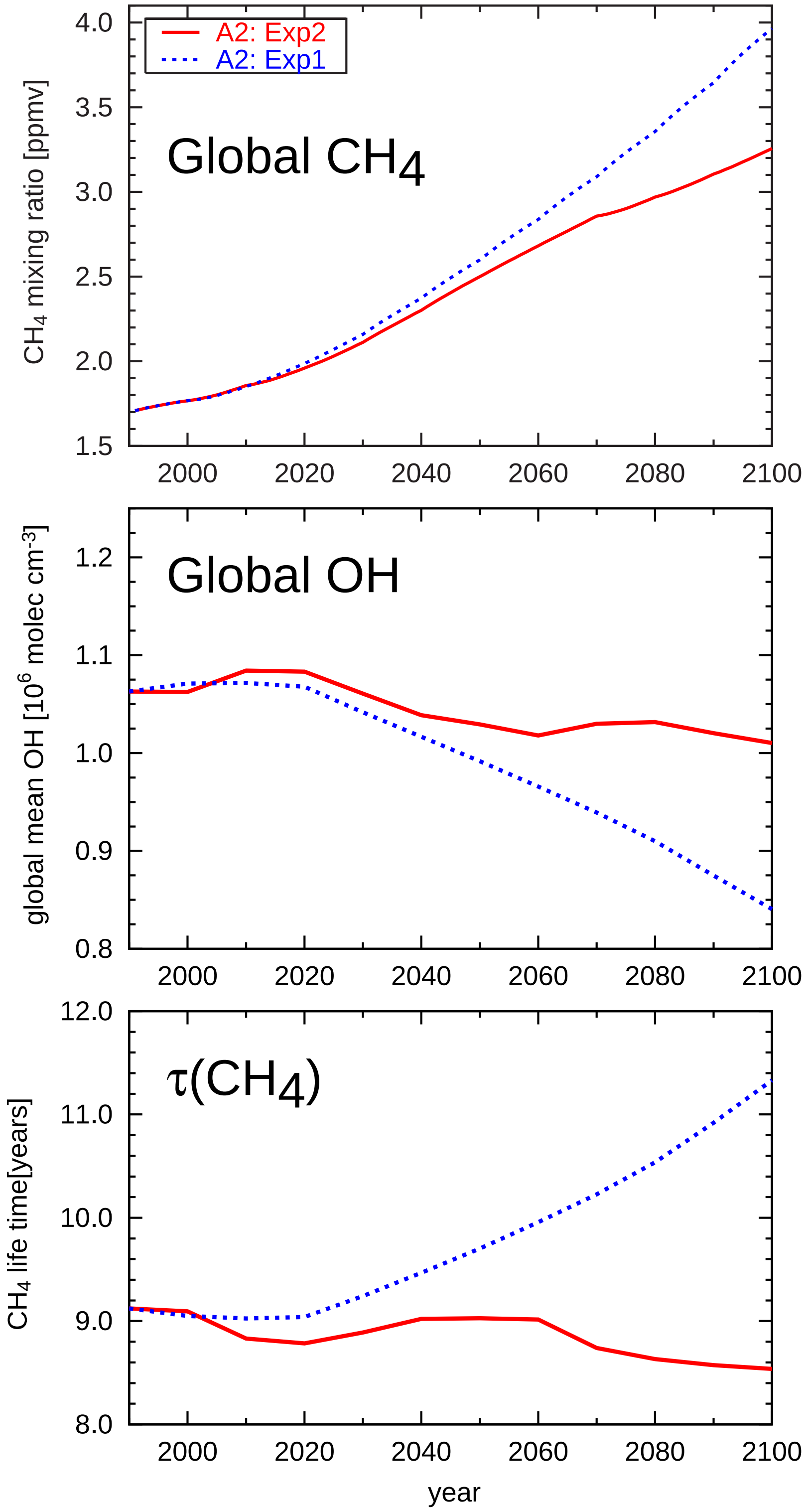

Figure 5.12. Global mean concentrations of tropospheric CH_4 (top) and OH (middle) and CH_4 lifetime against tropospheric OH (bottom) for 1990 to 2100 calculated in Exp1 (control) and Exp2 (climate change) experiments.

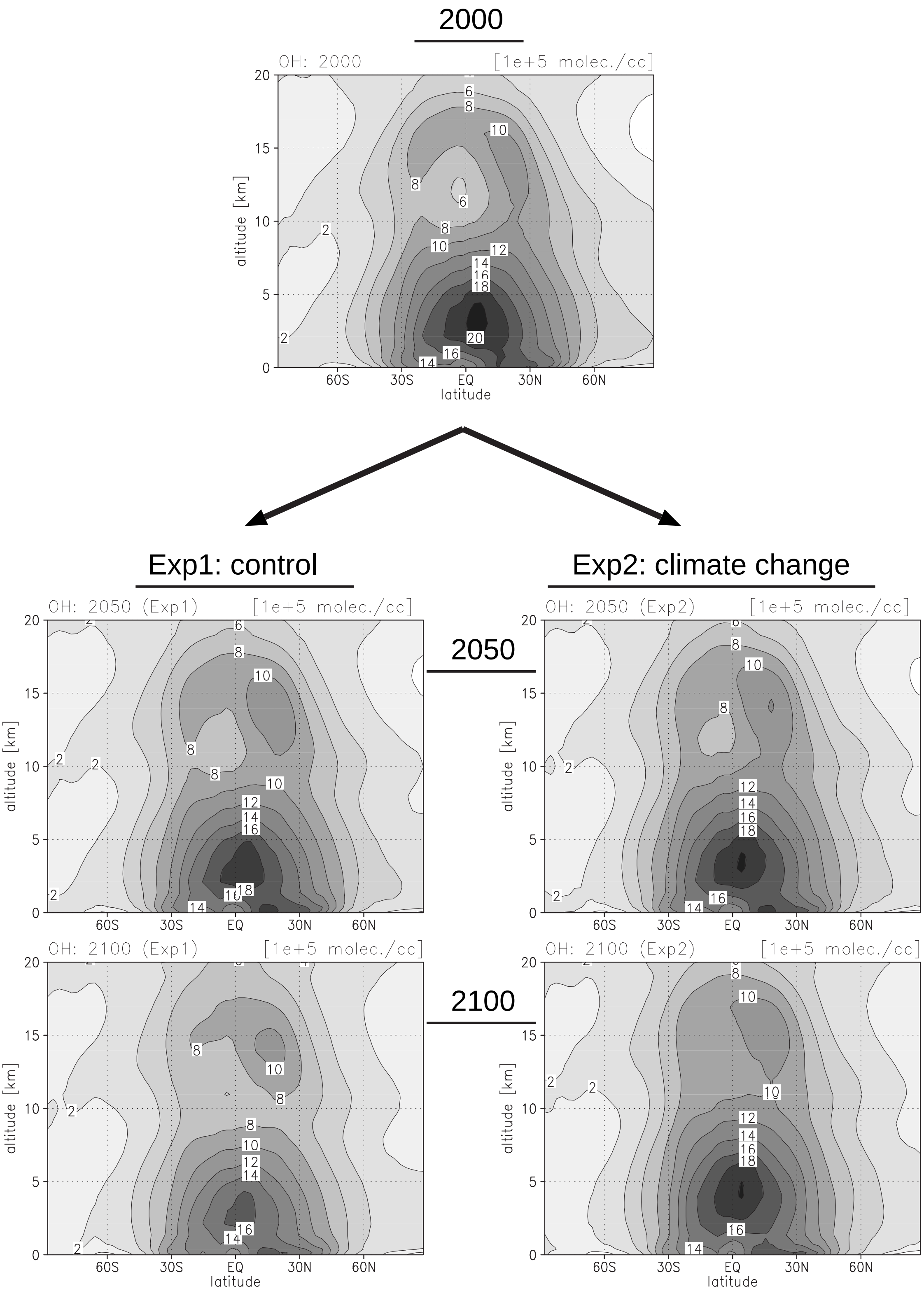

Figure 5.13. Zonal annual mean OH distributions simulated for 2000, and for 2050 and 2100 in Exp1 (control) and Exp2 (climate change) with the SRES A2 scenario.

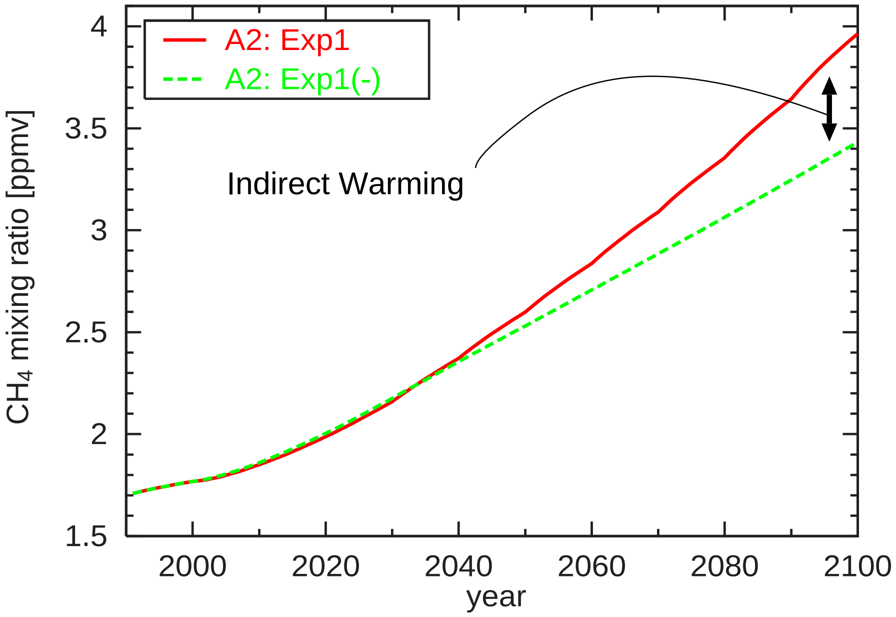

Figure 5.14. Global mean CH_4 concentrations for 1990-2100 calculated with considering chemical feedback from OH concentrations (Exp1) and with no chemical feedback, Exp1(-). Values are for the SRES A2 scenario.

To evaluate the impact of chemical feedback from emission-induced OH changes associated with changes in CO, CH_4, O_3, and NO_x aside from climate change, we also calculate CH_4 concentrations for 2000-2100 using the same OH field as for 2000 in Exp1 (Exp1(-), Figure 5.14). The OH reduction in Exp1 appears to enhance the CH_4 increases $\sim$10% after 2050 (indirect warming), leading to an additional CH_4 increase of 0.5 ppmv (+15%) in 2100 relative to the CH_4 prediction with CH_4 emission change only (Exp1(-)).

5.3.3 Sulfate

Figure 5.15 shows the surface concentrations of SO_2 and sulfate for 1990, 2050, and 2100 in Exp1. In accordance with the increases in SO_2 emission as shown in Figure 5.1, SO_2 and sulfate increase especially in eastern Asia around India and China in 2050. Annual mean SO_2 levels in India increase from 1-2 ppbv in 1990 to 8-10 ppbv in 2050, causing sulfate increases from 2-3 μg m^{-3} in 1990 to 9-10 μg m^{-3} ($\sim$ treble increases) in 2050. Also in China, SO_2 and sulfate increase by a factor of 2 in 2050 relative to 1990. As *Takemura et al.* [2002] suggested, SO_4 levels in Japan appear to be much influenced by transport from the China continent. In 2100, the model predicts still high SO_2 and sulfate levels in India and China despite reduction in SO_2 emission. Contrarily, SO_2 and sulfate in the United States, Europe decrease during the course of the simulation for 1990-2100. Although SO_2 emission in Japan also decreases, the calculation shows high concentrations around Japan for both SO_2 and sulfate, influenced by transport from the China continent. The calculated sulfate increases in the low latitudes as in India appear to be related to enhancement of

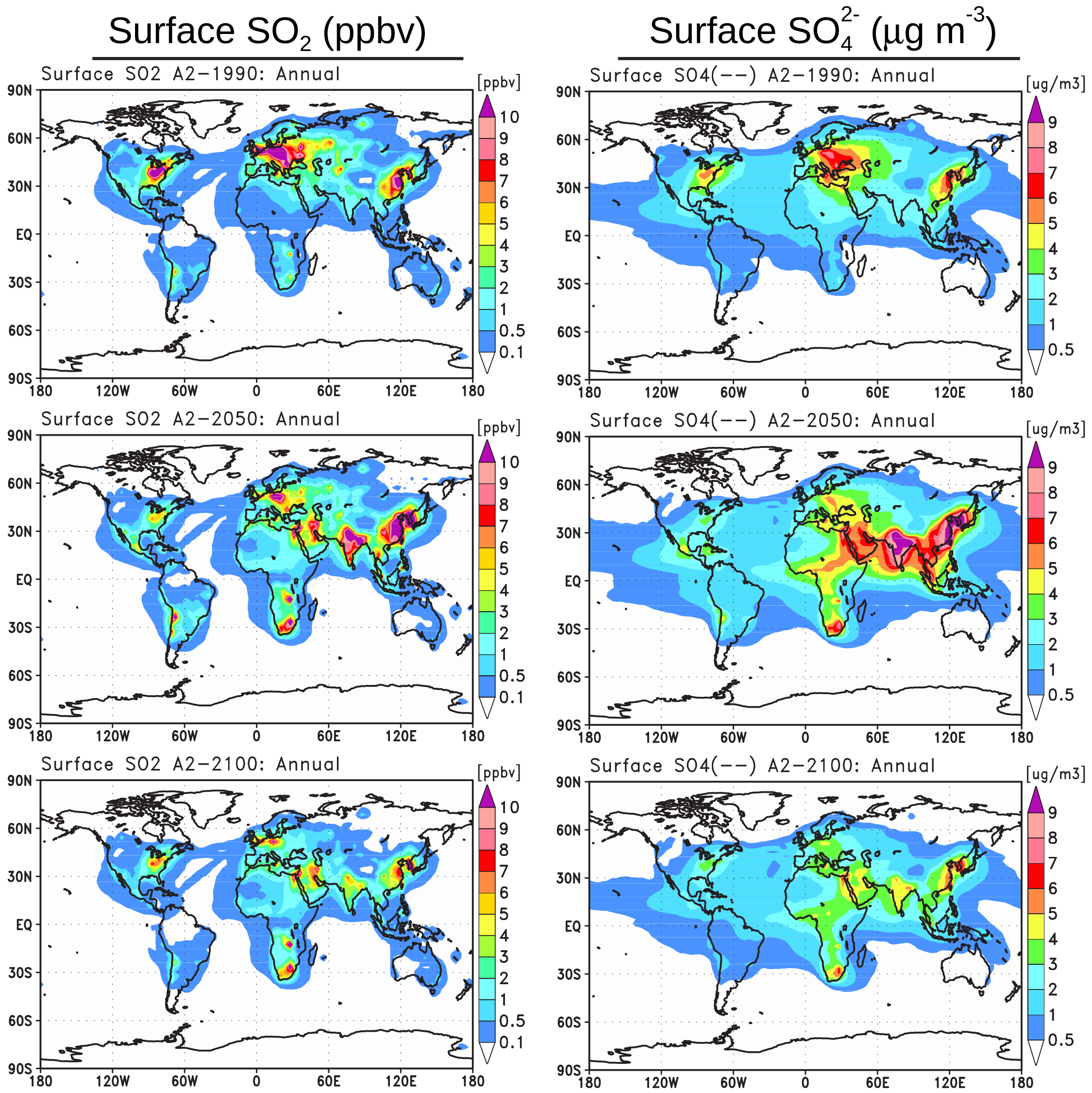

Figure 5.15. Surface distributions of SO_2 and sulfate (SO_4^{2-}) for 1990, 2050, and 2100 simulated in Exp1 (no climate change) with the SRES A2 scenario.

liquid-phase SO_2 oxidation due to H_2O_2 increases. In the simulation, H_2O_2 around India increases by a factor of 2-3 in 2100 relative to 1990.

Table 5.3 shows global budgets of sulfate for 2050 and 2100 in Exp1 and Exp2, and for 2000. In Exp1 with no climate change, sulfate formation due to the gas-phase SO_2 + OH reaction increases $\sim$70% in 2050. The liquid-phase reaction with H_2O_2 increases by about 55% in 2050 relative to 2000, owing to increases in both emission and H_2O_2, whereas the reaction with O_3 decreases slightly, due to higher acidity (lower pH values) of cloud drops relative to 2000. However, it should be noted here that the model in this study, calculating pH values in cloud drops in quite simple scheme (Appendix 2B, page 106), may mispredict pH values in cloud drops in the future

Table 5.3. Global sulfate budget (TgS/yr) for control (Exp1) and climate change (Exp2) experiments for 2050 and 2100 with the SRES A2 and for 2000

		Exp1: control		Exp2: climate change	
	2000	2050	2100	2050	2100
Sources	50.85	74.60	50.19	74.35	50.73
SO_2 + OH	15.31(30%)[a]	26.23(35%)	14.79(29%)	27.61(37%)	17.93(35%)
S(IV) + O_3(aq)[b]	10.58(21%)	9.61(13%)	6.85(14%)	9.02(12%)	5.75(11%)
S(IV) + H_2O_2(aq)[b]	24.96(49%)	38.76(52%)	28.55(57%)	37.72(51%)	27.05(54%)
Sinks	-50.99	-75.06	-50.69	-74.89	-51.37
Dry deposition	-4.32	-6.42	-4.44	-6.71	-5.17
Wet deposition	-46.67	-68.64	-46.25	-68.18	-46.20
Burden (TgS)	0.55	0.91	0.60	0.98	0.78

[a] Contribution to the total source.
[b] Liquid-phase reaction in cloud drops.

atmospheres, since the scheme is adjusted to simulate cloud water pH close to present-day observations. Sulfate burden increases from 0.55 TgS/yr in 2000 to 0.91 TgS/yr in 2050, causing a ∼50% increase in sulfate wet deposition in 2050. In 2100, Exp1 calculates a sulfate budget well similar to that in 2000 except for the liquid-phase reactions; reduction in the reaction with O_3 due to lower cloud water pH, and enhancement of the H_2O_2 reaction associated with H_2O_2 increases. The enhanced liquid-phase reaction with H_2O_2 contributes largely (∼60%) to the total sulfate formation in 2100, resulting in a total formation of the same magnitude as in 2000 despite emission decrease in 2100 relative to 2000 (Figure 5.1). Exp2 with climate change also predicts similar changes in sulfate budget, but appears to calculate larger sulfate burden especially for 2100. The larger burden in Exp2 appears to be related principally to reduced precipitation in eastern Asia leading to less efficient wet removal of sulfate. Exp2 generally predicts increases in precipitation, but shows 10-20% precipitation decreases around eastern Asia in 2100.

Figure 5.16 shows the evolution of sulfate burden calculated for 1990 to 2100 in Exp1 and Exp2. According to SO_2 emission increases, sulfate burden increases to 0.9-1 TgS/yr in 2030-3050 for both Exp1 and Exp2. It should be noted again that sulfate burdens after 2080 are still larger than in 1990 or 2000 despite lower SO_2 emission levels relative to 1990-2000. The larger sulfate burdens after around 2080 in Exp1 are attributed to the enhanced liquid-phase reaction with H_2O_2 particularly in the low latitudes where significant H_2O_2 increases (by a factor of 3 in 2100 relative to 2000) are predicted. In the case of Exp2, the changes in precipitation in the model also contribute to the additional increases in sulfate burden after around 2030 as mentioned above.

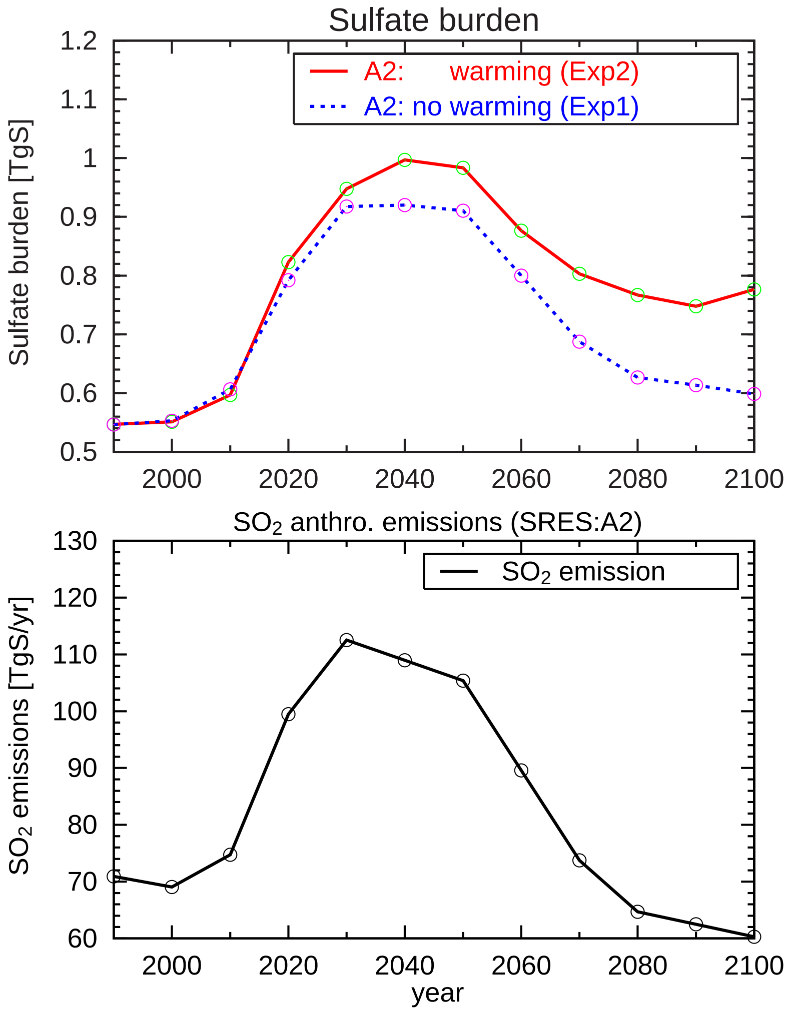

Figure 5.16. Global sulfate burdens for 1990-2100 simulated in Exp1 and Exp2 with the SRES A2 scenario. Also shown are the global anthropogenic SO_2 emissions prescribed by the A2 scenario.

5.3.4 Acid deposition and precipitation pH

Figure 5.17 shows the total (wet+dry) deposition of nitrates (NO_3^-) and sulfate (SO_4^{2-}) for 1990, 2050, and 2100 in Exp1. For the total deposition of nitrates, dry and wet deposition processes contribute almost equally, while the sulfate deposition is mostly of wet deposition origin. In 2050, significant increases in acid deposition are predicted for both NO_3^- and SO_4^{2-} particularly in eastern Asia including Japan. NO_3^- deposition increases by a factor of 3-4 in India, China, Korea, and Japan in 2050. Concurrently, SO_4 deposition also increases significantly (by a factor of 3-5) over the large region from India to Japan. Since the chemical lifetime of SO_2 (precursor of sulfate) is generally longer than that of NO_x (precursor of NO_3^-), the deposition effect of SO_4^{2-} appears to extend farther from source regions compared to NO_3^- deposition. In 2100, NO_3^- deposition is simulated to increase additionally in eastern Asia. NO_3^- deposition in the United States and Europe increases gradually from 1990 to 2100 in this scenario, showing increases of ∼50% in 2100 relative

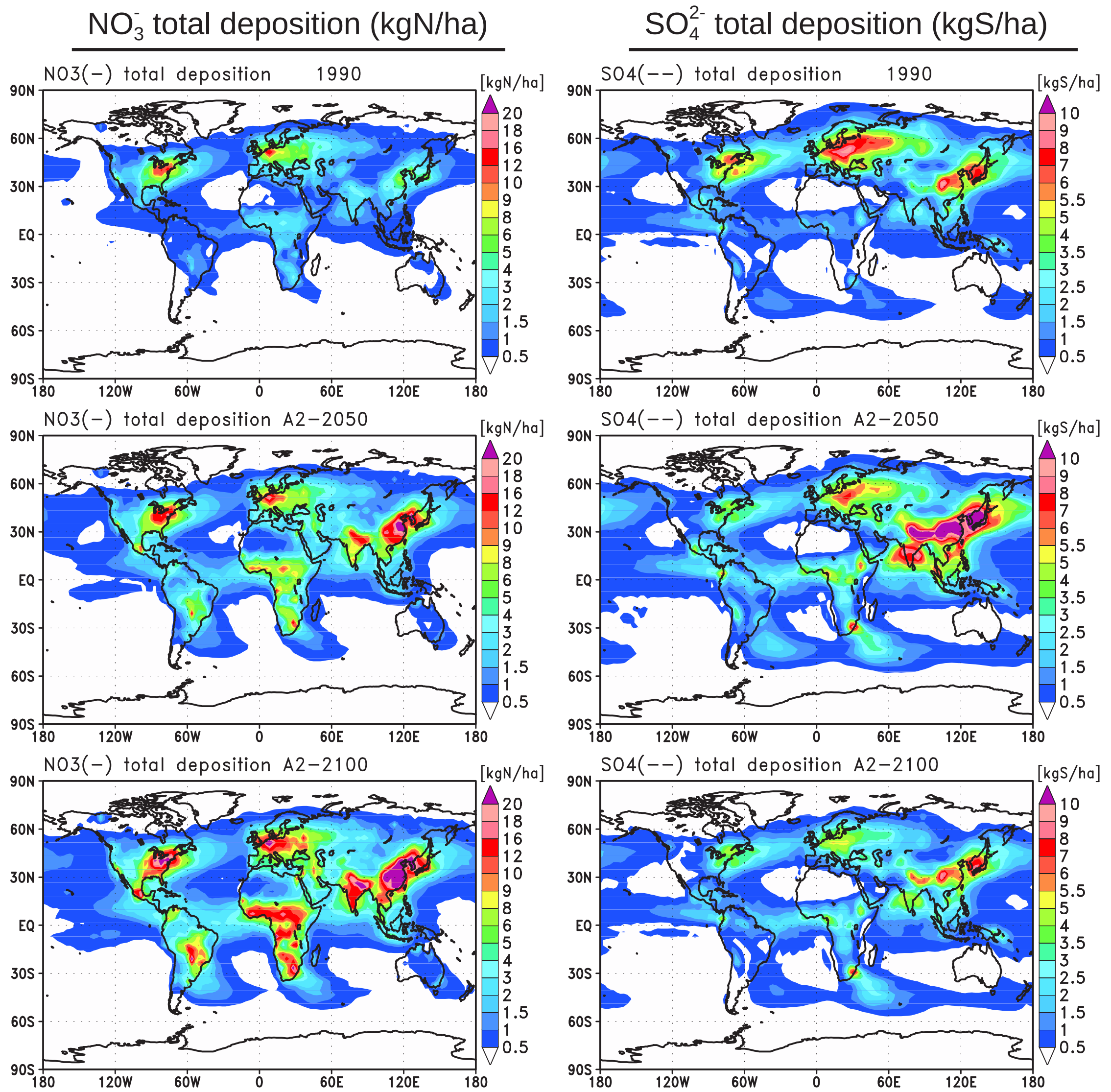

Figure 5.17. Total (wet + dry) deposition of NO_3^- (nitrates) and SO_4^{2-} (sulfate) for 1990, 2050, 2100 in Exp1. Values are in annual total.

to 1990. The model predicts SO_4^{2-} deposition decreases from 2050 to 2100 according to reduction in SO_2 emissions, but calculates SO_4^{2-} deposition of the same magnitude as in 1990 around China and Japan despite emission decreases there (Figure 5.1), reflecting enhanced sulfate formation by the liquid-phase reaction with H_2O_2 (Table 5.3).

Deposition of NO_3^- and SO_4^{2-} is a key factor to control the acidity in precipitation (acid rain). This study estimates the contributions from NO_3^- and SO_4^{2-} deposition to the pH values in precipitation. As described in section 2.2.3, the contributions are calculated as $\mathrm{pA_N} \equiv -\log[NO_3^-]$ and $\mathrm{pA_S} \equiv -\log[SO_4^{2-}]$ using the concentrations (eq l^{-1}) of NO_3^{-1} and SO_4^{2-} in precipitation. Figure 5.18 shows the estimated contributions from NO_3^- and SO_4^{2-} deposition to pH in precipitation

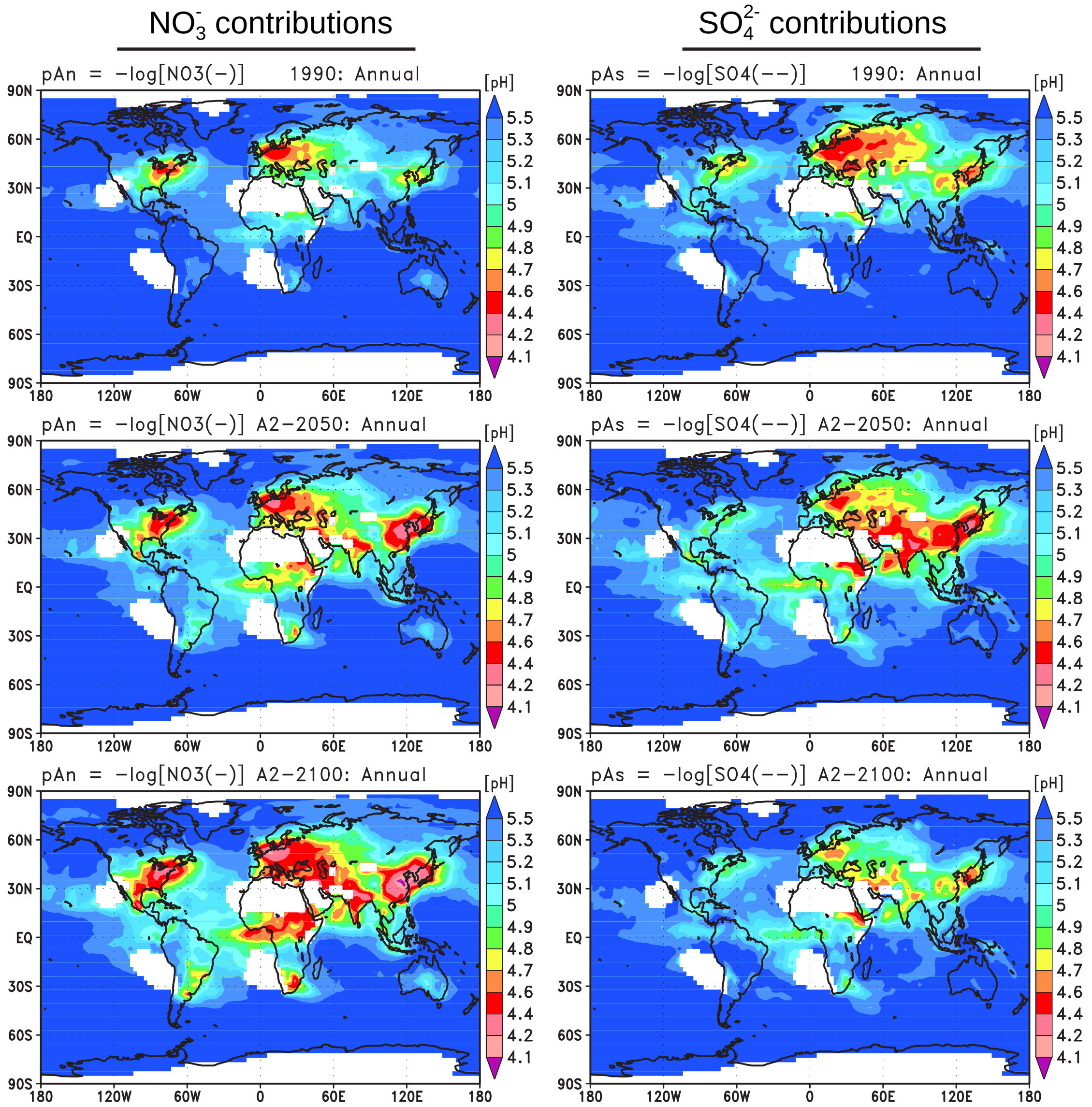

Figure 5.18. Contributions from NO_3^- (nitrates) and SO_4^{2-} (sulfate) deposition to precipitation pH calculated for 1990, 2050, and 2100 in Exp1 (no climate change). Contributions are calculated as $-\log\,[NO_3^-]$ and $-\log\,[SO_4^{2-}]$.

for 1990, 2050, and 2100 in Exp1 (the figure shows volume-weighed values for pA_N and pA_S). These contributions (pA_N and pA_S) would give actual pH, if it were not for cations (NH_3^+, Ca^{2+}, Mg^{2+}, etc.) to neutralize $[NO_3^-]$ and $[SO_4^{2-}]$ in precipitation. Both NO_3^- and SO_4^{2-} contributions hugely increase in eastern Asia (India to Japan) in 2050. The annual mean pA_N and pA_S around China and Japan decrease from 5.0-4.7 in 1990 to 4.2-4.5 in 2050, indicating significant increases in the precipitation acidity. As a consequence of increases in both NO_3^- and SO_4^{2-} deposition in eastern Asia, precipitation acidity $[H^+]$ associated with $[NO_3^-]$ and $[SO_4^{2-}]$ increases by a factor of no less than 10 particularly in India, China, and Japan, implying a serious environmental problem of acid rain in future eastern Asia. In these regions in 2050, the model shows particularly high precipitation acidity during winter to spring, predicting low pA_N and pA_S values of 4-3.5. In this scenario (SRES A2), the NO_3^- contributions after 2050 continue increasing in the polluted regions (i.e., United States, Europe, and eastern Asia), leading to pA_N lower than 4.4 in those regions in 2100, while pA_S decreases in 2100 relative to 2050.

5.4 Conclusions

This study has simulated future tropospheric chemistry involving ozone and sulfate using the CHASER model, a coupled chemistry GCM based on the CCSR/NIES atmospheric GCM [*Sudo et al.*, 2002a]. The horizontal resolution of T42 ($2.8^\circ \times 2.8^\circ$) has been adopted with 32 layers in the vertical. In the present model version of CHASER (used in this study), some improvements are included for the wet deposition and sulfate formation processes (see section 2.2). This study evaluates the impacts of both emission changes and climate change with the SRES A2 scenario, conducting two kinds of experiments; control (Exp1) and climate change (warming) experiments (Exp2). In Exp2 with climate change, the GCM simulates future climate change with greenhouse gases specified by the A2 scenario, and SST and sea ice distributions prescribed by the CCSR/NIES atmosphere-ocean coupled GCM [*Nozawa et al.*, 2001] with the A2 scenario. The simulations for Exp1 and Exp2 are performed for individual decades from 1990 to 2100 (time-slice simulation). Global CH_4 concentrations are predicted using the A2 emission scenario for CH_4, and global OH and temperature fields calculated for every decades in the simulation.

In Exp2, the GCM predicts large temperature increases after 2050, calculating a $\sim$5 °C increase in global mean surface temperature in 2100. The predicted warming in this study (Exp2), larger than other simulations, may be overestimated due to high climate sensitivity of the CCSR/NIES atmosphere-ocean coupled GCM [*Nozawa et al.*, 2001]. The Hadley Circulation and subtropical jet appear to intensify as a result of the larger temperature increases in the low latitudes (i.e., increases in meridional temperature gradients). Exp2 also predicates rises in convective cloud top height in accordance with warming in the model, and thereby generates larger NO_x emissions from lightning. Exp2 predicts a 20% increase in global lightning NO_x emission in 2100 relative to the present-day, consistent with the suggestion by *Price and Rind* [1994].

In the simulation of O_3, significant O_3 increases are predicted in eastern Asia particularly in India. Annual mean surface O_3 concentrations in eastern Asia increase from 40-50 ppbv in 2000 to 60-80 ppbv in 2050, and to 70-90 ppbv in 2100, indicating serious large-scale O_3 pollution in the area. O_3 production in eastern Asia increases largely in both the boundary layer and the upper troposphere, with showing 2-3 times higher O_3 production efficiency. This study shows an increase of about 44% in global tropospheric O_3 burden in 2100 relative to 2000 in response to 2-3 times increases in precursors (NO_x, CO, and NMHCs) emissions with the SRES A2 scenario. O_3 levels in the troposphere increase almost linearly toward 2100 for individual altitudes and latitudes. In

Exp2 with climate change, the O_3 increases predicted in Exp1 are reduced 10-20% in the lower troposphere after around 2050, due to water vapor increases causing more efficient O_3 destruction. However, Exp2 calculates additional O_3 increases of 5-10% in the boundary layers around the polluted regions as eastern Asia relative to Exp1 (after 2050), resulting from more enhanced O_3 production due to temperature and water vapor increases in the polluted sites. Exp2 also predicts additional increases in upper tropospheric O_3 as a result of enhanced O_3 transport from the stratosphere due to intensification of the Hadley Circulation and stratospheric circulation in the model. Exp2 calculates significant increases in global stratospheric O_3 input from about 600 TgO_3/yr in 2000 to more than 1200 TgO_3/yr in 2100 in accordance with warming in the model. Exp2 may overestimate the warming impact on stratospheric O_3 influx, due to high climate sensitivity of the CCSR/NIES GCM as mentioned above. As a result of water vapor increases and enhanced stratospheric O_3 input, Exp2 shows large reduction in the net chemical O_3 production for after 2050, calculating a slight negative net production (-4.7 TgO_3/yr) in 2100, whereas Exp1 predicts a large net O_3 production of 740 TgO_3/yr in 2100. The simulations for Exp2 calculate 10-30% decreases in net ozone production in the upper troposphere with 20-40% enhancement of ozone destruction in the middle troposphere relative to Exp1 after 2050.

Global mean CH_4 concentration in Exp1 increases from 1.7 ppmv in 1990 to about 4 ppmv in 2100 in response to the A2 emission and simulated OH changes. Global mean OH concentration decreases from 1.06 $\times 10^6$ molecules cm^{-3} in 1990 to 0.84 $\times 10^6$ molecules cm^{-3} in 2100 owing to CO and CH_4 increases, causing CH_4 lifetime to increase from 9.2 years in 1990 to 11.4 years in 2100. On the contrary, Exp2 (with climate change) shows reduction in CH_4 lifetime (8.6 years in 2100) due to temperatures increases and relative OH increases associated with water vapor increases, and predicts a global mean CH_4 concentration of 3.3 ppmv in 2100. These results for future CH_4 concentrations and their sensitivity to climate change are well consistent with the transient simulation of *Johnson et al.* [2001], implying validity of our method to derive future CH_4 with a time-slice simulation. However, future investigation is needed to validate CH_4 prediction in this study, since the method to derive future CH_4 in this study does not capture short-term ($<$ ten years) interaction between CH_4 and tropospheric chemistry compared to a transient CH_4 simulation.

According to the SRES A2 scenario, Exp1 predicts significant increases in both SO_2 and sulfate particularly in eastern Asia including India and China in 2050, indicating sulfate increases by a factor of 2-3 in eastern Asia. After around 2030, sulfate formation efficiency in the low latitudes as in India intensifies due to H_2O_2 increases in the lower troposphere. Global sulfate burden increases from 0.55 TgS in 2000 to 0.9-1 TgS in 2050, and decreases to $\sim$0.6 TgS in 2100. After 2080, the simulations calculate sulfate burden larger than that in 2000 despite decreases in SO_2 emission relative to 2000, owing to H_2O_2 increases which enhance the liquid-phase sulfate formation. Exp2 predicts even larger sulfate burdens after 2030 compared to Exp1, resulting from changes in precipitation due to warming.

Acid deposition of both NO_3^- and SO_4^{2-} increases by a factor of 3 in eastern Asia in 2050. The calculated NO_3^- deposition and SO_4^{2-} deposition equally contribute to precipitation pH around eastern Asia in 2050, causing significant increases (by a factor of 5-10) in precipitation acidity ($[H^+]$) associated with NO_3^- and SO_4^{2-}. As a consequence, this future simulation, based on the SRES A2 scenario, implies serious acid rain and deposition in future eastern Asia.

This study simulates future changes in sulfate distribution considering changes in cloud water pH which largely controls the sulfate formation (SO_2 oxidation) process in liquid-phase. However, note that the present model version of CHASER, used in this study, calculates cloud water pH with a quite simple scheme (Appendix 2B) and may mispredict pH in cloud drops and hence sulfate formation. Further model development is necessary for a better simulation of the sulfate formation process especially in the future atmospheres. It should be also noted that the CCSR/NIES GCM, which CHASER is based on, has high climate sensitivity, and may exaggerate the impact of climate change on tropospheric chemistry in this study. This study performs future simulations using the SRES A2 scenario only. In the further investigation, we will conduct simulations for other scenarios and evaluate sensitivity of tropospheric chemistry involving O_3, CH_4, sulfate, and precipitation acidity to emission scenario.

Chapter 6

General Conclusions

This study has newly developed a global chemical model of the troposphere, named CHASER (CHemical AGCM for Study of atmospheric Environment and Radiative forcing). The CHASER model, developed in the framework of Center for Climate System Research/National Institute for Environment Studies (CCSR/NIES) atmospheric general circulation model (AGCM) [*Numaguti*, 1993; *Numaguti et al.*, 1995], is aimed to study the tropospheric chemistry involving ozone and its influences on climate. CHASER is driven on-line by meteorology generated by the AGCM to allow meteorological fields (climate) and tropospheric chemistry to interact in the model. The model in this study calculates concentrations of 54 chemical species with 139 reactions (gas/liquid, and heterogeneous phase). The model simulates detailed O_3-HO_x-NO_x-CH_4-CO and NMHCs chemistry on-line with a time step of 10 min (section 2.2.1), and includes also detailed dry/wet deposition schemes (section 2.2.3). The present version of CHASER, introduced and used in this study, newly includes an improved wet deposition scheme, heterogeneous reactions on aerosols for N_2O_5 and several peroxyradicals RO_2, and also the sulfate formation process (section 2.2.1), compared to the previous version [*Sudo et al.*, 2002a]. The wet deposition scheme in the previous version of CHASER [*Sudo et al.*, 2002a] has been improved to simulate the deposition process on ice cloud (cirrus) particles and reversible below-cloud scavenging process in this study (section 2.2.3). With the improved wet deposition scheme, the present model is capable to simulate the liquid/ice-phase concentrations of individual species dissolved in precipitation. The model computes NO_3^- and SO_4^{2-} concentrations in precipitation well consistent with the observation (Figure 2.10 and 2.11). The sulfate (SO_4^{2-}) formation process is simulated using concentrations of H_2O_2, O_3, and OH computed on-line in the model. In the sulfate simulation, cloud water acidity $[H^+]$, calculated as a function of the liquid-phase concentrations of NO_3^- and SO_4^{2-} in the model, is reflected on the liquid-phase oxidation of SO_2. The model considers emission sources for NO_x (44.3 TgN/yr including lightning NO_x of 5 TgN/yr), CO (1267 TgCO/yr), and NMHCs (including isoprene, 400 TgC/yr and terpenes, 102 TgC/yr). In CHASER, NO_x emissions from lightning are parameterized in the CCSR/AGCM convection, based on *Price and Rind* [1992] and *Price et al.* [1997]. SO_2 and DMS emissions (79.4 and 15 TgS/yr, respectively) are also included for the sulfate simulation in the model. Seasonal variation of biomass burning emissions is simulated using the satellite derived hot-spot data (from ATSR and AVHRR). The sulfate simulation is reflected on-line on the heterogeneous reaction process in the model, but not coupled with the AGCM radiation component at this stage. For this study, the T42 horizontal resolution ($\sim 2.8^\circ \times 2.8^\circ$) is chosen with 32 vertical layers from the surface to about 40 km altitude. The basic time step for the dynamical and physical processes in the model is 20 min.

In the detailed evaluation of CHASER(section 2.3), the model results have been evaluated with a number of observations. The evaluation shows that the model generally calculates ozone and precursor gases quite consistent with observations, well capturing distributions and seasonal variations of individual species as observed. The model calculations show excellent agreement with observations in most cases for important trace gases such as CO, NMHCs, NO_y species, HO_x and related species (formaldehyde, acetone, and peroxides) as well as for ozone. In the evaluation of NO_y species, simulation of HNO_3 appears to be improved with the new wet deposition scheme in this study, compared to the previous version of CHASER [*Sudo et al.*, 2002b]. The model in this study, however, overestimates PAN in the central Pacific as in the previous simulation [*Sudo et al.*, 2002b], implying the need for further evaluation of the adopted oxidation scheme for NMHCs species (section 2.2.1) and also investigation to check the sensitivity to heterogeneous uptake (loss) of unsaturated peroxyradicals (RO_2) on aerosols in the model. In this study, the simulated HO_x species ($= OH + HO_2$) are also evaluated in detail. The model appears to calculate OH and HO_2 distributions much close to the observations during the PEM-Tropics-B and TRACE-P expeditions. The global methane lifetime against the tropospheric OH reaction, an useful measure for OH abundance in the troposphere, is estimated at 9.4 years in this study (the IPCC estimate is 9.6 years). The ozone distributions simulated in this study are generally in excellent agreement with a number of observations, well capturing the seasonal variation of ozone in both polluted and remote locations. The model, however, tends to overestimate slightly upper tropospheric ozone in the midlatitudes in both hemispheres, which may imply overestimation of stratospheric influx of ozone in the midlatitudes. The calculated global budget of tropospheric ozone shows a chemical production of 4746 TgO_3/yr (with a net production of 367 TgO_3/yr), well within the range suggested by the previous works (3206 TgO_3/yr, *Roelofs and Lelieveld* [1995] to 5258 TgO_3/yr, *Horowitz et al.* [2002]). The estimated net stratospheric O_3 influx is 531.4 TgO_3/yr, consistent with the previous studies (300-800 TgO_3/yr). However, this estimated value (531.4 TgO_3/yr) may be overestimated, since the model in this study tends to overestimate upper tropospheric O_3 in the midlatitudes. This point will be a focus of the further development in the next version of CHASER. The sulfate simulation in this study generally shows good agreement with observations for SO_2 and sulfate, but tends to overestimate surface SO_2 and sulfate levels in polluted areas (especially in Europe) in summer, indicating overestimation of cloud water acidity $[H^+]$ and/or the need of including seasonal variation of residential SO_2 emissions in the model. This study simulates the liquid-phase SO_2 oxidation using cloud water acidity $[H^+]$ computed as a function of NO_3^- and SO_4^{2-} with a constant neutralizing factor (Appendix 2B). The next model version is expected to include more detailed oxidation schemes for both SO_2 and DMS.

Using the developed model, this study estimates the radiative forcing due to tropospheric ozone increase since preindustrial times (chapter 3). This study calculates a tropospheric ozone increase from 197 TgO_3 in preindustrial times to 311 TgO_3 in presentday, corresponding to a 10.4 DU increase in tropospheric column ozone. The resultant radiative forcing from anthropogenic ozone is 0.49 W m^{-2} (0.40 longwave, 0.085 short wave), well comparable with the CH_4 radiative forcing ($\sim$0.5 W m^{-2}). The calculated ozone radiative forcing is most significant in the northern midlatitudes with showing peak values larger than 1 W m^{-2} over around the Middle East. The model estimates peak ozone forcings larger than 1.5 W m^{-2}, comparable with the CO_2 forcing, over the United States and the Middle East in summer. However, the ozone abundances simulated for preindustrial times appear to be overestimated by a factor of 1.5-2 as in *Mickley et al.* [2001], implying possible underestimation of radiative forcing from tropospheric ozone increase in this study. Further investigation on the preindustrial atmosphere including natural emissions such as lightning NO_x and biogenic NMHCs is needed for an accurate estimate of the radiative forcing from tropospheric ozone.

Chapter 4 has evaluated the tropical ozone distributions simulated by CHASER with satellite based observations using TOMS. The model appears to reproduce the well-known zonal wavenumber 1 pattern in tropical tropospheric column ozone (TCO), with a peak over the Atlantic and a minimum over the Pacific as observed. This study shows that the wavenumber 1 in tropical TCO comes primarily from upper tropospheric ozone production from lightning NO_x emission and biogenic and biomass burning emissions particularly in South America and Africa. The large-scale Walker Circulation also appears to contribute much to the wave 1 in TCO. The differences between the observed and modeled TCO distributions increase with latitude especially in the region encompassing North Africa, the Middle East, and India. Further development of the observational method for deriving tropospheric ozone in higher latitudes outside the tropics is expected to contribute to a better comparison with models. This chapter has also revealed the relationship between tropical meteorology and ozone distribution, simulating the meteorological impact of the 1997-1998 El Niño on the tropical tropospheric ozone distributions. The simulation, well reproducing the observed ozone anomalies (increase and decrease) in October 1997, suggests that the zonal shift in the Walker Circulation and convection pattern during the El Niño , together with the large changes in water vapor distributions, significantly influences the ozone production and destruction processes and contributes much to the observed large-scale ozone changes. This study indicates the key factors controlling the simulated ozone changes as (1) the downward/upward motions associated with the zonal convergence/divergence in the upper troposphere, (2) the suppressed/enhanced convection, and (3) the associated water vapor (H_2O) changes in the tropics. As a consequence, the simulations in this study imply that tropospheric ozone and related chemistry are significantly controlled by natural meteorological conditions such as large-scale and convective transport, and water vapor distributions.

This study has simulated future tropospheric chemistry involving ozone and sulfate using the CHASER model. This study evaluates the impacts of both emission changes and climate change with the SRES A2 scenario, conducting two kinds of experiments; control (Exp1) and climate change (warming) experiments (Exp2). In Exp2 with climate change, the GCM simulates future climate change with greenhouse gases specified by the A2 scenario, and SST and sea ice distributions prescribed by the CCSR/NIES atmosphere-ocean coupled GCM [*Nozawa et al.*, 2001] with the A2 scenario. The simulations for Exp1 and Exp2 are performed for individual decades from 1990 to 2100 (time-slice simulation). Global CH_4 concentrations are predicted using the A2 emission scenario for CH_4, and global OH and temperature fields calculated for every decades in the simulation. Global tropospheric ozone simulated in Exp1 linearly increases by 23% in 2050 and by $\sim$44% in 2100 relative to 2000. Annual mean surface O_3 concentrations in eastern Asia increase from 40-50 ppbv in 2000 to 60-80 ppbv in 2050, and to 70-90 ppbv in 2100. In Exp2 with climate change (warming), the ozone increases as predicted in Exp1 are reduced by 10-20% in the lower-middle troposphere after around 2050 due to water vapor increases. On the contrary, Exp2 predicts additional ozone increases in the upper troposphere in the low to midlatitudes compared to Exp1, owing to enhanced ozone transport from the stratosphere associated with intensification of the Hadley Circulation and stratospheric circulation due to warming in the model. Exp2 calculates significant increases in global stratospheric O_3 input from about 600 TgO_3/yr in 2000 to more than 1200 TgO_3/yr in 2100 in accordance with warming in the model. As a result of enhanced stratospheric ozone input compensating for additional ozone destruction due to water vapor increases, Exp2 predicts evolution of global tropospheric ozone well similar to that in Exp1 during the course of the simulation (2000-2100). Although Exp2 predicts ozone reduction due to water vapor increases in the remote areas relative to Exp1, ozone in the polluted regions (in the boundary layer) is simulated to increase resulting from enhanced ozone production in response to temperatures and water vapor increases in Exp2. Global mean methane concentration increases to 4 ppmv in 2100 in Exp1 according to the prescribed methane emission increases and to OH decreases causing longer lifetime of methane. In Exp2, methane increases to only 3.4 ppmv in 2100 (15% reduction relative to Exp1), as a result of higher OH levels associated with water vapor increases and temperatures increases which lead to shorter lifetime of methane. In the simulation of sulfate, Exp1 predicts a peak increase in sulfate burden during 2030-2050, calculating a burden of 0.9-1 TgS. The simulations in Exp1 suggest that the sulfate formation efficiency increases after around 2030 due to H_2O_2 increases to enhance liquid-phase SO_2 oxidation particularly in the low latitudes, and causes sulfate burdens larger than in 2000 even after 2080 despite decreases in global SO_2 emission relative to 2000. Exp2 predicts additional sulfate increases after 2030, as a result of larger increases in H_2O_2 relative to Exp1 and changes in precipitation. This study suggests that levels of pollutant as ozone and sulfate increase significantly in eastern Asia including India, China, and Japan in the next hundred years, and also predicts that both nitrates (NO_3^-) and sulfate (SO_4^{2-}) deposition increases precipitation acidity largely, implying a serious acid deposition problem around eastern Asia. Although this study suggests that tropospheric ozone, methane, and sulfate in the future atmospheres are much influenced by climate change (warming), it should be noted that this study may exaggerate the warming impact on tropospheric chemistry such as enhancement in ozone production/destruction and increases in stratospheric ozone input, in view of the high climate sensitivity of the CCSR/NIES GCM [*Nozawa et al.*, 2001].

As summarized above, this study has evaluated changing processes of tropospheric chemistry involving ozone and sulfate, focusing on the impact of changes in meteorological fields (climate). Such discussions, however, seem to be quite sensitive to the representation of meteorology and climate in the model. Further investigation is expected to evaluate the representation of the physical and dynamical processes in the model as well as the chemistry process, for an accurate prediction of future climate and atmospheric environment. This study predicts future tropospheric chemistry with time-slice simulations for individual decades to 2100. As an issue for further investigation, we plan to predict future tropospheric chemistry with fully transient simulations and evaluate the role of the system of ozone-methane-aerosols in future climate and atmospheric environment.

References

Allen, M. D., and O. G. Raabe, Reevaluation of Milikan's oil drop data for the motion of small particles in air, *J. Aerosol. Sci., 13,* 537–547, 1982.

Andres, R. J., and A. D. Kasgnoc, A time-averaged inventory of subaerial volcanic sulfur emissions, *J. Geophys. Res., 103,* 25,251–25,261, 1998.

Arino, O., J.-M. Rosaz, and J.-M. Melinotte, World Fire Atlas with AVHRR and ATSR, *Proceedings of the IUFRO Conference on Remote Sensing and Forest Monitoring,* Rogow Poland, 1999.

Arnold, F., V. Burger, B. Droste-Franke, F. Grimm, A. Krieger, J. Schneider, and T. Stilp, Acetone in the upper troposphere and lower stratosphere: Impact on trace gases and aerosols, *Geophys. Res. Lett., 24,* 3017–3020, 1997.

Atkinson, R., D. L. Baulch, R. A. Cox, R. F. Hampson, J. A. Kerr, M. J. Rossi, and J. Troe, Evaluated kinetic and photochemical data for atmospheric chemistry: Supplement VII - IUPAC subcommittee on gas kinetic data evaluation for atmospheric chemistry, *J. Phys. Chem. Ref. Data*, *28*, 191–393, 1999.

Atkinson, R., D. L. Baulch, R. A. Cox, R. F. Hampson, J. A. Kerr, and M. J. Rossi, Evaluated kinetic and photochemical data for atmospheric chemistry: Supplement VIII - IUPAC subcommittee on gas kinetic data evaluation for atmospheric chemistry, *J. Phys. Chem. Ref. Data*, *29*, 167–266, 2000.

Atlas, E., and B. A. Ridley, The Mauna Loa Observatory Photochemistry Experiment: An introduction, *J. Geophys. Res., 101,* 14,531–14,541, 1996.

Aumont, B., S. Madronich, M. Ammann, M. Kalberer, U. Baltensperger, D. Hauglustaine, and F. Brocheton, On the $NO_2 +$ soot reaction in the atmosphere, *J. Geophys. Res., 104,* 1729–1736, 1999.

Balkanski, Y. Y., D. J. Jacob, and G. M. Gardner, Transport and residence times of tropospheric aerosols inferred from a global three-dimensional simulation of ^{210}Pb, *J. Geophys. Res., 98,* 20,573–20,586, 1993.

Bates, T. S., R. J. Charlson, and R. H. Gammon, Evidence for the climate role of marine biogenic sulphur, *Nature*, *329,* 319–321, 1987.

Battan, L. J., and C. H. Reitan, *Droplet size measurements in convective clouds, in Artificial simulation of Rain,* Pergamon Press, pp. 184-191, New York, 1957.

Berntsen, T. K., and I. S. A. Isaksen, A global three-dimensional chemical transport model for the troposphere, *J. Geophys. Res.*, *102,* 21,239–21,280, 1997a.

Berntsen, T. K., I. S. A. Isaksen, G. Myhre, J. S. Fuglestvedt, F. Stordal, T. Alsvik, Larsen, R. S. Freckleton, and K. P. Shine, Effects of anthropogenic emissions on tropospheric ozone and its radiative forcing, *J. Geophys. Res.*, *102*, 28,101–28,126, 1997b.

Bottenheim, J. W., S. Sirois, K. A. Brice, and A. J. Gallant, Five years of continuous observations of PAN and ozone at a rural location in eastern Canada, *J. Geophys. Res.*, *99*, 5333–5352, 1994.

Brasseur, G. P., D. A. Hauglustaine, S. Walters, and P. J. Rasch, MOZART, a global chemical transport model for ozone and related chemical tracers, 1., Model description, *J. Geophys. Res.*, *103*, 28,265–28,289, 1998.

Cantrell, C. A., W. R. Stockwell, L. G. Anderson, K. L. Busarow, D. Perner, A. Schmeltekopf, J. G. Calvert, and H. S. Johnston, Kinetic study of the NO_3-CH_2O reaction and its possible role in nighttime tropospheric chemistry, *J. Phys. Chem.*, *89*, 139–146, 1985.

Carter, W., A detailed mechanism for the gas-phase atmospheric reactions of organic compounds, *Atmos. Environ.*, *24A*, 481–518, 1990.

Chalita, S., D. Hauglustaine, H. L. Treut, and J.-F. Müller, Radiative forcing due to increased tropospheric ozone concentrations, *Atmos. Environ.*, *30*, 1641–1646, 1996.

Chameides, W. L., et al., Ozone precursor relationships in the ambient atmosphere, *J. Geophys. Res.*, *97*, 6037–6055, 1992.

Chandra, S., J. R. Ziemke, W. Min, and W. G. Read, Effects of 1997-1998 El niño on tropospheric ozone and water vapor, *Geophys. Res. Lett.*, *25*, 3867–3870, 1998.

Chandra, S., J. R. Ziemke, P. Bhartia, and R. V. Martin, Tropical tropospheric ozone: Implications for dynamics and biomass burning, *J. Geophys. Res.*, *107*(D14), 10.129/2001JD000,447, 2002a.

Chandra, S., J. R. Ziemke, and R. V. Martin, Tropospheric ozone at tropical and middle latitudes derived from TOMS/MLS residual: Comparison with a global model, *J. Geophys. Res.*, submitted, 2002b.

Cohan, D. S., M. G. Schultz, D. J. Jacob, B. G. Heikes, and D. R. Blake, Convective injection and photochemical decay of peroxides in the tropical upper troposphere: Methyl iodide as a tracer of marine convection, *J. Geophys. Res.*, *104*, 5717–5724, 1999.

Crawford, J., et al., Photochemistry state analysis of the NO_2-NO system based on airborne observations from the western and central North Pacific, *J. Geophys. Res.*, *101*, 2053–2072, 1996.

Crawford, J., et al., An assessment of ozone photochemistry in the extratropical western North Pacific: Impact of continental outflow during the late winter/early spring, *J. Geophys. Res.*, *102*, 28,469–28,487, 1997.

Crutzen, P. J., and P. H. Zimmermann, The changing photochemistry of the troposphere, *Tellus*, *43*, 136–151, 1991.

Daniel, J. S., and S. Solomon, On the climate forcing of carbon monoxide, *J. Geophys. Res.*, *103*, 13,249–13,260, 1998.

DeMore, W. B., S. P. Sander, D. M. Golden, R. F. Hampson, M. J. Kurylo, C. J. Howard, A. R. Ravishankara, C. E. Kolb, and M. J. Molina, *Chemical Kinetics and Photochemical Data for Use in Stratospheric Modeling*, *JPL Publ*, *97-4*, Jet Propul. Lab., Pasadena, Calif., 1997.

Dentener, F. J., and P. Crutzen, Reaction of N_2O_5 on tropospheric aerosols: impact on the global distributions of NO_x, O_3, and OH, *J. Geophys. Res.*, *98*, 7149–7162, 1993.

Emmons, L. K., D. A. Hauglustaine, J.-F. Müller, M. A. Carroll, G. P. Brasseur, D. Brunner, J. Staehelin, V. Thouret, and A. Marenco, Data composites of airborne observations of tropospheric ozone and its precursors, *J. Geophys. Res.*, *105*, 20,497–20,538, 2000.

Emori, S., T. Nozawa, A. Abe-Ouchi, A. Numaguti, M. Kimoto, and T. Nakajima, Coupled Ocean-Atmosphere Model Experiments of Future Climate Change with an Explicit Representation of Sulfate Aerosol Scattering, *J. Meteor. Soc. Japan*, *77*, 1299–1307, 1999.

Emori, S., T. Nozawa, A. Numaguti, and I. Uno, Importance of Cumulus Parameterization for Precipitation Simulation over East Asia in June, *J. Meteor. Soc. Japan*, *79*, 939–947, 2001.

Fan, S.-M., S. C. Wofsy, P. S. Bakwin, D. J. Jacob, and D. R. Fitzjarrald, Atmosphere-biosphere exchange of CO_2 and O_3 in the Central Amazon Forest, *J. Geophys. Res.*, *95*, 16,851–16,864, 1990.

Fan, S.-M., D. J. Jacob, D. L. Mauzerall, J. D. Bradshaw, S. T. Sandholm, D. R. Blake, R. W. T. H. B. Singh, G. L. Gregory, and G. W. Sachse, Photochemistry of reactive nitrogen in the sub Arctic troposphere in summer 1990: Observation and modeling, *J. Geophys. Res.*, *99*, 16,867–16,878, 1994.

Fishman, J., and J. C. Larsen, Distribution of total ozone and stratospheric ozone in the tropics: Implications for the distribution of tropospheric ozone, *J. Geophys. Res.*, *92*, 6627–6634, 1987.

Fishman, J., et al., The NASA GTE TRACE A Experiment (September-October 1992): Overview, *J. Geophys. Res.*, *101*, 23,865–23,879, 1996.

Folkins, I., R. Chatfield, H. Singh, Y. Chen, and B. Heikes, Ozone production efficiencies of acetone and peroxides in the upper troposphere, *Geophys. Res. Lett.*, *25*, 1305–1308, 1998.

Forster, P. M., C. E. Johnson, K. S. Law, J. A. Pyle, and K. P. Shine, Further estiates of radiative forcing due to tropospheric ozone changes, *Geophys. Res. Lett.*, *23*, 3321–3324, 1996.

Frössling, N., The evaporating of falling drops, *Beitr. Geophys.*, *52*, 170–216, 1938.

Fuglestvedt, J. S., J. E. Johnson, W.-C. Wang, and I. S. A.Isaksen, Responses in tropospheric chemistry to changes in UV fluxes, temperatures and water vapour densities, in *Atmospheric Ozone as a Climate Gas,* edited by W.-C. Wang and I. S. A. Isaksen, NATO ASI Series vol. I32, Springer-Verlag, pp.145-162, 1995.

Fuglestvedt, J. S., I. S. A. Isaksen, and W.-C. Wang, Estimates of indirect global warming potentials for CH_4, CO and NO_x, *Climate Change, 34,* 405–437, 1996.

Fujiwara, M., K. Kita, S. Kawakami, T. Ogawa, N. Komala, S. Saraspriya, and A. Suripto, Tropospheric ozone enhancements during the indonesian forest fire events in 1994 and 1997 as revealed by ground-based observations, *Geophys. Res. Lett.*, *26*, 2417–2420, 1999.

Fujiwara, M., K. Kita, T. Ogawa, S. Kawakami, T. Sano, N. Komala, S. Saraspriya, and A. Suripto, Seasonal variation of tropospheric ozone in indonesia revealed by 5-year ground-based observations, *J. Geophys. Res.*, *105*, 1879–1888, 2000.

Gierczak, T., J. B. Burkholder, S. Bauerle, and A. R. Ravishankara, Photochemistry of acetone under tropospheric conditions, *Chem. Phys.*, *231*, 229–244, 1998.

Giorgi, F., and W. L. Chameides, The rainout parameterization in a photochemical model, *J. Geophys. Res.*, *90*, 7872–7880, 1985.

Graedel, T. E., et al., A compilation of inventories of emissions to the atmosphere, *Global Biogeochem Cycles*, *7*, 1–26, 1993.

Greenberg, J. P., D. Helmig, and P. Zimmmerman, Seasonal measurements of nonmethane hydrocarbons and carbon monoxide at Mauna Loa Observatory during the Mauna Loa Observatory, *J. Geophys. Res.*, *101*, 14,581–14,598, 1996.

Gregory, G. L., H. E. Fuelberg, S. P. Longmore, B. E. Anderson, J. E. Collins, and D. R. Blake, Chemical characteristics of tropospheric air over the tropical South Atlantic Ocean: Relationship to trajectory history, *J. Geophys. Res.*, *101*, 23,957–23,972, 1996.

Grewe, V., et al., Impact of future subsonic aircraft emissions on the atmospheric compositions, *Geophys. Res. Lett.*, *26*, 47–50, 1999.

Guenther, A., et al., A global model of natural volatile organic compound emissions, *J. Geophys. Res.*, *100*, 8873–8892, 1995.

Hao, W. M., and M.-H. Liu, Spatial distribution of tropical biomass burning in 1980 with $5^\circ \times 5^\circ$ resolution, *Global Biogeochem. Cycles*, *8*, 495–503, 1994.

Hauglustaine, D. A., C. Granier, G. P. Brasseur, and G. Megie, The importance of atmospheric chemistry in the calculation radiative forcing on the climate systemu, *J. Geophys. Res.*, *99*, 1173–1186, 1994.

Hauglustaine, D. A., B. A. Ridley, S. Solomon, P. G. Hess, and S. Madronich, HNO_3/NO_x ratio in the remote troposphere during MLOPEX2: Evidence for nitric acid reduction on carbonaceous aerosols?, *Geophys. Res. Lett.*, *23*, 2609–2612, 1996.

Hauglustaine, D. A., G. P. Brasseur, S. Walters, P. J. Rasch, J.-F. Müller, L. K. Emmons, and M. A. Carroll, MOZART, a global chemical transport model for ozone and related chemical tracers, 2., Model results and evaluation, *J. Geophys. Res.*, *103*, 28,291–28,335, 1998.

Hauglustaine, D. A., G. P. Brasseur, and J. S. Levine, A sensitivity simulation of tropospheric ozone changes due to the 1997 Indonesian fire emissions, *Geophys. Res. Lett.*, *26*, 3305–3308, 1999.

Haywood, J. M., M. D. Schwarzkopf, and V. Ramaswamy, Estimates of radiative forcing due to modeled increases in tropospheric ozone, *J. Geophys. Res.*, *103*, 16,999–17,007, 1998.

Heikes, B., et al., Ozone, hydroperoxides, oxides of nitrogen, and hydrocarbon budget in the marine boundary layer over the South Atlantic, *J. Geophys. Res.*, *101*, 24,221–24,234, 1996.

Hertel, O., R. Berkowicz, and J. Christensen, Test of two numerical schemes for use in atomospheric transport-chemistry models, *Atmos. Environ.*, *27A*, 2591–2611, 1993.

Hoffmann, M. R., and J. G. Calvert, *Chemical Transformation Modules for Eulerian Acid Deposition Models, Volume 2, The Aqueous-Phase Chemistry*, EPA/600/3-85/017. U.S. Environmental Protection Agency, Research Triangle Park, NC, 1985.

Horowitz, L. W., J. Liang, G. M. Gardner, and D. J. Jacob, Export of reactive nitrogen from North America during summertime: Sensitivity to hydrocarbon chemistry, *J. Geophys. Res.*, *103*, 13,451–13,476, 1998.

Horowitz, L. W., et al., A global simulation of tropospheric ozone and related tracers: Description and evaluation of MOZART, version 2, *J. Geophys. Res.*, submitted, 2002.

Houghton, J. T., et al., *Climate Change 1994: The IPCC Scientific Assessment*, Cambridge Univ. Press, New York, 1995.

Houghton, J. T., et al., *Climate Change 1995: The IPCC Scientific Assessment*, Cambridge Univ. Press, New York, 1996.

Houweling, S., F. Dentener, and J. Lelieveld, Impact of nonmethane hydrocarbon compounds on tropospheric photochemistry, *J. Geophys. Res.*, *103*, 10,673–10,696, 1998.

Hudson, R. D., and A. M. Thompson, Tropical tropospheric ozone from total ozone mapping spectrometer by a modified residual method, *J. Geophys. Res.*, *103*, 22,129–22,145, 1998.

Intergovernmental Panel on Climate Change (IPCC), *Climate Change 2001: The Scientific Basis*, J. T. Houghton, Y. Ding, D.J. Griggs, M. Noguer, P. J. van der Linden and D. Xiaosu (Eds.), Cambridge University Press, UK. pp 944, 2001.

Jacob, D. J., Heterogeneous chemistry and tropospheric ozone, *Atmos. Environ.*, *34*, 2131–2159, 2000.

Jacob, D. J., B. D. Field, E. M. Jin, I. Bye, Q. Li, J. A. Logan, and R. M. Yantosca, Atmospheric budget of acetone, *J. Geophys. Res.*, *107(D10)*, 10.1029/2001JD000,694, 2002.

Jacob, D. J., et al., Deposition of ozone to tundra, *J. Geophys. Res.*, *97*, 16,473–16,479, 1992.

Jacob, D. J., et al., Origin of ozone and NO_x in the tropical troposphere: A photochemical analysis of aircraft observations over the South Atlantic basin, *J. Geophys. Res.*, *101*, 24,235–24,250, 1996.

Jacob, D. J., et al., Evaluation and intercomparison of global atmospheric transport models using ^{222}Rn and other short-lived tracers, *J. Geophys. Res.*, *102*, 5953–5970, 1997.

Jaeglé, L., et al., Observed OH and HO_2 in the upper troposphere suggest a major source from convective injection of peroxides, *Geophys. Res. Lett.*, *24*, 3181–3184, 1997.

Jaeglé, L., et al., Photochemistry of HO_x in the upper troposphere at northern midlatitudes, *J. Geophys. Res.*, *105*, 3877–3892, 1999.

Jenkin, M. E., S. M. Saunders, and M. J. Pilling, The tropospheric degradation of volatile organic compounds: A protocol for mechanism development, *Atmos. Environ.*, *31*, 81–104, 1997.

Jiang, Y. B., and Y. L. Yung, Concentrations of tropospheric ozone from 1979 to 1992 over tropical Pacific South America from TOMS data, *Science*, *272*, 714–716, 1996.

Johnson, C. E., and R. G. Derwent, Relative radiative forcing consequences of global emissions of hydrocarbons, carbon monoxide and NOx from human activities estimated with a zonally averaged two-dimensional model, *Climate Change*, *34*, 439–462, 1996.

Johnson, C. E., W. J. Collins, D. S. Stevenson, and R. G. Derwent, Relative roles of climate and emissions changes on future tropospheric oxidant concentrations, *J. Geophys. Res.*, *104*, 18,631–18,645, 1999.

Johnson, C. E., D. S. Stevenson, W. J. Collins, and R. G. Derwent, Role of climate feedback on methane and ozone studied with a coupled Ocean-Atmosphere-Chemistry model, *Geophys. Res. Lett.*, *28*, 1723–1726, 2001.

Kanakidou, M., and P. J. Crutzen, Scale problems in global tropospheric chemistry modeling: Comparison of results obtained with a three-dimensional model adopting longitudinally uniform and varying emissions of NO_x and NMHC, *Chemosphere*, *26*, 787–801, 1993.

Kim, J. H., and M. J. Newchurch, Climatology and trends of tropospheric ozone over the eastern Pacific Ocean: The influence of biomass burning and tropospheric dynamics, *Geophys. Res. Lett.*, *23*, 3723–3726, 1996.

Kim, J. H., M. J. Newchurch, and K. Han, Distribution of tropical tropospheric ozone determined by the scan-angle method applied to TOMS measurements, *J. Atmos. Sci.*, *58*, 2699–2708, 2001.

Kirchhoff, V. W. J. H., A. W. Setzer, and M. C. Pereira, Biomass burning in Amazonia: Seasonal effects on atmospheric, *Geophys. Res. Lett.*, *16*, 469–472, 1989.

Kley, D., P. J. Crutzen, H. G. J. Smit, H. Vömel, S. J. Oltmans, H. Grassl, and V. Ramanathan, Observations of near-zero ozone concentrations over the convective Pacific: Effects on air chemistry, *Science*, *274*, 230–233, 1996.

Konovalov, I. B., Application of newral networks for studying nonlinear relationships between ozone and its precursors, *J. Geophys. Res.*, *107*, 10.1029/2001JD000,863, 2002.

Kritz, M. A., S. W. Rosner, and D. Z. Stockwell, Validation of an off-line three-dimensional chemical transport model using observed radon profiles, 1., Observations, *J. Geophys. Res.*, *103*, 8425–8432, 1998.

Lacis, A. A., D. J. Wuebbles, and J. A. Logan, Radiative forcing of climate by changes in the vertical distribution of ozone, *J. Geophys. Res.*, *95*, 9971–9981, 1990.

Landgraf, J., and P. J. Crutzen, An efficient method for online calculations of photolysis and heating rates, *J. Atmos. Sci.*, *55*, 863–878, 1998.

Langner, J., and H. Rodhe, A global three-dimensional model of the tropospheric sulfur cycle, *J. Atmos. Chem.*, *13*, 225–263, 1991.

Lawrence, M. G., and P. J. Crutzen, The impact of cloud particle gravitational settling on soluble trace gas distributions, *Tellus, Ser. B*, *50*, 263–289, 1998.

Lawrence, M. G., P. J. Crutzen, P. J. Rasch, B. E. Eaton, and N. M. Mahowald, A model for studies of tropospheric photochemistry: Description, global distributions, and evaluation, *J. Geophys. Res.*, *104*, 26,245–26,277, 1999.

Lee, H. N., and J. Feichter, An intercomparison of wet precipitation scavenging schemes and the emission rates of ^{222}Rn for the simulation of global transport and deposition of ^{210}Pb, *J. Geophys. Res.*, *100*, 23,253–23,270, 1995.

Lelieveld, J., and R. van Dorland, Ozone chemistry changes in the troposphere and consequent radiative forcing of climate, in *Atmospheric Ozone As a Climate Gas*, edited by W.-C. Wang and I. S. A. Isaksen, pp. 227–258, Springer–Verlag, New York, 1995.

Levy, H., II, Normal atmosphere: Large radical and formaldehyde concentrations predicted, *Science*, *173*, 141–143, 1971.

Levy, H., II, J. D. Mahlman, and W. J. Moxim, Tropospheric ozone: The role of transport, *J. Geophys. Res.*, *90*, 3753–3772, 1985.

Levy, H., II, P. S. Kasibhatla, W. J. Moxim, A. A. Klonecki, A. I. Hirsch, S. J. Oltmans, and W. L. Chamedies, The global impact of human activity on tropospheric ozone, *Geophys. Res. Lett.*, *24*, 791–794, 1997.

Li, Q., et al., A tropospheric ozone maximum over the Middle East, *Geophys. Res. Lett.*, *28*(17), 3235–3238, 2001.

Lin, S.-J., and R. B. Rood, Multidimensional flux-form semi-lagrangian transport schemes, *Mon. Wea. Rev.*, *124*, 2046–2070, 1996.

Liu, S. C., M. Trainer, F. C. Fehsenfeld, D. D. Parrish, E. J. Williams, D. W. Fahey, G. Hübler, and P. C. Murphy, Ozone production in the rural troposphere and the implications for regional and global ozone distributions, *J. Geophys. Res.*, *92*, 4191–4207, 1987.

Logan, J. A., An analysis of ozonesonde data for the troposphere: Recommendations for testing 3-D models and development of a gridded climatology for tropospheric ozone, *J. Geophys. Res.*, *104*, 16,115–16,149, 1999.

Lucus, D. D., and R. G. Prinn, Mechanism studies of dimethylsulfide oxidation products using an observationally constrained model, *J. Geophys. Res.*, *107(D14)*, 10.1029/2001JD000,843, 2002.

Lyons, W. A., T. E. Nelson, E. R. Williams, J. A. Cramer, and T. R. Turner, Enhanced positive cloud-to-ground lightning in thunderstorms ingesting smoke from fires, *Science*, *282*, 77–80, 1998.

Mahowald, N. M., P. J. Rasch, B. E. Eaton, S. Whittlestone, and R. G. Prinn, Transport of ^{222}Radon to the remote troposphere using MATCH and assimilated winds from ECMWF and NCEP/NCAR, *J. Geophys. Res.*, *102*, 28,139–28,152, 1997.

Marenco, A., H. Gouget, P. Nédélec, J. P. Pagés, and F. Karcher, Evidence of a long-term increase in tropospheric ozone from Pic du Midi data series: Consequences: Positive radiative forcing, *J. Geophys. Res.*, *99*, 16,617–16,632, 1994.

Mari, C., et al., Sources of upper tropospheric HOx over the South Pacific Convergence Zone: a case study, *J. Geophys. Res.*, PEM-Tropics B special issue, submitted, 2001.

Martin, R. S., H. Westberg, E. Allwine, L. Ashman, J. C. Farmer, and B. Lamb, Measurement of isoprene and its atmospheric oxidation products in a central Pennsylvania deciduous forest, *J. Atmos. Chem.*, *13*, 1–32, 1991.

Martin, R. V., et al., Global model analysis of TOMS and in-situ observations of tropical tropospheric ozone, *J. Geophys. Res.*, in press, 2002.

Mason, B. J., *The physics of Clouds*, Clarendon, Oxford, 1971.

Massman, W. J., J. Pederson, A. Delany, D. Grantz, G. den Hartog, H. H. Neumann, S. P. Oncley, and R. Pearson, Jr., An evaluation of the regional acid deposition model surface module for ozone uptake at three sites in the san joaquin valley of california, *J. Geophys. Res.*, *99*, 8281–8294, 1994.

McFarlane, N. A., The effect of orographically exited gravity wave drag on the general circulation of the lower stratosphere and troposphere, *J. Atmos. Sci.*, *44*, 1775–1800, 1987.

McFarquhar, G. M., and A. J. Heymsfield, Microphysical characteristics of three anvils sampled during the Central Equatorial Pacific Experiment, *J. Atmos. Sci.*, *53*, 2401–2423, 1996.

McKeen, S. A., et al., The photochemistry of acetone in the upper troposphere: A source of odd-hydrogen radicals, *Geophys. Res. Lett.*, *24*, 3177–3180, 1997.

McLinden, C. A., S. C. Olsen, B. Hannegan, O. Wild, M. J. Prather, and J. Sundet, Stratospheric ozone in 3-D models: A simple chemistry and the cross-tropopause flux, *J. Geophys. Res.*, *105*, 14,653–14,665, 2000.

Meilinger, S. K., B. Kärcher, R. von Kuhlmann, and T. Peter, On the Impact of Heterogeneous Chemistry on Ozone in the Tropopause Region, *Geophys. Res. Lett.*, *28*, 515–518, 2001.

Mellor, G. L., and T. Yamada, A hierarchy of turbulence closure models for planetary boundary layers, *J. Atmos. Sci.*, *31*, 1791–1806, 1974.

Mickley, L. J., P. P. Murti, D. J. Jacob, J. A. Logan, D. M. Koch, and D. Rind, Radiative forcing from tropospheric ozone calculated with a unified chemistry-climate model, *J. Geophys. Res.*, *104*, 30,153–30,172, 1999.

Mickley, L. J., D. J. Jacob, and D. Rind, Uncertainty in preindustrial abundance of tropospheric ozone: Implications for radiative forcing calculations, *J. Geophys. Res.*, *106*, 3389–3399, 2001.

Montzka, S. A., M. Trainer, W. M. Angevine, and F. C. Fehsenfeld, Measurements of 3-methyl furan, methyl vinyl ketone, and methacrolein at a rural forested site in the southeastern United States, *J. Geophys. Res.*, *100*, 11,393–11,401, 1995.

Moxim, W. J., H. Levy, II, and P. S. Kashibhatla, Simulated global tropospheric PAN: Its transport and impact on NO_x, *J. Geophys. Res.*, *101*, 12,621–12,638, 1996.

Müller, J.-F., Geographical distribution and seasonal variation of surface emissions and deposition velocities of atmospheric trace gases, *J. Geophys. Res.*, *97*, 3787–3804, 1992.

Müller, J.-F., and G. P. Brasseur, IMAGES: A three-dimensional chemical transport model of the global troposphere, *J. Geophys. Res.*, *100*, 16,445–16,490, 1995.

Müller, J.-F., and G. P. Brasseur, Sources of upper tropospheric HO_x: A three-dimensional study, *J. Geophys. Res.*, *104*, 1705–1715, 1999.

Nakajima, T., and M. Tanaka, Matrix formulation for the transfer of solar radiation in a plane-parallel scattering atmosphere, *J. Quant. Spectrosc. Radiat. Transfer*, *35*, 13–21, 1986.

Nakajima, T., M. Tsukamoto, Y. Tsusima, and A. Numaguti, Modeling of the radiative process in a AGCM, in *Reports of a New Program for Creative Basic Research Studies, Studies of Global Environment Change With Special Reference to Asia and Pacific Regions, Rep., I-3*, pp.104–123, CCSR, Tokyo, 1995.

Newchurch, M. J., D. Sun, and J. H. Kim, Tropical tropospheric ozone derived using clear-cloudy pairs (CCP) of TOMS measurements, *J. Atmos. Sci.*, submitted, 2002.

Novelli, P. C., L. P. Steele, and P. P. Tans, Mixing ratios of carbon monoxide in the troposphere, *J. Geophys. Res.*, *97*, 20,731–20,750, 1992.

Novelli, P. C., J. E. Collins, Jr., R. C. Myers, G. W. Sachsem, and H. E. Scheel, Reevaluation of the NOAA/CMDL carbon monoxide reference scale and comparisons to CO reference gases at NASA-Langley and the Fraunhofer Institute, *J. Geophys. Res.*, *99*, 12,833–12,839, 1994.

Nozawa, T., S. Emori, A. Numaguti, Y. Tsuhima, T. Takemura, T. Nakajima, A. Abe-Ouchi, and M. Kimoto, Projections of future climate change in the 21st century simulated by the CCSR/NIES CGCM under the IPCC SRES scenarios. *Present and Future of Modeling Global Environmental Change toward Integrated Modeling*, T. Matsuno and H. Kida, Eds., Terra Scientific Publishing, 15-28, 2001.

Numaguti, A., Dynamics and energy balance of the hadley circulation and the tropical precipitation zones: Significance of the distribution of evaporation, *J. Atmos. Sci.*, *50*, 1874–1887, 1993.

Numaguti, A., Origin and recycling processes of precipitating water over the Eurasian continent: Experiments using an atmospheric general circulation model, *J. Geophys. Res.*, *104*, 1957–1972, 1999.

Numaguti, A., M. Takahashi, T. Nakajima, and A. Sumi, Development of an atmospheric general circulation model, in *Reports of a New Program for Creative Basic Research Studies, Studies of Global Environment Change With Special Reference to Asia and Pacific Regions, Rep., I-3*, pp.1–27, CCSR, Tokyo, 1995.

Olivier, J. G. J., et al., Description of EDGAR Version 2.0. A set of global emission inventories of greenhouse gases and ozone-depleting substances for all anthropogenic and most natural sources on a per country basis and on 1ox1o grid, *RIVM Rep. 771060 002/TNO*, Natl. Inst. for Public Health and the Environ., Bilthoven, Netherlands, 1996.

Oltmans, S. J., and H. Levy, II, Surface ozone measurements from a global network, *Atmos. Environ.*, *28*, 9–24, 1994.

Parrish, D. D., et al., The total reactive oxidized nitrogen levels and the partitioning between the individual species at six rural sites in eastern North America, *J. Geophys. Res.*, *98*, 2927–2939, 1993.

Penner, J. E., D. H. Lister, D. Griggs, D. J. Docken, and M. M. (Eds.), *Aviation and the global atmosphere*, pp. 373, Cambridge University Press, UK, 1999.

Perry, R. H., and D. Green, *Perry's Chemical Engineers Handbook*, pp. 3-285, McGraw-Hill, New York, 1984.

Pickering, K. E., A. M. Thompson, J. R. Scala, W. K. Tao, R. R. Dickerson, and J. Simpson, Free tropospheric ozone production following entrainment of urban plumes into deep convection, *J. Geophys. Res.*, *97*, 17,985–18,000, 1992.

Pickering, K. E., Y. Wang, W.-K. Tao, C. Price, and J.-F. Müller, Vertical distributions of lightning NO_x for use in regional and global chemical transport models, *J. Geophys. Res.*, *103*, 31,203–31,216, 1998.

Pöschl, U., R. von Kuhlmann, N. Poisson, and P. J. Crutzen, Development and intercomparison of condensed isoprene oxidation mechanisms for global atmospheric modeling, *J. Atmos. Chem.*, *37*, 29–52, 2000.

Prather, M., Lifetimes and eigenstates in atmospheric chemistry, *Geophys. Res. Lett.*, *21*, 801–804, 1994.

Prather, M., et al., *Atmospheric Chemistry and Greenhouse Gases, In: Climate Change 2001: The Scientific Basis. Contribution of Working Group I to the Third Assessment Report of the Intergovernmental Panel on Climate Change*, Cambridge Univ. Press, New York, 2001.

Price, C., and D. Rind, A simple lightning parameterization for calculating global lightning distributions, *J. Geophys. Res.*, *97*, 9919–9933, 1992.

Price, C., and D. Rind, Possible implications of global climate change on global lightning distributions and frequencies, *J. Geophys. Res.*, *99*, 10,823–10,831, 1994.

Price, C., J. Penner, and M. Prather, NO_x from lightning, 1., Global distribution based on lightning physics, *J. Geophys. Res.*, *102*, 5929–5941, 1997.

Prinn, R. G., R. F. Weiss, B. R. Miller, J. Huang, F. N. Alyea, D. M. Cunnold, P. J. Fraser, D. E. Hartley, and P. G. Simmonds, Atmospheric trends and lifetime of CH_3CCl_3 and global OH concentrations, *Science*, *269*, 187–192, 1995.

Randel, W. J., Seasonal cycles and QBO variations in stratospheric CH4 and H2O observed in UARS HALOE data, *J. Atmos. Sci.*, *55*, 163–185, 1998.

Rehfeld, S., and M. Heimann, Three dimensional atmospheric transport simulation of the radioactive tracers ^{210}Pb, ^{7}Be, ^{10}Be, and ^{90}Sr, *J. Geophys. Res.*, *100*, 26,141–26,161, 1995.

Ridley, B. A., and E. Robinson, The Mauna Loa Observatory Photochemistry Experiment, *J. Geophys. Res.*, *97*, 10,285–10,290, 1992.

Ridley, B. A., et al., Measurements of NO_x and PAN and estimates of O_3 production over the seasons during Mauna Loa Observatory Photochemistry Experiment 2, *J. Geophys. Res.*, *103*, 8323–8339, 1998.

Ritter, J. A., J. D. Barrick, C. E. Watson, G. W. Sachse, G. L. Gregory, B. E. Anderson, M. A. Woerner, and J. E. Collins, Jr., Airborne boundary layer flux measurements of trace gas species over canadian boreal forest and northern wetland regions, *J. Geophys. Res.*, *99*, 1671–1685, 1994.

Roelofs, G.-J., Radiative forcing by tropospheric ozone: Impact of cloud representation, *Geophys. Res. Lett.*, *26*, 467–470, 1999.

Roelofs, G.-J., and J. Lelieveld, Distribution and budget of O_3 in the troposphere calculated with a chemistry general circulation model, *J. Geophys. Res.*, *100*, 20,983–20,998, 1995.

Roelofs, G.-J., and J. Lelieveld, Tropospheric ozone simulation with a chemistry-general circulation model: Influence of higher hydrocarbon chemistry, *J. Geophys. Res.*, *105*, 22,697–22,712, 2000.

Roelofs, G.-J., J. Lelieveld, and R. van Dorland, A three-dimensional chemistry/general circulation model simulation of anthropogenically derived ozone in the troposphere and its radiative climate forcing, *J. Geophys. Res.*, *102*, 23,389–23,401, 1997.

Russel, J. M., III, et al., The halogen occultation experiment, *J. Geophys. Res.*, *98*, 10,777–10,798, 1993.

Sander, S. P., et al., *Chemical Kinetics and Photochemical Data for Use in Stratospheric Modeling, Supplement of Evaluation 12: Update of Key Reactions*, *JPL Publ*, *00-3*, Jet Propul. Lab., Pasadena, Calif., 2000.

Sawa, Y., H. Matsueda, Y. Tsutsumi, J. Jensen, H. Y. Inoue, and Y. Makino, Tropospheric carbon monoxide and hydrogen measurements over Kalimantan in Indonesia and northern Australia during October 1997, *Geophys. Res. Lett.*, *26*, 1389–1392, 1998.

Schultz, M., et al., On the origin of tropospheric ozone and NO_x over the tropical South Pacific, *J. Geophys. Res.*, *104*, 5829–5843, 1999.

Schwartz, S. E., Mass-transport considerations pertinent to aqueous phase reactions of gases in liquid water clouds, in *Chemistry of Multiphase Atmospheric Systems, NATO ASI Ser.*, edited by W. Jaeschke, Springer, Berlin, 1986.

Shiotani, M., and F. Hasebe, Stratospheric ozone variations in the equatorial region as seen in Stratospheric Aerosol and Gas Experiment data, *J. Geophys. Res.*, *99*, 14,575–14,584, 1994.

Sillman, S., and P. J. Samson, Impact of temperature on oxidant photochemistry in urban, polluted rural and remote environments, *J. Geophys. Res.*, *100*, 11,497–11,508, 1995.

Singh, H. B., M. Kanakidou, P. J. Crutzen, and D. J. Jacob, High concentrations and photochemical fate of oxygenated hydrocarbons in the global troposphere, *Nature*, *378*, 50–54, 1995.

Singh, H. B., et al., Reactive nitrogen and ozone over the western Pacific: Distribution, partitioning, and sources, *J. Geophys. Res.*, *101*, 1793–1808, 1996.

Six, K. D., and E. Maier-Reimer, Effects of plankton dynamics on seasonal carbon fluxes in an ocean general circulation model, *Global Biogeochem. Cycles*, *10*, 559–583, 1996.

Solberg, S., C. Dye, N. Schmidbauer, A. Herzog, and R. Gehrig, Carbonyls and nonmethane hydrocarbons at rural European sites from the Mediterranean to the Arctic, *J. Atmos. Chem.*, *25*, 33–66, 1996.

Spivakovsky, C. M., et al., Three-dimensional climatological distiribution of tropospheric OH: Update and evaluation, *J. Geophys. Res.*, *105*, 8931–8980, 2000.

Staehelin, J., J. Thudium, R. Buehler, A. Volz-Thomas, and W. Graber, Trends in surface ozone concentrations at Arosa (Switzerland), *Atmos. Environ.*, *28*, 75–87, 1994.

Stevenson, D. S., C. E. Johnson, W. J. Collins, R. G. Derwent, and J. M. Edwards, Future estimates of tropospheric ozone radiative forcing and methane turnover - the impact of climate change, *Geophys. Res. Lett.*, *27*, 2073–2076, 2000.

Stockwell, D. Z., M. A. Kritz, M. P. Chipperfield, and J. A. Pyle, Validation of an off-line three-dimensional chemical transport model using observed radon profiles, 2., model results, *J. Geophys. Res.*, *103*, 8433–8445, 1998.

Sudo, K., and M. Takahashi, Simulation of tropospheric ozone changes during 1997-1998 El Niño: Meteorological impact on tropospheric photochemistry, *Geophys. Res. Lett.*, *28*, 4091–4094, 2001.

Sudo, K., M. Takahashi, J. Kurokawa, and H. Akimoto, CHASER: A global chemical model of the troposphere 1. Model description, *J. Geophys. Res.*, *107*(D17), 10.1029/2001JD001113, 2002a.

Sudo, K., M. Takahashi, and H. Akimoto, CHASER: A global chemical model of the troposphere 2. Model results and evaluation, *J. Geophys. Res.*, *107*(D21), 10.1029/2001JD001114, 2002b.

Tabazadeh, A., O. B. Toon, S. L. Clegg, and P. Hammill, A new parameterization of H_2SO_4/H_2O aerosol composition: Atmospheric implications, *Geophys. Res. Lett.*, *24*, 1931–1934, 1997.

Takemura, T., H. Okamoto, Y. Maruyama, A. Numaguti, A. Higurashi, and T. Nakajima, Global three-dimensional simulation of aerosol optical thickness distribution of various origins, *J. Geophys. Res.*, *105*, 17,853–17,873, 2000.

Takemura, T., T. Nakajima, T. Nozawa, and K. Aoki, Simulation of Future Aerosol Distribution, Radiative Forcing, and Long-Range Transport in East Asia, *J. Meteor. Soc. Japan*, *79*, 1139–1155, 2001.

Takemura, T., T. Nakajima, O. Dubovik, B. N. Holben, and S. Kinne, Single-Scattering Albedo and Radiative Forcing of Various Aerosol Species with a Global Three-Dimensional Model, *J. Climate*, *15*, 333–352, 2002.

Takigawa, M., M. Takahashi, and H. Akiyoshi, Simulation of ozone and other chemical species using a center for climate system research/national institute for environmental studies atmospheric gcm with coupled stratospheric chemistry, *J. Geophys. Res.*, *104*, 14,003–14,018, 1999.

Talbot, R. W., et al., Chemical characteristics of continental outflow over the tropical South Atlantic Ocean from Brazil and Africa, *J. Geophys. Res.*, *101*, 24,287–24,202, 1996.

Talukdar, R. K., C. A. Longfellow, M. K. Gilles, and A. R. Ravishankara, Quantum yields of $\mathrm{O}(^1\mathrm{D})$ in the photolysis of ozone between 289 and 329 nm as a function of temperature, *Geophys. Res. Lett.*, *25*, 143–146, 1998.

Thompson, A. M., The oxidizing capacity of the Earth's atmosphere: Probable past and future changes, *Science*, *256*, 1157–1165, 1992.

Thompson, A. M., and R. D. Hudson, Tropical tropospheric ozone (TTO) maps from Nimbus 7 and Earth Probe TOMS by the modified-residual method: Evaluation with sondes, ENSO signals, and trends from Atlantic regional time series, *J. Geophys. Res.*, *104*, 26,961–26,975, 1999.

Thompson, A. M., R. W. Stewart, M. A. Owens, and J. A. Herwehe, Sensitivity of tropospheric oxidants to global chemical and climate change, *Atmos. Environ.*, *23*, 519–532, 1989.

Thompson, A. M., K. E. Pickering, D. P. McNamara, M. R. Schoeberl, R. D. Hudson, J. H. Kim, E. V. Browell, V. W. J. H. Kirchhoff, and D. Nganga, Where did tropospheric ozone over southern Africa and the tropical Atlantic come from in October 1992? Insights from TOMS, GTE/TRACE-A and SAFARI-92, *J. Geophys. Res.*, *101*, 24,251–24,278, 1996.

Thompson, A. M., J. C. Witte, R. D. Hudson, H. Guo, J. R. Herman, and M. Fujiwara, Tropical tropospheric ozone and biomass burning, *Science*, *291*, 2128–2132, 2001.

Thompson, A. M., et al., SHADOZ (Southern Hemisphere Additional Ozonesondes) tropical ozone climatology 1. Comparisons with TOMS and ground-based measurements, *J. Geophys. Res.*, in press, 2002.

van Dorland, R., F. J. Dentener, and J. Lelieveld, Radiative forcing due to tropospheric ozone and sulfate aerosols, *J. Geophys. Res.*, *102*, 28,079–28,100, 1997.

van Leer, B., Toward the ultimate conservative difference scheme. Part IV: A new approach to numerical convection, *J. Comput. Phys.*, *23*, 276–299, 1977.

Van Pul, W. A. J., *The flux of ozone to a maize crop and the underlying soil during a growing season*, Ph.D. thesis, Wageningen Agric. Univ., Wageningen, Netherlands, 1992.

Velders, G. J. M., and C. Granier, Sensitivity of washout on HNO_3/NO_x ratio in atmospheric chemistry transport models, *J. Geophys. Res.*, *106*, 3125–3132, 2001.

Walcek, C. J., H.-H. Yuan, and W. R. Stockwell, The influence of aqueous-phase chemical reactions on ozone formation in polluted and nonpolluted cloud, *Atmos. Environ.*, *31*, 1221–1237, 1997.

Wang, W., J. P. Pinto, and Y. L. Yung, Greenhouse effects due to man-made perturbations of trace gases, *J. Atmos. Sci.*, *37*, 333–338, 1980.

Wang, Y., and D. J. Jacob, Anthropogenic forcing on tropospheric ozone and OH since preindustrial times, *J. Geophys. Res.*, *103*, 31,123–31,135, 1998d.

Wang, Y., D. J. Jacob, and J. A. Logan, Global simulation of tropospheric O_3-NO_x-hydrocarbon chemistry 1. Model formulation, *J. Geophys. Res.*, *103*, 10,713–10,725, 1998a.

Wang, Y., J. A. Logan, and D. J. Jacob, Global simulation of tropospheric O_3-NO_x-hydrocarbon chemistry 2. Model evaluation and global ozone budget, *J. Geophys. Res.*, *103*, 10,727–10,755, 1998b.

Wang, Y., D. J. Jacob, and J. A. Logan, Global simulation of tropospheric O_3-NO_x-hydrocarbon chemistry 3. origin of tropospheric ozone and effects of nonmethane hydrocarbons, *J. Geophys. Res.*, *103*, 10,757–10,767, 1998c.

Wennberg, P. O., et al., Hydrogen radicals, nitrogen radicals and the production of O_3 in the upper troposphere, *Science*, *279*, 49–53, 1998.

Wesely, M. L., Parameterization of surface resistance to gaseous dry deposition in regional-scale numerical models, *Atmos. Environ.*, *23*, 1293–1304, 1989.

Westcott, N. E., Summertime cloud-to-ground lightning activity around major midwestern urban areas, *J. App. Meteor.*, *34*, 1633–1642, 1995.

Whelpdale, D. M., and J. W. Miller, GAW and precipitation chemistry measurement activities , Fact Sheet Number 5, Background Air Pollution Monitoring Program, World Meteorological Organization, Geneva, Switzerland, 1989.

Wild, O., and H. Akimoto, Intercontinental transport of ozone and its precursors in a three-dimensional global CTM, *J. Geophys. Res.*, *106*, 27,729–27,744, 2001a.

Wild, O., M. J. Prather, and H. Akimoto, Indirect long-term global radiative cooling from NO_x emissions, *Geophys. Res. Lett.*, *28*, 1719–1722, 2001b.

WMO, *Report of the International Ozone Trends Panel: 1988*, Global Ozone Research and Monitoring Project: Report No. 18, Geneva, 1990.

WMO, *Scientific Assessment of Ozone Depletion: 1998*, Global Ozone Research and Monitoring Project: Report No. 44, Geneva, 1999.

World Health Organization (WHO), *Update and revision of the WHO air quality guidelines for Europe. Classical air pollutants ; ozone and other photochemical oxidants.*, European centre for environment and health, Bilthoven, the Netherlands, 1996a.

World Health Organization (WHO), *Update and revision of the WHO air quality guidelines for Europe. Ecotoxic effects, ozone effects on vegetation.*, European centre for environment and health, Bilthoven, the Netherlands, 1996b.

Yienger, J. J., and H. Levy, II, Empirical model of global soil-biogenic NO_x emissions, *J. Geophys. Res.*, *100*, 11,447–11,464, 1995.

Ziemke, J. R., and S. Chandra, Seasonal and interannual variabilities in tropical tropospheric ozone, *J. Geophys. Res.*, *104*, 21,425–21,442, 1999.

Ziemke, J. R., S. Chandra, and P. K. Bhartia, Two new methods for deriving tropospheric column ozone from TOMS measurements: Assimilated UARS MLS/HALOE and convective-cloud differential techniques, *J. Geophys. Res.*, *103,* 22,115–22,127, 1998.

Ziemke, J. R., S. Chandra, and P. K. Bharita, ”Cloud slicing”: A new technique to derive upper tropospheric ozone from satellite measurements, *J. Geophys. Res.*, *106*, 9853–9867, 2001.

Zimmerman, P. R., J. P. Greenberg, and C. E. Westberg, Measurements of atmospheric hydrocarbons and biogenic emission fluxes on the Amazon boundary layer, *J. Geophys. Res.*, *93*, 1407–1416, 1988.